Functional Organic Fluorophores Based on 1,3-Dithiafulvene and Pyrene

by

A thesis submitted to the School of Graduate Studies in partial fulfilment of

the requirements for the degree of

Ph.D.

Department of Chemistry

Memorial University of Newfoundland

October 2020

St. John's Newfoundland

Abstract

This thesis demonstrates the design, synthesis, and application of fluorene and pyrene-based organic π-systems, in which redox-active 1,3-dithiafulvenyl (DTF) groups are incorporated. The detailed studies encompass three classes of novel redox-active organic fluorophores. The first project deals with fluorene-cored π-conjugated phenylene vinylene dendrimers with DTF end groups attached to the peripheral positions. The oxidative coupling reactivity of the DTF group allowed these dendrimers to undergo facile electropolymerization on conductive substrates. By means of multi-cycle cyclic voltammetric scans, redox-active microporous polymer thin films were successfully generated. The redox-active polymer prepared through a double-layer strategy, in which a polymer thin film prepared from a dithiafulvenyl-substituted phenylacetylene precursor was surface-modified with a fluorene-cored phenylene vinylene dendrimer carrying dithiafulvenyl end groups. The experimental results indicated that the polymers can act as highly sensitive and selective electrochemical sensors for 2,4,6-trinitrotoluene (TNT), one of the most important nitroaromatic explosives.

In the second project, a group of DTF-functionalized pyrene derivatives was prepared and investigated. The redox activities and electrochemical properties of these compounds were examined by voltammetric analysis. Polymer films generated through electropolymerization of these redox-active pyrenes have been found to show responsiveness to nitromethane. In addition, one of the derivatives shows an unusually high efficiency in terms of hydrogen/deuterium exchange, which can be potentially used for trapping deuterium isotope.

The third project focuses on a comparative study of a series of new K-region functionalized pyrene derivatives. Three new K-region functionalized pyrene derivatives were synthesized using pyrene-4,5-dione as the starting material. The X-ray single crystal structures of three compounds were determined and examined by the Hirshfeld surface analysis. The molecular geometries of these pyrene derivatives were found to strongly affect the intramolecular noncovalent interactions in the solid state. Moreover, the electronic and electrochemical redox properties of these pyrene derivatives were characterized. Among the three pyrene derivatives, a dithiafulvenyl substituted derivative presents an intriguing D–A conjugated system with a small bandgap (E_g) and amphoteric redox behavior, making this compound a potentially useful organic semiconductor. The findings disclosed in this work show promise for the development of pyrene-based organic solid materials for advanced optoelectronic applications.

The fourth and last project investigates a new class of pyreno/phenanthro-annulated 1,3-diaza-4-azulenones, which could be readily synthesized through a straightforward one-pot condensation approach. The molecular properties of these compounds were analyzed by single-crystal X-ray crystallography, UV-vis absorption, and fluorescence spectroscopy. Our results showed that the emission behavior of these compounds is highly sensitive to solvent polarity and acidity, rendering them novel fluorosolvatochromic and acidochromic dyes that can be potentially utilized in chemosensing and bioimaging applications.

Acknowledgements

First of all, I would like to express my sincere thanks to my supervisor Dr. Yuming Zhao for his guidance and support during my research work and thesis writing. Yuming is a person who I always wanted to be. He is kind, supportive, knowledgeable, and the best teacher. He is the most helpful person that I know. I have learned so much from him in chemistry, science, and lifestyle, and this was such a great research experience for me. I would also like to thank my supervisory committee members Drs. Sunil Pansare and Christopher Flinn, for their help and guidance throughout my program. I would also like to thank Dr. Michael Katz for helping me to solve and better understanding the crystal structure of complex molecule. I would like to thank Dr. Jian-Bin Lin, one of the best crystallographers in Canada. Dr. Lin is very supportive, hard worker, and knowledgeable. I would also like to thank my lovely parents for their encouragement and support during my entire life. I wish to thank my love, Rezvan, who has stood by me through my journey, absences, and impatience. She gave me support and help, discussed ideas, and prevented several wrong turns. She always encourages me for further success. I would also like to thank my fantastic colleagues: Mohammadreza Khadem, Eyad Younes, Cheng Wang, Matthew Johnson, Christopher Qiu, Zahra Ahmadian, Ramin Eradeh, Monther Zeird, Maryam Faghih, Roxana Fazli, Fatemeh Salami, Azin Afzali in our research group as well as other research groups in the Chemistry and Physics Department. They helped me a lot during my program. I would like to thank all of my friends in St. John's. They were like a family for me, and I had lots of happy times with them. Last but not least, I would also like to thank all the faculty members

and staff of the Chemistry Department and Memorial University for creating such a great and friendly environment for students. I sincerely thank Memorial University and NSERC for funding and support.

List of Figures

List of Schemes

List of Abbreviations and Symbols

AFM	atomic force microscopy
AIEE	aggregation-induced enhanced emission
APPI	atmospheric pressure photo-ionization
aq	aqueous
BCP	bond critical point
BN	binaphthalene
ca.	circa
calcd	calculated
CBPQT	cyclobis(paraquat-*p*-phenylene)
CCDC	Cambridge Crystallographic Data Centre
CD	circular dichroism
CDCA	chenodeoxycholic acid
CL	chemiluminescence

cm	centimeter(s)
CP	conducting probe
C-T	charge-transfer
CV	cyclic voltammetry
d	doublet
COF	covalent organic framework
D-A	donor-acceptor
DFT	density functional theory
DMF	dimethylformamide
DMSO	dimethyl sulfoxide
DNA	deoxyribonucleic acid
DNT	2,4-dinitrotoluene
DPV	differential pulse voltammetry
DSSC	dye-sensitized solar cell
DTF	dithiafulvene or dithiafulvenyl
ESI	electronic supplementary information
Et	ethyl

E_g	band gap
exTTF	π-extended tetrathiafulvalene
FTIR	fourier transform infrared
FMO	frontier molecular orbital
g	gram(s)
GNPs	gold nanoparticles
h	hour(s)
HOMO	highest occupied molecular orbital
HRMS	high-resolution mass spectrometry
Hz	hertz
I	current
ICT	intramolecular charge transfer
ITO	indium tinoxide
IR	infrared
ISE	isomerization stabilization energy
J	coupling constant
LUMO	lowest unoccupied molecular orbital

m	multiplet
m/z	mass-to-charge ratio
MALDI-TOF	matrix-assisted laser desorption/ionization–time of flight
MCBJ	mechanically controlled break-junction
Me	methyl
mg	milligram(s)
MHz	megahertz
min	minute(s)
mL	milliliter(s)
mmol	millimole(s)
mol	mole(s)
MOF	metal organic framework
m.p.	melting point
MS	mass spectrometry
mV	millivolt(s)
mW	milliwatt(s)
NBO	natural bonding orbital

NCI	noncovalent interaction
NICS	nucleus independent chemical shift
NIR	near-infrared
NLO	nonlinear optical
nm	nanometer(s)
NMR	nuclear magnetic resonance
NMI	*N*-methylimidazole
OFET	organic field-effect transistor
OLED	organic light-emitting diode
OPE	oligo(phenylene ethynylene)
OPV	organic photovoltaic cell
ORTEP	Oak Ridge thermal ellipsoid plot
ox	oxidation
η	power conversion efficiency
PAH	polycyclic aromatic hydrocarbon
PET	photoinduced electron transfer
PI	pyrenoimidazole

PIMNA	pyrenoimidazole coupled with naphthalene
ppm	parts per million
PV	photovoltaic
PVSC	perovskite solar cell
PXRD	powder X-ray diffraction
ϕ	quantum yield
QTAIM	quantum theory of atoms in molecules
red	reduction
RDG	reduced density gradient
s	singlet
SAM	self-assembled monolayer
SEM	scanning electron microscopy
STM-BJ	scanning tunneling microscopy break-junction
SWCNT	single-walled carbon nanotube
t	triplet
TBAF	tetrabutylammonium fluoride
TD-DFT	time-dependent density functional theory

TFA	trifluoroacetic acid
THF	tetrahydrofuran
TLC	thin-layer chromatography
TPA	triphenylamine
TPPy	tetraphenylpyrene
DLS	dynamic light scattering
TNT	2,4,6-trinitrotoluene
TTF	tetrathiafulvalene
TTFAQ	anthraquinone-type π-extended tetrathiafulvalene
TTFV	tetrathiafulvalene vinylogue
UV-Vis	ultraviolet-visible
V	volt(s)
XRD	X-ray diffraction
δ	chemical shift
ϵ	molar extinction coefficient
λ_{max}	maximum absorption wavelength

Chapter 1

Introduction

1.1 Introduction to Tetrathiafulvalene (TTF) and Derivatives

Sulfur-containing heterocyclic compounds have found a wide range of application in current synthetic and medicinal chemistry. Among the vast number of such compounds, tetrathiafulvalene (TTF) stands out as the most popular and thoroughly investigated system in the literature.[1–7] TTF exhibits very good electron-donating ability and has been used as a π-electron donor in various redox-active π-conjugated materials and molecular devices. The molecular structure of TTF contains two non-aromatic 1,3-dithiole rings, which can be readily transformed into aromatic dithiolium rings via a two-step oxidation illustrated in Scheme 1.1. In the stepwise single-electron transfer reaction, **TTF1** first loos one electron at $E^1_{ox} = +0.34$ V to forma radical cation and then it loos another electron at $E^2_{ox} = +0.78$ V to form the dication.[8]

The first application of tetrathiafulvalene (TTF) was reported by Fred Wudl and

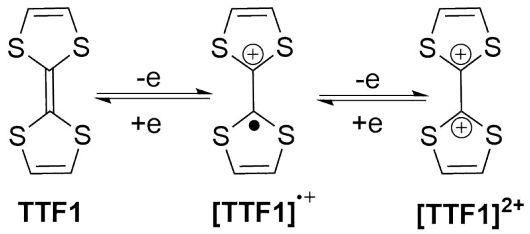

Scheme 1.1: Stepwise single-electron transfer reactions of TTF.

co-workers in the early 1970s. In their work, TTF was used as an active component for the generation of organic semiconductors.[9] Wudl's seminal work immediately captivated the attention of other researchers. Extensive studies focusing on TTF-based materials were quickly carried out, which promoted the rapid development of modern TTF chemistry.[10]

TTF is a redox-active molecular building block and has an electron-rich nature. TTF can form charge-transfer (C-T) complexes when interacting with proper electron acceptors. Many examples of TTF-based C-T complexes have been demonstrated with very good metallic conductivity and semiconductivity.[3,11,12] The excellent electron-donating properties of TTF can be ascribed to its unique aromaticity-stabilized cationic states resulting from one and two-electron oxidation (Scheme 1.1). Besides, notable changes in the molecular structure would occur in association with the oxidation of TTF. For instance, the TTF dication (TTF^{2+}) takes a geometry in which the two dithiolium moieties are perpendicular. The change in geometry also contributes to stabilizing the TTF dication by minimizing the disfavored charge repulsion within the molecule.[13]

1.1.1 Synthesis and Properties of TTFs

In the literature, the synthesis of TTF and related analogues can be divided into two main categories. The first category involves the synthesis of TTFs and π-extended TTFs (exTTFs) with different extension on the side chains of the dithiole five member ring. In the second category, the synthesis of TTFs was conducted by connecting the two dithioles through various π-conjugated bridges. The structure of TTF can be constructed through numerous routes using a range of small-molecule precursors as outlined Scheme 1.2.

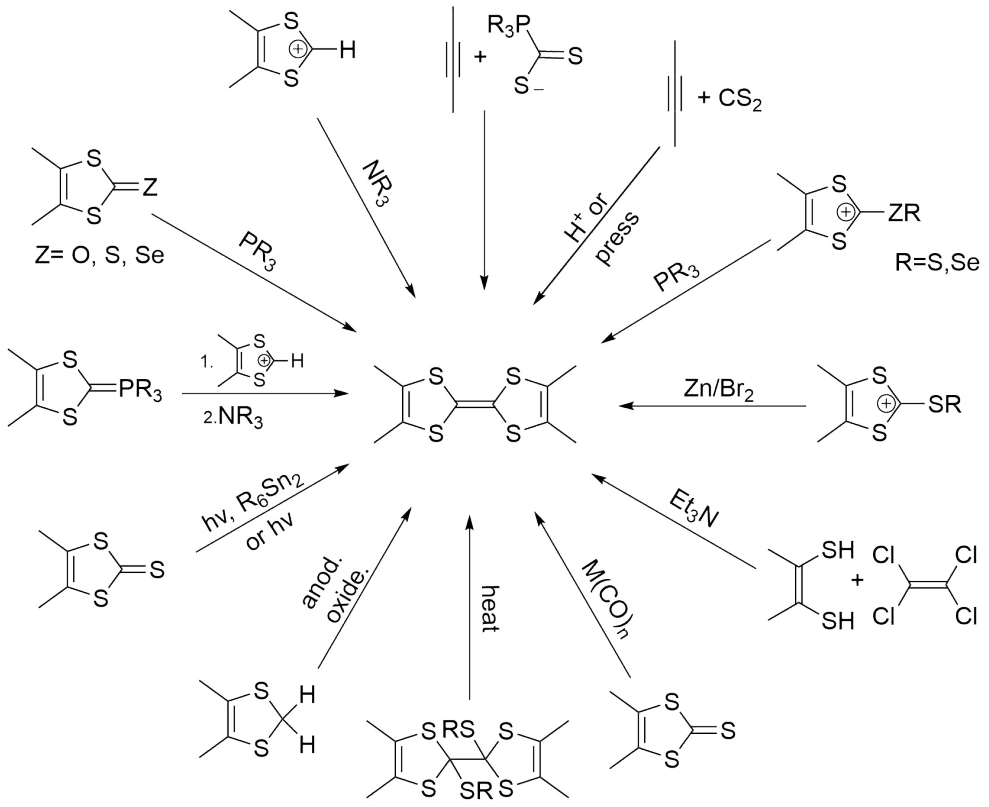

Scheme 1.2: Summary of synthetic methods for the preparation of the TTF skeleton.

Among the many known synthetic methods for TTFs, the phosphite-promoted

olefination of 1,3-dithiole-2-thiones is the most popular one. As illustrated in Scheme 1.3 (**A**), a 1,3-dithiole-2-thione **1-1** can be directly converted into the corresponding TTF product **1-2** in the presence of a trialkyl phosphite under heating. This approach leads to the formation of TTFs with a symmetric substitution pattern, but is unsuitable for the synthesis of unsymmetrically substituted TTFs. The reaction of a 1,3-dithiole-2-thione **1-4** with a 1,3-dithiole-2-one counterpart **1-3** promoted by triethyl phosphite can generate unsymmetrically-substituted TTF products (Scheme 1.3 (**B**)), which is complementary to the previous method. For the phosphite-promoted olefination reactions, high temperature is necessary to ensure good reaction yields. On the other hand, the condition of high temperature may negatively impact the synthesis of TTF derivatives that have limited thermal stability. To address this problem, an alternative olefination method based on Wittig-type reactions is often used (Scheme 1.3 (**C**)).[14]

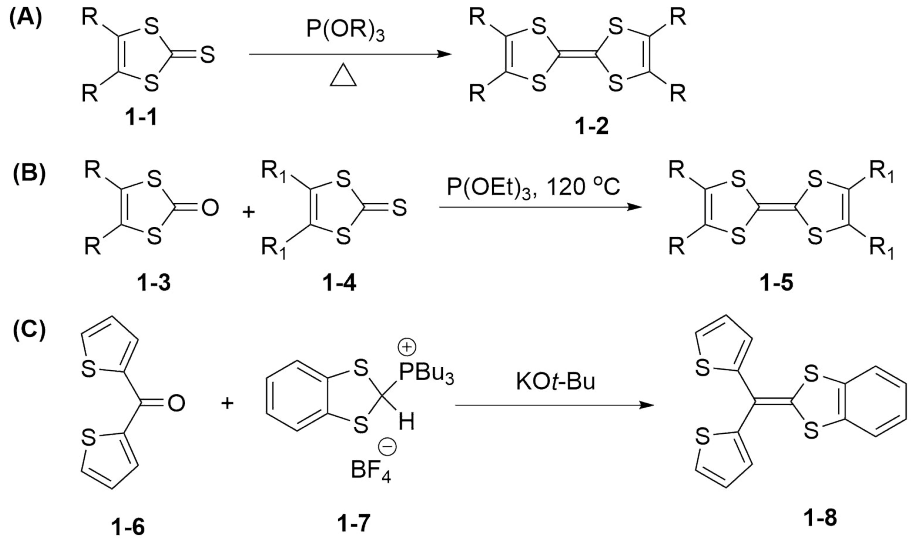

Scheme 1.3: Synthetic methods for symmetrical TTF **1-2**, unsymmetrical TTF **1-5** and DTF **1-8**.

1.1.2 π-Extended TTFs

Functionalization of TTF through the attachment of diverse groups has become a very efficient strategy for the development of new π-extended TTF derivatives (exTTFs). Many exTTFs have been found to show excellent electron-donating properties and versatile electrochemical redox activity as a result of the π-extension and substituents in their molecular structures. Most exTTFs show oxidation potentials lower than those of unsubstituted TTF because of the stabilizing effect of the extended π-conjugation on their cationic states. Also, the conformational properties of exTTFs are significantly different from those of TTF in the neutral and oxidized states. As such, exTTFs have been frequently employed as redox-controlled π-building blocks for the construction of nanoscale devices featuring responsiveness to external stimuli at the molecular and supramolecular levels.[12,15] The most notable application of exTTFs in molecular devices can be found in the class of rotaxane and catenane-based molecular machines developed by Sir Fraser Stoddart, who shared the 2016 Nobel Prize in Chemistry with Jean-Pierre Sauvage and Bernard L. Feringa for their contributions to the for the design and synthesis of molecular machines.[16]

For decades, materials chemists were motivated by the unique properties and flexibility of exTTFs in order to design functional organic electronic materials and molecular devices. There has been a large number of exTTFs synthesized and characterized in the literature.[17–19] The construction of exTTF derivatives can be conducted through two main routes: (i) the attachment of π-conjugated units to the dithiole rings (e.g., dibenzo-TTF in Fig. 1.1), (ii) the insertion of π-spacers in between the two dithiole rings, (e.g., anthraquinone-type π-extended

tetrathiafulvalene (TTFAQ) and tetrathiafulvenyl vinylogue (TTFV) in Fig. 1.1). Such exTTFs are highly redox-active and have shown great potential in the fields of nanotechnology and materials science.[8,12,20,21]

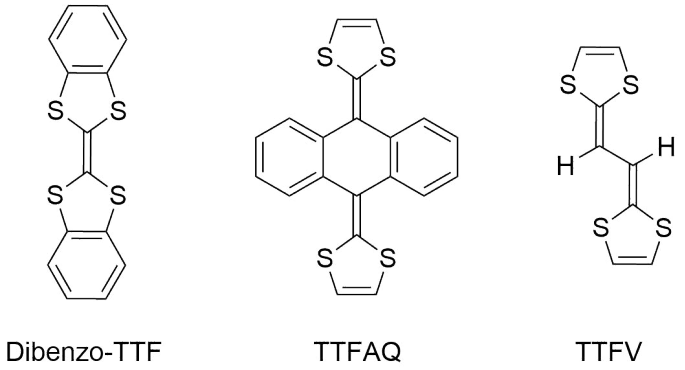

Figure 1.1: Selected examples of exTTFs.

1.1.3 Application of TTF in Functional Molecular Devices

TTF and exTTFs are widely applicable in materials chemistry because of their unique redox properties. They are excellent π-electron donors and can form C-T complexes with electron-accepting molecules to generate organic semiconductors, conductors, and even superconductors. TTFs can show C-T and π-π interactions with other conjugated materials, which enhance their application in supramolecular chemistry and molecular machinery. In this section, a brief literature review is outlined in regard to the application of TTFs and exTTFs in materials chemistry over the past years.

1.1.3.1 TTF Derivatives as Chemosensors

The electrochemical properties and redox-activity of TTF derivatives can be used for preparation of molecular sensors, redox fluorescent switches, redox-controlled gels,

molecular clips and tweezers.[22–26] In the application of electrochemical sensors, TTFs were used as the redox-active components for sensing various molecules and chemical species such as metal cations.[27] In the molecular design, a TTF core can be covalently linked to a receptor group through different types of linkage groups to generate a sensor system. In this type of sensors, TTF acts as a reporter unit to signal the binding event(s) through changes in redox current and/or potential. For instance, in the crown ether-TTFs shown in Fig. 1.2, the crown ether groups are the binding sites to selectively capture different metal ions. The binding of a metal cation with the crown ether group induces enhanced inductive effects on the TTF unit decreasing its electron density. As a result, the oxidation potential of the TTF core is shifted to a higher value upon binding with a metal cation. Experimentally, this process can be monitored by various voltammetric analyses to achieve sensitive detection and quantification of certain metal ions in the solution phase. The Becker group pioneered the studies of crown ether-annulated or tethered TTF derivatives as cation sensors.[2,28]

The synthesis of crown-ethers is challenging and needs ultra-high dilution conditions to attain satisfactory yields. Also, the construction of crown-TTF systems is often obstructed by relatively low solubility due to limited conformational flexibility. To avoid these problems, Bryce and co-workers designed some TTF sensors equipped with podand receptors in lieu of crown-ethers for certain transition metal ions (Fig. 1.3). Like the crown-ether systems, podand groups can act as binding sites for specific transition metal ions,[29,30] while the preparation of a podand structure is much easier and cost-effective. It is worth noting that podand receptors show different binding properties and selectivity for various metal ions than crown-ethers do. Therefore, the podand-TTF sensors are complementary to rather than replacements

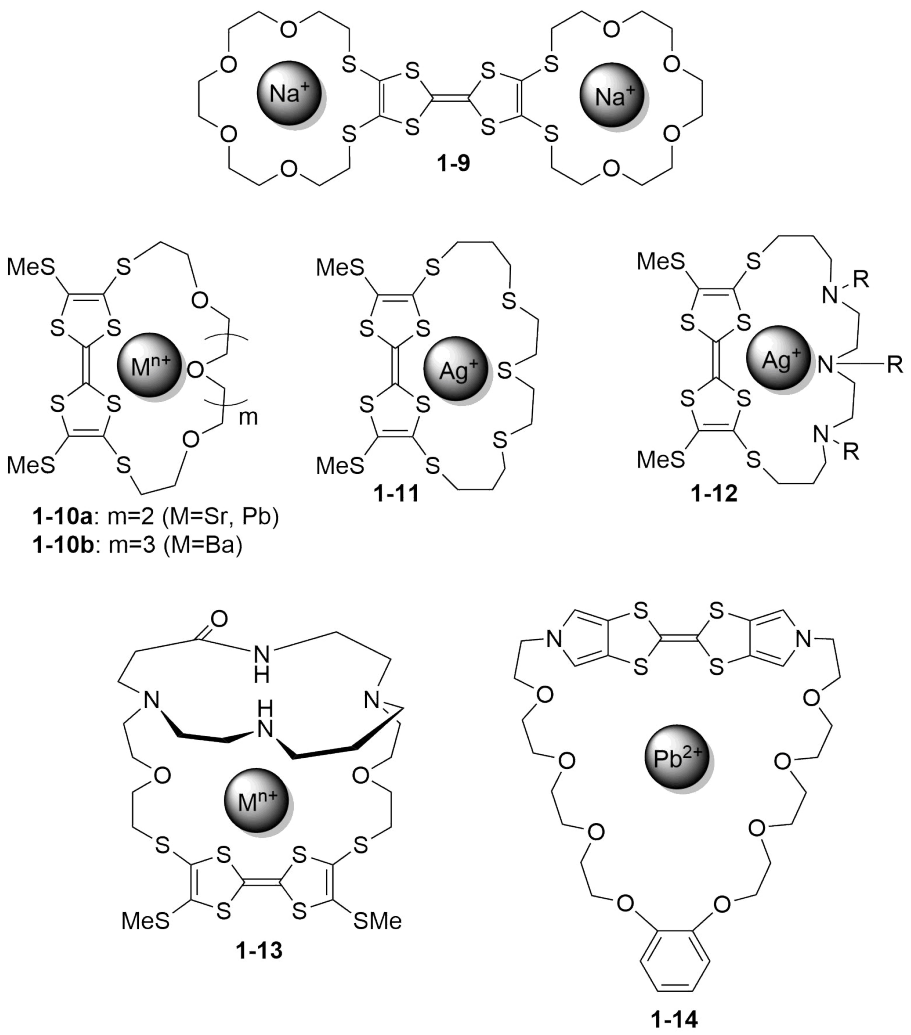

Figure 1.2: Examples of crown-annulated or tethered TTFs as metal cation sensors.

of the crown-TTF sensors.

The calix[4]arene system can also be utilized as a metal ion receptor. The rigid backbone of calix[4]arene generates a three-dimensional cavity that enhances the binding capacity, stoichiometry, and selectivity for certain metal ion guests. As such, sensors equipped with a calix[4]arene receptor usually show more robust metal ion binding ability. Fig. 1.4 illustrates an example of TTF-calix[4]arene hybrid **1-17** that acts as an effective sensor for sodium cation.[31,32]

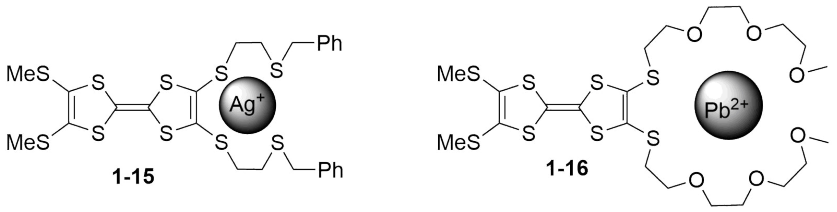

Figure 1.3: Examples of TTF-podand systems as transition metal ion sensors.

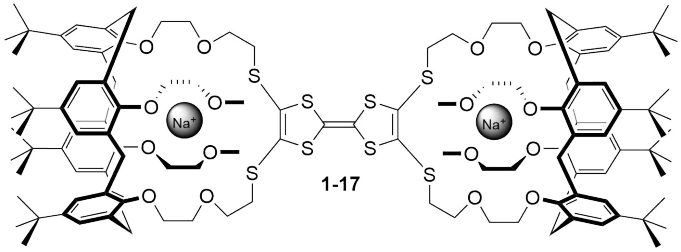

Figure 1.4: Bis(calix[4]arene)-TTF **1-17** as a robust Na^+ ion sensor.

Other types of TTF-based chemosensors worth mentioning are sensors for neutral and anionic chemical species. For instance, the anthryl-TTF derivatives **1-18** shown in Fig. 1.5 were synthesized and applied as chemiluminescent traps for the detection of singlet oxygen.[33,34] Singlet oxygen is a cytotoxic chemical that is very important in live cells.[35,36] An efficient detection technique for it is therefore highly desired.

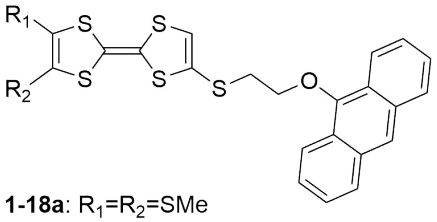

Figure 1.5: Anthryl-TTF derivatives for sensing of singlet oxygen.

In the structures of **1-18a-c**, the anthryl unit behaves as a reactive luminophore to trap singlet oxygen. The TTF group, as a strong electron donor, transfers electrons

in response to singlet oxygen trapping. The designed sensing mechanism involves photo-induced electron transfer (PET) as the key step. The reaction of singlet oxygen with the anthryl group results in strong chemiluminescence, with fluorescence quantum yields of $\Phi = 0.0039$ and $\Phi = 0.21$, respectively. The same magnitude of selectivity was not observed for other reactive oxygen species, such as H_2O_2, OCl^-, and O_2^-. Moreover, the observed chemiluminescence changes have confirmed that the introduction of electron-rich TTF into the 9-position of anthracene can greatly activate its reactivity towards singlet oxygen. There are three steps involved in the proposed sensing mechanism as shown in Scheme 1.4. By adding polar functional groups, the molecular sensor will gain water solubility. The anthracene moiety activated by TTF unit **1-19** predominantly traps O_2 to yield an unstable endoperoxide **1-20**, the decomposition of which in turn causes the excitation of the anthracene core. The excited anthracene then emits light through radiative deactivation. Oxidation of the electron-rich TTF moiety occurs to turn the molecule into a cationic species. In such a tandem reaction, the formation of the final cationic species triggers the chemiluminescent reaction. Meanwhile, it prohibits the PET process between TTF and excited anthracene units, and finally enhances chemiluminescence.

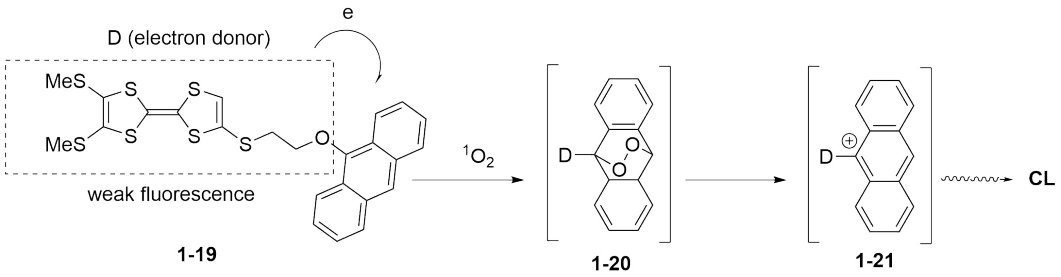

Scheme 1.4: Possible mechanism for strong chemiluminescence (CL) resulting from the interactions of sensor **1-19** with O_2.

Sensors based on TTF, anthracene, and phenylboronic acid units have been designed to detect saccharides. Compounds **1-22** and **1-23** (Fig. 1.6) are representatives of this type of saccharide sensors.[37,38] In these systems, the anthracene acts as the fluorophore and the phenylboronic acid as the saccharide receptor. The compounds are non-fluorescent before saccharide binding, because the fluorescence of anthracene is quenched by a PET mechanism. When the phenylboronic acid group is bound to a saccharide molecule, the PET process is disrupted and the fluorescence of the anthracene unit is turned on.

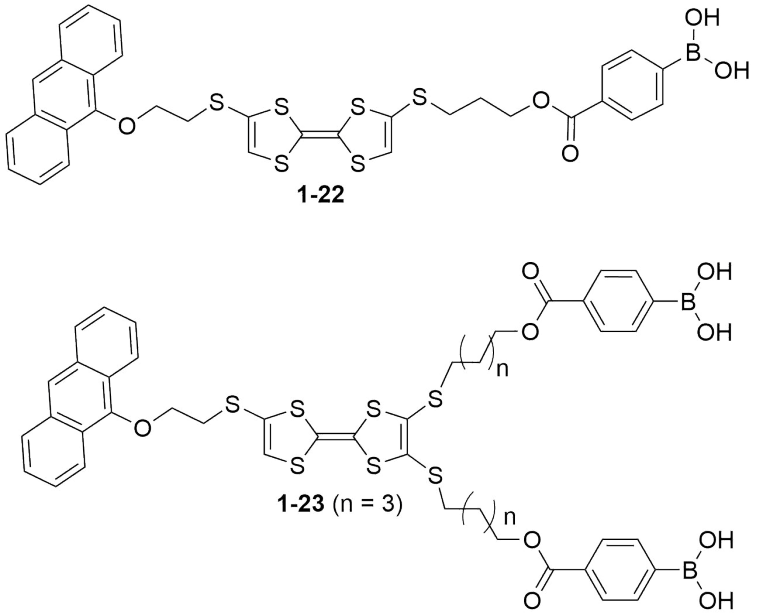

Figure 1.6: TTF-anthracene systems functionalized with phenylboronic acid groups as selective fluorescence sensors for saccharides.

The reverse process of PET can explain this phenomenon. PET happens between TTF (electron donor) and anthracene (fluorophore). When the boronic acid is complexed with a saccharide molecule to form the corresponding boronate, the

boron center becomes a stronger Lewis acid (stronger electron acceptor) than free boronic acid. PET is then diverted from TTF to boronate instead of anthracene (Scheme 1.5), which results in enhanced fluorescence of anthracene. Experimentally, sensor **1-22** was found to exhibit a good selectivity for D-fructose, while sensor **1-23** was selective towards D-glucose. The results indicate that the number of boronic acid receptors integrated in the sensor structure plays an important role in tuning saccharide selectivity.

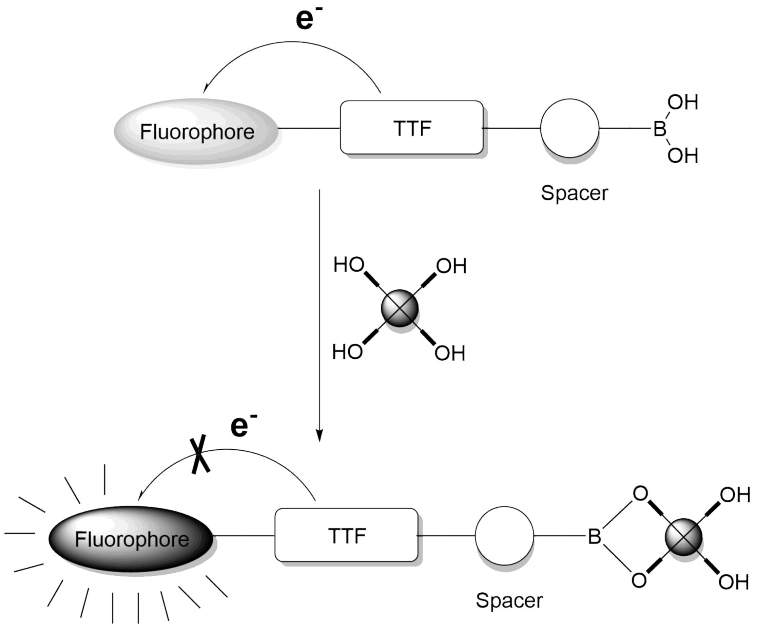

Scheme 1.5: TTF-anthracene systems functionalized with phenylboronic acid groups as fluorescence turn-on sensors for saccharides.

1.1.3.2 TTF Derivatives as Molecular Machines and Switches

TTFs can be used as switchable units in advanced molecular devices due to their reversible redox behavior. The redox properties of TTFs can be modified and finely

tuned at the molecular level and applied in molecular switches and machines.[12,39,40] The observation of color change (e.g., from pale yellow to dark green or deep blue) usually indicates TTF oxidation. This colorimetric property has been investigated by Zhou *et al.*[41] In their work, TTF groups were covalently connected to chiral binaphthyl units to form chiroptical systems. Axially chiral binaphthalene molecules usually give rise to strong circular dichroism (CD) signals that are easily detectable.[42] Changes in the oxidation states of the TTF units lead to either repulsion or attraction between the two TTFs. As a result, there can be different dihedral angles on the binaphthalene molecule, and the CD signals vary accordingly (Scheme 1.6).

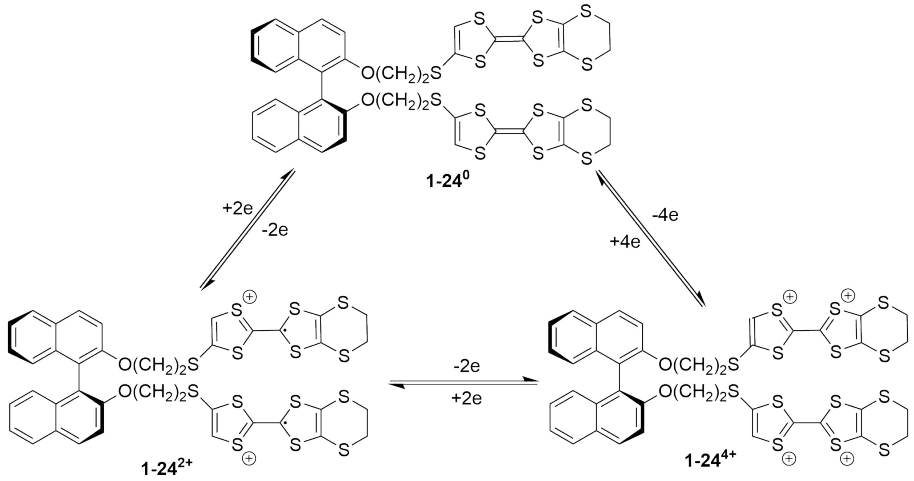

Scheme 1.6: Illustration of the three states of compound **1-24** associated with its oxidation and reduction.

The operational mechanism of the dihedral angle changes in response to the oxidation and reduction of TTF can be described in detail by the schematic drawings in Scheme 1.7.

In the first step, each TTF is oxidized to its radical cation. At this stage, the

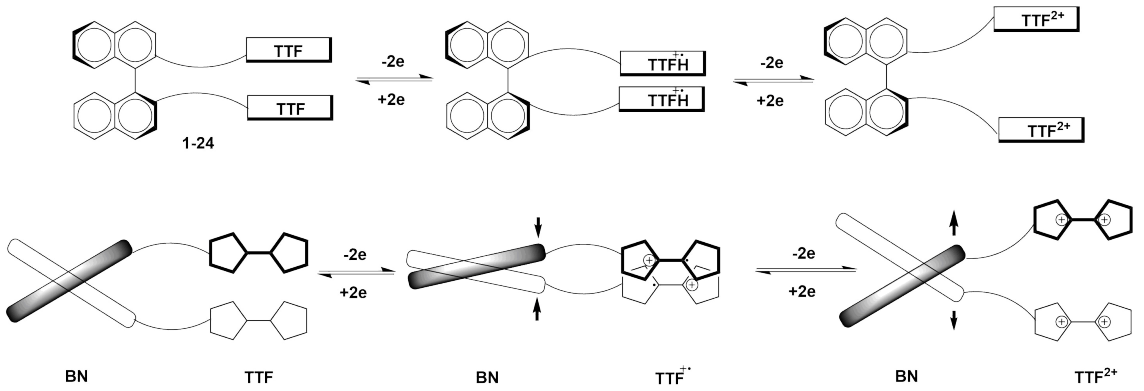

Scheme 1.7: Schematic illustration of the three states of **1-24** showing different dihedral angles after oxidation of TTF units (BN: binaphthalene unit).

intramolecular attraction between the two TTF radical cations draw them closer and decrease the dihedral angle between two naphthalene rings. Further oxidation on the TTF units leads to the formation of two dicationic TTF units. The Coulombic repulsion between them increases the dihedral angle between two naphthalene rings, resulting in the reduction of the intensities of CD signals.

Redox fluorescent switches based on TTF-porphyrin systems have been reported. TTF electron transfer to porphyrins can quench the fluorescence of the porphyrin. On the other hand, oxidation of TTF increases the fluorescence intensity through shutting down the electron transfer. Compounds **1-25**, **1-26**, and **1-27** shown in Fig. 1.7 are examples of such systems.[43]

Stoddart's group recently reported a molecular machine **1-28** built upon TTF moieties (see Fig. 1.8).[44,45] When the TTF units in this molecule were subjected to reversible oxidation/reduction processes by chemical or electrical means, the redox-bistable rotaxane underwent controllable and reversible movement. The design principle is based on the chemistry of guest-host recognition.[22]

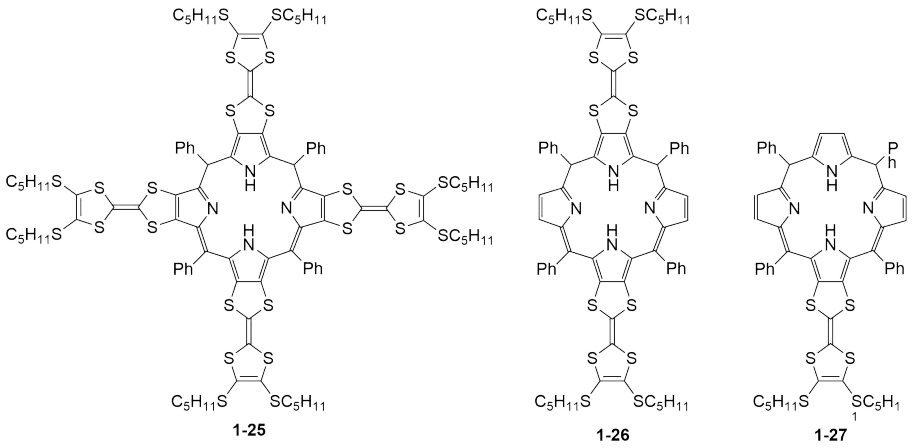

Figure 1.7: TTF-porphyrin-based redox fluorescent switches.

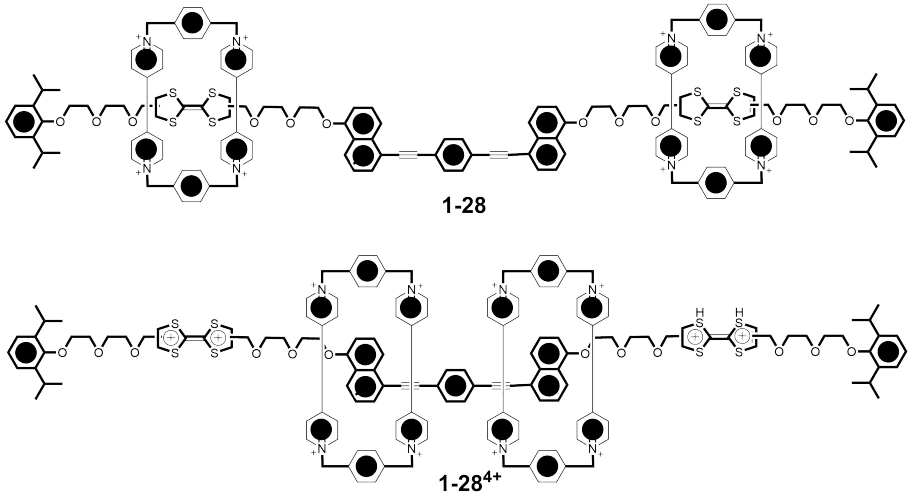

Figure 1.8: Rotaxane **1-28** as a redox-controlled molecular machine.

As illustrated in Fig. 1.8, the positions of the CBPQT^{4+} (cyclobis(paraquat-*p*-phenylene)) rings favor being close to the two TTF stations as these are electron rich sections R^{8+}(rotaxane^{8+}) also this opposed to the two naphthalene (NP) stations. Chemical oxidation of the TTF units leads to their dicationic states (TTF^{2+}). The Coulombic repulsion of similar charges then pushes the CBPQT^{4+} rings to the NP stations. Overall, the main driving force for the movement of this molecular machine comes from electrostatic repulsion between the CBPQT^{4+} rings and the TTF^{2+}

stations before and after the oxidation of TTF.

1.2 Introduction to 1,4-Dithiafulvene (DTF)

The half structure of TTFV is 1,4-dithiafulvene (DTF), which is also a very important organic electron-donating functional group (Scheme 1.8). DTF can be functionalized through π-insertion and/or π-annulation to generate the so-called π-extended TTFs (exTTFs). They are good electron donors and can be used as organic semiconducting materials.

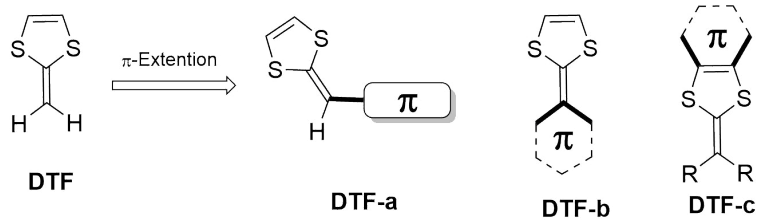

Scheme 1.8: General strategies for integrating the DTF unit into various π-conjugated systems.

1.2.1 Electron-donating Properties of DTF

DTF is an electron-rich heterocycle that can readily release an electron upon oxidation. In the literature, the unsubstituted DTF, 2-methylene-1,3-dithiole, was investigated theoretically in terms of its thermochemical and structural properties.[46,47] Unsubstituted DTF, according to nucleus independent chemical shift (NICS) and isomerization stabilization energy (ISE) calculations, should behave as a good organic π-electron donor;[48] however, it has limited stability and hence is not

easy to synthesize.

DTF can be substituted and linked to other functional groups through π-conjugation to gain better stability and enhanced electronic properties. Interestingly the π-extended DTF derivatives can result in improved synthetic accessibility, stability, redox activities, and electronic properties, which can open new directions towards a large number of applicable derivatives.

The DTF group can be embedded in π-conjugated molecular systems through three different patterns as presented in Scheme 1.8. The DTF group can be directly connected to a π-conjugated unit through covalent linkages on the vinylidene position or via fusion of the 1,3-dithiole ring with other conjugated structures as can be seen in Scheme 1.8.[8,49] The studies in this thesis were mainly focused on the systems where DTF groups are connected to a π-conjugated group at the vinylidene position **DTF-a,b**.

1.2.2 Synthetic Methods for DTF-functionalization

There are many methods for the synthesis of functionalized DTF; however, only the most popular ones will be discussed in this section. The first DTF synthesis was reported by Kirmse and Horner in 1958.[50] In their study, 4-phenyl-1,2,3-thiadiazole **1-29** underwent photolysis to give the biradical intermediate **1-30**, and then thiokene **1-31** was obtained through the Wolff rearrangement. Finally, the diphenyl-substituted DTF **1-32** was formed by the combination of intermediate **1-30** with **1-31**. This method showed a low reaction yield and lacked stereoselectivity, so it was not adopted as a useful approach for DTF-functionalization (Scheme 1.9).

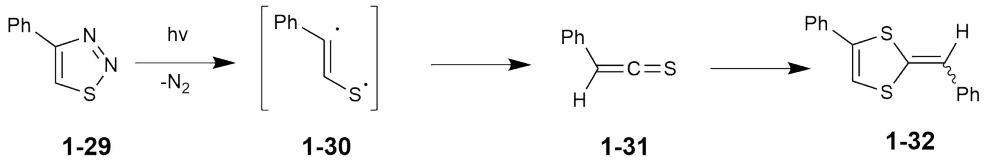

Scheme 1.9: Formation of DTF through photolysis of 1,2,3-thiadiazole.

A more useful synthetic method was developed later based on Wittig-type olefination reactions. Hartzler devised a rapid one-pot synthesis for 2-benzylidene-1,3-dithioles (i.e., phenyl-substituted DTFs) in 1971.[51] In this reaction two steps are involved. First, the complex of aliphatic phosphine–CS_2 **1-33** undergoes a cycloaddition reaction with acetylene **1-34** to form a phosphorane intermediate **1-35**, which then undergoes the Wittig reaction with a benzaldehyde counterpart to form the final product **1-36**. Cava and co-workers[52] reported a new modified approach for the preparation of 1,3-dithiol-2-yl phosphonium salts through protonation of the phosphorane intermediates with HBF_4 (Scheme 1.10). The phosphonium salts can be converted into Wittig reagents under basic conditions, which can further react with various aldehydes and ketones to form olefinated products. Later on, a large number of phosphonate reagents and phosphonium salts was reported for DTF functionalization on different π-conjugated system through the Wittig-type olefination reactions.

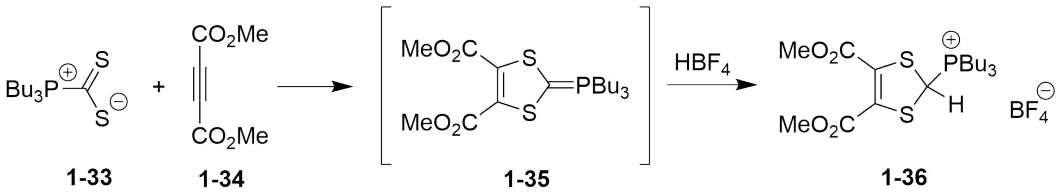

Scheme 1.10: Synthesis of 1,3-dithiol-2-yl phosphonium tetrafluorborate.

Another method, often referred to as phosphite-promoted olefination, was

developed by Bryce and co-workers[53] in 2007. In this method, an aldehyde or ketone is reacted directly with 1,3-dithiole- 2-thione (e.g., **1-38**) in the presence of an excess amount of $P(OMe)_3$ or $P(OEt)_3$ (Scheme 1.11) under heating.

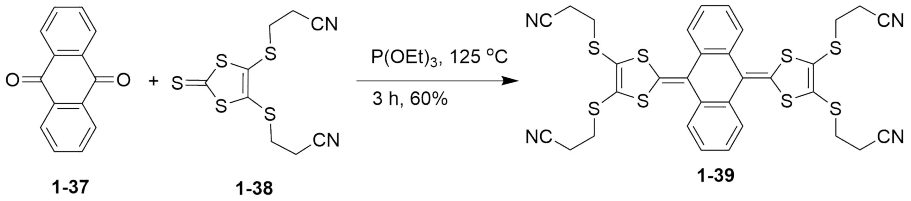

Scheme 1.11: DTF functionalization through the phosphite-promoted olefination reaction.

Phosphite-promoted olefination reactions have become popular in recent years because of the following reasons: (i) it is a one-step and straightforward reaction to perform. The starting materials can be various π-conjugated aldehydes and ketones that are readily available from commercial sources; (ii) the starting precursor 1,3-dithiole-2-thione can be readily synthesized and easily tailored. A detailed mechanism of phosphite-promoted olefination reaction is proposed in Scheme 1.12.

Besides the above mentioned methods, a double *S*-vinylation approach can also be employed for the post-olefination functionalization.[54,55] For example, 1,2-benzenedithiol can react with a *gem*-dihalovinyl system under basic conditions to achieve DTF functionalization (Scheme 1.13). The DTF product **1-50** features a π-extended benzo-*d*[1,3]dithiole structure. This method has been successfully applied to handle some difficult DTF synthesises where phosphite-promoted olefination and Wittig-type methods failed. For instance, Morin and Nielsen reported that this reaction could achieve highly efficient DTF-functionalization on large polycyclic

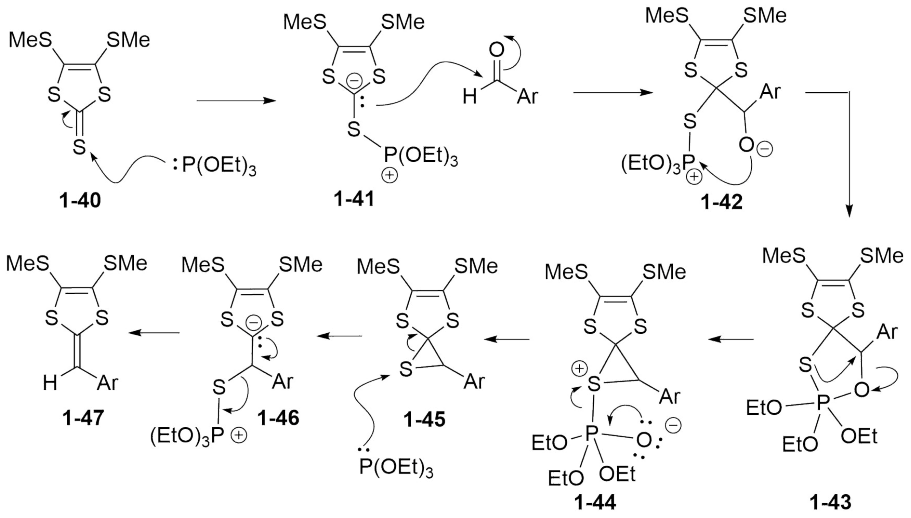

Scheme 1.12: Reaction mechanism for the phosphite-promoted olefination reaction.

aromatic hydrocarbon (PAH) cores under very mild conditions.[56,57]

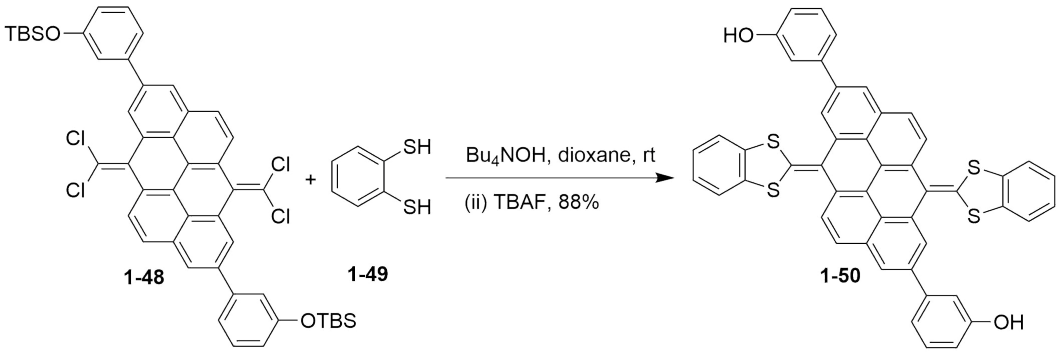

Scheme 1.13: Post-olefination functionalization through double *S*-vinylation.

1.2.2.1 Synthetic Methods for 1,3-Dithiole-2-thiones

1,3-Dithiole-2-thiones are widely used starting materials in the preparation of different types of DTFs and TTF derivatives, as they can be readily functionalized with a large variety of side groups (R). In this thesis, the phosphite-promoted olefination reaction was extensively used for the synthesis of different DTF products. An exemplar of

this synthetic route for the preparation of a 1,3-dithiole-2-thiones **1-55** is presented in Scheme 1.14.

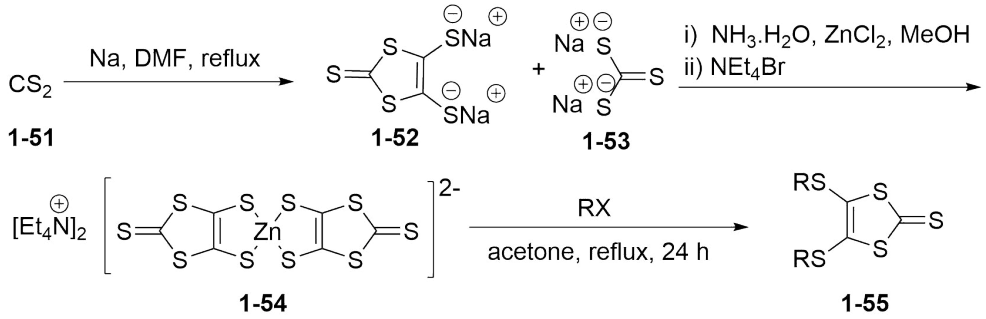

Scheme 1.14: Synthetic route for 1,3-dithiole-2-thione **1-55** involving the reduction of CS_2 with Na as the key step.

It is convenient to prepare various 1,3-dithiole-2-thiones using this method on a large scale and at relatively low cost. The intermediate zinc salt **1-54** is stable and can be readily synthesized as a precursor for the final step. Hoyer's group developed this method from the treatment of CS_2 **1-51** with an alkali metal (e.g., Na or K). Meanwhile, the alkali metal plays a role as a reducing agent to convert CS_2 to 1,3-dithiole-2-thione-4,5-dithiolate **1-52**. A plausible mechanism for this transformation is illustrated in the Scheme 1.15.[58]

In this reaction, CS_2 is first reduced by Na metal to form a radical anion **1-56**. Radical anion react with another radical anion to form dithiolate **1-57**. The dithiolate anion is then chelated with zinc (II) cation to form a stable ammonium zincate salt **1-54**. An appropriate electrophile can be used, depending on the structure of 1,3-dithiole-2-thione desired, to react with the zinc salt **1-54**, yielding the thione product **1-55**.

In addition to the above-mentioned methods, other synthetic approaches are also

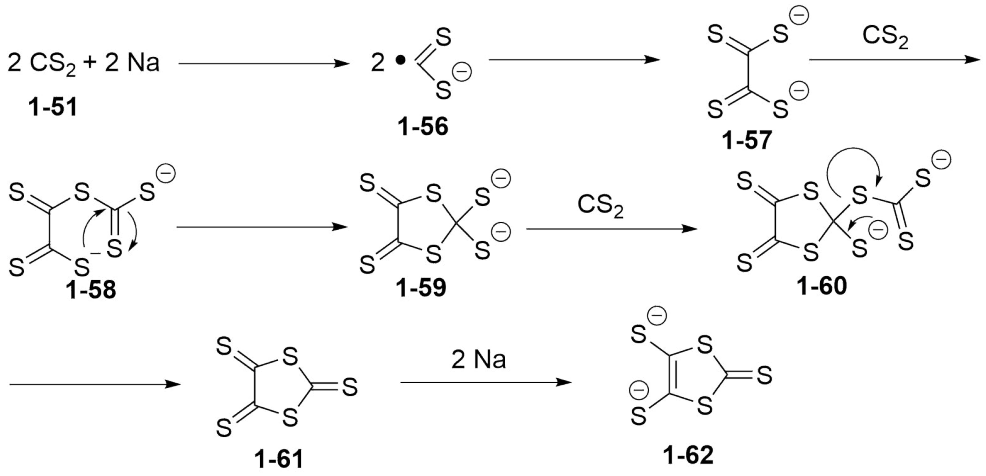

Scheme 1.15: Mechanism for the reduction and coupling of CS_2 with Na metal.

available for the preparation of 1,3-dithiole-2-thiones. These synthetic methods are briefly summarized in Scheme 1.16.

1.2.3 Chemical and Redox Reactivities of DTFs

DTF is an electron-rich heterocycle, which can readily release one electron to form a radical cation upon oxidation. Kirmse and Horner[50] reported the oxidative dimerization reaction of DTF in 1958. In this reaction, DTF **1-63** could be oxidized to form a reddish-violet salt **1-64**. Later in 1974, Mayer and Krober investigated a series of diaryl-substituted DTFs oxidation (**63a-d**, Scheme 1.17) and deduced the structures of oxidized products as **64a-d** based on elemental and UV-Vis absorption analyses. Their proposed mechanism involves the formation of radical cation **1-66** after the oxidation step. Then, two intermediate radical cations dimerize to yield a stable dication salt.

The attachment of an aryl group to the DTF vinyl position facilitates the formation of radical cation intermediate, while the presence of the vinyl proton is

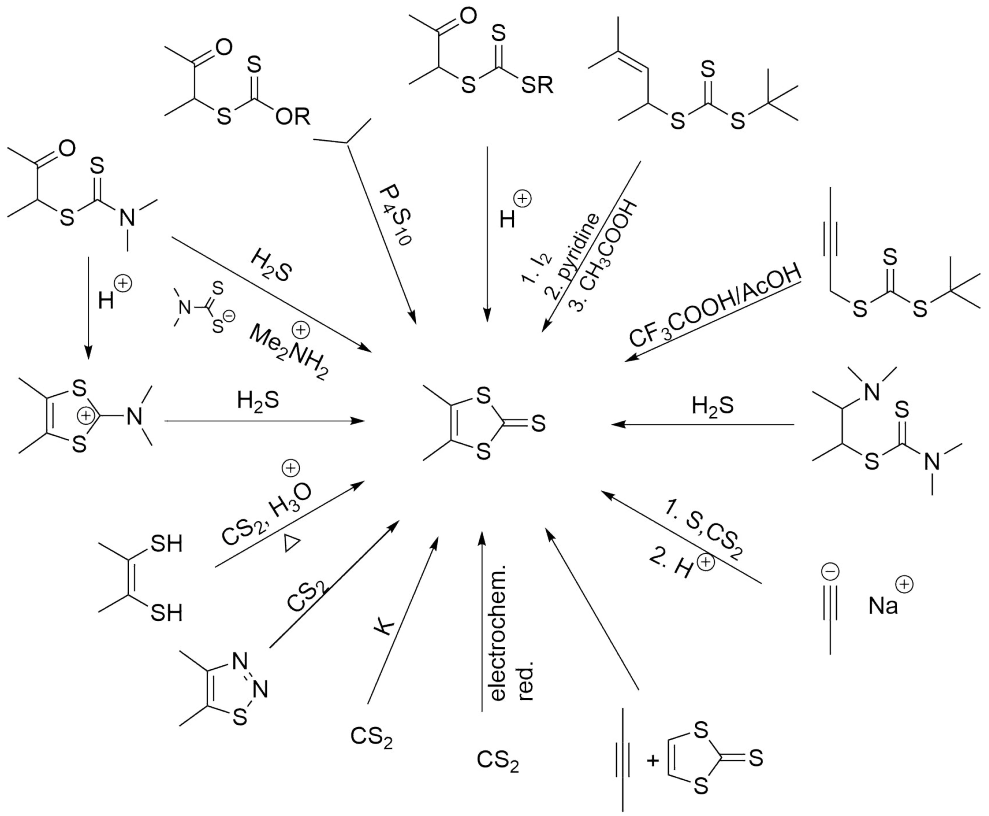

Scheme 1.16: Synthetic methods for 1,3-dithiole-2-thiones.

vital for the elimination step to yield a stable dication product, the neutralized form of which is commonly known as a tetrathiafulvenyl vinylogue (TTFV). Various oxidants can be applied to promote the DTF dimerization reaction, such as $(BrC_6H_4)_3SbCl_6$,[59,60] I_2,[61,62] Br_2,[63,64] and $AgBF_4$[65–67]. Electrochemical conditions can also induce DTF dimerization reactions, affording various TTFV products.[64,68–70] The oxidative dimerization DTF mechanism was thoroughly investigated by Hapiot et al.[71] in 1996 through cyclic voltammetric (CV) analysis. In their reported mechanism, a DTF radical cation **1-66** is first generated through a fast single-electron transfer and then rapidly forms a dication dimer **1-67** (Scheme 1.18).

In the next step, the two vinylidene hydrogens are abstracted, and the double

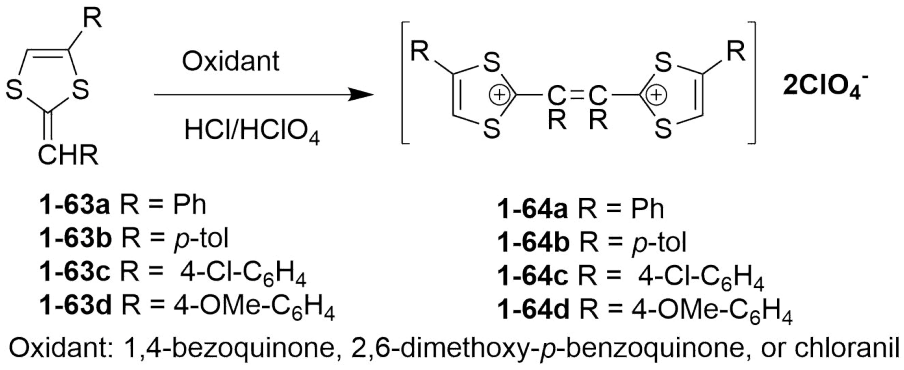

Scheme 1.17: Oxidative dimerization of DTFs.

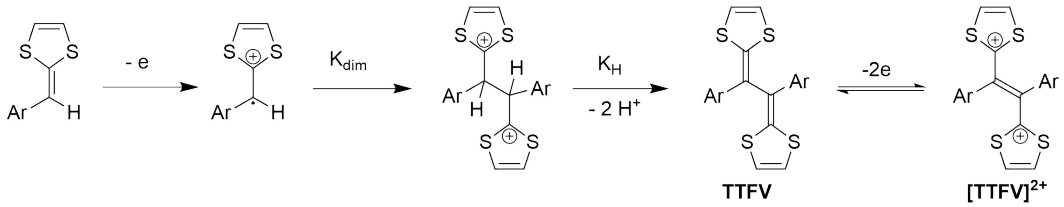

Scheme 1.18: Mechanism for DTF oxidative dimerization.

elimination step leads to TTFV **1-68**, which is rapidly oxidized to form a stable TTFV dication at a lower potential than that of the starting DTF.

Some other reactivities for DTF were also reported in the literature. The details are illustrated in Scheme 1.19.[72]

In most of reaction mechanisms, The DTF vinylidene proton is displaced by different electrophilic groups. Hartzler proposed that benzylidenedithioles (i.e., phenyl-DTFs) were quasi-aromatic systems due to resonance effects.[51] As such, the exo-ring C=C bond can undergo various substitution reactions, including bromination,[73] addition to a diazonium salt, nitrosylation,[74] and formylation with oxalyl chloride.[75] In this thesis, chapter3, DTF was discovered to be easily protonated by the addition of strong acid and then undergoes hydrogen/deuterium exchange upon quenching with D_2O. The activated C=C bond of DTF can also undergo

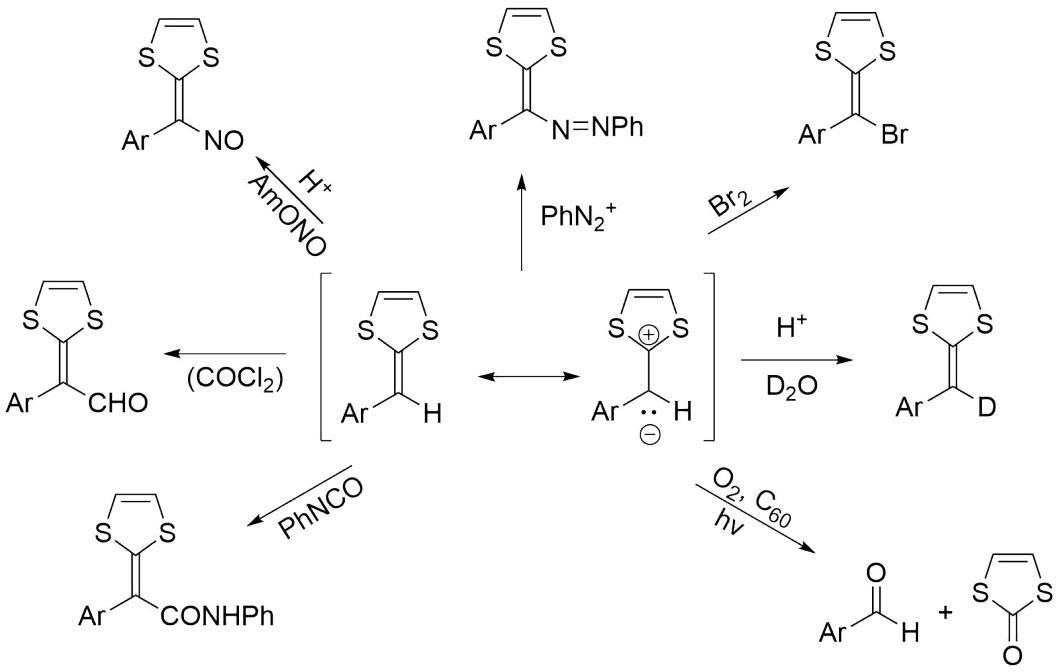

Scheme 1.19: Summary of the reactivities of DTFs with various electrophiles.

cycloaddition reactions.[76] Moreover, DTF in the presence of C_{60} fullerene and air can undergo a photo-oxidative cleavage reaction.[59,77] First, the photo-excitation of C_{60} prompts the formation of singlet oxygen, which then reacts with the C=C bond to cleave DTF into the corresponding aldehyde and 1,3-dithiol-2-one. Certain unique properties of DTF have been disclosed in the recent studies by the Zhao group. For example, the iodione promoted oxidative coupling reaction yields an unusual bis-spiro-tricyclic structure such as compounds **1-70a/b**, when phenyl-DTF has an *ortho*-substituent (e.g., CH_3 or Br) (Scheme 1.20).

Herein, the *ortho*-substituted group hinders the deprotonation step in the oxidative dimerization mechanism. As such, $Na_2S_2O_3$ reacts with the protonated dication intermediate during the workup step to yield a bis-spiro-tricyclic final product **1-71**. In some cases, the π-extended aryl groups, which are linked to DTF,

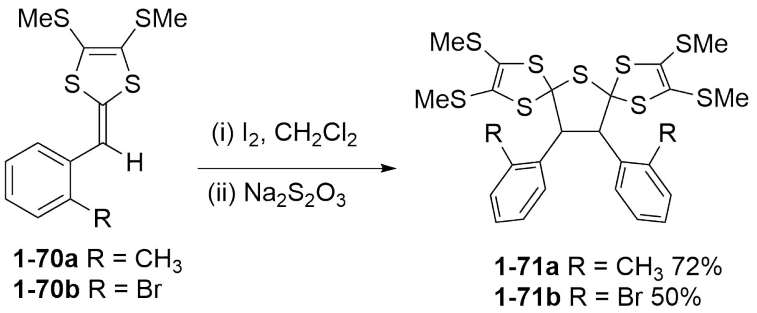

Scheme 1.20: An unusual oxidative dimerization of phenyl-DTFs with *ortho*-substituents.

can stabilize the radical cation intermediate due strong resonance effects and become inert to oxidative dimerization. Another interesting DTF reaction is the substitution reactions of 1-naphthyl or 9-anthryl-substituted DTFs **1-72** with 1,3,4-thiadiazole-2-thiols **1-73**, in which iodine oxidizes DTF **1-72** and then the resulting radical cation reacts with 1,3,4-thiadiazole-2-thioles **1-73** to form thiadiazolyl-substituted products **1-74** in good yields (Scheme 1.21).[78]

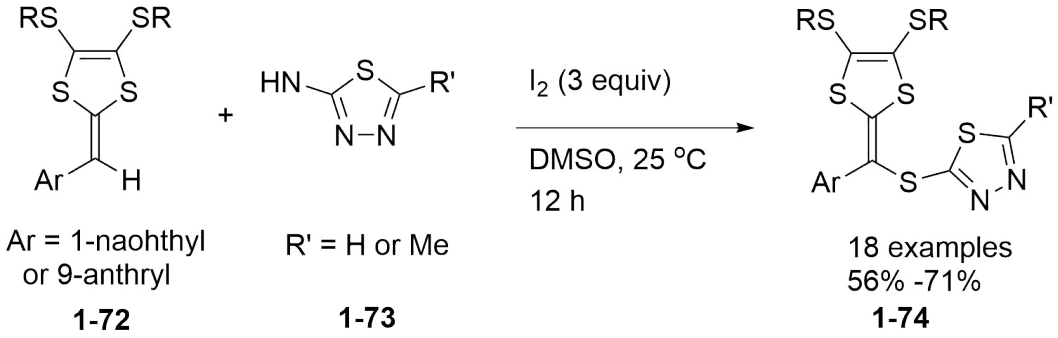

Scheme 1.21: Iodine-mediated oxidative vinylic C(sp^2)–H sulfenylation.

Recently, the Zhao group serendipitously discovered an intramolecular alkyne-dithiolium cycloaddition reaction. Initially, a bis-DTF **1-75** was prepared as a precursor for oxidative polymerization through iodine promoted DTF oxidative

coupling. However, this reaction yielded the bis(indenothiophene) **1-76** as the major product.[79] When **1-75** was treated with a strong acid, TFA, the formation of cyclized product **1-77** was observed. Based on the experimental results, a key step in this cyclization reaction was identified to be the protonation of the vinylic carbon of DTF **1-75**. Density functional theory (DFT) studies disclosed that a dithiolium cation was formed due to protonation and this intermediate underwent reaction with the *ortho*-alkynyl group to yield an intramolecular cycloaddition product (Scheme 1.22).[80]

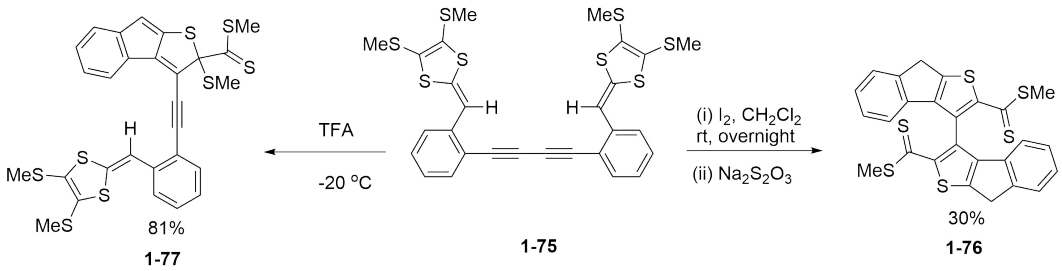

Scheme 1.22: Intramolecular alkynyl-dithiolium cycloaddition reactions.

1.3 Recent Progress in DTF and TTFV Functionalized Organic Materials

1.3.1 Organic Solar Cells

The DTF functional group can enhance the optoelectronic performance of the π-conjugated systems that it is attached to. For example, Leriche and co-workers[81] synthesized six different DTF-functionalized triphenylamines (TPAs) (Fig. 1.9) in 2008. They tested these compounds as active materials in organic field-effect transistors (OFETs) and photovoltaic (PV) devices.

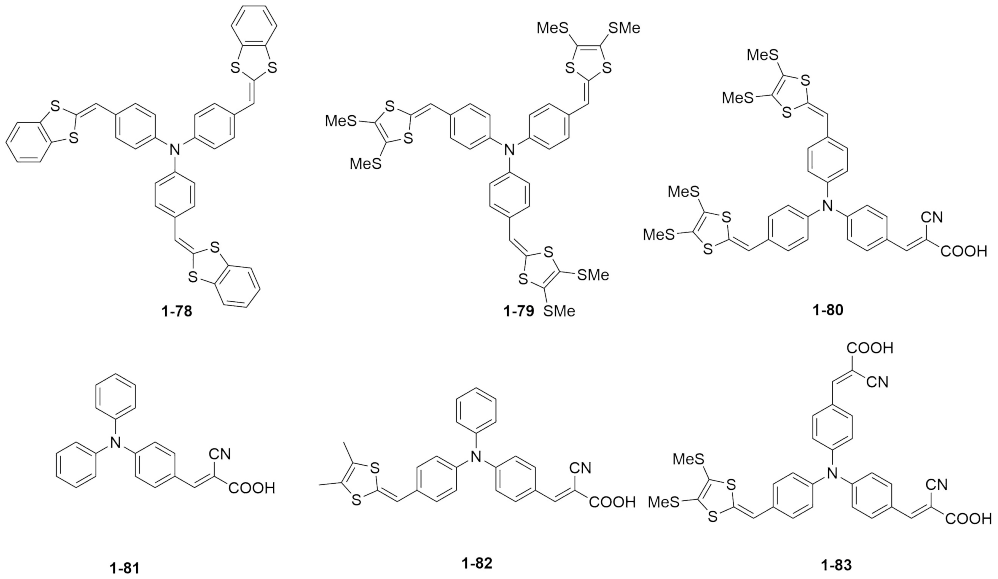

Figure 1.9: DTF-functionalized triphenylamines for solar cell devices.

It was found that compound **1-78** shows a better hole mobility than other compounds in this figure due to its stronger π-stacking in the solid-state. Interestingly, compound **1-78** could be paired with C_{60} fullerene to form a bilayer bulk heterojunction (BHJ) solar cell. The solar cell achieved an acceptable power conversion efficiency, but the stability of the device was low. Later in 2012, Yang and co-workers[82] synthesized a group of DTF-π-A-type metal-free organic sensitizers for the preparation of efficient dye-sensitized solar cells (DSSCs) (**1-84, 1-85, 1-86** Fig. 1.10).

The performance of the devices based on the DTF sensitizers improves with increasing π-bridge length. Compound **1-86** shows the highest power conversion efficiency (η) of 8.29%. By comparing these compounds to the metal-based sensitizers, a promising future of developing high-performance organic DSSCs based on DTF-functionalized dye molecules can be anticipated (the power conversion efficiency (η) for Ru-based **N719** is 8.76%). Research in this direction has been actively

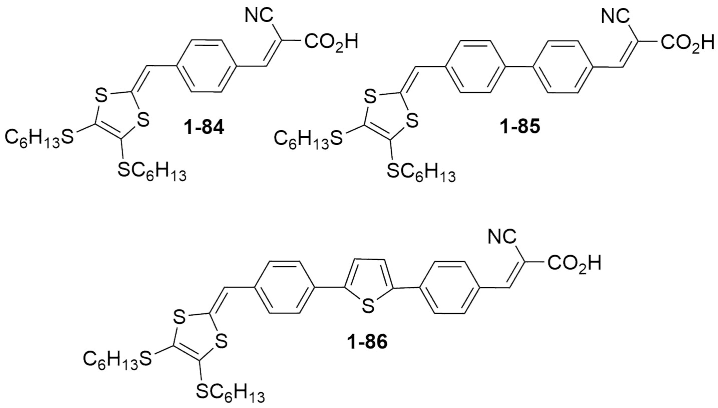

Figure 1.10: DTF-unit as a donor for high-efficiency dye-sensitized solar cells.

carried out. Recently, Guo and co-workers[83] reported DTF functionalized systems as highly efficient dye-sensitized solar cells. In this work, they synthesised two V-shaped dye compounds (**1-87, 1-88** Fig. 1.11), which were subsequently co-adsorbed with chenodeoxycholic acid (CDCA) on TiO_2 to achieve a high value of η (9.04%). To achieve a high performance for the DSSC, a similar DTF/(2-cyanoacetic acid)-functionalization strategy was applied to star-shaped TPA systems.

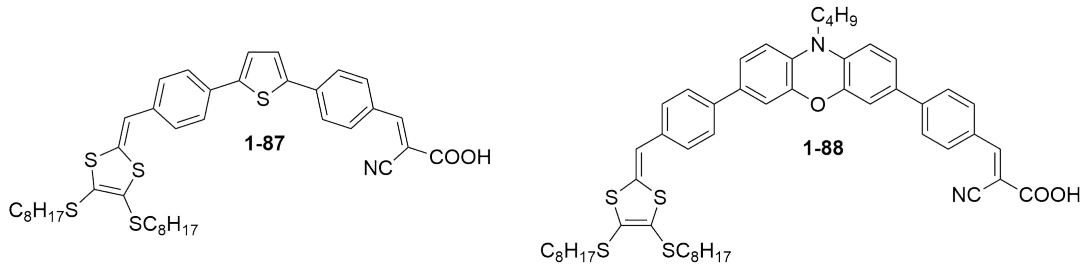

Figure 1.11: V-shaped DTF-functionalized dyes for high-performance DSSCs.

Wu and co-workers[84] designed and synthesized dithiafulvenyl functionalized spiro[fluorene-9,9'-xanthene] molecules (**1-89** and **1-90**, Fig. 1.12). They investigated the application of two compounds for dopant-free hole-transporting materials in perovskite solar cells (PVSCs). In fact, the DTF group led to a high hole mobility and

good air stability because of the beneficial S–S contact in the solid state. Compound **1-89** showed a hole mobility almost five times greater than that of **1-90**. Their studies indicated that the DTF-functionalized positions on the spiro[fluorene-9,9'-xanthene] structure have a significant impact on device performance.

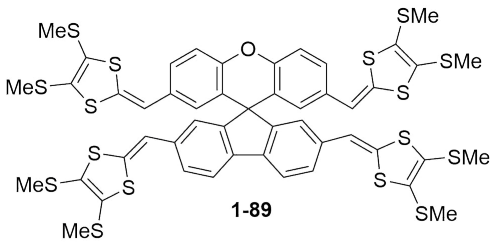

1-89

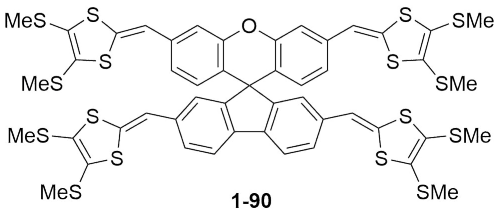

1-90

Figure 1.12: DTF-functionalized spiro[fluorene-9,9'-xanthene]s as hole-transporting materials for PVSCs.

1.3.2 Molecular Wires

Linear π-conjugated oligomers and polymers can be developed into useful molecular wires for different purposes, such as nanoscale electronic and optoelectronic devices.[85–89] Nielsen and co-workers[90–94] have synthesized a range of DTF-functionalized oligo(phenylene ethynylene)s (OPEs) (Fig. 1.13) since 2006.

To understand their molecular wire behavior and related structure–property relationships, the molecular conductance of these OPE wires were examined by

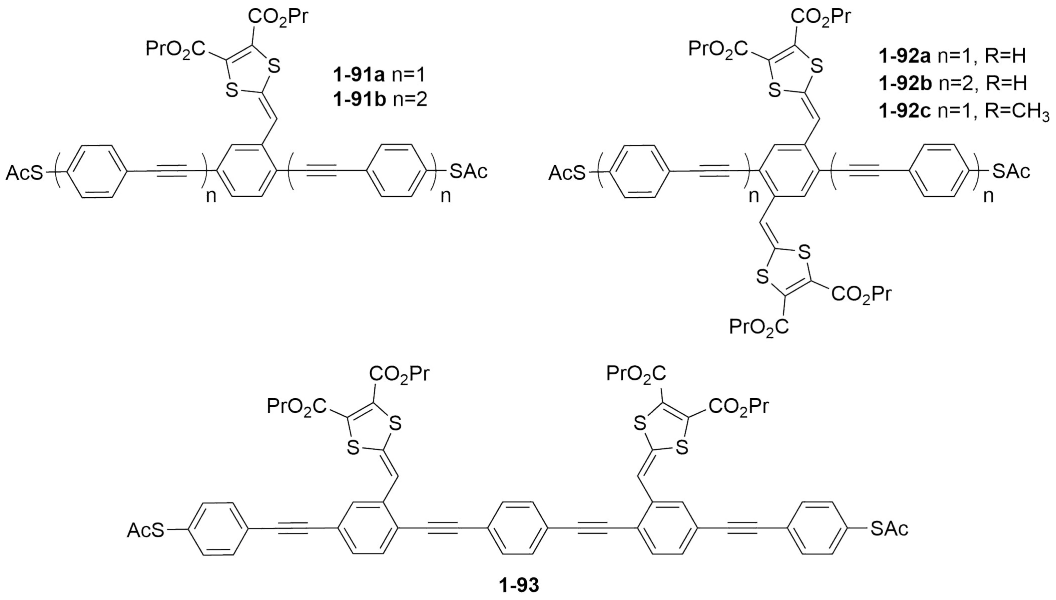

Figure 1.13: DTF-functionalized OPEs as molecular wires.

conducting probe (CP) atomic force microscopy (AFM) measurements on self-assembled monolayers (SAMs), mechanically controlled break-junction (MCBJ) experiments on single molecules, and scanning tunneling microscopy break-junction (STM-BJ) experiments on single molecules.[95,96] CP-AFM analysis disclosed that the molecular conductance of these OPE wires increases with increasing number of DTF groups orthogonally placed along the wires. On the other hand, DTF groups cause the junction formation probability to decrease and exert insignificant effects on the single-molecule conductance, which was suggested by single-molecule measurements using STM-BJ and MCBJ methods. Other factors, such as interfacial structures, also play important roles. However, the measurement of molecular conductance is a very complex and challenging task.

Lissau et al.[97] recently studied a group of D–A substituted OPE wires with linear and cross-conjugated structures. They examined and compared the molecular

properties of two DTF functionalized OPEs (**1-94** and **1-95**, Fig. 1.14)

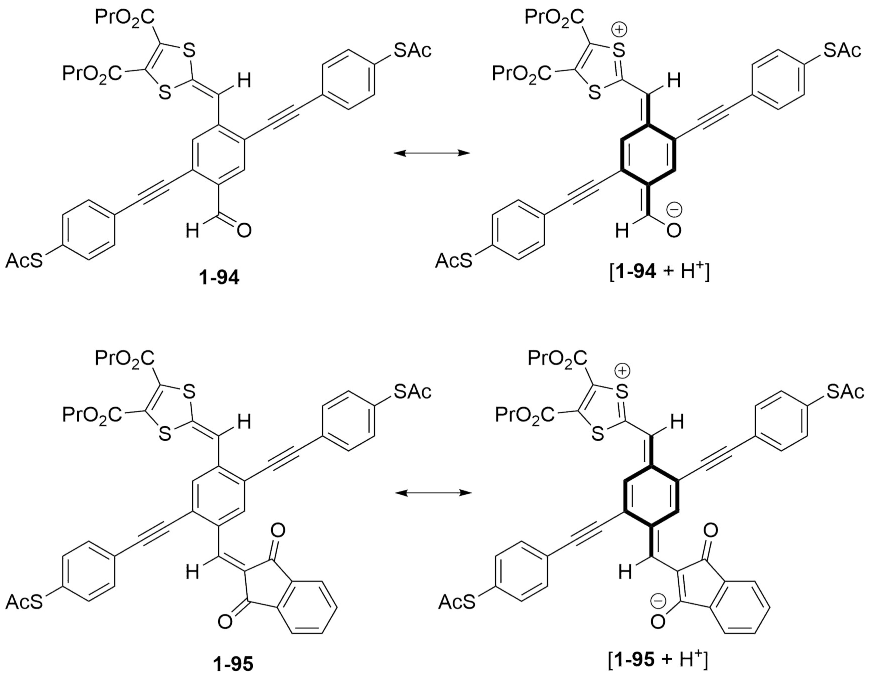

Figure 1.14: Cruciform-shaped D–A substituted OPE molecular wires.

Both compounds displayed notably broadened conductance peaks measured by the MCBJ technique with gold contacts. Compound **1-94** exhibits linear conjugation, whereas **1-95** shows cross-conjugation because of different resonance effects, so their measured conductance histograms appeared to be different.

1.3.3 DTF Building Blocks for Redox-active Sensors

As mentioned previously, the oxidative coupling of DTF leads to the formation of a C−C bond. This reactivity can be utilized in the synthesis of polymers, oligomers, and even macrocycles using multi-DTF-substituted precursors. Hascoat and co-workers[70] in 1997 reported the synthesis of macrocyclic products **1-97a** and **1-97b** from the

oxidative coupling of bis(DTF) compound **1-96** (Scheme 1.23).

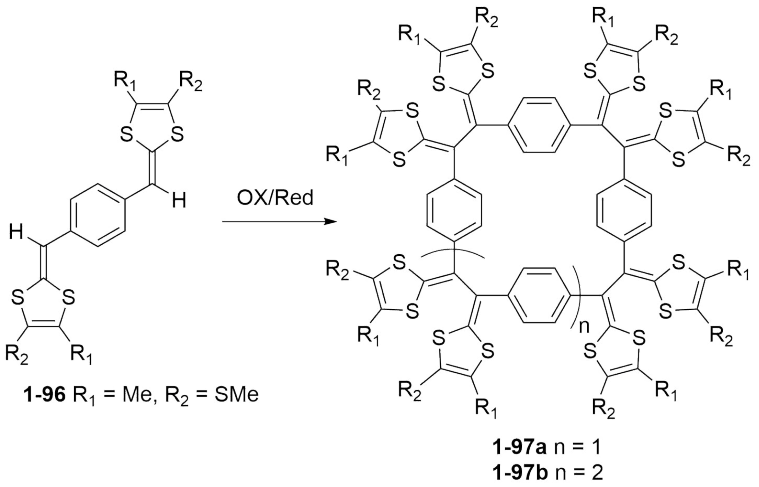

Scheme 1.23: Preparation of TTFV macrocycles under oxidative conditions.

In 2016, Mohammadreza and co-workers[98] reported the synthesis of a TTFV-pyrene macrocycle **1-99** through the oxidative coupling of bis(DTF)-pyrene **1-98**. As shown in Scheme 1.24, the synthesis involved two steps. In the first step, the monomer, DTF-pyrene **1-98** was subjected to oxidation with iodine. The reaction was stopped after about 45 min of reaction time, resulting in a mixture of monomer and dimer. The mixture was subjected to mechanical grinding in the presence of iodine to afford macrocycle **1-99** with a good yield of 37%. In the synthesis of this macrocycle, the reaction time plays a critical role.

Studies also showed that macrocycle **1-99** could act as a supramolecular host for nitrobenzene. A molecular modeling study proposed that the presence of DTF groups facilitates the binding of macrocycle **1-99** with electron-deficient aromatics. Inspired by this observation and thus deciding to continue in this area, Mohammadreza next designed and synthesized a class of multivalent DTF-functionalized polyarene building

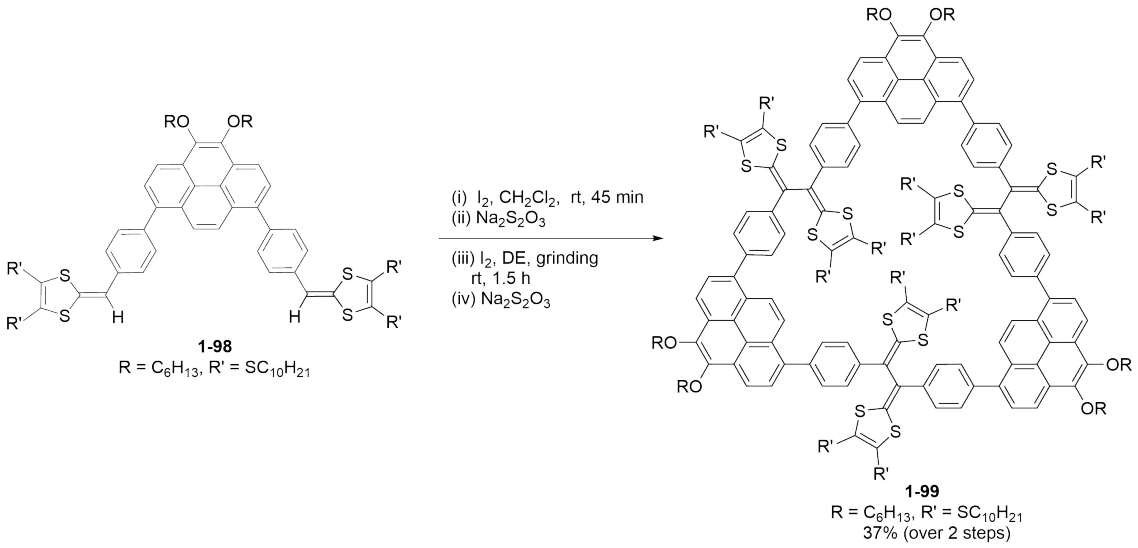

Scheme 1.24: Synthesis of a pyrene-TTFV macrocycle **1-99**.

blocks **1-100** and **1-101** (Fig. 1.15) for the construction of redox-active polymer thin film sensors that show high sensitivity for nitrobenzene explosives.[99]

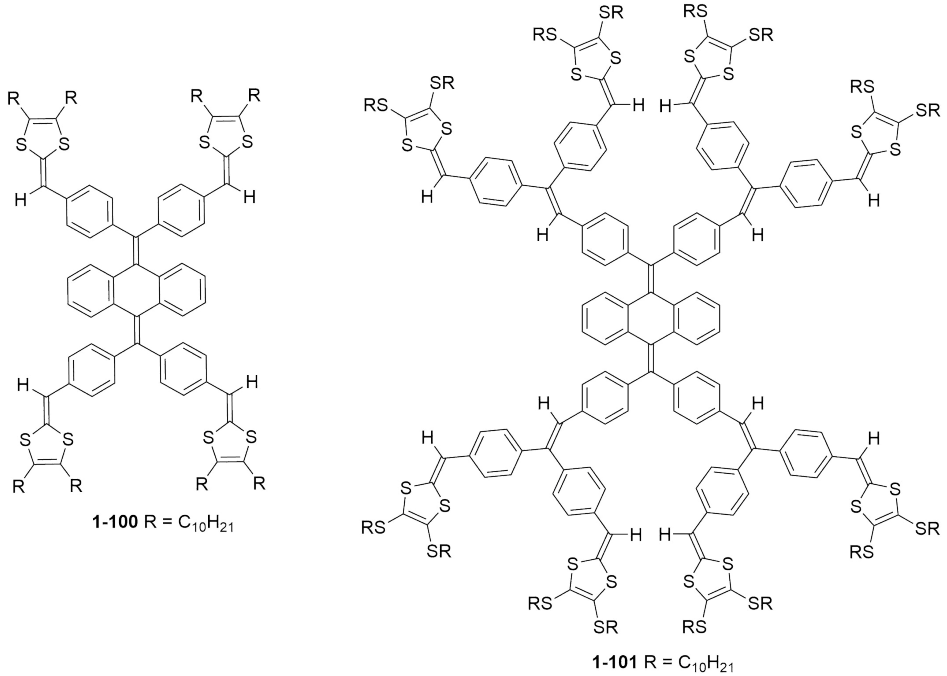

Figure 1.15: Multivalent DTF building blocks for redox-active polymers.

The octa-DTF compound **1-101** formed a relatively stable microporous cross-linked polymer thin film on the surface of a working electrode upon multi-cycle cyclic voltammetric scans. However, the tetra-DTF did not form a stable polymer thin film. The thin film formed on the working electrode surface showed sensitive electrochemical response to nitrobenzene at sub-mM concentrations. The durability and stability of the film were not good enough, limiting the reusability of the thin film sensors. To improve the stability of the cross-linked polymer thin films, a double-layer strategy was proposed and tested by the Zhao group. The details of this research are described in Chapter 2 of this thesis.

1.3.4 Selective Dispersants for Single-walled Carbon Nanotubes

Single-walled carbon nanotubes (SWNTs) have great electronic, optical, and mechanical properties.[100–104] The purification or enrichment of SWNTs is a crucial step for their application. SWNTs are generally produced as mixtures of different electronic types, tube diameters, and chiral indices.[105] Purification of SWNTs could be done through the approach of non-covalent functionalization. For example, π-conjugated polymers can wrap around SWNTs through π-stacking, and the resulting assemblies allow SWNTs to be effectively dispersed in various solvents. Conjugated polymers have been prepared to show particular binding with certain types of SWNTs, therefore achieving selective SWNT dispersion.[106] Furthermore, the alliance of stimuli-responsive groups into polymers could gain control over dispersion and release of SWNTs in the solution phase. π-Conjugated polymers can be functionalized

by DTF and employed as SWNTs dispersants. Bao and co-workers[107] in 2013 synthesized a series of poly(dithiafulvalene-fluorene-co-m-thiophene)s (**1-102**, Scheme 1.16) for selective SWNT dispersion.

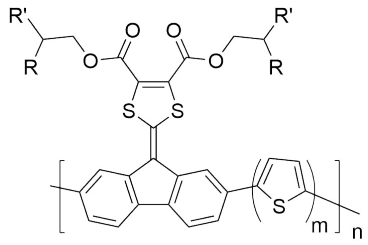

1-102 R=C_8H_{17}, R'=$C_{10}H_{21}$

Figure 1.16: DTF-functionalized π-conjugated polymers for selective dispersion of SWNTs.

DTF can be utilized as a building block for these polymers, given its strong interactions with SWNTs. The polymers could selectively disperse SWNTs in toluene after sonication and centrifugation. The selectivity for semiconducting SWNTs was improved upon increasing the ratio of thiophene to DTF units in the polymer structure.

The Zhao group previously designed and synthesized a series of TTFV-phenylacetylenebased co-polymers **1-103** (Fig. 1.17), which showed high efficiency in dispersing SWNTs in organic solvents.[108,109]

Co-polymer **1-103** could wrap around SWNTs to form supramolecular assemblies via favorable π-π interactions. This led to effective dispersion of SWNTs with **1-103** in organic solvents, such as chloroform. Meanwhile, the addition of trifluoroacetic acid (TFA) to the SWNT-**1-103** suspension caused protonation of co-polymer **1-103**, which was accompanied by dramatic conformational changes to interrupt the polymer-

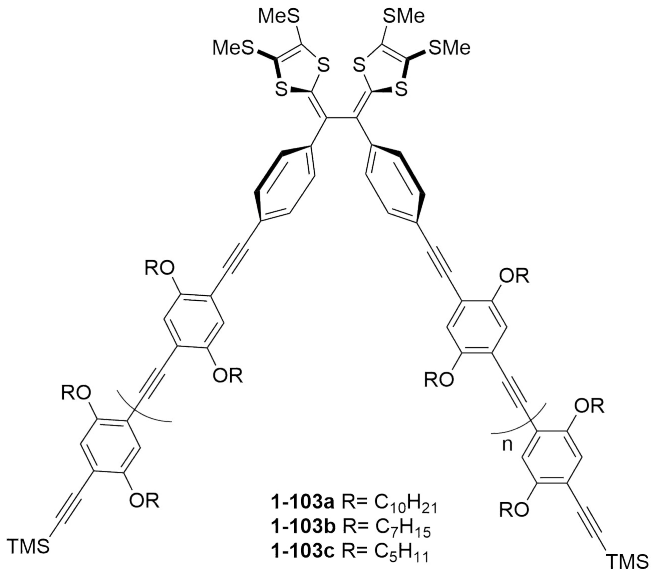

Figure 1.17: DTF-functionalized π-conjugated polymer **1-103** for selective dispersion of SWNTs.

SWNT interactions. As such the SWNT-polymer assemblies were dissociated, leading to the precipitation of pristine SWNTs out of the solution phase. The addition of a base neutralized the protonated polymer to recover and reuse them for another round of SWNT dispersion. The polymers demonstrated controllable wrapping/unwrapping around SWNTs, and hence allowed multi-cycles of dispersion and release of SWNTs to be executed. Later in 2014, Adronov and co-workers[110] reported a TTFV-fluorene-based co-polymer **1-104**, which showed high selectivity for dispersing small-diameter SWNTs in organic solvents.

Adronov and co-workers[111] further designed and synthesized two fluorene-based co-polymers **1-105** and **1-106**, in which DTF groups are included in the polymer backbones. The synthesized polymers exhibited effective interactions with high-pressure carbon monoxide (HiPCO) SWNTs, resulting in their effective dispersion in organic solvents.

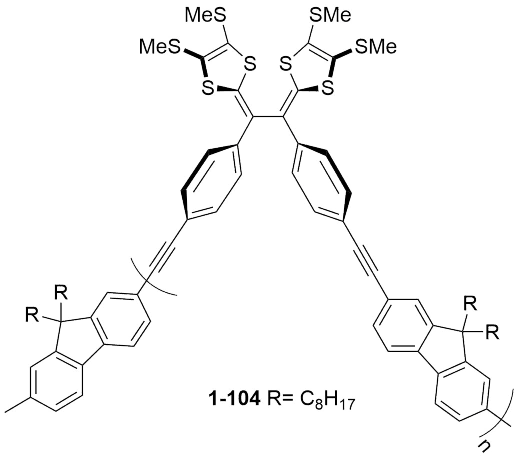

Figure 1.18: DTF-functionalized π-conjugated polymer **1-104** for selective dispersion of small SWNTs.

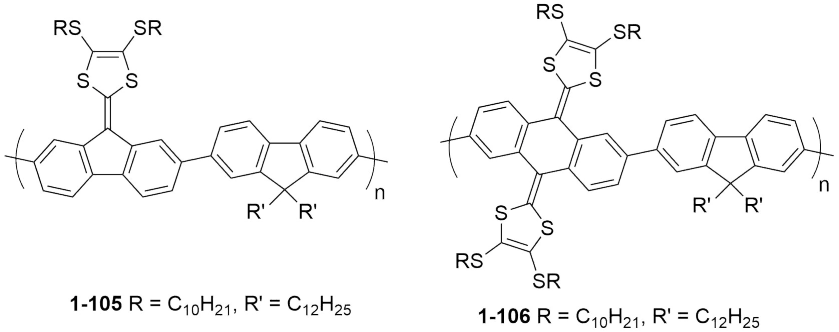

Figure 1.19: DTF-functionalized π-conjugated polymers **1-105** and **1-106** for selective dispersion of small-diameter SWNTs.

Mulla and Zhao reported the synthesis of DTF-functionalized polymers through "click chemistry" to obtain two poly(*p*-phenylene ethynylene)s **1-107** and **1-108** (Fig. 1.20).

Molecular modeling studies revealed that these polymers could interact with SWNTs by a "centipede" like wrapping mode. Experimental results showed that the polymers have excellent selectivity for dispersing small-diameter semiconducting SWNTs. They also reported that addition of hexane to the SWNT-polymer

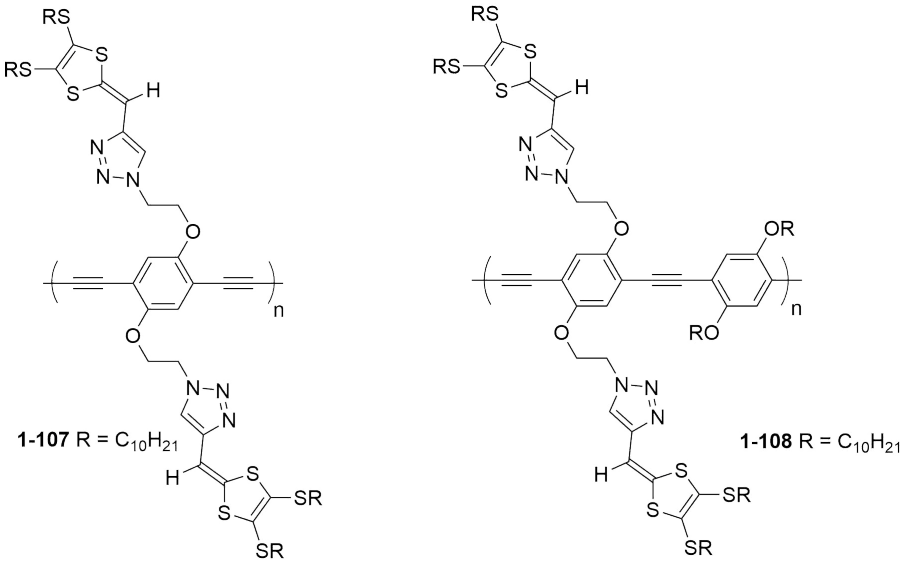

Figure 1.20: DTF-functionalized π-conjugated polymer for selective dispersion of small-diameter SWNTs.

suspensions in chloroform led to the release of dispersant-free SWNTs from the polymer. Also, electrolysis at a voltage of +0.8 V (vs. Ag/AgCl) could release the SWNTs from the polymer-SWNT suspension. Meanwhile, certain π-conjugated oligomers with short chains were also found to act as efficient dispersants for SWNTs. Mulla et al.[77] in 2013 designed and synthesised compounds **1-109**, **1-110**, **1-111**, **1-112** (Fig. 1.21) as a series of DTF-end-capped π-oligomers. They presented reasonable efficiencies in dispersing SWNTs although they have relatively short π-conjugated frameworks. The DTF-oligomers exhibited selectivity for small diameter SWNTs, and the resulting SWNT-oligomer suspensions could be readily dissociated upon the addition of hydrocarbon solvents such as hexane, releasing dispersant-free SWNTs as a precipitate.

Khadem and Zhao in 2015 reported a class of TTFV-fluorene co-oligomers **1-113a-c** that were prepared through oxidative DTF coupling reactions.[112] The TTFV

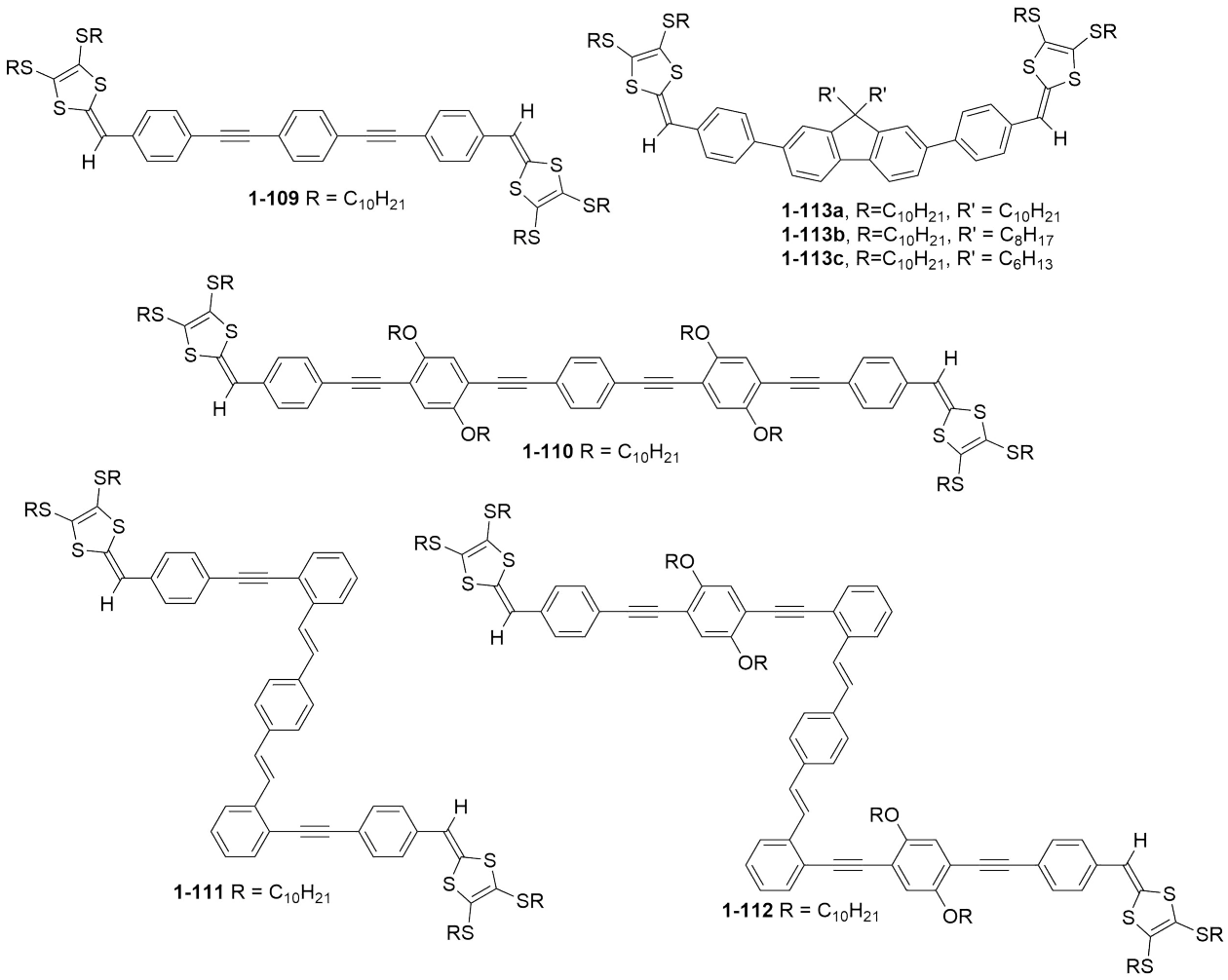

Figure 1.21: DTF-functionalized π-conjugated polymer for selective dispersion of small-diameter SWNTs.

oligomers afforded good diameter-selectivity in dispersing SWNTs in chloroform and THF.

Lagowski and co-workers[113–115] conducted a series of molecular modeling studies based on density functional theory (DFT) calculations to explain the roles of DTF-functionalized π-oligomers in the dispersion of SWNTs. Their results revealed that the DTF group in phenylacetylene and fluorene-based π-oligomers notably enhance the binding energies of SWNT/oligomer complexes. The studies also revealed that

the small-diameter SWNTs show stronger bonding in comparison to larger-diameter SWNTs.

1.3.5 DTF as a Reducing Agent for the Synthesis of Gold Nanoparticles

Gold-nanoparticles (GNPs) are important nanomaterials with important application in biology, catalysis, and nanotechnology.[116] Reduction of Au(III) species in the presence of suitable ligands as stabilizers can lead to stabilized GNPs. Chujo and co-workers[117,118] reported the first application of DTF as a reducing agent in 2001. They synthesized a DTF polymer **1-114** (Scheme 1.25) through a cycloaddition polymerization of a corresponding aldothioketene precursor. The polymer could reduce $HAuCl_4$ because of its excellent electron-donating properties. The polymer also could produce Pd and Pt nanoparticles through similar reduction reactions.[118]

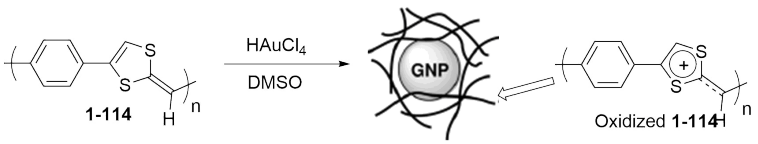

Scheme 1.25: Formation of GNPs through reduction of $HAuCl_4$ with a DTF polymer.

In 2016, Adows and Zhao[119] designed and synthesized a group of carboxylated DTFs and TTFVs (**1-115**–**1-118**, Fig. 1.22). They examined the reduction reactions of $HAuCl_4$ with these compounds in different polar solvents. They also reported the formation of stable GNPs (about 10 nm) through the redox reactions of DTF **1-117** with $HAuCl_4$ in DMF and DMSO. They further discovered that TTFV derivatives **1-116** and **1-118** could reduce $HAuCl_4$ in organic solvents; however, the resulting

Au(0) species were gold microcrystals rather than GNPs. The formation of GNPs was found to be strongly solvent dependent.

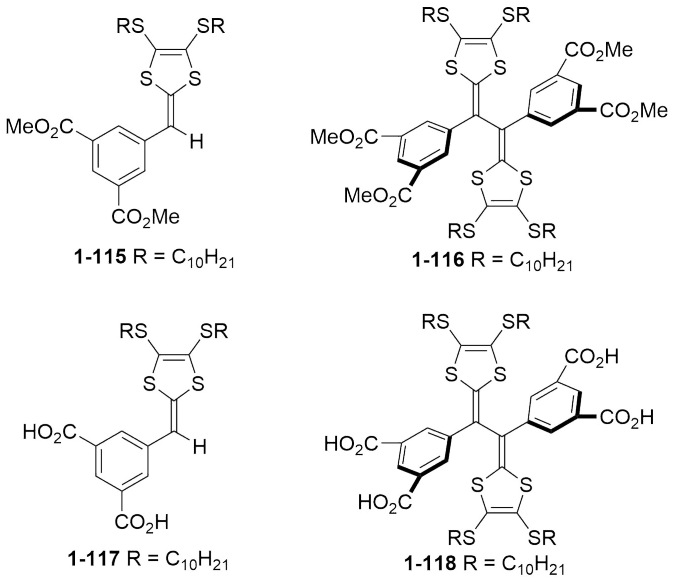

Figure 1.22: Carboxylated DTFs and TTFVs **1-115**, **1-116**, **1-117**, and **1-118**.

1.3.6 DTF-based Functional Organic Chromophores

DTF has long been recognized as a valuable electron-donating (D) group for the design of functional organic chromophores. A common design strategy is to combine DTF and other electron acceptors (A) through π-conjugated linkages. Earlier, a series of DTF–π–A type of push-pull systems was prepared as nonlinear optical (NLO) chromophores.[120–122] In recent years, new types of DTF-based organic chromophores have been designed and investigated. Deng et al.[123] synthesized a DTF–TPA–dicarbazole (**1-120** Scheme 1.26) as a precursor for electrochemical polymerization. The polymer film was prepared on an indium tin oxide (ITO) surface upon the electrochemical polymerization of compound **1-119**. The film showed color

changes at different voltages. The color changes were reversible, from light yellow to green to blue-grey. However, the proposed structure of poly **1-120** was not confirmed by any characterization methods, so the evidence for it being the active colorful species was not sufficient.

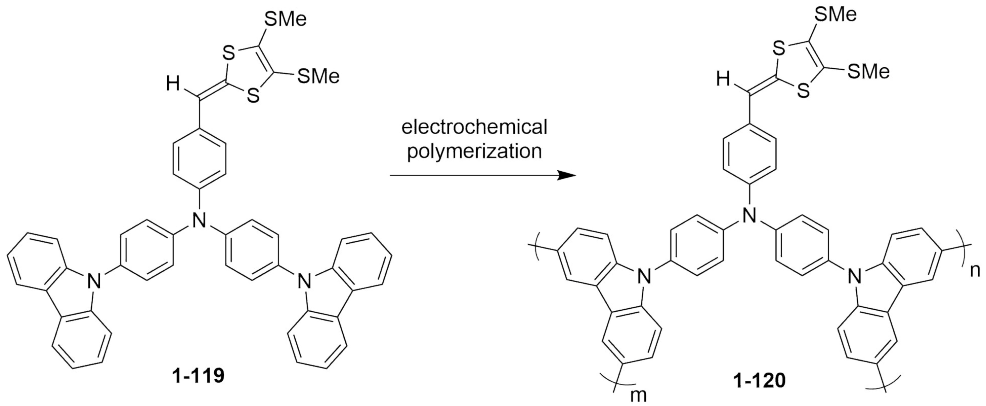

Scheme 1.26: Preparation of electrochromic polymer **1-120** via electrochemical polymerization.

Guo and co-workers[124] recently synthesized a bis(DTF)-substituted π-oligomer (**1-121**, Fig. 1.23). Surprisingly, they observed intriguing aggregation-induced enhanced emission (AIEE) behavior for compound **1-121**. The fluorescence quantum yield of **1-121** increases from 8% (in THF) to 13% (in the solid film). Usually, DTF functionalization on π-conjugated systems results in quenched fluorescence. The formation of an excimer was proposed as a mechanism for the observed AIEE behavior. DTF is a strong electron donor in this system, which can increase the intramolecular charge transfer (ICT), resulting in an excimer's formation. When the excimer was formed in their research, they observed shifting of fluorescence peak to the longer wavelength and higher intensity. The excimer formation decreases the

gap between the transition state and ground state, resulting in a shift to the longer wavelength.

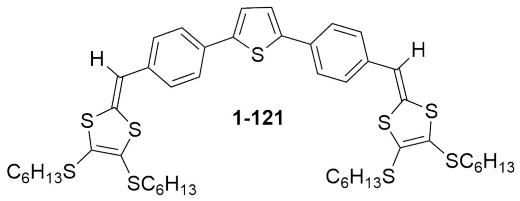

Figure 1.23: DTF-substituted organic chromophore **1-121** that shows AIEE behavior.

1.4 Pyrene-based Molecular Materials

Pyrene is a small polycyclic aromatic hydrocarbon (PAH) first isolated from the residue of coal tar.[125] After the modernization of coal tar distillation, pyrene became commercially available. Pyrene can be selectively functionalized at different positions to provide various synthetic precursors for the construction of more complex π-conjugated systems with special regioselectivity. Pyrene presents ten peripheral reactive positions. Researchers classified pyrene's positions into three sets of chemically non-equivalent sites (Fig. 1.24) Electrophilic substitution on pyrene has been known to take place on 1-, 3-, 6-, and 8-positions based on reported experimental results[126,127] and molecular orbital calculations, as the HOMO has its most significant coefficients at these positions (Fig. 1.25),[128,129] with the only exception of *tert*-butylated pyrene.[130] However, unsymmetrical substitution at these four positions is very challenging due to the various possible isomers that can be formed.

Pyrene can also be substituted at the 2- and 7-positions. This substitution needs a demanding route as these positions are not directly accessible by electrophilic

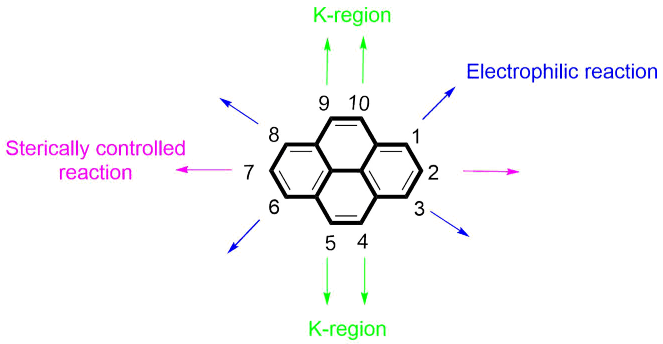

Figure 1.24: Chemically non-equivalent sites on pyrene.

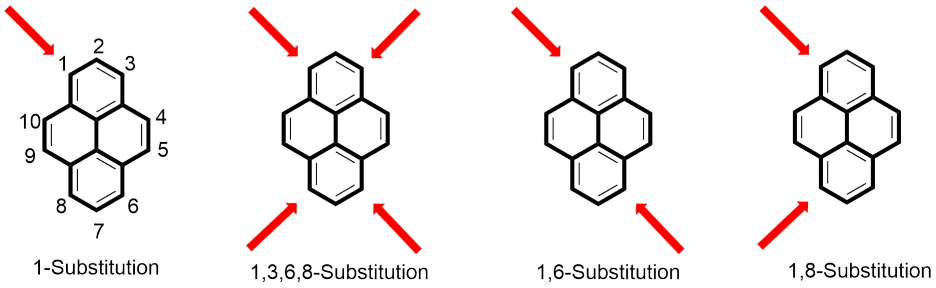

Figure 1.25: General structures of possible substituted pyrenes.

substitution of pyrene itself. Also, substituents on 2,7-positions do not interact with the HOMO/LUMO of pyrene as they lie on the nodal plane. As a result, this substitution usually has a low yield. Two main approaches are known to achieve this type of substitution. The first one is through the reduction of pyrene to 4,5,9,10-tetrahydropyrene, followed by electrophilic substitution and subsequent re-aromatization. The second approach is the use of *cine* substitution through a 1,2-dehydropyrene intermediate to convert 1-bromopyrene to a mixture of 1- and 2-aminopyrene. However, these are multi-step synthesis with very low yields. In 2005, Marder and co-workers reported a one-step high yielding synthesis to gain pyrene-2,7-bis(boronate)ester using an iridium-based catalyst.[131] The 4,5,9,10-positions of the pyrene ring are called the K-region. These positions are also difficult to be

functionalized (Fig. 1.24).

Researchers have made numerous attempts to prepare pyrene-4,5-diones and pyrene-4,5,9,10-tetraones directly from pyrene. Pyrene-4,5-dione can be made by the oxidation of pyrene using highly toxic osmium tetroxide as oxidant, resulting in a low yield.[132] Some synthetic routes have been reported to produce pyrene-4,5-dione and pyrene-4,5,9,10-tetraone in one pot.[133–135] The oxidation of pyrene using a heterogeneous mixture of ruthenium(III) chloride ($RuCl_3$) and sodium periodate ($NaIO_4$) in CH_2Cl_2, H_2O, and CH_3CN was developed to yield pyrene-4,5-dione as the major product without further oxidation. Later in 2016, the Bodwell group[136] reported a scalable and efficient method for the synthesis of pyrene-4,5-dione (Scheme 1.27) on a 15 g scale. They also improved the yield and simplified the workup process dramatically by using *N*-methylimidazole (NMI, 5 mol %) as an additive in the reaction. With this synthetic approach available, the studies of pyrene-4,5-dione derivatives have grown significantly in recent years.

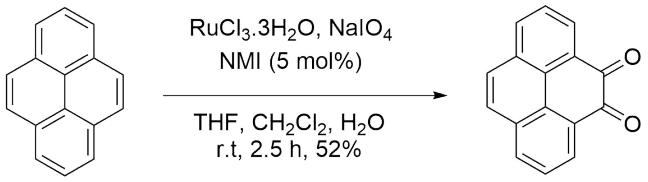

25g
1-122

15g
1-123

Scheme 1.27: K-Region oxidation reactions of pyrene on a 15 g scale.

1.4.1 Photophysical Properties of Pyrene Derivatives

Pyrene is an important molecular building block for organic π-conjugated optoelectronic materials. Pyrene shows interesting photophysical properties, along with high chemical stability and charge-carrier mobility. Pyrene is among the most popularly studied organic chromophores.[137] Pyrene derivatives have been used in applications ranging from organic light-emitting diodes (OLEDs), organic field-effect transistors (OFETs), to organic photovoltaic cells (OPVs). To adjust the properties of the target molecule for a specific application, electron donors or acceptors are usually added to a pyrene core as they can greatly change the frontier molecular orbitals. Pyrene substitution with donors or acceptors provides derivatives with different properties such as a permanent dipole moment, charge-transfer (C-T) excited states, strong solvatochromism, environment-sensitive photophysics, the likelihood for energy or electron transfer, and narrowed energy gaps.[138,139] Müllen and co-workers studied the donor and acceptor substituents at pyrene's K-regions to engineer its optoelectronic properties. They examined the influence of the substitution pattern on frontier molecular orbitals and solid-state packing properties. They synthesized two pyrene derivatives (**1-124** and **1-125** Fig. 1.26) with D-A groups substituted in the K-region.

The UV–vis absorption of D-A substituted pyrenes shows a significant decrease in the optical energy gap, resulting from an intramolecular charge-transfer process. Therefore, a raised HOMO level and a smaller energy gap could be attained by choosing a stronger donor moiety. Moreover, solvatochromism was observed for both D–A pyrenes, making these molecules potential candidates for sensing solvent polarity.

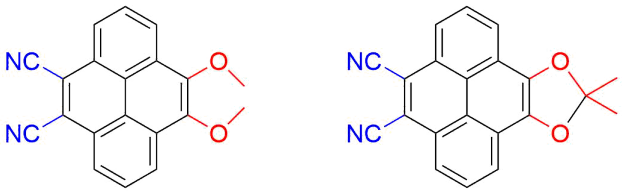

Figure 1.26: Pyrene derivatives with donor and acceptor groups subsituted in the K-region.

Pyrene possesses some unique properties such as intense blue emission and a long-lived excited singlet state together with excimer and exciplex formation. Forster and Kasper reported the first intermolecular excimers of pyrene in solution.[140] The pyrene fluorescence properties have been studied for more than six decades. So far, pyrene has been the most generally applied dye in fluorescence-labeled polymers.[141,142] Hydrophobic pyrene units can be attached to water-soluble polymers to alter the properties of the polymers. The pyrene chromophore is frequently employed as a probe to measure surfactant micelles, phospholipid vesicles, and surfactant/polymers aggregates. The formation of pyrene excimers has been widely employed in supramolecular design and probing the structural properties of macromolecular systems. Pyrene has also been widely used as a fluorescence probe in chemo-biosensors, fluorescence labelling, bioimaging, and electroluminescent devices. Pyrene labels have been integrated in the structures of proteins and peptides,[143–146] and in DNA recognition.[147–151] The fluorescence of pyrene excimers has been employed to sense environmental parameters such as temperature,[152] pressure,[153] or pH. Any changes in the fluorescence intensity of an excimer reflects changes in its environment. Besides, it can detect guest molecules such as gases (O_2 or NH_3), organic molecules, metals, or other different analytes. Furthermore, chromophores containing a pyrene

core can absorb and emit light in the near-infrared (NIR) region, which is in demand for applications such as bioimaging and cell recognition, since NIR light can penetrate biological tissues deeper and gives minimum interference from background autofluorescence by biomolecules.[139]

1.4.2 Recent Progress in Pyrene-based Organic Fluorophores

Pyrene-4,5-diones **1-123** have found growing applications in recent years. Pyrene-4,5-dione **1-123** can be subjected to various reactions to generate different π-conjugated materials with interesting electronic and photophysical properties. Condensation reactions have been demonstrated as a very appealing approach for extending π-conjugated structures, due to their excellent efficiency and simplicity in operation. For example, pyrenoimidazole derivatives can be directly prepared through the condensation reactions of pyrene-4,5-dione **1-123** with various counterparts, and the resulting pyrenoimidazole systems often exhibit intense fluorescence, which make them useful organic fluorophores.

In 2013, Ho and co-workers[154] reported a pyrenoimidazole-based organic dye (**1-126** Fig 1.27), which can be used for co-sensitization of the photoanodes of organic DSSCs. The use of compound **1-126** resulted in a more intense and broader absorption spectrum of the dye, which in turn improved the cell efficiency. Furthermore, the at-rest long-term stability of the DSSC, with a co-sensitized photoanode, showed an unfailing efficiency for up to 1000 h.

Later in 2014, Huang and co-workers[155] designed and synthesized a series of

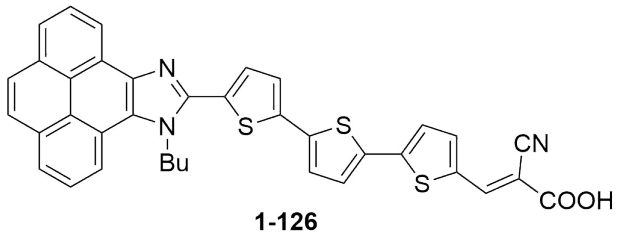

1-126

Figure 1.27: Molecular structure of pyrenoimidazole **1-126**.

symmetrical oligothiophene and benzene-based bispyrenoimidazole derivatives (**1-127** and **1-128** Fig. 1.28) through the Debus-Radziszewski reaction. As a result of the extension of π-conjugation via oligothiophene and benzene linkers and N-alkylation of the pyrenoimidazole chromophore, these compounds exhibit strong fluorescence emission and good thermal stability.

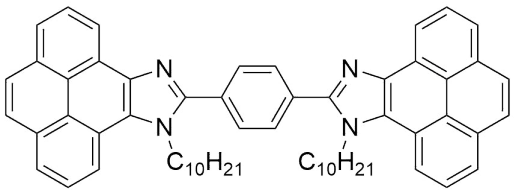

1-127

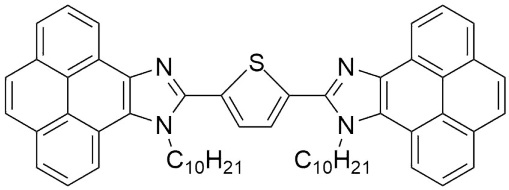

1-128

Figure 1.28: Bispyrenoimidazole derivatives **1-127** and **1-128**.

In 2015, Baitalik and co-workers reported the synthesis of an imidazolyl-pyrenoimidazole conjugate (**1-129** Fig. 1.29) and tested its performance as an efficient fluorescence sensor for cyanide anion in a mixed solvent of water/DMSO (9:1).

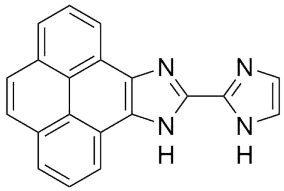

1-129

Figure 1.29: Imidazolyl-pyrenoimidazole **1-129**.

Misra and co-workers[156] reported the design and synthesis of pyrene-based solid state emitters **1-130** and **1-131** (Fig. 1.30). In their work, the single crystal structures and solid-state packing properties of the synthesised compounds were disclosed. The solid-state structures of these compounds show twisted conformations and the absence of strong $\pi - \pi$ stacking among the pyrene units. As a result, these compounds retain fluorescence in the solid state and show aggregation induced emission (AIE) and mechanochromic behavior.

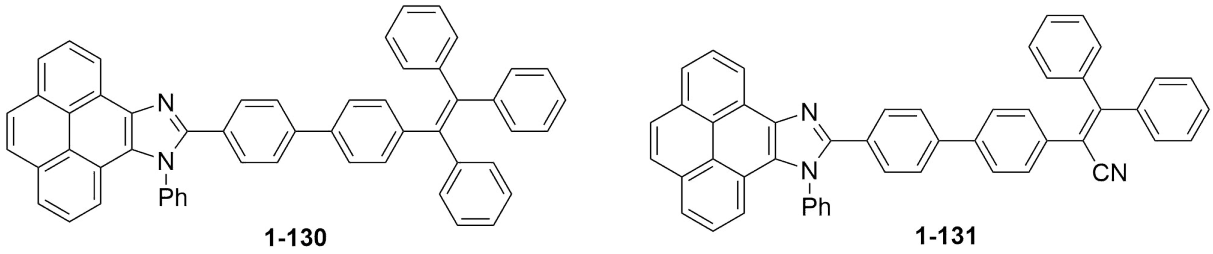

Figure 1.30: Pyrene-based solid state emitters **1-130** and **1-131**.

Lu and co-workers[157] reported the synthesis of pyreneimidazole coupled with naphthalene, termed PIMNA (**1-132**, Fig. 1.31). It was found that PIMNA can be used in building deep blue emitters with an ambipolar nature. PIMNA gives deep blue emission with the smallest CIE of 0.034 ever reported in non-doped OLEDs.

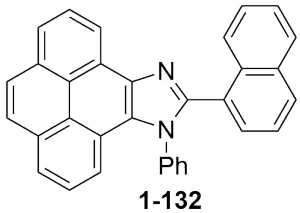

Figure 1.31: PIMNA **1-132** as a highly efficient deep-blue OLED.

Recently, Tabasi and co-workers[158] reported the synthesis of pyrenoimidazolyl-

benzaldehyde fluorophores (**1-133** Fig. 1.32) and discovered their sensing properties for fluoride anion. They studied their crystal structures and reported hydrogen bonding interactions, which play an essential role in the solid-state supramolecular assemblies. They also investigated the fluoride anion binding mechanism in polar solvents, and observed two separate steps. First, a hydrogen-bonded 1:1 complex was formed, and then deprotonation of the imidazolyl N-H group occurred. The UV-vis spectral changes in response to fluoride anion titration indicate a colorimetric sensing function.

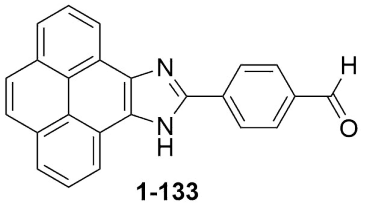

1-133

Figure 1.32: A pyrenoimidazolyl-benzaldehyde fluorophore as fluoride anion sensor.

1.4.3 Objectives and Organization of This Thesis

This PhD thesis work has accomplished four major research projects. These projects deal with the synthesis and characterization of functionalized π-conjugated oligomers, PAHs, and DTF-based molecular materials. Suzuki-Miyaura cross-coupling, olefination, Ramirez dibromoolefination, condensation, and oxidative coupling reactions have been utilized to a great extent in the synthetic portion, while advanced instrumental analytical techniques such as NMR, mass spectrometry, IR, UV-Vis absorption spectroscopy, fluorescence, X-ray single crystallography, and cyclic voltammetry (CV), have been employed to understand the various properties of the

new molecular materials developed. The detailed research results are outlined in Chapters 2 to 6.

Chapter 2 focuses on the design and synthesis of a new family of DTF-end-capped redox-active dendrimers with a fluorene core. The electronic properties and redox activity of the synthesized molecules were characterized, and a double-layer strategy was employed to generate a polymer thin film that can act as selective electrochemical sensor for TNT.

In Chapter 3, a new family of multi-DTF functionalized pyrene derivatives is reported. Their synthesis, electronic properties, and redox activity were investigated. The experimental results demonstrated that the substitution patterns of the DTF groups are key parameters affecting their molecular properties. These multi-DTF-pyrene compounds were further electrochemically polymerized to form redox-active thin films. The substituted DTFs underwent hydrogen/deuterium exchange reactions with varied efficiencies in acidic media.

Chapter 4 describes the synthesis, and comparative studies of three K-region functionalized pyrene derivatives. The electronic and electrochemical redox properties of the three pyrene derivatives were investigated by UV-Vis and cyclic voltammetric analyses. Their single crystal structural and solid-state packing properties were also examined and compared to understand the effects of functional groups attached to the pyrene K-region on various non-covalent interactions in the solid state.

Chapter 5 describes a new approach to generate functional organic fluorophores based on the self-condensation reaction of pyrene-4,5-dione. Plausible reaction mechanisms for this type of condensation were proposed based on experimental data, and the single-crystal structural and fluorescence properties of the new pyrene

fluorophores were analyzed. Interesting solvatochromic and acidochromic effects were observed, suggesting these fluorophores could be useful in fluorescence sensing applications.

All these projects mentioned above have met success, and the results led to three research articles published in peer-reviewed scientific journals and one manuscript just accepted. In all these papers, the author of this thesis is the first author, who made major contribution to the experimental work and data analysis. The author also actively participated in the manuscript preparation in collaboration with his supervisor and other co-workers. So, Chapters 2–5 of this thesis are organized in a paper-based structure.

Chapter 6 provides a summary of this thesis work, while some ongoing research projects carried out during this PhD research program are mentioned in Chapter 7. Based on the preliminary results of these incomplete and ongoing projects, future research directions are pointed out in Chapter 7.

Chapter 2

A Tetrathiafulvalene Vinylogue-Based Double-Layer Polymer Thin Film as a Highly Sensitive and Selective TNT Sensor

The contents of this chapter were published as an article on *New J. Chem.* **2019**, *43*, 5277-5281. Contributions of authors are described below:

Farshid Shahrokhi is the first author, who conducted all the experimental work, data analysis, and contributed to the manuscript preparation and editing. Yuming Zhao is the corresponding author of this paper, who is the supervisor of Farshid Shahrokhi and helped design and develop this project.

Abstract

A redox-active polymer thin film prepared by electropolymerization of a dithiafulvenyl-substituted phenylacetylene precursor was surface-modified with a fluorene-cored phenylene vinylene dendrimer carrying dithiafulvenyl endgroups. The resulting double-layer polymer thin film showed excellent sensitivity and selectivity in electrochemical sensing of TNT.

2.1 Introduction

Tetrathiafulvalene vinylogue (TTFV) is an organic π-electron donor that exhibits excellent redox properties at relatively low oxidation potentials.[60,159,160] Synthetically, TTFVs can be prepared through a facile oxidative dimerization reaction of dithiafulvene (DTF) precursors as exemplified in Figure 2.1A.[71] Such a reaction thus allows a wide range of π-extended functional molecules and macromolecules to be assembled *via* chemical and electrochemical oxidative approaches.[160] In our recent studies, a TTFV-pyrene-containing macrocycle was synthesized and found to bind with electron-deficient nitrobenzene derivatives through intermolecular charge-transfer (C-T) interactions.[98] TTFV-based cross-linked microporous polymers were prepared to modify the surface of a glassy carbon electrode by electropolymerization, giving rise to effective electrochemical sensing for nitrobenzene.[99] Nevertheless, these TTFV-based polymer thin films on the electrode surface showed limited durability, and their selectivity for specific nitroaromatic substances has not yet been demonstrated.

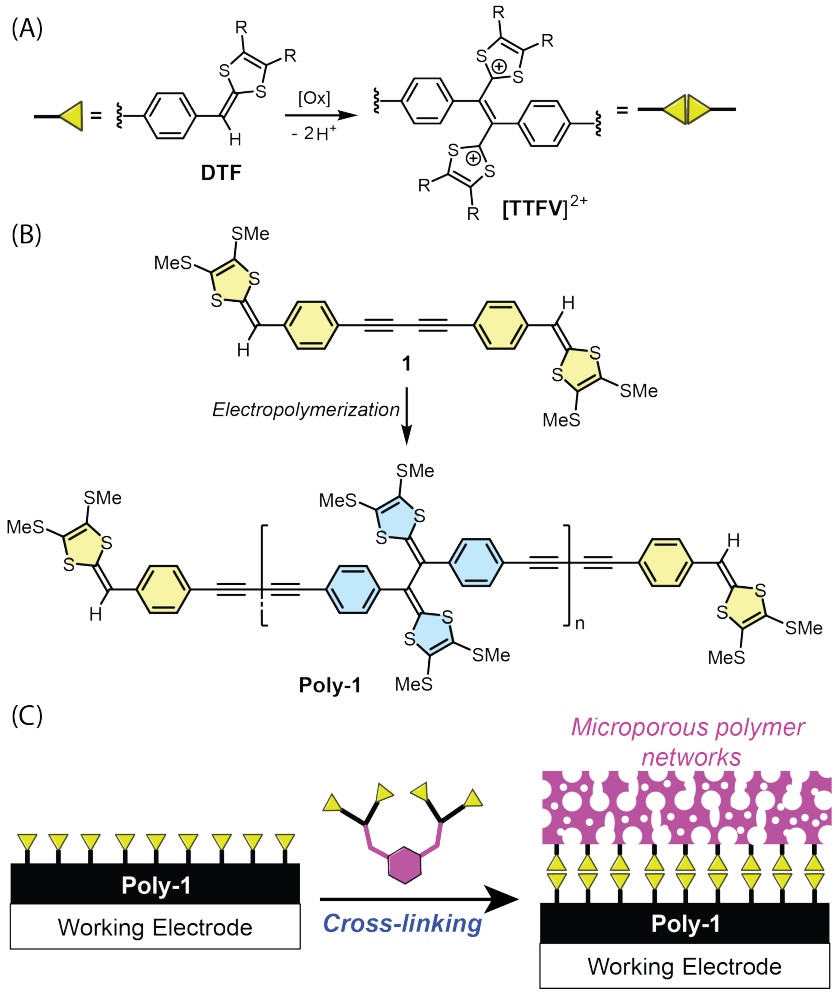

Figure 2.1: (A) Oxidative dimerization of two DTF groups to form a TTFV linkage. (B) Electropolymerization of bis(DTF)-phenylacetylene **1** to form **poly-1** thin film. (C) Schematic illustration of covalent modification of the thin film of **poly-1** with another layer of cross-linked microporous polymer networks.

Currently, there is a growing need for efficient detection technologies of nitroaromatic explosives, particularly 2,4,6-trinitrotoluene (TNT), due to their applications in national security, counter-terrorism,[161–163] and environmental control.[164–168] Electrochemical sensors for TNT have the advantages of easy fabrication, low cost, excellent portability, and depolyability for on-site and *in*

situ real-time operations as well as adaptability with disposable and wearable devices.[169,170] In this work, we report a new type of TTFV-polymer-based electrochemical sensor that exhibits high selectivity and good sensitivity for TNT. This was achieved by implementing a "double-layer polymer thin film" strategy. Herein, a bis(DTF)-functionalized phenylacetylene (compound **1**, Figure 2.1) was chosen as the first redox-active layer to be directly deposited on the working electrode, in view of its ability to form highly robust and durable polymer thin films (**poly-1**) on various conductive substrates through simple electropolymerization.[17,171] In our previous studies, the thin films of **poly-1** were observed to reliably maintain its electrochemical redox behavior and mechanical stability after numerous cycles of cyclic voltammetric (CV) scans over a wide range of applied potentials. Such performance can be ascribed to the linear molecular shape of compound **1**, which enables its electrochemically generated polymer to be tightly bound to the surface of a working electrode with high uniformity and mechanical stability. As illustrated in Figure 2.1B, electrochemically generated **poly-1** should carry DTF end groups, which in turn serve as synthetic handles allowing the surface of a **poly-1** thin film to be further covalently functionalized. Figure 2.1C illustrates the concept of forming another functional polymer layer on top of **poly-1**. In this step, a multi-DTF endcapped arene is subjected to electropolymerization on the surface of a **poly-1** thin film, resulting in cross-linked microporous polymer networks covalently bound to **poly-1** through TTFV linkages. The intrinsic nanometer-scale pores/cavities in the cross-linked polymer should provide suitable binding sites for electron-deficient aromatics,[172] while the two layers of TTFV-based polymers are expected to respond synergistically to the binding events with variation of redox

current and/or potential. We envisioned that a suitable choice of the multi-DTF-arene building block for the surface modification would eventually lead to high selectivity for certain nitrobenzene derivatives, such as TNT. Recently, fluorene-based oligomers and microporous polymers were reported to give enhanced TNT sensing function.[173–176] Based on this progress, we hence designed and synthesized a new fluorene-cored phenylene vinylene dendrimer **2** (Scheme 2.1) carrying four DTF groups on its peripheral positions. This arene building block was designed to generate cross-linked polymer networks through oxidative DTF coupling reactions, while the incorporation of fluorene units was expected to induce selective interactions with TNT.

2.2 Results and Discussion

As outlined in Scheme 2.1, the synthesis of **2** was carried out by sequential Ramirez dibromoolefination, Suzuki-Miyaura coupling, and phosphite-promoted olefination reactions. For the purpose of comparative studies, two bis(DTF)-substituted analogues **9a/b** were also prepared. All the reactions gave reasonably good yields. The purity and chemical structures of new compounds were confirmed by various spectroscopic characterizations (see the Appendix (I) for details).

X-ray single crystal structures of aldehyde precursors **5** and **7** were obtained. In the structure of compound **5**, the diphenyl groups rotate into a perpendicular orientation with respect to the central fluorene core due to the steric interactions among them (see Scheme 2.1). A similar conformation is seen in the core structure of dendritic compound **7**. In addition, the four peripheral phenyl groups of **7** assume a highly twisted spatial arrangement as a result of steric crowdedness. It is reasonable to assume that the structure of tetra(DTF) **2** would possess a highly twisted fluorene-phenylene vinylene backbone similar to that of **7**. Accordingly, the cross-linking reaction of **2** through DTF oxidative coupling should generate rigid, 3-dimensional polymer networks with nanometer-scale intrinsic porosity. Such features would be beneficial for selectively capturing nitroaromatic compounds through π-stacking and/or C-T interactions.

Prior to the examination of the electrochemical redox activity, bis(DTF) **9a** was first tested as a model compound under chemical oxidative conditions. It was found that when treated with iodine in CH_2Cl_2 at room temperature, **9a** gradually formed oligomers *via* DTF oxidative coupling at a moderate rate. When the reaction time

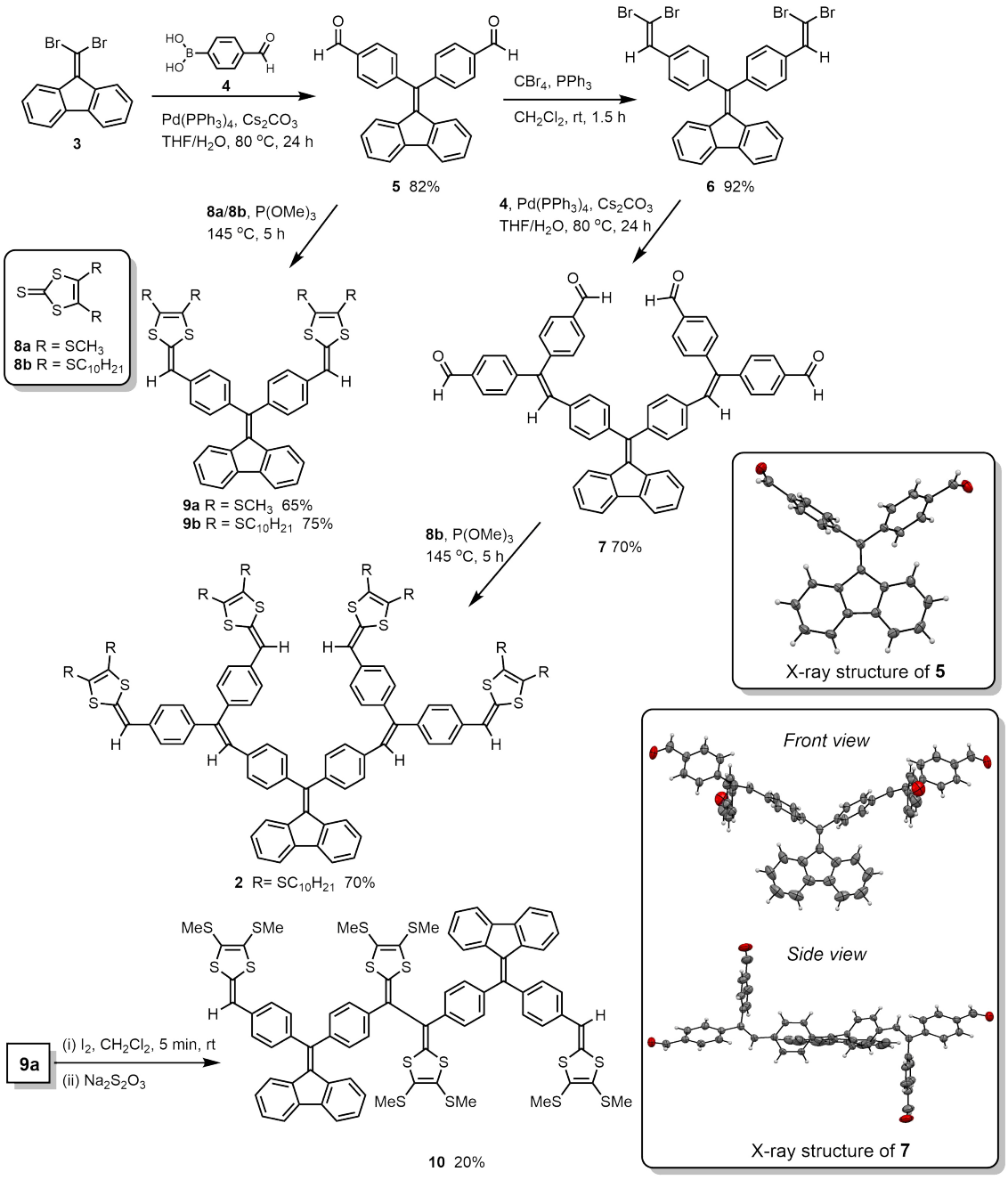

Scheme 2.1: Synthesis of tetra(DTF)-substituted fluorene-cored phenylene vinylene dendrimer **2**. Insets: ORTEP plots (at 50% ellipsoidal probability) of compounds **5** (CCDC 1861152) and **7** (CCDC 1861151).

was controlled at 5 min, a dimerized product **10** (see Scheme 2.1) could be isolated with a yield of 20% and its structure was confirmed by spectroscopic characterizations (see the Appendix (I)).

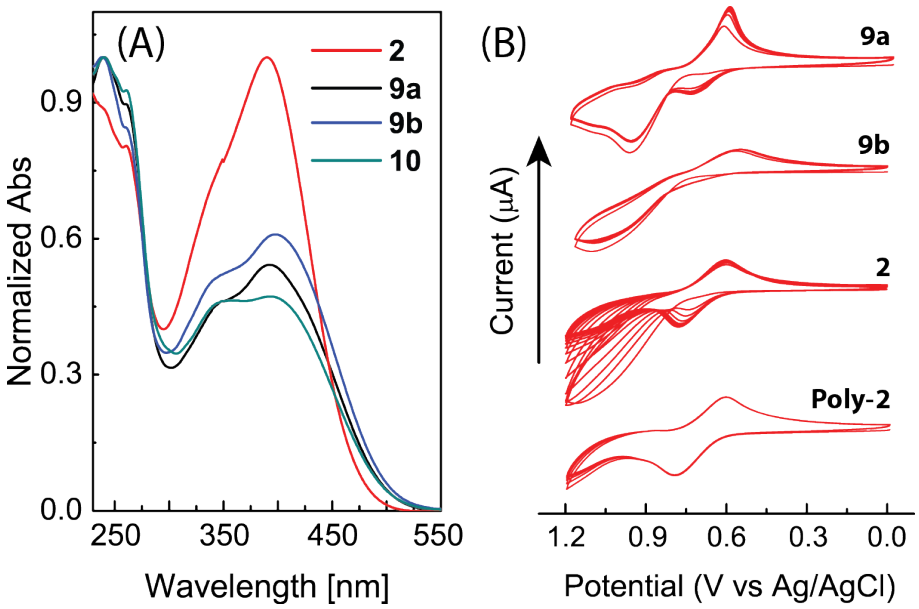

Figure 2.2: (A) Normalized UV-Vis absorption spectra of compounds **2**, **9a**/**b**, and **10**. (B) Cyclic voltammograms of compounds **2**, **9a**/**b**, and **poly-2** measured in CH_2Cl_2. Experimental conditions for CV analysis: electrolyte: Bu_4NBF_4 (0.1 M), working electrode: glassy carbon, counter electrode: Pt wire, reference electrode: Ag/AgCl, scan rate: 0.1 V/s.

The electronic absorption properties of DTF-functionalized compounds **2**, **9a**/**b**, and **10** were analyzed by UV-Vis absorption spectroscopy (see Fig. 2.2A). The UV-Vis data show that the low-energy absorption bands of these compounds are at very similar wavelengths, suggesting that all these compounds have a similar degree of $\pi-$electron delocalization. Fig. 2.2B shows the cyclic voltammograms of compounds **9a**/**b**, **2**, and the polymer thin film generated by electropolymerization of **2** after

multi-cycle cyclic voltammetric (CV) scans (referred to as **poly-2**). It is interesting to note that bis(DTF) compounds **9a** and **9b** give very different electrochemical behavior, even though their structures only differ in the alkylthio (SR) groups attached to the DTF units. Bis(DTF) **9a**, which carries SCH_3 side groups, exhibits the typical electrochemical reactivity of DTF. In the first cycle of CV scan in the positive direction, an anodic peak (E_{pa}) can be observed at +0.98 V, which is assigned to the simultaneous oxidation of the two DTF groups of **9a** into radical cations. In the reverse scan, a cathodic peak (E_{pc}) appears at +0.74 V. Associated with this peak there is a new anodic peak at +0.61 V during the second cycle of CV scans and thereafter. They are the quasi-reversible redox couple arising from the TTFV units of oxidatively coupled products, such as **10**. The $SC_{10}H_{21}$ substituted bis(DTF), **9b**, does not show significant formation of oxidatively coupled TTFV products in its cyclic voltammogram. The reason for it is not quite clear yet; however, steric effects are believed to play a key role here. The cyclic voltammogram of tetra(DTF) **2** shows an anodic peak at +1.16 V and a cathodic peak at +0.60 V in the first cycle of CV scans. From the second cycle of scans, the characteristic redox couple (E_{pa} = +0.74 V, E_{pc} = +0.60 V) of TTFV could be observed. With increasing scan cycles, the peak at +0.74 V gradually grows in intensity and shifts to more positive potential. After multiple cycles of CV scans, a thin film was deposited on the surface of the working electrode. The CV profiles of this thin film mainly feature the characteristic redox couple of TTFV (see Fig. 2.2B), which clearly testifies to the ability of **2** to form a cross-linked polymeric product (*i.e.*, **poly-2**) through electropolymerization.

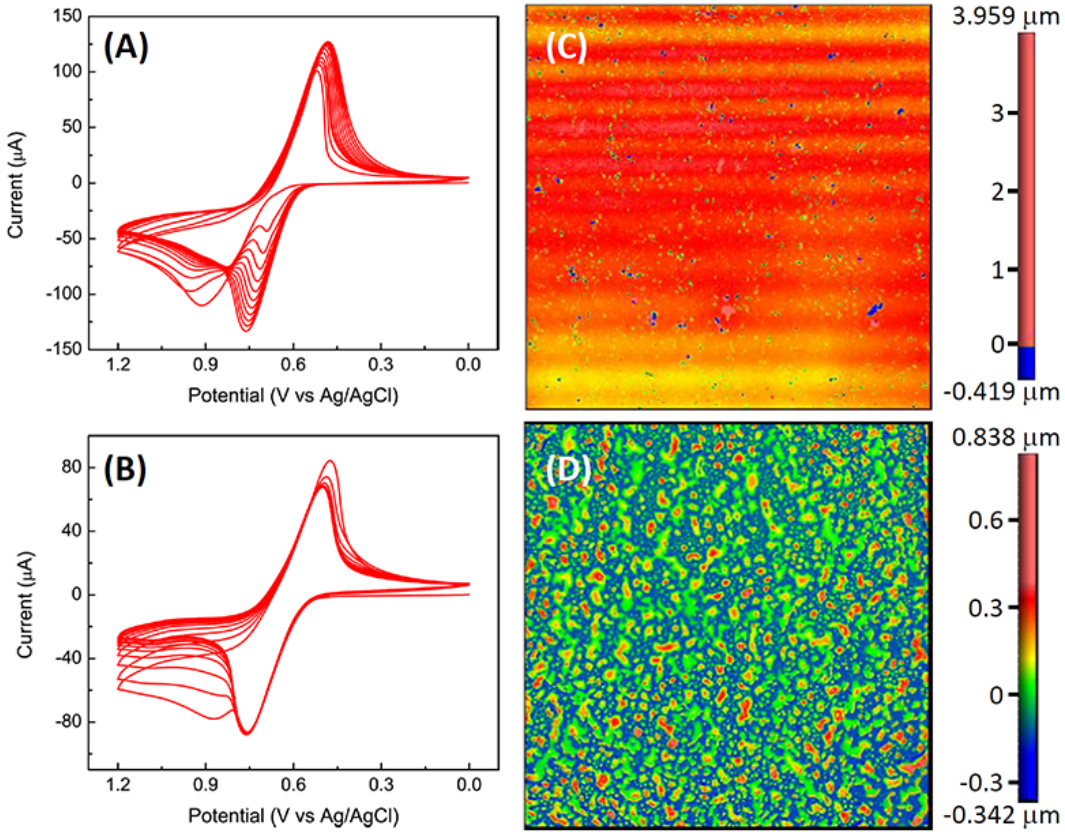

Figure 2.3: (A) CV profiles monitoring the deposition of **poly-1** on a glassy carbon electrode. (B) CV profiles monitoring the deposition of **poly-2** on the surface of **poly-1** pre-deposited on a glassy carbon electrode. (C) Surface morphology of the thin film of **poly-1** deposited on an ITO substrate. (D) Surface morphology of the double-layer thin film of **poly-2**—**poly-1** on an ITO substrate.

To prepare the double-layer thin film sensor, bis(DTF) **1** was first subjected to 20 cycles of CV scans (0 to +1.2 V) to form a robust thin film of **poly-1** on the surface of a glassy carbon electrode. Fig. 2.3A shows the cyclic voltammogram corresponding to the formation of **poly-1** thin film on the glassy carbon electrode. To the top of this polymer film a second layer of cross-linked polymer, **poly-2**, was covalently attached by running another 20 cycles of CV scans in the solution of **2** (see Fig. 2.3B). This process yielded a double-layer polymer thin film, designated as **poly-2**—**poly-1**. To compare the differences in microscopic morphology between **poly-1** and **poly-2**—**poly-1**, their thin films generated on indium tin oxide (ITO) coated glass slides under similar electrochemical conditions were imaged by optical profiling analysis. Fig. 2.3C shows that the film of **poly-1** smoothly and tightly covers the ITO surface, while **poly-2**—**poly-1** exhibits a "forest-like" microscopic pattern (Fig. 2.3D), which renders the film of **poly-2**—**poly-1** a large surface area and high porosity. Optical profiling imaging on the edge of the **poly-2**—**poly-1** film indicated that the film thickness is *ca.* 1–2 μm (Fig. S-23B, Appendix (I)). SEM imaging revealed that the surface of the film is full of "worm-like" micro-crevices with diameters in the range of 60–80 nm (Fig. S-21, Appendix (I)). Such morphological properties are expected to not only increase the efficiency of electrochemical sensing, but also enhance the selectivity for certain nitroaromtic analytes.

The performance of the **poly-2**—**poly-1** thin film on a glassy carbon electrode as an electrochemical sensor for nitroaromatics was then investigated by differential pulse voltammetric (DPV) analysis. The CH_2Cl_2 solutions containing various amounts of nitrobenzene, 2,4-DNT, and TNT, respectively, were examined by DPV. It was observed that the DPV signals of the **poly-2**—**poly-1** thin film did not show any

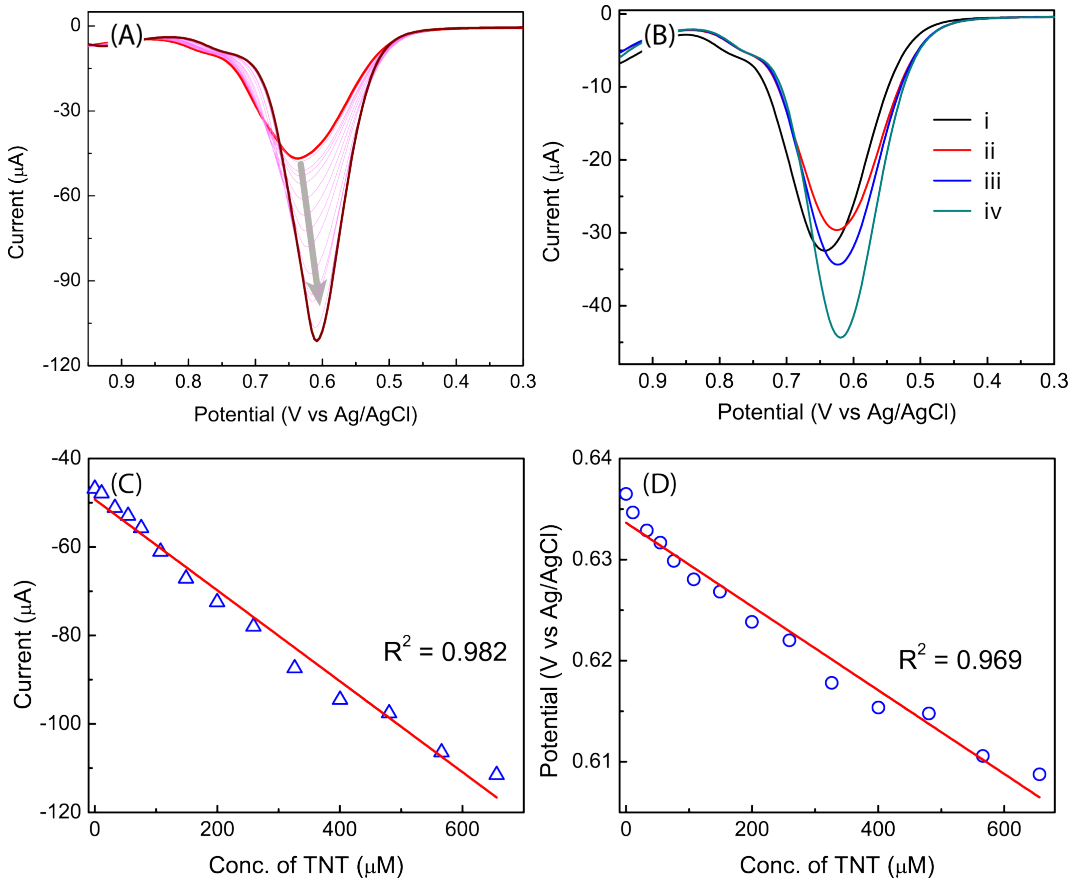

Figure 2.4: (A) DPV profiles showing the responses of **poly-2**—**poly-1** thin film to TNT at varied concentrations (0 to 0.656 mM) in CH_2Cl_2. (B) DPV profiles of **poly-2**—**poly-1** thin film measured, curve i: blank solution, curve ii: nitrobenzene (100 mM), curve iii: nitrobenzene (100 mM) and TNT (0.107 mM), and curve iv: nitrobenzene (100 mM) and TNT (0.200 mM) in CH_2Cl_2. Linear regression plots of the concentration of TNT against (C) the peak current (I), and (D) the peak potential (V) of the DPV signals.

significant changes in response to nitrobenzene and 2,4-DNT. For TNT, however, the thin film exhibited notable changes in both the current intensity (I) and potential (V) of the oxidation peak (Fig. 2.4A). The measured I and V values were found

to show very good linear correlation with the concentration of TNT in the range of 10^{-5} to 10^{-3} M (Fig. 2.4C and D). With these relationships, quantitative analysis of TNT could be readily achieved at the sub-mM level, with limits of detection (LoD) at 2.22×10^{-6} M and 3.09×10^{-9} M by measuring the responses of ΔI and ΔV, respectively. It is also worth noting that the selective sensing of TNT is indeed unique for the double-layer **poly-2**—**poly-1** thin film, as compared with the performance of the single-layer thin film of **poly-2** or **poly-1** deposited on the glassy carbon electrode (see Fig. S-15 to S-20 in the Appendix (I)).

To further assess the selectivity of the double-layer thin film, detection of a sub-mM level of TNT (*ca.* 10^{-4} M) in a CH_2Cl_2 solution spiked with a large excess of nitrobenzene (*ca.* 0.1 M) was tested. As shown in Fig. 2.4B, when the concentrations of TNT were increased from 0.107 mM and 0.200 mM in the presence of nitrobenzene, the double-layer thin film gave DPV changes of $\Delta V = -7$ mV and $\Delta I = -9.93$ μA. These results are in line with the DPV responses ($\Delta V = -4$ mV and $\Delta I = -9.55$ μA) calculated according to the linear regressions in Fig. 2.4C and D, and hence confirm that the thin film can keep satisfactory electrochemical sensing performance for TNT with little interference from nitrobenzene (see Fig. 2.4B). Moreover, the double-layer thin film is re-useable by simply rinsing it with organic solvents such as CH_2Cl_2.

2.3 Conclusions

In summary, the double-layer strategy utilized in this study has successfully led to an efficient and highly selective electrochemical sensor for TNT. The newly designed cross-linked TTFV-fluorene polymer, **poly-2**, is an active sensing component for

TNT. The robust thin film of **poly-1**, on the other hand, plays an essential role in sequestering **poly-2** on the working electrode, so that the performance of **poly-2** maintains reliable and durable. In theory, numerous double-layer thin films can be generated by electropolymerization of different multi-DTF functionalized arenes on the surface of a **poly-1** thin film. Our "double-layer" strategy thus opens a new avenue for the development of functional redox-active polymer thin films and related electrochemical devices.

Chapter 3

Redox-Active Dithiafulvenyl-Functionalized 1,3,6,8-Tetraphenylpyrene Derivatives: Synthesis, Spectroscopic, and Electrochemical Redox Properties

The contents described in this chapter are being prepared as a manuscript to be submitted to an ACS or RSC journal. Contributions of authors are described below:

Farshid Shahrokhi is the first author, who conducted all the experimental work, data analysis, and contributed to the manuscript preparation and editing. Yuming

Zhao is the corresponding author of this manuscript, who is the supervisor of Farshid Shahrokhi and helped design and develop this project.

Abstract

A series of 1,3,6,8-tetraphenylpyrene (TPPy) derivatives substituted with redox-active 1,4-dithiafulvenyl groups was synthesized and investigated. The conformational properties of these TPPys were assessed by X-ray single crystallographic and NMR analyses. Their electronic properties and electrochemical redox reactivities were examined by UV-Vis absorption spectroscopy and cyclic voltammetry. Furthermore, the dithiafulvenyl groups attached to the TPPy core were found to undergo efficient deuterium/proton exchange with D_2O under acidic conditions.

3.1 Introduction

The studies of redox-active organic π-conjugated compounds and polymers have experienced substantial growth during the past decade, owing to their appealing application in advanced optoelectronic devices and energy storage materials.[16,177–182] Among the vast array of organic π-conjugated motifs developed in the literature, molecular structures based on polycyclic aromatic hydrocarbons (PAHs) are of particular interest owing to their rigid molecular structures and highly delocalized π-electron density. Pyrene is an important member of the PAH family that exhibits high emission efficiency and strong supramolecular self-assembling properties.[137–139] It also features a highly symmetric molecular structure (D_{2h} point group) that

can be selectively functionalized at various positions.[125–128] As such, pyrene has been widely used a core building block, taking advantage of its unique structural symmetry, π-delocalization, and highly fluorescent properties, in the construction of functional organic macrocycles, polymers, and 2-dimensional frameworks.[137,183–189] On the other hand, pyrene-based materials with redox activity have been relatively less developed,[190–192] since pyrene itself lacks electrochemical redox activity and requires functionalization with certain functional groups to gain such properties.

1,3-Dithiafulvene (DTF) is a five-membered heterocycle that not only acts as an excellent π-electron donor, but also shows interesting oxidative coupling reactivity useful for the preparation of functional redox-active polymers.[8,49,72,160] Scheme 3.1A illustrates the general mechanism for the oxidative DTF dimerization.[71] Usually, the DTF group that is directly linked to an aryl group can easily release an electron upon oxidation to form a radical cation intermediate. This intermediate can further undergo a facile radical dimerization, followed by deprotonation, to yield a tetrathiafulvalene vinylogue (TTFV) product. The DTF oxidative dimerization reaction offers a facile C–C bond forming methodology, through which a variety of TTFV-based organic materials can be prepared. For instance, oxidative polymerization of di(DTF) or poly(DTF)-substituted arenes can be performed (see Figure 3.1B) to generate linear or cross-linked polymers with versatile redox, electrochromic, and electrochemical sensing properties.[17,72,160,171,193,194]

Previously, we prepared pyrene **1** and **2** derivatives with DTF groups attached to the 1 and 8 positions (see Figure 3.1).[98] Our studies showed that both compounds are redox-active, while the 1,8-diphenylpyrene-cored derivative **2** could undergo a sequence of oxidative DTF coupling reactions to yield a macrocyclic product in a good

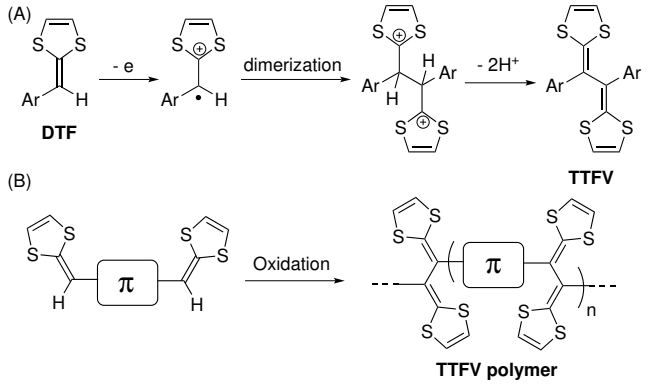

Scheme 3.1: (A) General reaction mechanism for the oxidative dimerization of an aryl-substituted DTF. (B) Oxidative polymerization of a di(DTF)-arene precursor to yield a TTFV-based polymer product.

yield. In this work, we aimed at the study of a class of tetra(DTF)-pyrene systems by employing a 1,3,6,8-tetraphenylpyrene (TPPy) as the core group (Figure 3.2). The main motivations for this work are described as follows. First, the TPPy core possesses a symmetric tetradentate topology that is ideal for the assembly of ordered 2-dimensional and 3-dimensional organic frameworks.[195–199] Second, the TPPy unit has been demonstrated to show intriguing photophysical properties and can form relatively stable radical cation upon oxidation.[200,201] Third, the four phenyl rings of TPPy prefer a nearly perpendicular orientation with respect to the central pyrene unit due to steric interactions. Such a conformation allows channels or cavities to be formed in crystal packing, which in turn facilitates the assembly of supramolecular guest-host inclusion systems.[202–204] Finally, it is worth noting that the substitution pattern on the phenyl groups of TPPy can be flexibly modified (*ortho*, *meta*, and *para*), so that the possibility to create diverse tetra(DTF)-substituted TPPys would be further enhanced. In this work, we report the design and synthesis of a series

of tetra(DTF)-substituted TPPys (**7**–**9**, Scheme 4.2). Their electronic properties and electrochemical redox properties were disclosed by UV-Vis absorption and cyclic voltammetric analyses.

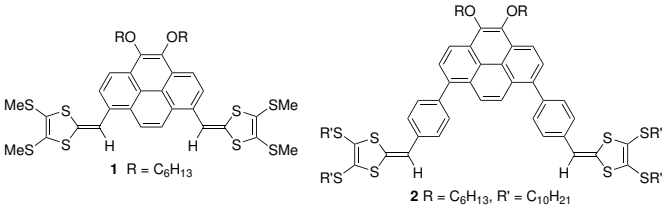

Figure 3.1: 1,8-Di(DTF)-substituted pyrenes **1** and **2** investigated in our previous studies.

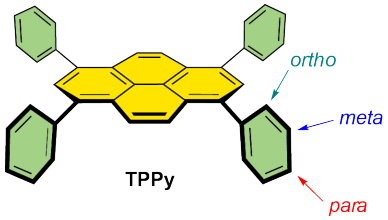

Figure 3.2: Structure of 1,3,6,8-tetraphenylpyrene (TPPy) utilized in this work.

3.2 Results and discussion

3.2.1 Synthesis and structural properties of tetra(DTF)-substituted TPPys

The synthesis of tetra(DFT)-substituted TPPys is outlined in Scheme 4.2. Herein, we first conducted Suzuki-Miyaura cross-coupling between 1,3,6,8-tetrabromopyrene (**3**)[205] and three formylphenylboronic acids (**4a**–**c**). The cross-coupling reactions

afforded formyl-substituted TPPys **5a**–**c**, respectively, in very good yields. Compounds **5a**–**c** were then subjected to phosphite-promoted olefination reactions[206] with 1,3-dithiole-2-thiones (**6a** and **6b**), respectively, in the presence of $P(OEt)_3$ at 150 °C. The reactions were accomplished within 2–3 hours and afforded DTF-substituted TPPys (**7**–**9**) in satisfactory yields (*ca.* 40–60%).

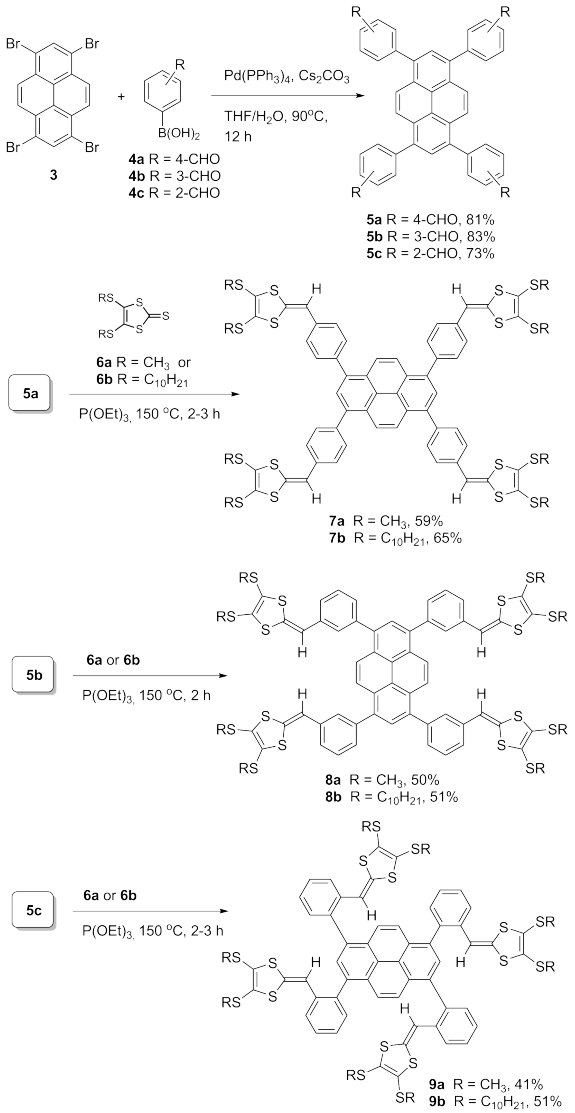

Scheme 3.2: Synthesis of DTF-functionalized pyrene derivatives **7**–**9**.

The molecular structures and purity of compounds **7**–**9** and TPPy intermediates **5** were confirmed by IR, NMR, and MS analyses (see the Appendix (II) for more details). Recrystallization of these compounds was performed in order to acquire single crystals for X-ray diffraction (XRD) analysis. In our attempts, only formyl-substituted TPPys **5a** and **5c** afforded good-quality single crystals. It is interesting to find out that the single crystals resulting from slow recrystallization of **5a** out of methanol turn out to be a new compound **10**, with the formyl groups of **5a** all converted into dimethyl acetals (see Figure 3.3A). In the X-ray crystal structure of **10**, the four phenyl groups show torsion angles of 48–63° relative to the central pyrene unit. For the X-ray structure of TPPy **5c** (Figure 3.3B), torsion angles between phenyl rings and the pyrene unit are 57–73°, which are slightly greater than those **10** as a result of increased steric interactions arising from the *ortho*-substituted formyl groups. In theory, compound **5c** may exist as five possible atropisomers as illustrated in Figure 3.4B. The structure determined in the single crystal is in line with the isomer **IV**, where the *ortho*-formyl groups are oriented as 1,3-up,6,8-down.

In the ^{1}H NMR spectrum of **5a**, the four formyl protons appear as a singlet at 10.16 ppm due to free rotation of the phenyl groups in the solution phase at room temperature. In the same way, the formyl protons of **5b** give a singlet at 10.16 ppm as well in its ^{1}H NMR spectrum, suggesting that the *meta*-substitution on the phenyl ring does not cause sufficient steric hindrance to result in distinct atropisomers. In the ^{1}H NMR spectrum of **5c**, however, there are thirteen distinct signals observed corresponding to the four formyl protons in its structure (Figure 3.4A). If each of the five possible atropisomers of **5c** takes an ideal molecular symmetry (i.e., the phenyl rings are exactly perpendicular to the pyrene unit), the mixture of them would give

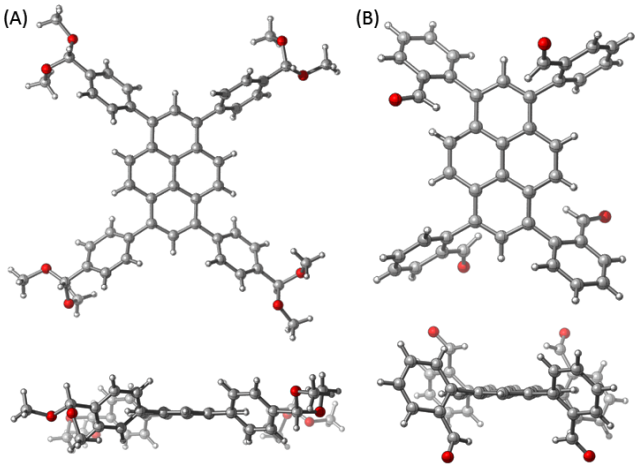

Figure 3.3: X-ray crystal structures of TPPys (A) **10** and (B) **5c** viewed from front (top) and side (bottom) sides. CCDC deposition numbers: 226759 (**5c**) and 2026762 (**10**).

rise to totally eight distinct proton signals; that is, one signal for **I**, four signals for **II**, one signals for **III**, one signal for **IV**, and one signal for **V**. The observation of more formyl signals than theoretically predict can be explained as follows. To maximize π-conjugation, the *ortho*-formyl groups would prefer a co-planar conformation with respect to the phenyl rings of TPPy **5c**. Two relatively stable orientations exist for each of the formyl groups, which are depicted as the *exo* and *endo* conformers in Figure 3.4C. The different formyl orientations in the atropisomers thus further increase the number of formyl proton signals in the ^{1}H NMR spectrum.

The existence of distinct atropisomers was also observed for *ortho*-DTF-substituted TPPys **9a** and **9b** by NMR analysis. In the ^{1}H NMR spectrum of **9a** (Figure 3.5A), eight singlets are clearly seen in the region of 6.02–6.22 ppm, which are due to the vinyl protons of the four DTF groups. Each of the vinyl signals shows similar integration, except that the singlet at 6.05 ppm is slightly greater than

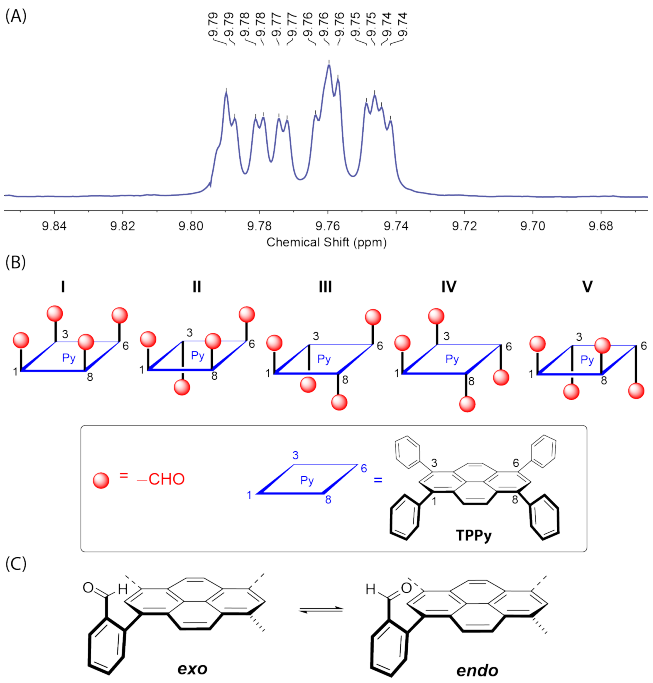

Figure 3.4: (A) Expanded ^{1}H NMR spectrum of **5c** showing the region of formyl proton signals. (B) Schematic illustration of four possible atropisomers of **5c** in terms of the relative orientations of the *ortho*-formyl groups. (C) Illustration of the *exo* and *endo* conformations for the *ortho*-formyl groups in **5c**.

the others. In the ^{13}C NMR spectrum of **9a** (Figure 3.5C), eight distinct signals around 114 ppm are also observed for the vinyl carbons of DTF groups, which is in good agreement with the ^{1}H NMR results. In theory, compound **9a** should have five possible atropisomers in the same way as proposed in Figure 3.4B. The observation of eight distinct vinyl proton/carbon signals in the NMR spectra of **9a** hence indicates the co-existence of all these atropisomers in the solution phase. Similar NMR patterns can be seen in the ^{1}H and ^{13}C NMR spectra of compound **9b** (Figures 3.5 B and D). Herein, the vinyl protons of **9b** also give eight distinct singlets in the region of 6.00–6.19 ppm; however, the integration values of these signals vary more significantly than

the case of **9a**. In the ^{13}C NMR spectrum, seven vinyl carbon signals are discernible in the region of 112–113 ppm and the spectral pattern shows a greater degree of signal broadening and overlap in comparison with **9a**. The NMR results indicate that the **9a** and **9b** show different distributions of atropisomers in the solution phase. Such differences can be attributed to the different alkyl groups (methyl versus decyl) present in their molecular structures.

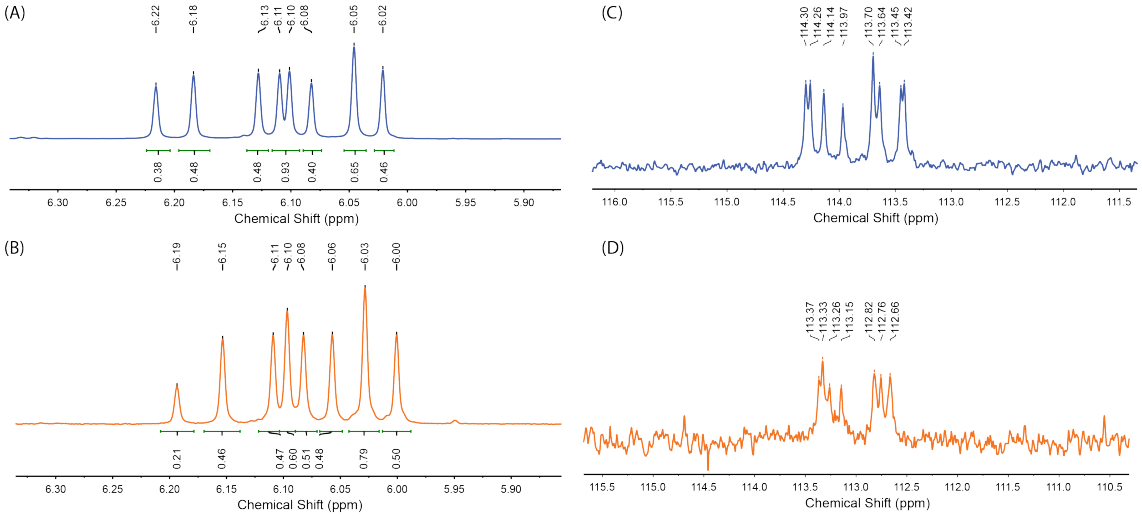

Figure 3.5: Expanded ^{1}H NMR spectra of (A) **9a** and (B) **9b** showing the region of vinyl proton signals. Expanded ^{13}C NMR spectra of (C) **9a** and (D) **9b** showing the region of vinyl carbon signals.

3.2.2 Electronic absorption properties

The electronic properties of the substituted TPPys were investigated by UV-Vis spectroscopic analysis. Figure 3.6A compares the UV-Vis spectra of *para*-substituted TPPys **5a** and **7a/b**. The *para*-formyl-substituted TPPy **5a** shows two prominent $\pi \rightarrow \pi^*$ transition bands at 396 nm and 302 nm, each of which takes a smooth

Gaussian shape. Such a spectral feature suggests flexible intramolecular motion (e.g., rotation) in the solution phase, which diminishes the vibronic features of the typically observed pyrene bands. The spectrum of *ortho*-DTF-substituted TPPy **7a** shows two similar $\pi \rightarrow \pi^*$ bands at 391 nm and 302 nm, which are barely shifted compared with those of **5a**. On the other hand, the low-energy absorption profile of **7a** shows a significant shoulder from *ca.* 430 to 500 nm along with an absorption band ranging from ca. 500 to 600 nm. These features are possibly originated from intermolecular aggregation in the solution phase. It is interesting to note that the UV-Vis spectrum of **7b** exhibits a very different profile in comparison with its analogue **7a**. In the low-energy region, a prominent shoulder band appears at 424 nm, which is significantly redshifted relative to those of **7a** and **5a**. The maximum absorption band is observed at 381 nm, which is blueshifted compared with the low-energy absorption bands of **7a** and **5a**. In addition, two more absorption bands can be seen at 340 nm and 302 nm, respectively. The strong absorption peak at 340 nm is in sharp contrast to the other two *para*-substituted TPPys, which show absorption minima at this wavelength.

Figure 3.6B compares the UV-Vis absorption profiles of *meta*-substituted-TPPys **5b** and **8a/b**. The UV-Vis spectrum of *meta*-formyl-substituted TPPy **5b** shows two $\pi \rightarrow \pi^*$ transition bands at 387 nm and 297 nm, which are slightly blueshifted relative to the two bands of **5a**. The spectrum of *meta*-DTF-substituted TPPy **8a** shows two absorption bands at 371 nm and 292 nm, which are blueshifted in comparison with those **5b**. Like the case of **7a**, the spectrum of **8a** also shows an absorption band in the range of 500 to 600 nm. The spectrum of **8b** shows two peaks at 375 nm and 301 nm, which are not significantly shifted compared with the spectrum of **8a**. However, the low-energy absorption band of **8b** has a much stronger relative intensity.

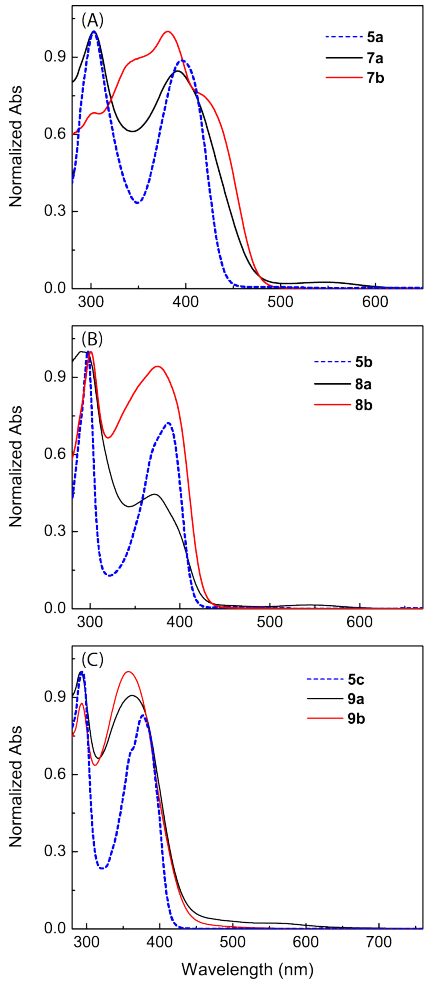

Figure 3.6: Normalized UV-Vis spectra of (A) *para*-substituted TPPys **5a** and **7a/b**, (B) *meta*-substituted TPPys **5b** and **8a/b**, and (C) *ortho*-substituted TPPys **5c** and **9a/b** measured in CH_2Cl_2.

Figure 3.6C compares the UV-Vis absorption spectra of *ortho*-substituted-TPPys **5c** and **9a/b**. The spectrum of *ortho*-formyl-substituted TPPy **5c** shows two $\pi \rightarrow \pi^*$ transition bands at 377 nm and 294 nm, which are more blueshifted than those of **5a** and **5b**. The spectra of two *ortho*-DTF-substituted TPPys **9a/b** show similar low-energy absorption bands at 362 nm and 357 nm, respectively, while their high-energy absorption bands appear to be nearly identical at 293 nm. Moreover, both the

spectra of **9a/b** show weak broad absorption tails extending from *ca.* 450 to 600 nm, which can be attributed to their intermolecular aggregation in the solution phase. Overall, the UV-Vis spectroscopic data indicate that the *para*-substituted TPPys are the most susceptible to the substitution effects with the largest extent of π-electron delocalization.

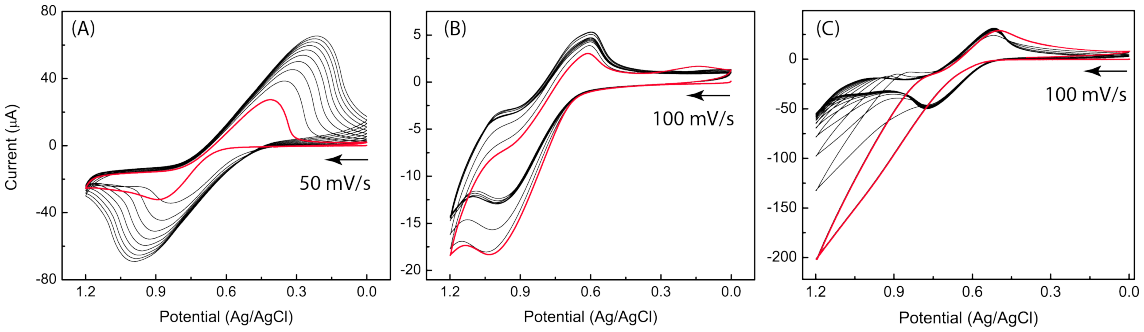

Figure 3.7: Cyclic voltammograms of (A) **7a** (scan rate = 50 mV/s), (B) **7b** (scan rate = 100 mV/s), and (C) **7b**/pyrene (1:1 molar ratio, scan rate = 100 mV/s) measured in CH_2Cl_2 with Bu_4NPF_6 as the electrolyte, glassy carbon as the working electrode, Pt wire as the counter electrode, and Ag/AgCl as the reference electrode. The profile of the first cycle of CV scans is highlighted in red color.

3.2.3 Electrochemical redox properties

The electrochemical redox properties of DTF-substituted TPPys **7**–**9** were investigated by cyclic voltammetric (CV) analysis. Figure 3.7A shows the cyclic voltammograms of *para*-DTF-substituted TPPy **7a** measured in a multi-cycle fashion. As can be seen, **7a** gives a quasi-reversible redox wave pair at E_{pa} = +0.89 V and E_{pc} = +0.41 V in the first cycle of CV scan. This redox pattern can be attributed

to the simultaneous oxidation and reduction of the four DTF groups in **7a** during the scans to the positive and negative directions, respectively. Starting from the second cycle of CV scans, the anodic and cathodic peaks are gradually shifted with a steady increase in both the E_{pa}-to-E_{pc} gap and their current intensities. After ten cycles of CV scans, the redox pair is shifted to $E_{pa} = +0.99$ V and $E_{pc} = +0.21$ V. There are not any new redox peaks emerge during the multi-cycle scans, and the current intensities of the anodic and cathodic peaks remain nearly identical in each cycle. These features indicate that **7a** is not prone to any electrochemical reactions, particularly the oxidative DTF coupling reaction commonly seen for many DTF-substituted arenes. The lack of redox-reactivity for **7a** can be explained by that the *para*-DTF substitution brings about good stabilizing effects on the DTF radical cation through π-conjugation, which in turn suppresses its reactivity. The gradually changed CV profiles with increasing scan cycles, on the other hand, are indicative of an electrodeposition process, where the CV scans facilitate the formation of insoluble aggregates of **7a** assembled via intermolecular π-stacking. Indeed, after about ten cycles of CV scans, a uniform blue-colored thin film could be clearly observed on the surface of the working electrode.

The cyclic voltammograms of *para*-DTF-subsituted TPPy **7b** (Figure 3.7B) also show a pair of quasi-reversible redox waves at $E_{pa} = +1.03$ V and $E_{pc} = +0.16$ V in the first cycle of CV scans. After multi-cycle scans, the voltammograms show similar profiles, and the redox potentials of the cathodic and anodic peaks are merely shifted in a slight degree. Unlike its methyl-substituted analogue, the CV scans of **7b** did not result in any deposition on the working electrode surface. The different electrochemical behavior from **7a** can be attributed to the long decyl chains present

in the molecular structure of **7b**, which enhance its solubility and effectively prevents the molecules from aggregating on the electrode surface.

In the literature, the TPPy scaffold has been known to favorably interact with various small arenes (e.g., pyrene), forming intriguing guest-host systems through co-crystallization.[202–204] Such properties thus motivated us to examine the complexation of **7b** and pyrene under electrochemical conditions. Figure 3.7C shows the cyclic voltammograms of a 1:1 (molar ratio) mixture of **7b** and pyrene measured in a multi-cycle mode. Interestingly, in the first cycle of CV scan, the voltammogram shows no apparent anodic peak, but a cathodic peak at $E_{pc} = +0.52$ V shows up in the reverse scan. Starting from the second scan cycle, a quasi-reversible redox wave pair can be clearly seen at $E_{pa} = +0.78$ V and $E_{pc} = +0.52$ V. The potentials of this redox couple remain unchanged with increasing CV scan cycles. The E_{pc}-to-E_{pa} gap (0.26 V) of the **7b**/pyrene mixture is much narrower than that of **7b** (*ca.* 0.40 V), indicating better electrochemical reversibility. After ten cycles of scans, a thin film was observed to be deposited on the working electrode surface. The experimental results suggest that **7b** and pyrene are capable of forming redox-active supramolecular assemblies under electrochemical conditions. The complexation is presumably through the π–π interactions of pyrene with the pyrenyl core of **7b**. Moreover, the π-stacking could lead to significant conformational changes in **7b**, further modifying the redox potentials of its DTF units.

The cyclic voltammograms of *meta*-DTF-substituted TPPys **8a/b** are compared in Figure 3.8. For the methyl-substituted **8a**, the first scan cycle reveals an anodic peak at $E_{pa} = +0.82$ V and a cathodic peak at $E_{pc} = +0.55$ V. The anodic peak can be assigned to the oxidation of DTF into its radical cation form, while the cathodic

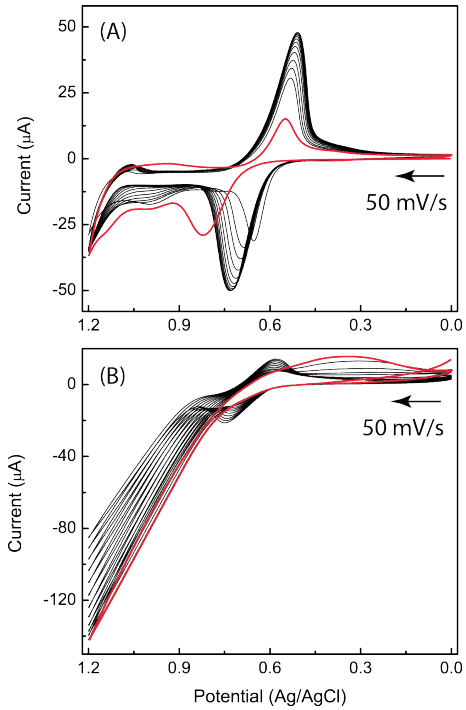

Figure 3.8: Cyclic voltammograms of (A) **8a** (scan rate = 50 mV/s) and (B) **8b** (scan rate = 50 mV/s) measured in CH_2Cl_2 with Bu_4NPF_6 as the electrolyte, glassy carbon as the working electrode, Pt wire as the counter electrode, and Ag/AgCl as the reference electrode. The profile of the first cycle of CV scans is highlighted in red color.

peak is the reduction of the TTFV dication species, resulting from a facile DTF dimerization on the working electrode. Such an assignment can be evidenced by the observation of a typical TTFV redox couple in the following scan cycles. In the second scan cycle, a new anodic peak emerges at +0.65 V, while the cathodic peak is slightly shifted to +0.53 V, but its current intensity is significantly increased. Continued CV scans result in a steady growth of this redox couple, with increasing intensity and slightly shifted potentials. A robust thin film was formed on the working electrode surface after multi-cycle CV scans. Overall, the CV results of **8a** confirm its ability to

can undergo DTF oxidative polymerization under electrochemical conditions, yielding a redox-active TTFV polymer as the product.

The CV results of decyl-substituted DTF-TPPy **8b** show relatively weak redox activity in comparison with its methyl-substituted analogue **8a**. As shown in Figure 3.8B, the first cycle of CV scans does not yield any discernible redox peaks. This can be attributed to the effects of the long decyl chains, which somewhat hinder the redox responses in the initial scan. However, in the following scan cycles, a redox wave pair (E_{pa} = +0.74 V, E_{pc} = +0.59 V) starts to grow steadily, indicating DTF oxidative polymerization on the working electrode. Like the case of **8a**, the multi-cycle CV scans of **8b** also led to the formation of a polymer film on the working electrode surface. Nonetheless, the increase of the TTFV redox couple in the voltammograms of **8b** shows a much smaller magnitude than **8a**, suggesting that the decyl groups exert an inhibitive effect on the oxditive DTF coupling reaction.

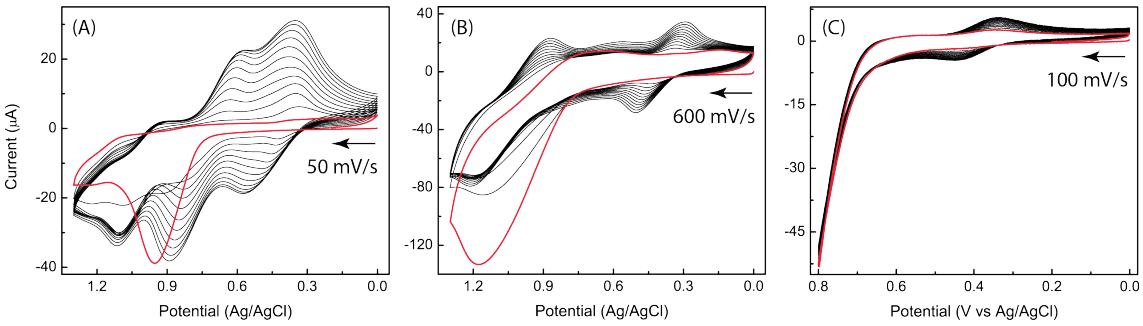

Figure 3.9: Cyclic voltammograms of (A) **9a** (scan rate = 50 mV/s), (B) **9a** (scan rate = 600 mV/s), and (C) **9b** (scan rate = 100 mV/s) measured in CH_2Cl_2 with Bu_4NPF_6 as the electrolyte, glassy carbon as the working electrode, Pt wire as the counter electrode, and Ag/AgCl as the reference electrode. The profile of the first cycle of CV scans is highlighted in red color.

The cyclic voltammograms of *ortho*-DTF-substituted TPPys **9a/b** are shown in Figure 3.9. It is interesting to note that the CV behavior of **9a** shows significant dependence on the scan rate. At a relatively slow scan rate (Figure 3.9A), the first scan cycle shows only an anodic peak at +0.95 V in the forward direction, while there is no apparent peak emerging in the reverse scan. In the following scan cycles, three redox wave pairs can be seen in the CV profiles. In the low-potential region, there are two redox couples, which show steady growth in intensity and significant shift in redox potential with increasing scans. After ten cycles of scans, they are shifted to $E_{pa1} = +0.57$ V/$E_{pc1} = +0.35$ V and $E_{pa2} = +0.89$ V/$E_{pc2} = +0.59$ V, respectively. The third redox wave pair appears at $E_{pa3} = +1.11$ V/$E_{pc3} = +0.94$ V after ten cycles of scans. Unlike the first two redox couples, the third one does not show significant changes after the third cycle of scans. The assignments of these three redox wave pairs can be made as follows. The first two pairs are due to the TTFV products resulting from DTF coupling occurring on the working electrode surface during the CV scans. Their growing intensities are indicative of the formation of TTFV polymers. In the literature, the TTFV unit that is *ortho*-substituted on an aryl group has been known to favor a *trans* conformation due to steric hindrance and its CV profile usually shows two steps of single electron transfers instead of a simultaneous bielectronic transfer.[160,207] The third redox couple at relatively high potentials is due to the redox features of DTF groups. It is reasonable to envision that the oxidative coupling of *ortho*-substituted DTF groups would result in highly twisted, cross-linked TTFV polymers, which impose considerable steric hindrance to inhibit the redox reactivity of certain DTF groups embedded in the polymer networks. Therefore, unlike the electropolymerization of the less hindered DTF-TPPys such as

8a, the electropolymerization of **9a** only involves partial DTF groups in its structure.

When compound **9a** was subjected to CV scans at a relatively high rate (e.g., 600 mV/s), the patterns of voltammograms are considerably changed (Figure 3.9B). In the first cycle of CV scans, an anodic is found at +1.18 V, which is greatly shifted to the positive direction compared with that measured at the low scan rate. There are no cathodic peaks observable in the reverse scan of the first cycle; however, after the second cycle of scans, a quasi-reversible redox wave pair can ben seen to grow steadily, which is indicative of the formation of TTFV polymers as a result of DTF oxidative coupling on the working electrode. After ten cycles of CV scans, the redox potentials are shifted to +0.50 V/+0.29 V. This redox pattern can be ascribed to the simultaneous two-electron transfers of the TTFV products resulting from the electropolymerization of **9a**. In the high-potential region, a quasi-reversible redox wave pair ($E_{pa} = +1.20$ V/$E_{pc} = +0.88$ V) is gradually developed, which is consistent with the presence of unreacted DTF units in the electropolymerized products. The multi-cycle CV scans at different scan rates led to the formation of TTFV polymer thin films on the working electrode surface with different appearances. At the low scan rate, the obtained polymer thin film shows a golden color, while the polymer film resulting from a high scan rate gives a blue color.

The cyclic voltammograms of **9b** show no significant redox peaks in the first cycle of scans. In the following scans, a redox couple characteristic of TTFV is gradually developed at $E_{pa} = +0.44$ V and $E_{pc} = +0.34$ V. Interestingly, the growth of the TTFV redox peaks is relatively weak and there is still no observation of other redox peaks corresponding to the DTF group after multi-cycles of scans. The CV results of **9b** are similar to those of its *meta* isomer **8b**, suggesting a limited degree of

electropolymerization due to the steric hindrance imposed by the long decyl chains. Nevertheless, a stable thin film could still be observed on the working electrode surface after the CV scans of **9b**.

3.2.3.1 Protonation and deuterium exchange

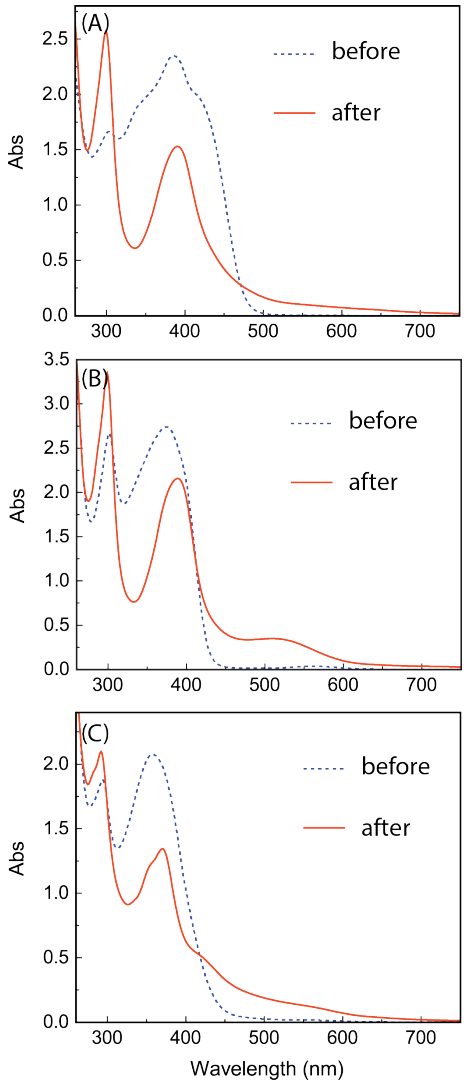

Figure 3.10: UV-Vis spectra of tetra(DTF)-substituted TPPys (A) **7b**, (B) **8b**, and (C) **9b** before and after addition of excess TFA (*ca.* 5.4 × molar equivalents).

In addition to oxidation, the DTF group has also been known to be susceptible to protonation, yielding an electron-withdrawing dithiolium cation as the product. Figure 3.10 compares the UV-Vis absorption spectra of tetra(DTF)-substituted TPPys (**7b**, **8b**, and **9b**) before and after treatment with excess trifluoroacetic acid (TFA) in CH_2Cl_2. For *para*-DTF-substituted TPPy **7b**, the low-energy $\pi \rightarrow \pi^*$ absorption bands in the range of 310 to 430 nm are considerably attenuated, while a high-energy band at 298 nm is enhanced after protonation. Similar trends of spectral changes can be seen in the UV-Vis spectra of *meta*-DTF-substituted and *ortho*-DTF-substituted TPPys (**8b** and **9b**). Of particular note is that each of the tetra(DTF)-substituted TPPys exhibits a new long-wavelength absorption tail in the UV-Vis spectrum after protonation. The results indicate that protonation of the DTF groups in these compounds leads to an increased degree of π-electron delocalization on the TPPy system.

The protonated DTF groups in the tetra(DTF)-substituted TPPys were found to undergo efficient deuterium/proton exchange reactions with D_2O. In our experiments, compounds **7b**, **8b**, and **9b** dissolved in $CDCl_3$ were respectively treated with TFA (*ca.* 13 molar equivalents) for 30 seconds and then quenched with D_2O. ^{1}H NMR analysis has confirmed that such a treatment could result in the vinylic protons in each of the compound being displaced with deuterium to a considerable extent (see Figure 3.11A–C). Based on the relative integration ratio between the vinyl protons and the pyrenyl protons, the deuterium exchange efficiencies can be determined as: 45% (**7b**), 83% (**8b**), and 94% (**9b**). Figure 3.11D illustrates the general mechanism for the deuterium/proton exchange reactions on the DTF group. The experimental results show that *ortho* and *meta*-DTF groups are more prone to deuterium/proton

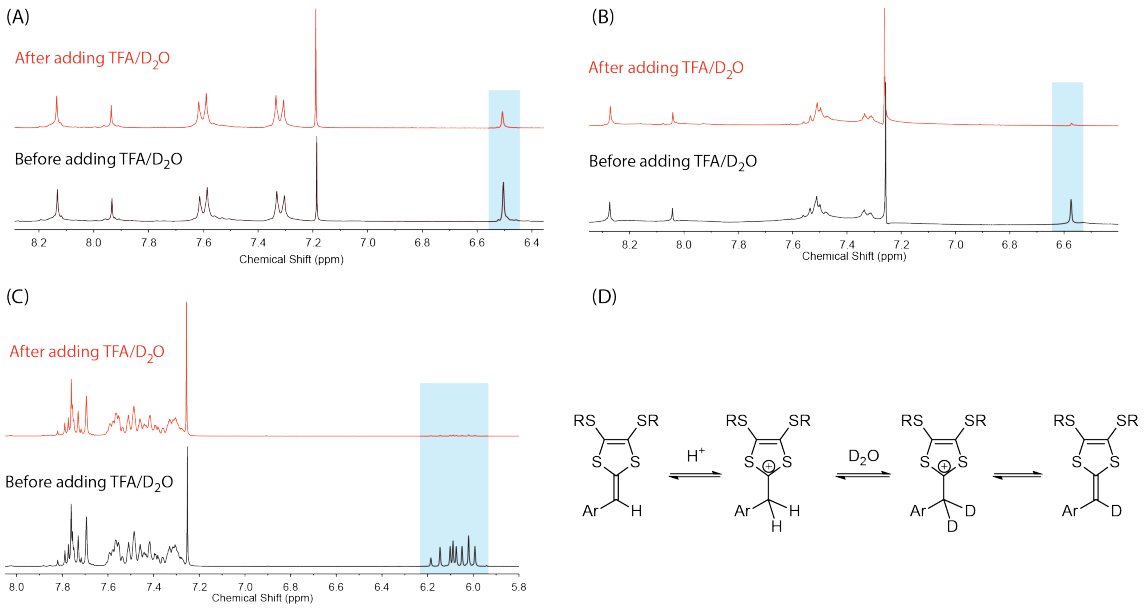

Figure 3.11: Expanded ^{1}H NMR spectra (300 MHz, $CDCl_3$) of (A) **7b**, (B) **8b**, and (C) **9b** before and after addition of excess TFA and D_2O. (D) Mechanism for the proton/deuterium exchange reaction on DTF.

exchange than *para*-DTF. This trend can be rationalized by that the *para*-DTF shows the largest degree of π-conjugation with the TPPy system (i.e., highest stability), and it is therefore the least reactive toward the deuterium/proton exchange process.

3.3 Conclusions

In this work, we have prepared six tetra(DTF)-substituted TPPy derivatives using Suzuki-Miyaura cross-coupling and phosphite-promoted olefination reactions as the key synthetic steps. Their molecular structures and conformational properties were investigated by X-ray single crystallographic and NMR analyses. Our results show that the *ortho*-substituted TPPy structures bear sufficient steric hindrance that allows the observation of distinct atropisomers in the solution

phase. Although separation of these atropisomers could not be possibly achieved by in our current study, the acquisition of individual atropisomers remains an intriguing objective of research, since the diverse spatial orientations of the *ortho*-substituents attached to the TPPy structure may further allow for the assembly of complex 3-D macromoleular/supramolecular networks with unprecedented properties and functions. Our UV-Vis and electrochemical analyses showed that the *para*-substitution pattern gave a higher degree of π-electron delocalization than *meta* and *ortho* substitutions. The substitution patterns and the alkyl side groups were found to have important effects on the electrochemical properties of the tetra(DTF)-substituted TPPys. Unlike typical DTF-attached arenes, *para*-DTF-substituted TTPys tend to form oxidized species that are stable and inert to DTF oxidative coupling reactions. Among the six DTF-TPPy derivatives, *ortho*-DTF-substituted **8a** exhibited the best electropolymerization behavior to form stable TTFV polymer products. The electropolymerization of *ortho*-DTF-substituted TPPy **9a** showed strong dependence on the scan rate, suggesting a possible way to exert control over the redox properties of the resulting polymer thin films. Finally, the tetra(DTF)-TPPys were found to undergo efficient deuterium/proton exchange reactions, while the exchange efficiencies show an decreasing order of *ortho*-DTF >*meta*-DTF >*para*-DTF. Such properties can be potentially used in deuterium trapping and labeling application. In summary, our studies here have established fundamental understanding of a new class of DTF-pyrene hybrids and we anticipate the diverse redox-activities of these compounds will allow them to be applied as useful molecular building blocks in advanced organic electronic and optoelectronic materials.

3.4 Experimental section

Chemicals and reagents were purchased from commercial suppliers and used directly without purification. All reactions were conducted in standard, dry glassware. Evaporation and concentration were carried out with a rotary evaporator. Flash column chromatography was performed with 240-400 mesh silica gel, and thin-layer chromatography (TLC) was carried out with silica gel F254 covered on plastic sheets and visualized by UV light. Melting points (m.p.) were measured using an SRS OptiMelt melting point apparatus and are uncorrected. ^{1}H and ^{13}C NMR spectra were measured on a Bruker Avance III 300 MHz multinuclear spectrometer. Chemical shifts (δ) are reported in ppm downfield relative to the signals of the internal reference $SiMe_4$ or residual solvents ($CHCl_3$: δ_H = 7.24 ppm, δ_C = 77.2 ppm; CH_2Cl_2: δ_H = 5.32 ppm, δ_C = 54.0 ppm). Coupling constants (J) are given in Hz. Infrared spectra (IR) were recorded on a Bruker Alfa spectrometer. High-resolution APPI-TOF MS analysis was done on a GCT premier Micromass Technologies instrument. UV-Vis absorption spectra were measured on a Cary 6000i spectrophotometer. Cyclic voltammetric (CV) analysis was carried out in a standard three-electrode setup, where a glassy carbon electrode was used as the working electrode, a Pt wire as the counter electrode, and Ag/AgCl as the reference. The experiments were controlled by a BASi Epsilon potentiostat.

Single-crystal X-ray diffraction (XRD) data was collected at 100(2) K on a XtaLAB Synergy-S, Dualflex, HyPix-6000HE diffractometer using Cu $K\alpha$ radiation (λ = 1.5406 Å). Crystal was mounted on nylon CryoLoops with Paraton-N. The data collection and reduction were processed within *CrysAlisPro* (Rigaku OD, 2019).

A multi-scan absorption correction was applied to the collected reflections. Using *Olex2*,[208] structures were solved with the *ShelXT* structure solution program using intrinsic phasing and refined with the *ShelXL* refinement package using Least Squares minimisation.[209] All non-hydrogen atoms were refined anisotropically, and the organic hydrogen atoms were generated geometrically.

Synthesis

4,4',4",4"'-(Pyrene-1,3,6,8-tetrayl)tetrabenzaldehyde (5a)

1,3,6,8-Tetrabromopyrene **3** (0.517 g, 1.00 mmol), 4-formylphenylboronic acid **4a** (0.894 g, 6.00 mmol), cesium carbonate (3.25 g, 10.0 mmol), THF (25 mL), and deionized water (10 mL) were added to a 100 mL round-bottomed flask. The mixture was bubbled with N_2 flow for 5 min and then $Pd(PPh_3)_4$ (0.346 g, 0.300 mmol) was added. The reaction mixture was stirred under N_2 protection and heated at reflux for 24 h. The solvent THF was then removed under slight heating and reduced pressure. The residue was subjected to suction filtration, resulting in a yellow solid that was sequentially washed with acetone (10 mL) and CH_2Cl_2 (5 mL) to give pure compound **5a** (0.501 g, 0.810 mmol, 81%) as a yellow solid. m.p. 336–338 °C; IR (neat): 3060, 2807, 2717, 1689, 1596, 1563, 1414, 1382, 1303, 1212, 1165, 1108, 1004, 983, 827, 814, 755, 733, 689, 608, 56 cm^{-1}; ^1H NMR (300 MHz, $CDCl_3$): δ 10.16 (s, 4H), 8.19–8.03 (m, 14H), 7.86 (d, J = 8.1 Hz, 8H) ppm. The NMR data are consistent with those reported in the literature.[210]

3,3',3",3"'-(Pyrene-1,3,6,8-tetrayl)tetrabenzaldehyde (5b)

1,3,6,8-Tetrabromopyrene **3** (0.517 g, 1.00 mmol), 3-formylphenylboronic acid **4b** (0.894 g, 6.00 mmol), cesium carbonate (3.25 g, 10.0 mmol), THF (25 mL), and deionized water (10 mL) were added to a 100 mL round-bottomed flask. The mixture was bubbled with N_2 flow for 5 min, and then $Pd(PPh_3)_4$ (0.346 g, 0.3 mmol) was added. The reaction mixture was stirred under N_2 protection and heated at reflux for 24 h. The solvent THF was then removed under slight heating and reduced pressure. The residue was subjected to suction filtration, resulting in a chartreuse color solid that was squentially washed with acetone (10 mL) and CH_2Cl_2 (5 mL) to give pure compound **5b** (0.512 g, 0.830 mmol, 83%) as a chartreuse color solid. m.p. 265–266 °C; IR (neat): 3054, 2803, 2713, 1691, 1594, 1578, 1475, 1434, 1363, 1281, 1205, 1160, 1148, 884, 828, 725, 696, 649 cm^{-1}; ^1H NMR (300 MHz, $CDCl_3$): δ 10.16 (s, 4H), 8.22–8.13 (m, 8H), 8.06–7.94 (m, 10H), 7.79–7.71 (m, 4H) ppm; ^{13}C NMR (75 MHz, $CDCl_3$): δ 192.28, 141.78, 136.90, 136.69, 136.43, 131.68, 129.69, 129.43, 129.19, 128.62, 126.00, 125.69 ppm; HRMS (APPI-TOF, positive mode) *m/z* calcd for $C_{28}H_{18}O_2$ 618.1831, found 618.1845 $[M + H]^+$.

2,2',2",2"'-(Pyrene-1,3,6,8-tetrayl)tetrabenzaldehyde (5c)

1,3,6,8-Tetrabromopyrene **3** (0.258 g, 0.500 mmol), 2-formylphenylboronic acid **4c** (0.447 g, 3.00 mmol), cesium carbonate (1.625 g, 5.00 mmol), THF (15 mL), and deionized water (5 mL) were added to a 50 mL round-bottomed flask. The mixture was bubbled with N_2 flow for 5 min, and then $Pd(PPh_3)_4$ (0.173 g, 0.150 mmol) was added. The reaction mixture was stirred under N_2 protection and heated at reflux

for 24 h. The reaction mixture was cooled down to room temperature and then poured into a separatory funnel including water and extracted twice with CH_2Cl_2. The organic layers were combined and dried over $MgSO_4$. After filtration and concentration under slight heating and reduced pressure, the resulting residue was dissolved in a small amount of CH_2Cl_2 and then hexane was added to induce the formation of a yellow precipitate. The mixture was cooled in a fridge for 1 h and then the precipitate was separated by vacuum filtration to give pure compound **5c** (0.226 g, 0.365 mmol, 73%) as a yellow crystalline solid. m.p. 300–302 °C; IR (neat): 3055, 2835, 2744, 1688, 1592, 1569, 1473, 1390, 1261, 1194, 1094, 1005, 980, 876, 817, 759, 736, 639, 540 cm^{-1}; ^1H NMR (300 MHz, $CDCl_3$): δ 9.80–9.73 (m, 4H), 8.18–8.12 (m, 4H), 8.02–7.97 (m, 2H), 7.88–7.80 (m, 4H), 7.78–7.70 (m, 4H), 7.68–7.57 (m, 8H) ppm; ^{13}C NMR (75 MHz, $CDCl_3$): δ 191.76, 191.70, 191.58, 191.56, 191.49, 191.41, 191.31, 143.57, 143.52, 143.48, 143.44, 143.36, 143.33, 135.21, 135.18, 135.14, 135.12, 135.08, 135.05, 134.99, 134.13, 134.10, 134.05, 133.99, 133.94, 133.87, 133.78, 133.69, 133.65, 133.58, 133.52, 133.52, 133.47, 132.51, 132.48, 132.45, 132.42, 132.37, 132.34, 132.29, 132.24, 131.18, 131.17, 131.04, 130.94, 130.78, 130.22, 130.19, 130.11, 128.88, 128.42, 128.27, 128.21, 128.06, 128.02, 127.92, 127.90, 126.36, 126.32, 126.30, 126.26, 126.22, 124.90, 77.16 ppm; HRMS (APPI-TOF, positive mode) *m/z* calcd for $C_{28}H_{18}O_2$ 618.1831, found 618.1849 $[M + H]^+$. X-ray.

1,3,6,8-Tetrakis(4-((4,5-bis(methylthio)-1,3-dithiol-2-ylidene)methyl)phenyl)pyrene (7a)

Compound **5a** (0.618 g, 1.00 mmol), 4,5-bis(methylthio)-1,3-dithiole-2-thione **6a** (1.356 g, 6.00 mmol), $P(OEt)_3$ (10 mL) were added to a 50 mL round-bottomed

flask. The reaction mixture was then heated to 150 °C with an oil bath and kept at this temperature for 3 h. Distillation under vacuum was conducted at the same temperature to remove unreacted $P(OEt)_3$. The residue was subjected to silica gel column chromatography (hexanes/CH_2Cl_2, 3:2) to give pure compound **7a** (1.284 g, 0.590 mmol, 59%) as a red-orange powder. (The product should be be stored in the dark at low temperature under the protection of inert gas to avoid decomposition.) m.p. ¿ 212°C (dec.); IR (neat): 2954, 2921, 2852, 1698, 1670, 1601, 1569, 1494, 1461, 1427, 968, 824 cm^{-1}; ^1H NMR (300 MHz, $CDCl_3$): δ 8.20 (s, 4H), 8.01 (s, 2H), 7.67 (d, J = 8.3 Hz, 8H), 7.39 (d, J = 8.2 Hz, 8H), 6.60 (s, 4H), 2.47 (s, 12H), 2.45 (s, 12H) ppm; ^{13}C NMR (75 MHz, $CDCl_3$): δ 138.49, 136.88, 135.36, 132.53, 130.86, 130.81, 128.14, 127.31, 126.79, 125.35, 124.44, 114.43, 29.70, 19.06, 18.93 ppm; HRMS (APPI-TOF, positive mode) m/z calcd for $C_{64}H_{50}S_{16}$ 1329.9444, found 1329.9463 [M + H]$^+$.

1,3,6,8-Tetrakis(4-((4,5-bis(decylthio)-1,3-dithiol-2-ylidene)methyl)phenyl)pyrene (7b)

Compound **5a** (0.618 g, 0.500 mmol), 4,5-bis(decylthio)-1,3-dithiole-2-thione **6b** (1.434 g, 3.00 mmol), $P(OEt)_3$ (2 mL) were added to a 50 mL round-bottomed flask. The reaction mixture was then heated to 150 °C with an oil bath and kept at this temperature for 2 h. Distillation under vacuum was conducted at the same temperature to remove unreacted $P(OEt)_3$. The residue was subjected to silica gel column chromatography (hexanes/CH_2Cl_2, 4:1) to give pure compound **7b** (0.761 g, 0.325 mmol, 65%) as a red-orange semi-solid. (The product should be be stored in the dark at low temperature under the protection of inert gas to avoid decomposition.)

IR (neat): 2955, 2921, 2852, 1672, 1602, 1509, 1463, 1259, 1089, 1019, 880, 799, 721, 3021, 2990, 2918, 2852, 1567, 1540, 1502, 1443, 1314, 1184 cm^{-1}; ^1H NMR (300 MHz, $CDCl_3$): δ 8.21 (s, 4H), 8.01 (s, 2H), 7.67 (d, J = 8.3 Hz, 8H), 7.39 (d, J = 8.4 Hz, 8H), 6.58 (s, 4H), 2.86 (t, J = 7.3 Hz, 16H), 1.72–1.62 (m, 16H), 1.35–1.22 (m, 112H), 0.91–0.84 (m, 24H) ppm; ^{13}C NMR (75 MHz, $CDCl_3$): δ 138.07, 136.60, 135.14, 132.61, 130.56, 127.84, 127.37, 126.47, 125.88, 125.05, 124.56, 113.57, 35.91, 35.80, 31.63, 31.60, 29.59, 29.43, 29.29, 29.27, 29.05, 29.02, 28.88, 28.32, 28.27, 22.41, 22.39, 13.84 ppm; HRMS (APPI-TOF, positive mode) m/z calcd for $C_{136}H_{194}S_{16}$ 2339.0712, found 2339.0740 $[M + H]^+$.

1,3,6,8-Tetrakis(3-((4,5-bis(methylthio)-1,3-dithiol-2-ylidene)methyl)phenyl)pyrene (8a)

Compound **5b** (0.062 g, 0.10 mmol), 4,5-bis(methylthio)-1,3-dithiole-2-thione **6a** (0.135 g, 0.600 mmol), and $P(OEt)_3$ (4 mL) were added to a 50 mL round-bottomed flask. The reaction mixture was then heated to 150 °C with an oil bath and kept at this temperature for 2 h. Distillation under vacuum was conducted at the same temperature to remove unreacted $P(OEt)_3$. The residue was subjected to silica gel column chromatography (hexanes/CH_2Cl_2, 3:2) to give pure compound **8a** (0.055 g, 0.041 mmol, 41%) as a yellow solid. (The product should be be stored in the dark at low temperature under the protection of inert gas to avoid decomposition.) m.p. ¿ 197 °C (dec.) IR (neat): 2957, 2919, 2850, 1697, 1593, 1574, 1559, 1498, 1461, 1419, 1310, 1261, 968, 894, 808, 705 cm^{-1}; ^1H NMR (300 MHz, $CDCl_3$): δ 8.27 (s, 4H), 8.04 (s, 2H), 7.55 – 7.46 (m, 12H), 7.34 – 7.28 (m, 4H), 6.59 (s, 4H), 2.43 (s, 12H), 2.34 (s, 12H) ppm; ^{13}C NMR (75 MHz, $CDCl_3$): δ 141.29, 137.07, 136.45, 132.95, 129.56,

129.07, 128.67, 128.24, 126.80, 125.98, 125.72, 125.46, 124.58, 114.63, 29.71, 18.96, 18.93 ppm; HRMS (APPI-TOF, positive mode) *m/z* calcd for $C_{64}H_{50}S_{16}$ 1329.9444, found 1329.9470 $[M + H]^+$.

1,3,6,8-Tetrakis(3-((4,5-bis(decylthio)-1,3-dithiol-2-ylidene)methyl)phenyl)pyrene (8b)

Compound **5b** (0.124 g, 0.200 mmol), 4,5-bis(decylthio)-1,3-dithiole-2-thione **6b** (0.574 g, 1.20 mmol), and $P(OEt)_3$ (8 mL) were added to a 50 mL round-bottomed flask. The reaction mixture was then heated to 150 °C with an oil bath and kept at this temperature for 3 h. Distillation under vacuum was conducted at the same temperature to remove unreacted $P(OEt)_3$. The residue was subjected to silica gel column chromatography (hexanes/CH_2Cl_2, 9:1) to give pure compound **8b** (0.239 g, 0.102 mmol, 51%) as red orange oil. (The product should be be stored in the dark at low temperature under the protection of inert gas to avoid decomposition.) IR (neat): 2952, 2919, 2850, 1674, 1593, 1561, 1460, 1416, 1302, 1272, 889, 835, 812, 720, 702, cm^{-1}; ^1H NMR (300 MHz, $CDCl_3$): δ 8.28 (s, 4H), 8.04 (s, 2H), 7.56 – 7.46 (m, 12H), 7.36 – 7.30 (m, 4H), 6.57 (s, 4H), 2.83 (t, J = 7.2 Hz, 8H), 2.75 (t, J = 7.2 Hz, 8H), 1.71–1.52 (m, 16H), 1.37–1.21 (m, 112H), 0.94–0.81 (m, 24H) ppm; ^{13}C NMR (75 MHz, Chloroform-*d*): δ 141.32, 137.09, 136.56, 133.30, 129.60, 129.19, 128.63, 128.23, 128.15, 127.39, 126.01, 125.52, 125.45, 124.86, 114.07, 36.11, 36.08, 31.91, 29.86, 29.69, 29.58, 29.55, 29.34, 29.17, 28.61, 28.49, 22.70, 14.13 ppm; HRMS (APPI-TOF, positive mode) *m/z* calcd for $C_{136}H_{194}S_{16}$ 2339.0712, found 2339.0732 $[M + H]^+$.

1,3,6,8-Tetrakis(2-((4,5-bis(methylthio)-1,3-dithiol-2-ylidene)methyl)phenyl)pyrene (9a)

Compound **5c** (0.062 g, 0.100 mmol), 4,5-bis(methylthio)-1,3-dithiole-2-thione **6a** (0.135 g, 0.600 mmol), $P(OMe)_3$ (3 mL), and $P(OEt)_3$ (1 mL) were added to a 50 mL round-bottomed flask. The reaction mixture was then heated to 150 °C with an oil bath and kept at this temperature for 2 h. Distillation under vacuum was conducted at the same temperature to remove unreacted $P(OEt)_3$. The residue was subjected to silica gel column chromatography (hexanes/CH_2Cl_2, 3:2) to give pure compound **9a** (0.066 g, 0.050 mmol, 50%) as a yellow solid. (The product should be be stored in the dark at low temperature under the protection of inert gas to avoid decomposition.) m.p. ¿ 205 °C (dec.); IR (neat): 2915, 2850, 1565, 1550,1469, 1460, 1440, 1417, 1309, 1005, 966, 891, 791, 761, 728, 653, 595, 563 cm^{-1}; ^1H NMR (300 MHz, $CDCl_3$): δ 7.82–7.69 (m, 6H), 7.60–7.29 (m, 16H), 6.22–6.00 (m, 4H), 2.40–2.35 (m, 12H), 2.33–2.28 (m, 12H) ppm; ^{13}C NMR (75 MHz, Chloroform-*d*): δ 138.91, 138.86, 138.81, 138.78, 138.76, 135.99, 135.96, 135.94, 135.90, 135.88, 135.79, 133.41, 133.38, 133.33, 133.22, 133.20, 133.18, 133.13, 132.01, 131.90, 131.81, 131.73, 131.63, 131.51, 131.08, 130.96, 130.77, 130.61, 130.41, 130.29, 129.26, 129.23, 129.17, 129.07, 129.03, 128.98, 128.04, 127.62, 127.59, 127.56, 127.46, 127.41, 127.32, 127.28, 126.34, 126.29, 126.13, 126.06, 126.01, 125.97, 125.89, 125.83, 125.78, 125.50, 125.38, 125.31, 125.27, 125.19, 124.22, 124.05, 123.99, 123.89, 123.77, 114.30, 114.26, 114.14, 113.97, 113.70, 113.64, 113.45, 113.42, 53.55, 36.21, 34.81, 34.65, 31.72, 29.83, 29.19, 27.05, 25.42, 22.82, 22.78, 22.75, 20.84, 19.11, 19.09, 19.01, 18.98, 18.94, 18.93, 18.86, 14.25, 11.56, 0.13 ppm; HRMS (APPI-TOF, positive mode) *m/z* calcd for $C_{64}H_{50}S_{16}$ 1329.9444, found

1329.9438 $[M + H]^+$.

1,3,6,8-Tetrakis(2-((4,5-bis(decylthio)-1,3-dithiol-2-ylidene)methyl)phenyl)pyrene (9b)

Compound **5c** (0.124 g, 0.200 mmol), 4,5-bis(decylthio)-1,3-dithiole-2-thione **6b** (0.574 g, 1.20 mmol), and $P(OEt)_3$ (8 mL) were added to a 50 mL round-bottomed flask. The reaction mixture was then heated to 150 °C with an oil bath and kept at this temperature for 2 h. Distillation under vacuum was conducted at the same temperature to remove unreacted $P(OEt)_3$. The residue was subjected to silica gel column chromatography (hexanes/CH_2Cl_2, 9:1) to give pure compound **9b** (0.239 g, 0.102 mmol, 51%) as a red-orange oil. (The product should be be stored in the dark at low temperature under the protection of inert gas to avoid decomposition.) IR (neat): 2960, 2922, 2851, 1568, 1552, 1463, 1382, 1270, 1047, 1033, 886, 802, 733, 701, 520 cm^{-1}; ^1H NMR (300 MHz, $CDCl_3$): δ 7.84–7.68 (m, 6H), 7.62–7.27 (m, 16H), 6.21–5.99 (m, 4H), 2.86–2.64 (m, 16H), 1.69–1.55 (m, 16H), 1.34–1.18 (m, 112H), 0.93–0.81 (m, 24H) ppm; ^{13}C NMR (75 MHz, $CDCl_3$): δ 138.76, 138.72, 138.66, 138.60, 138.58, 135.91, 135.88, 135.85, 135.83, 135.81, 133.75, 133.63, 133.47, 133.42, 133.35, 133.31, 131.81, 131.67, 131.60, 131.58, 131.54, 131.40, 129.15, 129.04, 128.95, 128.93, 128.87, 128.81, 127.85, 127.81, 127.69, 127.62, 127.57, 127.42, 127.39, 125.98, 125.93, 125.82, 125.76, 125.69, 125.66, 125.31, 125.19, 125.18, 125.11, 124.59, 124.39, 124.31, 124.28, 124.17, 123.98, 123.94, 113.37, 113.33, 113.26, 113.15, 112.82, 112.76, 112.66, 36.13, 36.02, 35.93, 35.89, 35.41, 31.92, 31.87, 29.71, 29.64, 29.57, 29.50, 29.34, 29.28, 29.24, 29.21, 29.16, 29.10, 29.06, 28.57, 28.53, 22.69, 14.13 ppm; HRMS (APPI-TOF, positive mode) *m/z* calcd for $C_{136}H_{194}S_{16}$ 2339.0712, found 2339.0778 $[M + H]^+$.

Chapter 4

Synthesis and Comparative Studies of K-Region Functionalized Pyrene Derivatives

The contents of this chapter have been accepted by *New J. Chem* as a full research article. Contributions of authors are described below:

Farshid Shahrokhi is the first author, who conducted most of the experimental work, data analysis, and contributed to the manuscript preparation and editing. Roxana Fazli Estabragh is the second author, who carried out optimization of the synthetic conditions for compound **5**. Yuming Zhao is the corresponding author of this paper, who is the supervisor of Farshid Shahrokhi and helped design and develop this project.

Abstract

Two new K-region functionalized pyrene derivatives, namely 5-(dibromomethylene) pyren-4(5H)-one and 5-(1,3-dithiol-2-ylidene)pyren-4(5H)-one, were synthesized through olefination reactions of pyrene-4,5-dione. In addition, another pyrene derivative, ethyl 5-hydroxypyrene-4-carboxylate, was acquired as a byproduct in the synthesis. Electronic, electrochemical redox, and molecular structural properties of these pyrene derivatives were characterized by UV-Vis absorption, cyclic voltammetric, and X-ray single crystallographic analyses in combination with density functional theory (DFT) calculations. The roles of various intramolecular and intermolecular noncovalent forces in molecular conformation and crystal packing were investigated through various theoretical calculations, including natural bonding orbital (NBO), quantum theory of atoms in molecules (QTAIM), noncovalent interaction (NCI), and Hirshfeld surface analyses.

4.1 Introduction

Pyrene is an important polycyclic aromatic hydrocarbon (PAH) with a very high degree of fluorescence. Many pyrene derivatives have found application in organic electroluminescent devices, chemical and biological sensors, supramolecular guest-host chemistry, and organic semiconductors.[137,211–213] In the molecular structure of pyrene, the 1-, 3-, 6-, and 8-positions are more activated that the nodal region (2-, 7-positions) and the K-regions (4-, 5-, 9,- and 10-positions). As a result, selective functionalization of the pyrene core at the non-active sites of the K-region is a quite

challenging task. On the other hand, K-region functionalized pyrenes can exhibit appealing optical, crystal packing, and electrochemical properties. In this regard, the development of efficient synthetic methods to address this regio-selectivity has captured increased attention in recent years.[214,215]

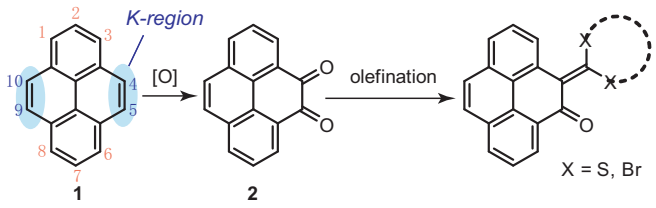

Figure 4.1: Derivatization of K-region functionalized pyrenes through olefination of pyrene-4,5-dione.

Among various functionalization methods for pyrene, selective oxidation in the K-region presents a powerful approach for generating novel pyrene derivatives. As early as 1975, Harvey and co-workers developed a direct approach for K-region oxidation of PAHs using osmium tetraoxide as the oxidant.[216] This method, however, has limited application due to the high toxicity and expensiveness of osmium tetraoxide. In 2005, Zhang and Harris reported that the use of ruthenium chloride/sodium periodate as oxidant could lead to K-region oxidation of pyrene through a single-step reaction, yielding pyrene-4,5-dione and pyrene-4,5,9,10-tetraone as products depending on the reaction temperature and the amount of oxidant used.[217] Harris' procedure, although being quite straightforward, is not very easy to control and unsuitable for large-scale synthetic applications. Most recently, the Bodwell group optimized the reaction conditions by changing the solvents and adding a small amount of additive, *N*-methylimidazole (NMI). Bodwell's modifications not only resulted in shortened

reaction time and improved reaction yield, but also alleviated the problem of the messy workup in the previous oxidation methods. Such advantages make this method more suitable for large-scale synthesis of pyrene-4,5-dione.[136,183]

We have recently synthesized a series of pyrenoimidazole derivatives through a facile one-pot condensation approach using pyrene-4,5-dione as the precursor.[158,218] The intriguing photophysical and crystallographic properties of these compounds thus motivated us to continue the exploration of new K-region functionalized pyrenes using pyrene-4,5-dione as an abundant and cost-effective precursor. The strategy employed in this work was to conduct olefination reactions on pyrene-4,5-dione (Figure 4.1). It was anticipated that one of the C=O groups would readily undergo olefination to extend π-conjugation, while the other C=O group would remain intact due to substantially increased steric crowding around it after the first olefination. Two straightforward olefination methods, Ramirez *gem*-dibromoolefination[219] and phosphite-promoted olefination with 1,3-dithiole-2-thione,[206] were carried out herein to produce new pyrene derivatives. The unsubstituted pyrene core has a flat, D_{2h}-symmetrical structure, rendering π-stacking and C–H$\cdots\pi$ interactions the dominant driving forces in its crystal packing.[220] In this work, the functionalities attached to the K-region of pyrene were expected to significantly alter their molecular conformational properties and induce other types of noncovalent forces to control the crystal packing. Moreover, electronic effects arising from the K-region functionalization should bring about novel electronic absorption and redox properties that may be beneficial for organic optoelectronic application. The following describes a comprehensive study on the synthesis and characterization of three new K-region functionalized pyrene derivatives.

4.2 Results and Discussion

4.2.1 Synthesis

The synthesis of K-region functionalized pyrene derivatives **4**–**6** is outlined in Figure 4.2. Pyrene-4,5-dione (**2**) was first subjected to a phosphite-promoted olefination reaction with excess 4,5-bis(methylthio)-1,3-dithiole-2-thione (**3**) in the presence of $P(OEt)_3$.[206] The reaction was conducted at 150 °C for 5 hours, yielding compound **4** in 10% yield. Elongation of the reaction time and an increase in reaction temperature did not result in further improvement of the reaction yield. It is worth noting that the 1,3-dithiole ring in **4** is a redox-active π-electron donor (D) group, which shows π-conjugation with the adjacent electron-accepting (A) carbonyl group. Its extended π-conjugation and electron push-and-pull features may lead to intriguing application to small-molecule organic semiconductors. In order to increase the synthetic yield of **4**, an alternative two-step approach was investigated and optimized (see Table S-1 in the ESI for details). In the first step, pyrene-4,5-dione (**2**) underwent the Ramirez dibromoolefination reaction to yield intermediate **5** in a good yield (88%). Compound **5** was then treated with **3** in a basic medium (KOH/ethanol) at reflux for 45 min, affording compound **4** in 45% yield. Interestingly, the formation of a significant amount of byproduct **6** (35%) was observed in this reaction, and this side reaction was somewhat competitive and could not be averted.

It is worth mentioning that both the phosphite-promoted and Ramirez olefination reactions on pyrene-4,5-dione (**2**) only led to the formation of mono-olefinated products. The second keto group of **2** remained intact, whether or not the first keto group was converted into an electron-donating or electron-withdrawing group.

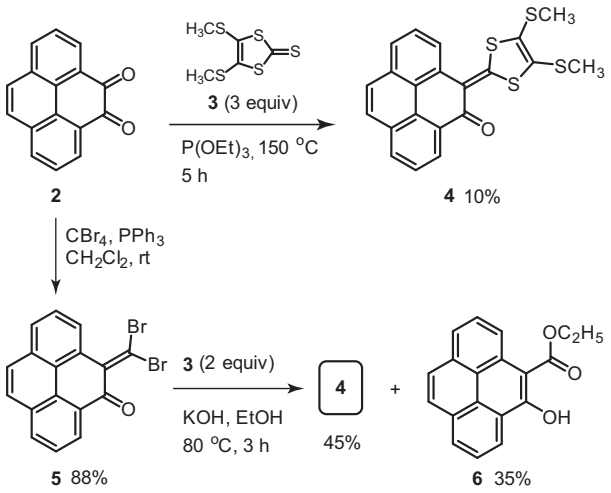

Figure 4.2: Synthesis of K-region functionalized pyrene derivatives from pyrene-4,5-dione (**2**).

The lack of reactivity of the second keto group can be attributed to the steric hindrance imposed by the adjacent group after the olefination, preventing it from further nucleophilic addition. Comparatively, the two-step synthesis of **4** through the geminal-vinyldibromide intermediate **5** is more efficient than the direct olefination method. The mechanism for the formation of **4** during the reaction of **5** and **3** under basic conditions is proposed in Figure 4.3A. Herein, 1,3-dithiole-2-thione **3** was first hydrolyzed into a dithiolate intermediate *in situ*, which then attacked the vinylbromide group to form the 1,3-dithiole structure. For the formation of byproduct **6**, vinyldibromide **5** was subjected to nucleophilic substitution with ethoxide and hydroxide anions. The resulting intermediate then underwent a tautomerization step to yield **6** (see Figure 4.3B).

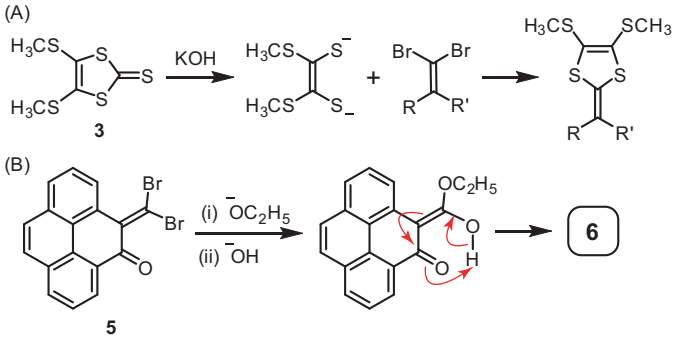

Figure 4.3: Proposed mechanisms for the formation of (A) **4** and (B) **6** in the reaction of **3** and **5** under basic conditions.

4.2.2 Electronic Absorption Properties

UV-Vis absorption spectra of pyrene derivatives **4**–**6** were determined and compared in order to understand their electronic properties. As shown in Figure 4.4, the absorption spectrum of compound **4** shows a prominent lowest-energy band at 488 nm, which can be attributed to the HOMO → LUMO transition according to time-dependent density functional theory (TD-DFT) calculations (see Table S-3 in the ESI for details). In addition to this band, the UV-Vis spectrum of **4** shows a series of relatively weak peaks ranging from 290 to 400 nm, which can be assigned to the $\pi \rightarrow \pi^*$ transitions of the pyrene core. Compared with the UV-Vis absorption spectra of pyrene derivatives **5** and **6**, the lowest-energy absorption band of **4** is considerably redshifted and relatively strong in intensity. For compound **5**, the lowest-energy absorption band appears as a broad and weak peak with a maximum absorption wavelength at 421 nm, while in the spectrum of **6**, a series of sharp low-energy absorption peaks are observed in the range of 314 to 391 nm, which are characteristic of the $\pi \rightarrow \pi^*$ transitions of pyrene. Of the pyrene derivatives **4**–**6**, compound **4** presents a typical electron push-and-pull system, where a good π-electron donor (1,3-

dithiole) is in direct π-conjugation with an electron-accepting keto group. Such a donor–acceptor (D–A) motif enables a significant degree of intramolecular charge-transfer (ICT), accounting for its substantially redshifted HOMO $\rightarrow$ LUMO band relative to the other pyrene derivatives. The absorption edge wavelength of the lowest-energy band in the spectrum of **4** is observed at 528 nm, which corresponds to an optical band gap (E_{opt}) of 2.35 eV. This value is similar to the E_{opt} of tetracene (2.54 eV),[221] hence suggesting the potential application of **4** as a small-organic semiconductor. The E_{opt} values of pyrene derivatives **5** and **6** are 2.75 eV and 3.07 eV, which are significantly greater than that of **4**. Detailed electronic absorption properties of **4**–**6** are summarized in Table S-8 in the ESI.

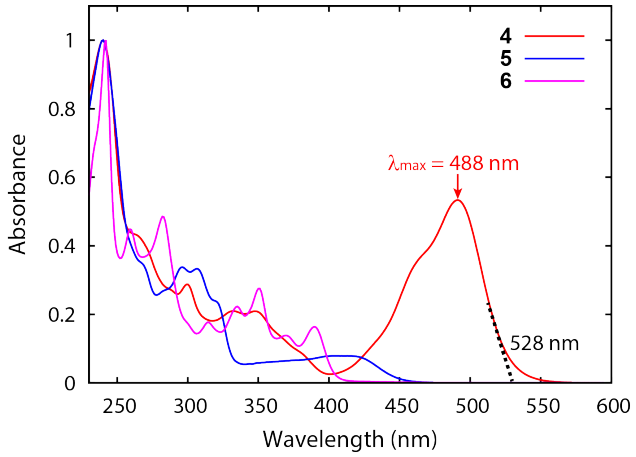

Figure 4.4: Normalized UV-Vis absorption spectrum of compounds **4**–**6** measured in acetonitrile at room temperature.

4.2.3 Redox Activity of Compound 4

Pyrene derivative **4** was found to show electrochemical redox activity as disclosed by cyclic voltammetric (CV) analysis. Figure 4.5 illustrates the multi-cycle CV profiles

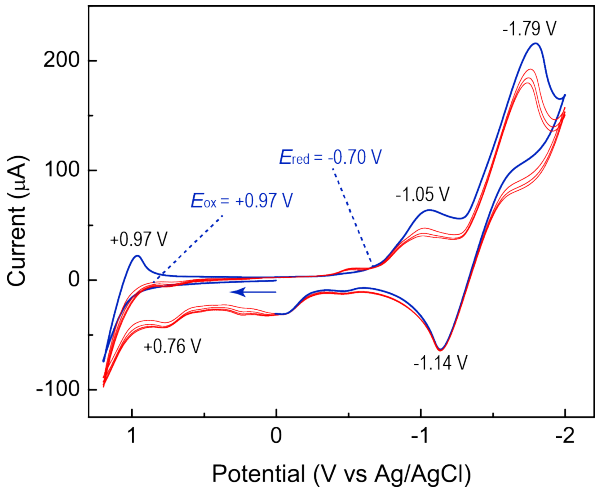

Figure 4.5: Multi-cycle cyclic voltammograms showing the multi-cycle scans of **4**. The first scan cycle is highlighted in blue color and the arrow indicates the scan direction. Experimental conditions: solvent: CH_2Cl_2; electrolyte: Bu_4NPF_6 (1.0 M); working electrode: glassy carbon; reference electrode: Ag/AgCl; counter electrode: Pt wire; scan rate: 200 mV/s.

of **4**. In the first cycle of CV scans, there is no anodic peak observed in the positive potential window, but an obvious cathodic peak emerges at +0.97 V. This peak can be attributed to the radical cation of dithiole resulting from the forward CV scan. After the first cycle, an weak anodic peak can be observed at +0.76 V, but the cathodic peak in the reverse scan disappears. The results suggest that the dithiole group is lacks reversible redox activity. In the negative potential window, the voltammograms show two cathodic peaks at -1.05 V and -1.79 V in the forward scan, which can be attributed to stepwise single electron injections that lead to the formation of the radical anion and dianion of **4**, respectively. In the reverse scan, only one anodic peak observed at -1.14 V, which can be assigned to a simultaneous bielectronic oxidation of the dianion of **4**. The band gap (E_g) of compound **4** was estimated as 1.67 eV,

according to the following equation:

$$E_g = E_{ox} - E_{red} \tag{4.1}$$

where E_{ox} and E_{red} are the onset potentials of oxidation and reduction in the first cycle of CV sans (see Figure 4.5). This band gap is narrower than the optical band gap (E_{opt}) determined from UV-Vis analysis. Overall, compound **4** exhibits amphoteric redox behavior, in which electron-accepting properties are dominant features and electron-donating properties are relatively insignificant.

4.2.4 Molecular Structural Properties

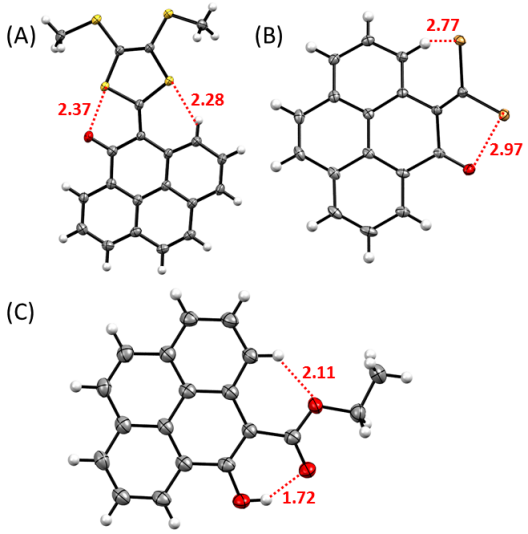

Figure 4.6: ORTEP drawing (50% ellipsoid probability) of the X-ray structures of pyrene derivatives (A) **4**, (B), **5**, and (C) **6**. Intramolecular distances are highlighted in Å.

Figure 4.6 shows the molecular structures of compounds **4**–**6** as determined by X-

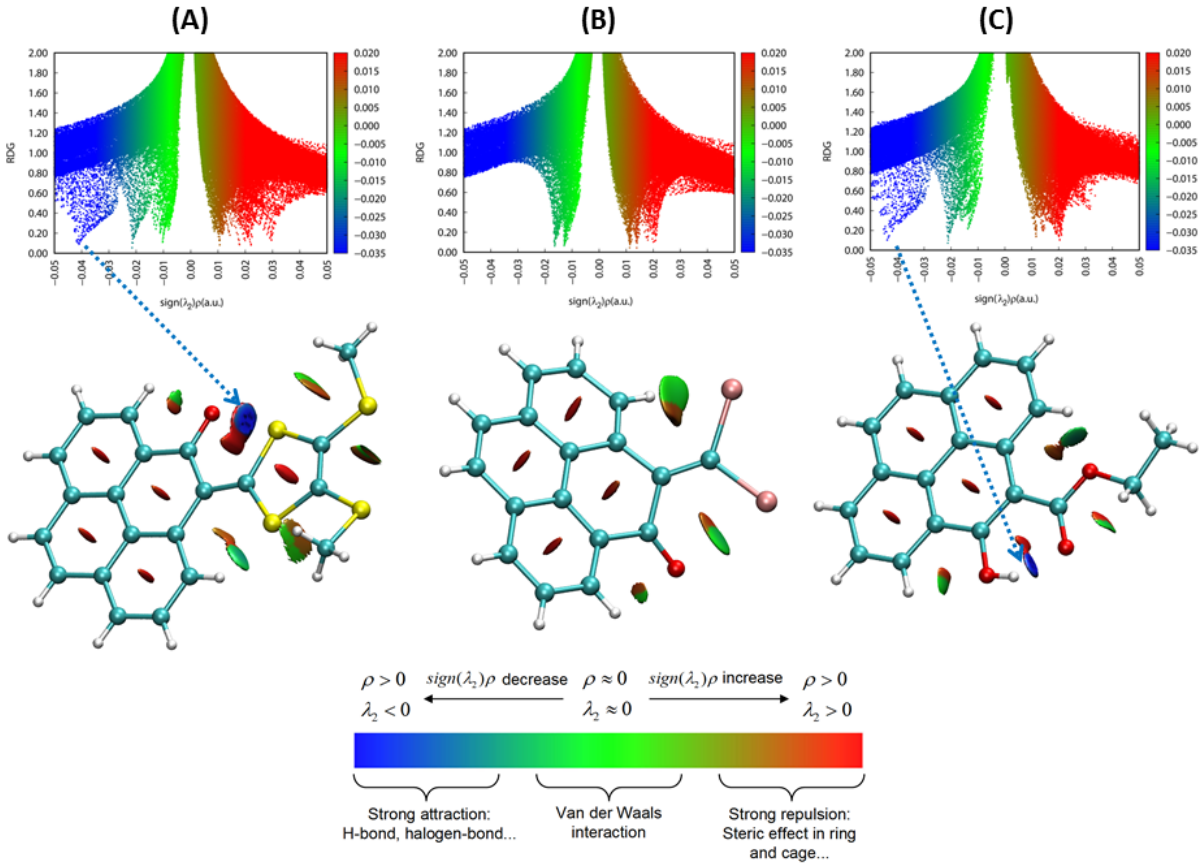

Figure 4.7: Reduced density gradient (RDG) isosurface plots (0.5 a.u.) and NCI-RDG 2D scatter maps for compounds (A) **4**, (B) **5**, and (C) **6**.

ray single crystallographic analysis. In the crystalline state, the molecule of **4** exhibits a nearly planar π-conjugated framework (Figure 4.6A). It is worth noting that the keto oxygen atom shows a close contact with the adjacent sulfur atom. In general, sulfur lone pair/oxygen lone pair interactions are repulsive; however, effects arising from electrostatic interactions (dipole/dipole) and orbital interactions between oxygen lone pair (lp(O)) and S–C antibonding oribtal (σ^*(S–C)) are known to make the O$\cdots$S contact attractive, eventually allowing the adjacent oxygen and sulfur atoms to engage in a noncovalent bond within the molecule.[222–226] The intramolecular S$\cdots$O distance in the X-ray structure of **4** is 2.37 Å, which is significantly shorter than the

sum of the van der Waals radii of sulfur and oxygen (3.25 Å) and hence indicates an attractive noncovalent bonding interaction. In recent years, this type of interactions was investigated as "chalcolgen bonding".[227–229] Herein, the S$\cdots$O bonding drives the molecular conformation of **4** to be planar. NBO analysis shows the presence of lp(O) $\rightarrow \sigma^*$(S–C) delocalization. The off-diagonal element of the Fock matrix $F(i,j)$ is 0.077 a.u. and the delocalization energy (E_2) is 11.88 kcal/mol, indicating a relatively small degree of delocalization. Quantum theory of atoms in molecules (QTAIM) analysis based on DFT calculations reveals a bond path connecting the adjacent sulfur and oxygen atoms in **4**, and a (3,-1) bond critical point (BCP) between them (see Figure S-11 in the ESI). The charge density (ρ_b) for this BCP is small (0.0418 a.u.) and the sign of both the Laplacian of the charge density ($\nabla^2\rho_b$) and the total energy density (H_b) are positive, suggesting a closed shell electrostatic interaction. The S$\cdots$O bonding in the structure of **4** was further visualized using the method of noncovalent interaction (NCI) analysis developed by Yang and co-workers.[230] As shown in Figure 4.7A, the blue-colored reduced density gradient (RDG) isosurface located between the oxygen and sulfur atoms corresponds to the spike appearing in the negative sign(λ_2)ρ region of the NCI-RDG 2D scatter map. Such features indicate a relatively strong noncovalent attraction between the oxygen and sulfur atoms.

The molecular structure of **5** adopts a non-planar conformation (Figure 4.6B), in which the exo-ring C=C bond and the C=O group show a torsion angle of 43.1°. The keto oxygen atom shows a close intramolecular contact with the neighboring bromine atom (O$\cdots$Br distance = 2.97 Å); however, in contrast to the case of **4**, the intramolecular Br$\cdots$O contact gives rise to a repulsive van der Waals interaction as revealed by the green-colored RDG isosurface in the NCI analysis (see Figure 4.7B).

In addition, an intramolecular Br$\cdots$H interaction is present between another bromine atom and adjacent pyrenyl hydrogen. The repulsive forces thus drive the molecular structure of **5** to adopt a non-planar, pringle-like conformation.

The molecular structure of compound **6** takes a fully planar conformation (Figure 4.6C), in which the hydroxy hydrogen forms a significant intramolecular hydrogen bond with the carbonyl oxygen atom (O$\cdots$H distance = 1.72 Å and O–H$\cdots$O angle = 147.1°). The hydrogen bonding interaction can be visualized as the blue colored isosurface in the NCI plot and the blue spike in the RDG scatter map (Figure 4.7C). Additionally, the ethoxy oxygen atom of **6** shows a distance of 2.11 Å to the adjacent pyrenyl hydrogen atom, which can be deemed as a weak hydrogen bonding interaction according to the QTAIM (Figure S-11, ESI) and NCI analyses (Figure 4.7C).

4.2.5 Crystal Packing Properties

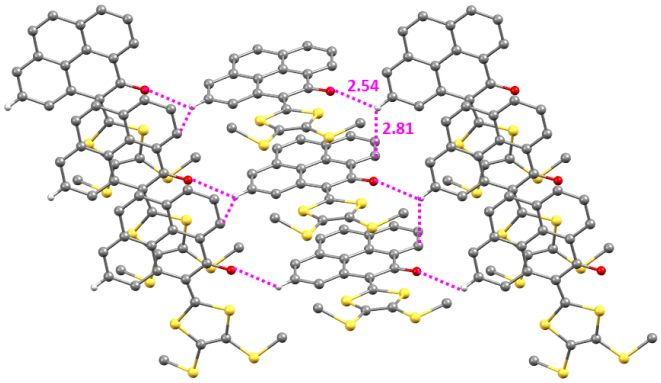

Figure 4.8: Packing diagram of **4** showing π-stacks of molecules. Intermolecular O$\cdots$H and C$\cdots$H bonds among the stacks are highlighted (in Å).

Figure 4.8 shows the crystal packing structure of compound **4**, in which highly

ordered stacks of molecules are seen to be formed through π–π interactions in a slipped geometry. The inter-layer distance in the π-stacks is 3.24 Å, which is much shorter than twice of the van der Waals radius of carbon (3.40 Å). Such close π-stacking alludes to significant intermolecular orbital interactions, which are beneficial for the development of organic semiconducting materials. In addition to the π-stacking, the hydrogen at the 7-position of each pyrene core interacts with the edges of two adjacent molecules through intermolecular O$\cdots$H and C–H$\cdots\pi$ interactions (highlighted as purple dashed bonds in Figure 4.8). It is also worth noting that intermolecular S$\cdots$S and S$\cdots$H contacts exist in the crystal packing structure (Figure 4.9). Overall, these noncovalent forces work together to dictate the supramolecular organization of compound **4** in its crystal structure.

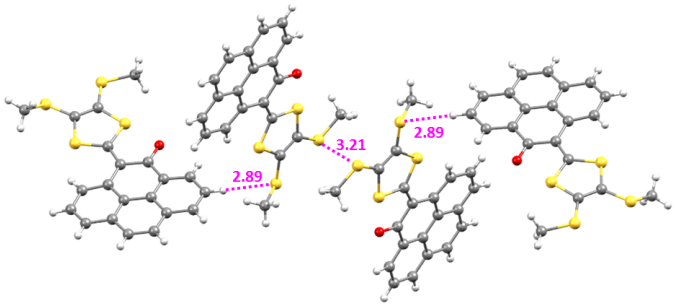

Figure 4.9: X-ray structure of **4** showing intermolecular S$\cdots$S and S$\cdots$H interactions. Distances are highlighted in Å.

To better understand the roles of various noncovalent interactions in the crystal packing of **4**, Hirshfeld surface analysis[231] was performed. In this analysis, the distance from the Hirshfeld surface to the nearest atoms outside and inside the surface are denoted as d_e and d_i, respectively, while d_{norm} is a normalized contact distance in terms of d_e, d_i, and the van der Waals radii of the atoms. Figure 4.10A shows

the Hirshfeld surface mapped with d_{norm}. The surface has relatively a large flat area, which contributes to the intermolecular π-π interactions in the crystal structures. The π-stacking feature is also reflected in the bright blue region in the two-dimensional fingerprint plot shown in Figure 4.10B. The relative contribution of π-π interactions is 8.5%. On the edge of the molecule, several red-color spots can be visualized, which account for the intermolecular S$\cdots$H (12.9%), O$\cdots$H (5.5%), and C–H$\cdots\pi$ (21.3%) contacts in the crystal packing.

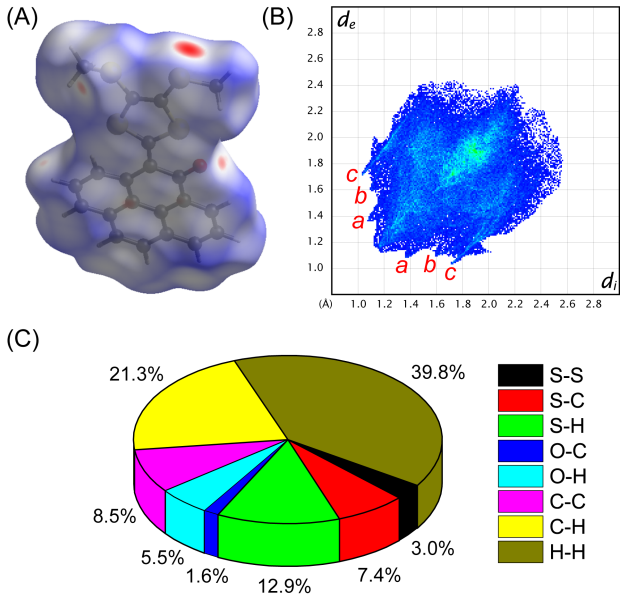

Figure 4.10: (A) Hirshfeld surface of **4** mapped with d_{norm}. (B) Two-dimensional fingerprint plot for the crystal packing of **4**. Spikes labelled as a, b, and c correspond to O$\cdots$H, C$\cdots$H, and S$\cdots$H contacts. (C) Relative contributions of various intermolecular contacts to the Hirshfeld surface area of **4**.

Figure 4.11 shows the packing diagram of **5**. In the crystal structure, the molecule of **5** takes a "pringle" shape and they form slightly slipped face-to-face stacks through π–π interactions. The inter-layer distance among the pyrene surfaces is 3.51 Å, which

is longer than that in the π-stacking of **4**. The π-stacking also involves a close O$\cdots$C contact (3.10 Å) between the keto oxygen atom and the pyrenyl carbon atom in the nearby molecule. In addition to π-stacking, the molecules of **5** also show edge-to-edge interactions through intermolecular Br$\cdots$H and O$\cdots$H bonds.

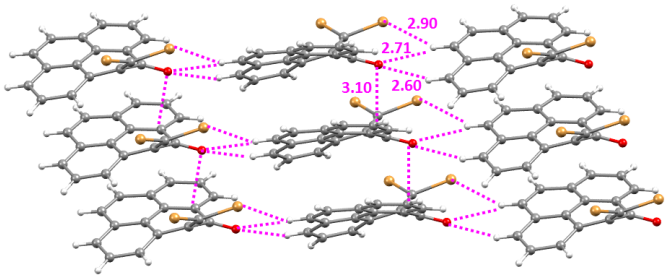

Figure 4.11: Packing diagram of **5** with intermolecular Br$\cdots$H, O$\cdots$H, and O$\cdots$C bonds highlighted (in Å).

The Hirshfeld surface of **5** mapped with d_{norm} shows red-color spots in the edge regions around bromine and oxygen atoms, as well as the 7, 8, 9-positions of the pyrene (Figure 4.12A). These spots correspond to the close intermolecular Br$\cdots$H, O$\cdots$C, and O$\cdots$H contacts observed in the crystal packing diagram. In the fingerprint plot of **5** (Figure 4.12B), two pairs of spikes labelled as *a* and *b* can be attributed to the O$\cdots$H and Br$\cdots$H contacts, the relative contributions of which are 6.8% and 30.4%, respectively. In addition to these, π-stacking, C–H$\cdots\pi$, and H$\cdots$H contacts are significant contributors to the intermolecular interactions in the crystal packing of **5**.

Figure 4.13 depicts the packing topologies of **6** in the crystal structure. The flat molecular shape of **6** facilitates a slipped face-to-face π-stacking motif with an inter-layer distance of 3.44 Å. This distance is longer than the packing distance in

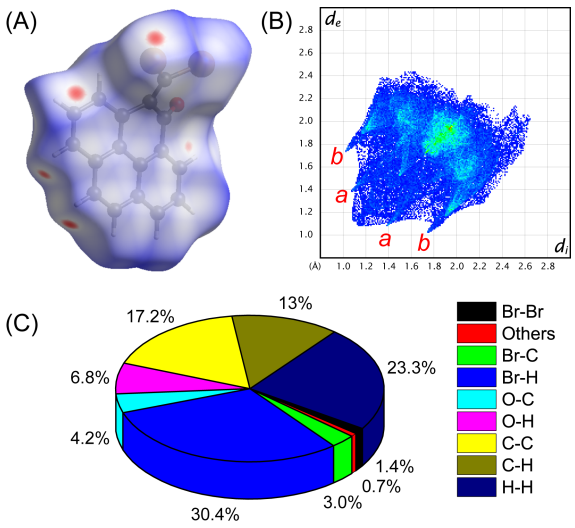

Figure 4.12: (A) Hirshfeld surface of **5** mapped with d_{norm}. (B) Two-dimensional fingerprint plot for the crystal packing of **5**. Spikes labelled as a and b correspond to O$\cdots$H and Br$\cdots$H contacts. (C) Relative contributions of various intermolecular contacts to the Hirshfeld surface area of **5**.

the crystal of **4**. Although both compounds possess similar planar π-surfaces, the attractive S$\cdots$S contacts in the crystal structure of **4** results in its π-stacking distance being shorter than that of **6**. An interesting feature in the crystal packing of **6** is the dimeric substructure assembled through a complementary pair of intermolecular O$\cdots$H bonds, which are formed between the ester C=O oxygen and ethyl hydrogen atoms. The dimeric assemblies show a flat shape and they form extended face-to-face stacks with a tilt angle of *ca.* 45°. Aside from the π-stacking, the hydrogen atom at the 10-position of the pyrene core also exhibits an intimate C–H$\cdots\pi$ interaction with the edge of an adjacent pyrene unit. As such, the π-stacks of **6** are assembled in a herringbone-like packing motif.

The Hirshfeld surface of **6** mapped with d_{norm} shows two significant red-color spots around the edges of ester C=O and ethyl C–H groups (Figure 4.14A). These

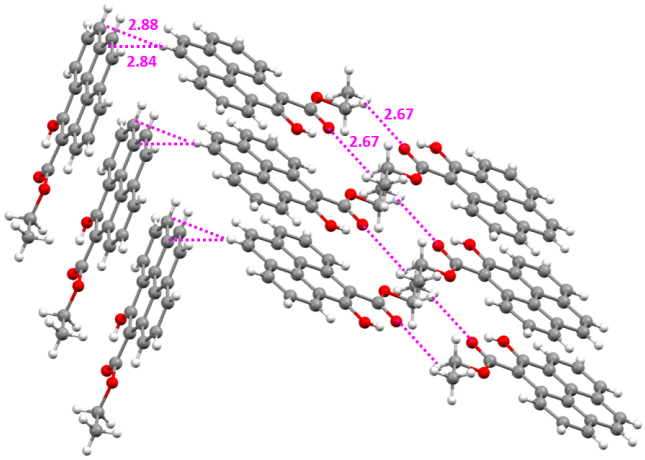

Figure 4.13: Packing diagram of **6** with intermolecular O···H, and C–H···π bonds highlighted (in Å).

features correspond to the complementary pair of intermolecular O···H bonds that give rise to the flat dimeric assembly. In the fingerprint plot (Figure 4.14B), the O···H contacts are revealed as a pair of spikes labelled as *b*. It is interesting to note that the relative contribution of H···H contacts (49.0%) in the crystal packing of **6** is much greater than those of **4** and **5**, and the origin can be attributed to the close C–H···π interactions occurring among the pyrene edges.

Overall, the Hirshfeld surface analysis provides a quantitative understanding of the effects of noncovalent forces on the crystal packing properties of the three K-region functionalized pyrene derivatives (**4**–**6**). The interplay of various intermolecular forces allows different solid-state structures to be assembled. As a summary, the packing topologies of **4**–**6** are compared in Figure 4.15. In all the crystal structures, π-π interactions among pyrene surfaces lead to the formation of column-shaped π-stacked assemblies with varied tilt angles. For compound **4**, attractive intermolecular S···S and O···H contacts occur among the edges of the π-stacks, affording cruciform-

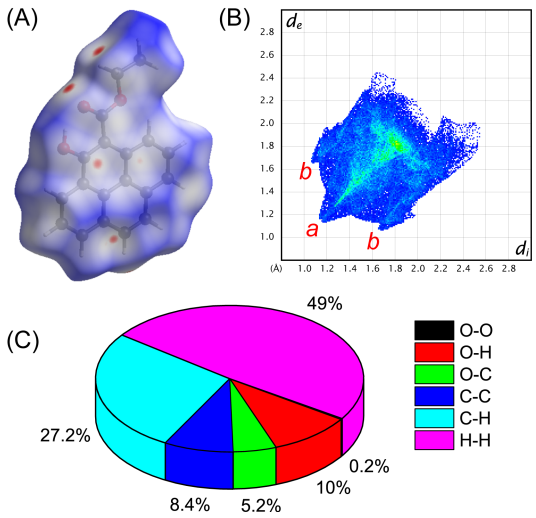

Figure 4.14: (A) Hirshfeld surface of **6** mapped with d_{norm}. (B) Two-dimensional fingerprint plot for the crystal packing of **6**. Spikes labelled as a and b correspond to H$\cdots$H and O$\cdots$H contacts. (C) Relative contributions of various intermolecular contacts to the Hirshfeld surface area of **6**.

shaped alignment as depicted in Figure 4.15A. For compound **5**, "pringle"-shaped molecules are assembled into twisted lamellar stacks, in which π-π interactions, intermolecular Br$\cdots$H, and O$\cdots$H bonds play dominant roles (Figure 4.15B). Finally, for compound **6**, pairs of molecules are formed through complementary intermolecular O$\cdots$H bonds. The molecular pairs take a planar conformation and hence form columnar π-stacks in a zig-zag shaped arrangement, in which the adjacent π-stacks show an angle of 87.8° (Figure 4.15C). The nearly perpendicular angle is in line with the geometry of C–H$\cdots\pi$ contacts, which play a major role in the crystal packing.

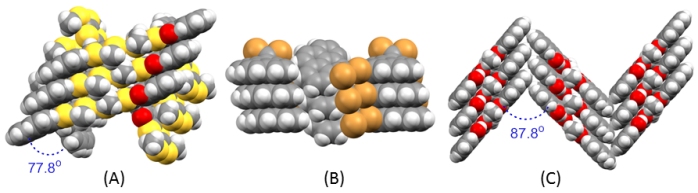

Figure 4.15: Space-filling models comparing the crystal packing motifs of (A) **4**, (B) **5**, and (C) **6**.

4.3 Experimental

4.3.1 Materials and Instrumentation

All chemicals and reagents were purchased from commercial suppliers and used without purification. Pyrene-4,5-dione (**2**) and 4,5-bis(methylthio)-1,3-dithiole-2-thione (**3**) were prepared according to the literature procedures.[136,171,183,232] All reactions were conducted in standard, dry glassware and under an inert atmosphere of nitrogen or argon unless otherwise noted. Evaporation and concentration were carried out with a rotary evaporator. Flash column chromatography was performed with 240-400 mesh silica gel, and thin-layer chromatography (TLC) was carried out with silica gel F254 coated on plastic sheets and visualized by UV light. Melting points (m.p.) were measured using an SRS OptiMelt melting point apparatus and are uncorrected. ^{1}H and ^{13}C NMR spectra were measured on a Bruker Avance III 300 MHz multinuclear spectrometer. Chemical shifts (δ) are reported in ppm downfield relative to the signals of the internal reference $SiMe_4$ or residual solvent CH_2Cl_2 (δ_H = 5.32 ppm, δ_C = 54.0 ppm). Coupling constants (J) are given in Hz. Infrared spectra (IR) were recorded on a Bruker Alfa spectrometer. High-resolution APPI-TOF MS analysis was done on a GCT premier Micromass Technologies instrument. UV-Vis absorption spectra were

measured on a Cary 6000i spectrophotometer. Cyclic voltammetric (CV) analysis was carried out in a standard three-electrode setup controlled by a BASi Epsilon potentiostat. Single-crystal X-ray diffraction data was collected at 100(2) K on a XtaLAB Synergy-S, Dualflex, HyPix-6000HE diffractometer using Cu $K\alpha$ radiation (λ = 1.5406 Å). Crystals were mounted on nylon CryoLoops with Paraton-N. Data collection and reduction were processed within CrysAlisPro (Rigaku OD, 2019). A multi-scan absorption correction was applied to the collected reflections. Using Olex2,[208] the structure was solved with the ShelXT[233] structure solution program using Intrinsic Phasing and refined with the ShelXL[234] refinement package using Least Squares minimisation. All non-hydrogen atoms were refined anisotropically. The organic hydrogen atoms were generated geometrically.

4.3.2 Computational Methods

Computational modeling studies were carried out using the Gaussian 16 software package.[235] Molecular geometries were taken from X-ray single crystal structures. TD-DFT calculations were performed at the CAM-B3LYP/6-311+G(d,p) level of theory[236] with only singlet to singlet transitions considered (nstates = 20) in acetonitrile. Solvent effects were computed using Truhlar's SMD solvation model.[237] Single-point calculations were carried out using the M06-2X density functional[238] in conjunction with the Def2-SVP basis set.[239] QTAIM and NCI analyses were conducted using the Multiwfn software.[240] Hirshfeld surface analysis was performed using the CrystalExplorer software (version 3.1).[241] Molecular structures and isosurfaces were visualized by VMD software package.[242]

4.3.3 Synthesis and Characterization

5-(4,5-Bis(methylthio)-1,3-dithiol-2-ylidene)pyren-4(5*H*)-one (4)

Method A: Pyrene-4,5-dione **2** (0.208 g, 1.00 mmol), 4,5-bis(methylthio)-1,3-dithiole-2-thione (**3**, 0.678 g, 3.00 mmol), $P(OEt)_3$ (5 mL) were added to a round-bottomed flask and heated at 150 °C for 5 h. Then the reaction was subjected to vacuum distillation at the same temperature to remove unreacted $P(OEt)_3$. The residue was subjected to silica gel column chromatography (hexanes/EtOAc, 80:20) to give pure compound **4** (0.041 g, 0.10 mmol, 10%) as a red crystalline solid. *Method B*: Compound **5** (0.200 g, 0.50 mmol), 4,5-bis(methylthio)-1,3-dithiole-2-thione **3** (0.226 g, 1.00 mmol), KOH (0.110 g, 2.00 mmol), EtOH (20 mL) were added to a round-bottomed flask, and the mixture was heated at 80 °C for 1 h. The solvent was then evaporated under reduced pressure. The residue was subjected to silica gel column chromatography (hexanes/CH_2Cl_2, 70:30) to afford pure compound **4** (0.090 g, 0.20 mmol, 45%). m.p. 191.3–191.8 °C; ^{1}H NMR (300 MHz, CD_2Cl_2) δ 8.72 (dd, J = 7.6, 1.3 Hz, 1H), 8.35 (dd, J = 7.0, 1.9 Hz, 1H), 8.21 (dd, J = 7.8, 1.3 Hz, 1H), 7.93–7.83 (m, 5H), 2.70 (s, 3H), 2.57 (s, 3H) ppm; ^{1}C NMR (75 MHz, CD_2Cl_2) δ 177.60, 163.14, 137.96, 131.79, 131.28, 131.05, 129.99, 128.32, 127.55, 127.34, 126.72, 126.64, 126.60, 126.29, 125.83, 124.92, 123.23, 121.54, 118.24, 19.41, 18.66 ppm; HRMS (APPI-TOF, positive mode) m/z calcd for $C_{21}H_{14}OS_4$ 409.9927, found 409.9906 $[M + H]^+$.

5-(Dibromomethylene)pyren-4(5*H*)-one (5)

Pyrene-4,5-dione **2** (2.322 g, 10.00 mmol), CBr_4 (6.620 g, 20.00 mmol), PPh_3 (7.860 g, 30.00 mmol), and CH_2Cl_2 (50 mL) were added to a round-bottomed flask, and the

mixture was stirred at room temperature for 2 h. The reaction mixture was then subjected to vacuum filtration, and the remaining solid was washed with CH_2Cl_2. The CH_2Cl_2 layers were combined and concentrated under reduced pressure, and the residue was subjected to silica gel column chromatography (hexanes/CH_2Cl_2, 80:20) to give pure compound **5** (3.41 g, 8.81 mmol, 88%) as a pale yellow crystalline solid. m.p. 197.3–198.1 °C; ^{1}H NMR (500 MHz, $CDCl_3$) δ 8.38 (dd, J = 7.6, 1.1 Hz, 1H), 8.26 (dd, J = 7.4, 1.3 Hz, 1H), 8.17 (dd, J = 8.0, 1.3 Hz, 1H), 7.97 (dd, J = 8.0, 1.1 Hz, 1H), 7.85 (s, 2H), 7.78–7.64 (m, 2H) ppm; ^{13}C NMR (75 MHz, CD_2Cl_2) δ 188.39, 140.41, 133.42, 131.50, 131.06, 130.93, 129.73, 128.76, 128.55, 128.21, 127.20, 126.40, 126.24, 126.05, 124.39, 99.56, 29.68 ppm; HRMS (APPI-TOF, positive mode) m/z calcd for $C_{17}H_8Br_2O$ 385.8941, found 385.8929 $[M + H]^+$.

Ethyl 5-hydroxypyrene-4-carboxylate (6)

Compound **6** was obtained as a yellow crystalline solid (0.050 g, 0.10 mmol, 35%) in the synthesis of **4** through *Method B*. m.p. 125.5–126.2 °C; ^{1}H NMR (300 MHz, CD_2Cl_2) δ 13.70 (s, 1H), 9.17 (dd, J = 8.1, 1.2 Hz, 1H), 8.80 (dd, J = 7.9, 1.2 Hz, 1H), 8.34 (dd, J = 7.7, 1.2 Hz, 1H), 8.10–7.97 (m, 5H), 4.70 (q, J = 7.1 Hz, 2H), 1.62 (t, J = 7.1 Hz, 3H) ppm; ^{13}C NMR (75 MHz, CD_2Cl_2) δ 173.35, 163.64, 131.14, 130.94, 128.96, 128.53, 128.23, 126.84, 126.62, 126.57, 126.29, 125.91, 124.50, 123.68, 122.26, 120.88, 102.19, 62.38, 14.17 ppm; HRMS (APPI-TOF, positive mode) m/z calcd for $C_{19}H_{14}O_3$ 290.0943, found 290.0938 $[M + H]^+$.

4.4 Conclusions

In conclusion, we have synthesized three new K-region functionalized pyrene derivatives (**4**–**6**) through olefination reactions of pyrene-4,5-dione as the starting material. The electronic and electrochemical redox properties of these pyrene derivatives were characterized and compared. Of the three compounds, dithiole-substituted pyrene **4** presents an intriguing D–A conjugated system and hence shows the smallest small band gap (E_g) and amphoteric redox behavior. Such properties make compound **4** a potentially useful organic semiconductor. The molecular geometries of the three pyrene derivatives were found to show strong dependence on the intramolecular noncovalent interactions around the K-region. The molecular shape and various intermolecular forces (e.g., S$\cdots$S, Br$\cdots$H, and O$\cdots$H contacts) induced by the functional groups attached to the K-region of pyrene strongly affect the crystal packing motif. Overall, the findings disclosed in this work will be beneficial to the development of pyrene-based organic solid materials for advanced optoelectronic applications.

Chapter 5

Self-Condensation of Pyrene-4,5-dione: An Approach to Generate Functional Organic Fluorophores

The contents of this chapter were published as an article in *Org. Lett.* **2019**, *21*, 9306-9310. Contributions of authors are described below:

Farshid Shahrokhi is the first author, who conducted all the experimental work, data analysis, and contributed to the manuscript preparation and editing. Yuming Zhao is the corresponding author of this paper, who is the supervisor of Farshid Shahrokhi and helped design and develop this project.

Abstract

In this work, a new class of π-conjugated organic fluorophores containing a 6H-phenanthro[4,5-cde]pyreno[4',5':4,5]imidazo[1,2-α]azepin-6-one core was synthesized by a facile one-pot condensation method. The molecular structures and solid-state packing properties of these compounds were investigated by X-ray single crystallographic analysis. UV-Vis absorption and fluorescence spectroscopic studies disclosed interesting mechanofluorochromic properties in the solid-state and highly sensitive acidochromic behavior in the solution phase.

Pyrene derivatives are popular molecular building blocks for the development of advanced organic optoelectronic materials, owing to the rich electronic and photophysical properties of pyrene.[137,243] Studies in this area have been continuously motivated by the development of new functionalized pyrenes, which serve as useful precursors for the preparation of advanced π-conjugated materials.[215,244–246] In recent years, pyrene-4,5-dione[134,136] has found growing application, especially after the disclosure of an efficient large-scale synthesis of pyrene-4,5-diones by Bodwell and co-workers.[136] Synthetically, pyrene-4,5-dione can undergo various reactions to yield more extended π-systems.[156,158,247–252] Among them, condensation reactions constitute a very appealing approach due to their high efficiency and simplicity in operation.

In our recent study of pyrenoimidazole derivatives,[158] an interesting type of self-condensation reaction was discovered. As shown in Scheme 5.1, a mixture of pyrene-4,5-dione **5-1a**, ammonium acetate and glacial acetic acid was heated at 100 °C for 10 h, resulting in the formation of 6*H*-phenanthro[4,5-*cde*]pyreno[4',5':4,5]imidazo[1,2-

a]azepin-6-one **5-2a** in 25% yield. Although **5-2a** shows relatively low solubility in

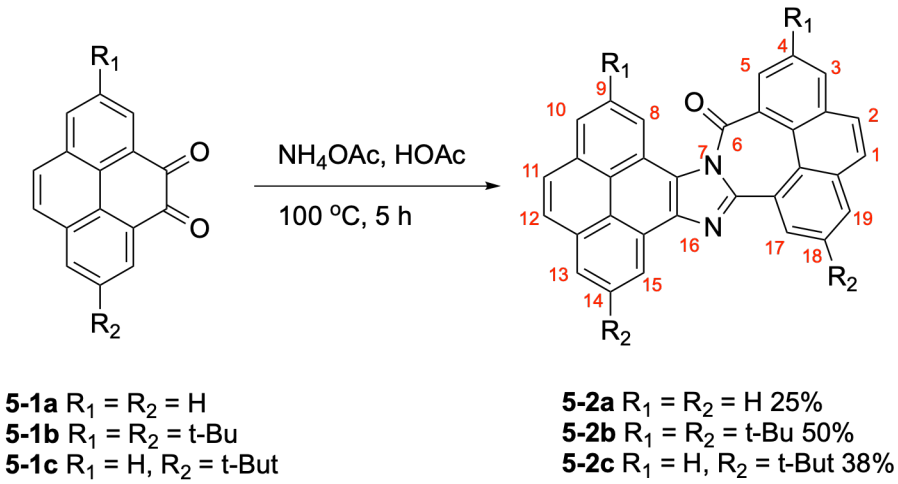

5-1a $R_1 = R_2 = H$
5-1b $R_1 = R_2 = t\text{-Bu}$
5-1c $R_1 = H$, $R_2 = t\text{-But}$

5-2a $R_1 = R_2 = H$ 25%
5-2b $R_1 = R_2 = t\text{-Bu}$ 50%
5-2c $R_1 = H$, $R_2 = t\text{-But}$ 38%

Scheme 5.1: Synthesis of pyrene derivatives **5-2a-c** through self-condensation of pyrene-4,5-diones.

common organic solvents, its molecular structure could still be reasonably elucidated based on ^{1}H NMR and MS analyses (see the Supporting Information). To address the solubility problem, *t*-butyl substituted pyrene-4,5-diones **5-1b** and **5-1c** were prepared,[136] and they were subjected to the same self-condensation conditions to afford analogous products with both improved solubility and yields (Scheme 5.1). The molecular structures of condensation products **5-2b** and **5-2c** were unambiguously confirmed by X-ray single crystallography in addition to NMR and MS analysis. The X-ray structure of **5-2b** (Figure 5.1A) shows that the steric interactions between 6-one and pyrenyl 8-*H* force the molecule to adopt a non-planar helical shape. Two types of enantiomers with opposite helicity are observed in the crystal structure. As shown in Figure 1A, enantiomeric pairs of **5-2b** are packed in a slip-stacked fashion. Density functional theory (DFT) calculations revealed that the racemization

energy barriers of **5-2** are quite low (e.g., 6.46 kcal/mol for **5-2a**, see Figure S-16, Supporting Information), suggesting that individual molecules of **5-2**, in the gas phase or dissolved in a solvent, would undergo rapid configurational exchanges under standard conditions.

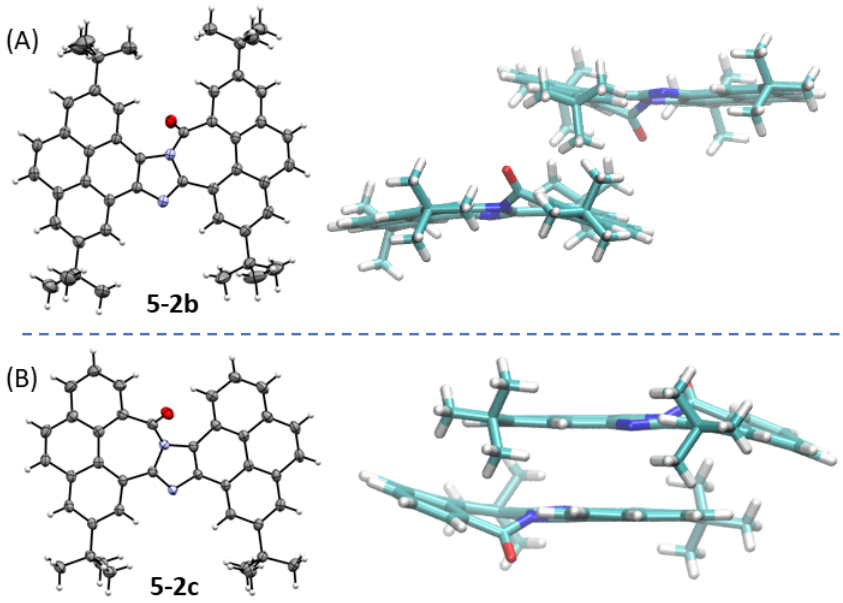

Figure 5.1: ORTEP drawings (50% probability) of (A) **5-2b** and (B) **5-2c** as well as the packing motifs of their enantiomeric pairs in the crystalline state.

The molecular structure of **5-2c** (Figure 5.1B) is similar to that of **5-2b**, but the π-stacking of each enantiomeric pair in the crystalline state appears to be more co-facial than **5-2b** as a result of less *t*-butyl groups present in **5-2c**. Note that 2-*t*-butylpyrene-4,5-dione (**5-2c**) is an unsymmetrical diketone, which in theory may yield four different regioisomeric products through self-condensation (see Figure S-17, Supporting Information). For example, Emery *et al.* reported that the self-condensation of an unsymmetric diketone under conditions similar to ours afforded

two regioisomers in nearly equal yields.[253] In our reaction, however, only one major product **5-2c** was obtained from the self-condensation of **5-1c**. As DFT calculations indicated that the structure of **5-2c** is the least thermodynamically stable one among other possible self-condensation products (Figure S-17, Supporting Information), the regioselectivity of this reaction is likely kinetically controlled rather than thermodynamically controlled.

To gain a deeper insight into the reaction mechanism of the above self-condensation reactions, two control reactions were carried out. First, phenanthrene-9,10-dione (**5-3**) was subjected to heating in the presence of ammonium acetate and glacial acetic acid. This reaction only yielded phenanthroimidazole **5-4** as the major product (Scheme 5.2). Product **5-4** was formed as a precipitate with very poor

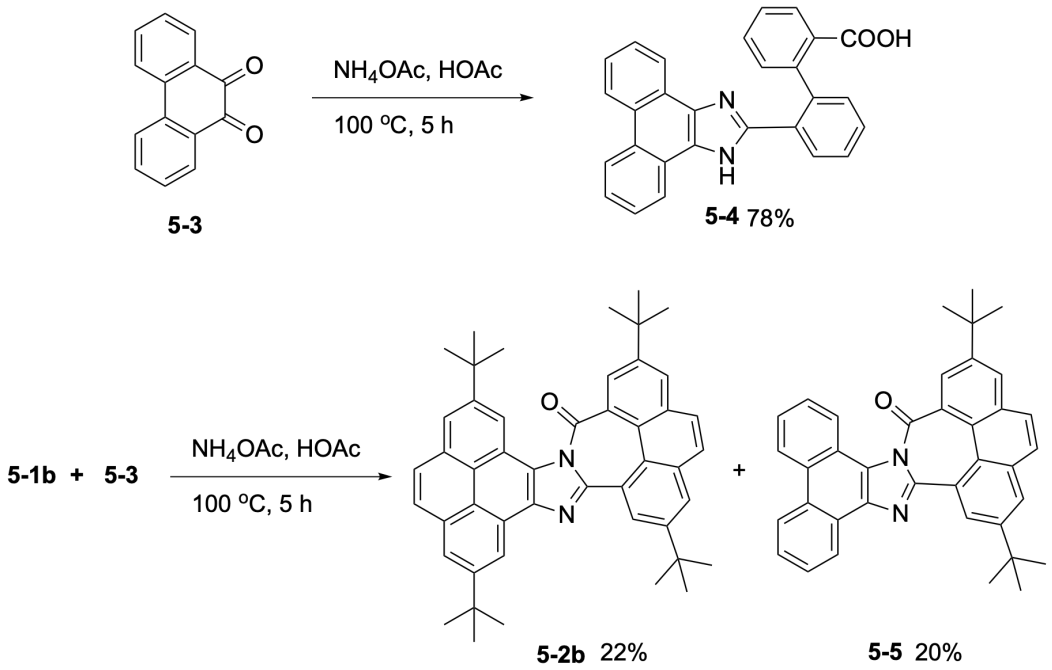

Scheme 5.2: Controlled condensation reactions of phenanthrene-9,10-dione **5-3** and pyrene-4,5-dione **5-1**.

solubility in common organic solvents due to the presence of a free carboxyl group. This outcome contrasts the cases of pyrene-4,5-diones, but is consistent with the observation reported by Lantos in 1975.[254] In another control reaction, a mixture of diones **5-1b** and **5-3** was subjected to the same condensation conditions. In this reaction, two soluble products were isolated in nearly equal yields. The first product is **5-2b**, resulting from the self-condensation of **5-1b**. The second product turns out be a cross-condensation product **5-5** (Scheme 5.2). The molecular structure of **5-5** was validated by X-ray structural analysis (Figure 5.2A) in addition to NMR and MS analyses. Similar to **5-2b/c**, enantiomeric pairs exist in the crystal structure of **5-5** and they form ordered columnar supramolecular assemblies through π-stacking (Figure 5.2B). In theory, cross-condensation of two different diketones should yield two products. The fact that only **5-5** was formed suggests a high degree of regioselectivity, which deserves more light to be shed upon.

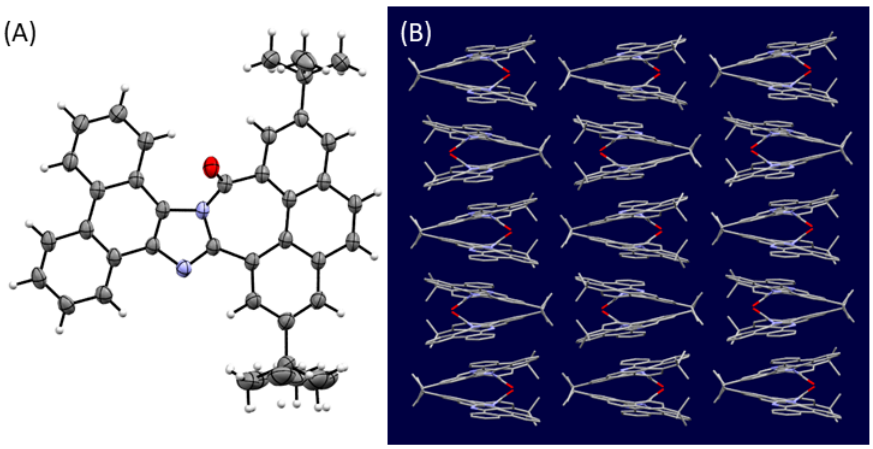

Figure 5.2: (A) ORTEP drawing (50% probability), and (B) crystal packing diagram of compound **5-5**. Hydrogen atoms are not shown for clarity.

The two control reactions underscore the indispensable role of pyrene-4,5-dione in

the formation of the seven-membered azepinone ring during the condensation process. Rationalization for the different reactivities of pyrene-4,5-dione versus phenanthrene-9,10-dione can be made based on the reaction mechanisms outlined in Scheme 5.3. Herein, two reaction pathways are illustrated for the self-condensation reactions of **5-3** and **5-1a**, respectively. Phenanthrene-9,10-dione yields a dimine intermediate **5-IM-1** when treated with ammonium acetate and glacial acetic acid. **5-IM-1** then reacts with **5-3** through condensation to form a spiro intermediate **5-IM-2**, which undergoes a ring opening process through water nucleophilic attack to give product **5-4**.[253–255] The rotational freedom at the biphenyl unit in **5-4** allows the carboxyl group to shun away from the imidazolyl group in order to minimize steric crowding. DFT optimized geometry of **5-4** shows that the distances between carboxyl carbon and two imidazolyl nitrogen atoms are 3.53 Å and 5.45 Å, respectively (Figure S-18, Supporting Information). Such a structure disfavors intramolecular condensation between the carboxyl and imidazolyl groups. Pyrene-4,5-dione **5-1a** can also form a dimine intermediate **5-IM-3**, followed by a spiro intermediate **5-IM-4**. Ring opening of **5-IM-4** leads to **5-IM-5**, in which the carboxyl group and the imidazolyl unit are closely positioned as a result of their direct linkage to the rigid phenanthrene unit. The distances between carboxyl carbon and two imidazolyl nitrogen atoms in the optimized geometry of **5-IM-5** (Figure S-19, Supporting Information) are 3.03 Å and 3.08 Å, which are much shorter than those in **5-4**. The preorganization of **5-IM-5** thus enables the intramolecular condensation between the carboxyl and imidazolyl groups, which eventually yields **5-2a** as a stable product.

Given the relatively good solubility of **5-2b** in organic solvents, it was further investigated by UV-Vis absorption and fluorescence spectroscopic analysis to probe

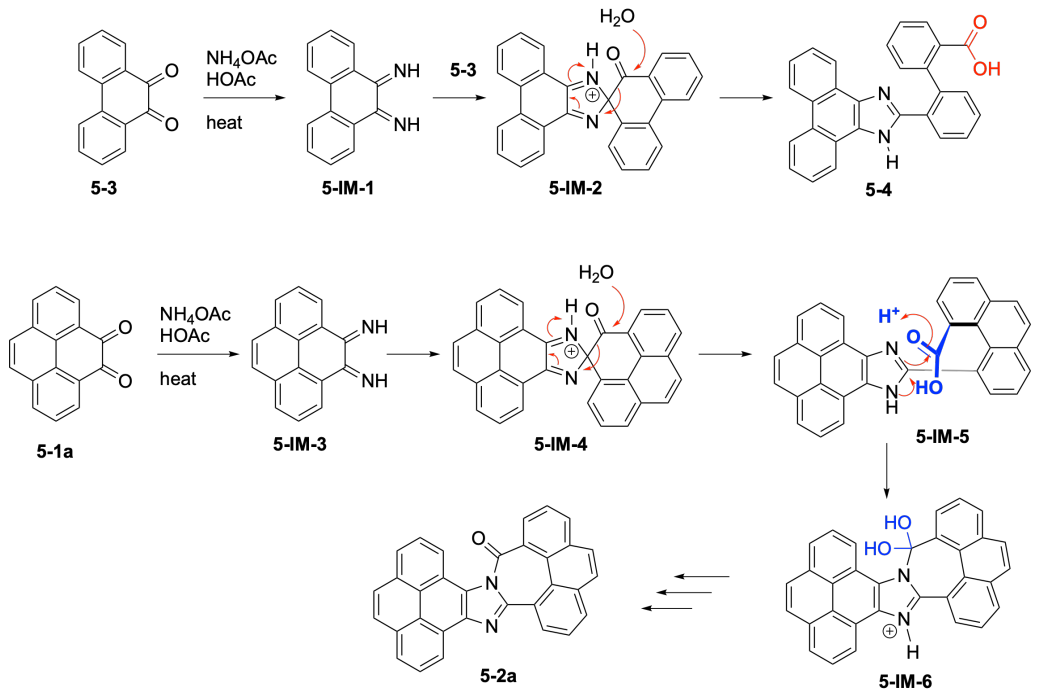

Scheme 5.3: Proposed mechanisms for the self-condensation reaction of phenanthrene-9,10-dione (**5-3**) and pyrene-4,5-dione (**5-1a**), respectively.

the electronic properties of these new pyrene based π-systems. Figure 5.3A compares the UV-Vis spectra of **5-2b** measured in different organic solvents. The absorption profiles of **5-2b** show similar features in most of the solvents examined, except in methanol and chloroform. In methanol, the lowest-energy $\pi \rightarrow \pi^*$ absorption band of **5-2b** is considerably blueshifted to 383 nm, while in chloroform it shows the most pronounced redshift (λ_{max} = 400 nm). The solvatochromic effects observed here do not follow a clear trend in correlation with solvent polarity. More likely, solubility and/or aggregation effects play important roles in the electronic absorption properties of **5-2b**. The emission properties of **5-2b** in the solution phase were studied by fluorescence spectroscopy. Carbon tetrachloride was used as the solvent, considering the good solubility it affords. Figure 5.3B shows the fluorescence spectra

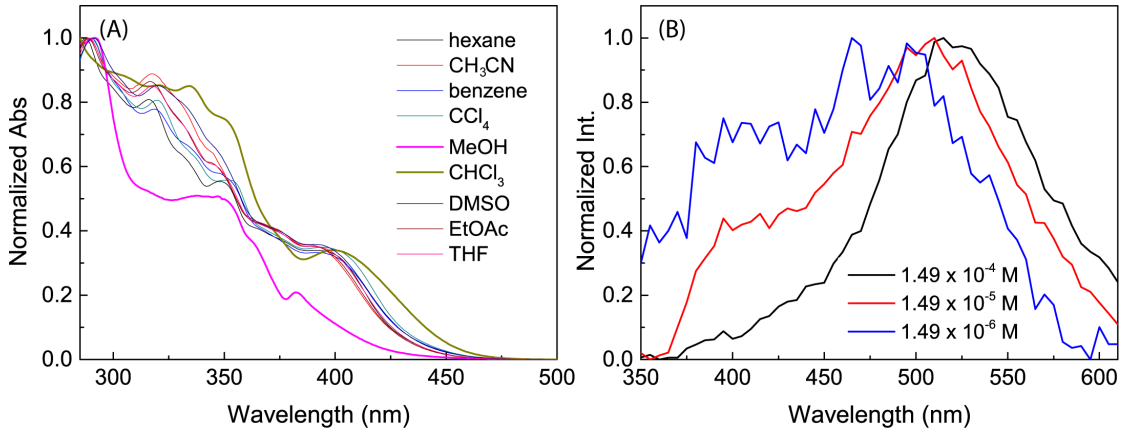

Figure 5.3: (A) Normalized UV-Vis absorption spectra of **5-2b** measured in different organic solvents. (B) Normalized fluorescence spectra of **5-2b** (in CCl_4) measured at different concentrations (λ_{ex} = 313 nm).

of **5-2b** measured at different concentrations. At relatively high concentration (10^{-4} M), the spectrum features only one broad band peaking at 520 nm. When the concentration is reduced by one order of magnitude (10^{-5} M), this emission band is slightly blueshifted to 505 nm. In the meantime, a new shoulder band emerges in the high-energy region (*ca.* 380-440 nm), and the relative intensity of this new band continues to increase under further diluted conditions (10^{-6} M). The concentration-dependent fluorescence behavior can be attributed to the formation of excimers in solution.[141,256] At high concentrations, excimers dominate the emission process to give the long-wavelength band at 520 nm. At low concentration, however, the emission of individual molecules of **5-2b** (i.e., monomers) becomes more significant in the range of 380-400 nm. As such, the fluorescence profile reflects the contributions of both excimers and monomers. When **5-2b** was dissolved in different organic solvents at concentration of 10^{-5} M, the solutions were found to emit different luminescent colors upon long-wavelength UV light irradiation (see Figure 5.4A). For solvents

with good solubility, such as carbon tetrachloride, *p*-xylene, benzene, THF, and ethyl acetate, the solutions of **5-2b** give greenish luminescence. For solvents with moderate solubility (chloroform, acetone, acetonitrile, and DMSO), the luminescent color is yellowish. For solvents with poor solubility such as methanol and ethanol, the luminescence is very weak. But in hexane the luminescent color is blue. The luminescent colors show a good correlation with the maximum emission wavelengths (λ_{ex}) observed in their fluorescence spectra (Figure 5.4D). It was further noticed that compound **5-2b** in the solid state exhibits mechanofluorochromic behavior. Crystals of **5-2b** yield blue-colored luminescence. Subjecting the crystals to mechanical grinding resulted in an amorphous powder, which gave green-colored luminescence (Figure 5.4B and 5.44C). Solid state fluorescence spectroscopic analysis showed that crystals of **5-2b** emit a broad peak around 508 nm, while the powder of **5-2b** (amorphous state) yields two emission bands at 441 nm and 508 nm, respectively (Figure 5.4E). The mechanofluorochromic properties of **5-2b** can be attributed to the emission of excimers and monomers. In the crystalline state, **5-2b** molecules are closely stacked to facilitate the formation of excimers when they are electronically excited. As such, the emission profile of **5-2b** only features the long-wavelength excimer band, which yields blue-colored luminescent light. In the amorphous solid state, **5-2b** molecules are randomly and disorderly packed, so they emit both long-wavelength (excimer) and short-wavelength (monomer) light. The combined emission bands thus constitute the observed green-colored luminescence.

The solutions of **5-2b** were also found to show acidochromic fluorescence behavior. As shown in Figure 5.5, the fluorescence intensity of **5-2b** grows steadily with increasing addition of a strong organic acid, trifluoroacetic acid (TFA). The

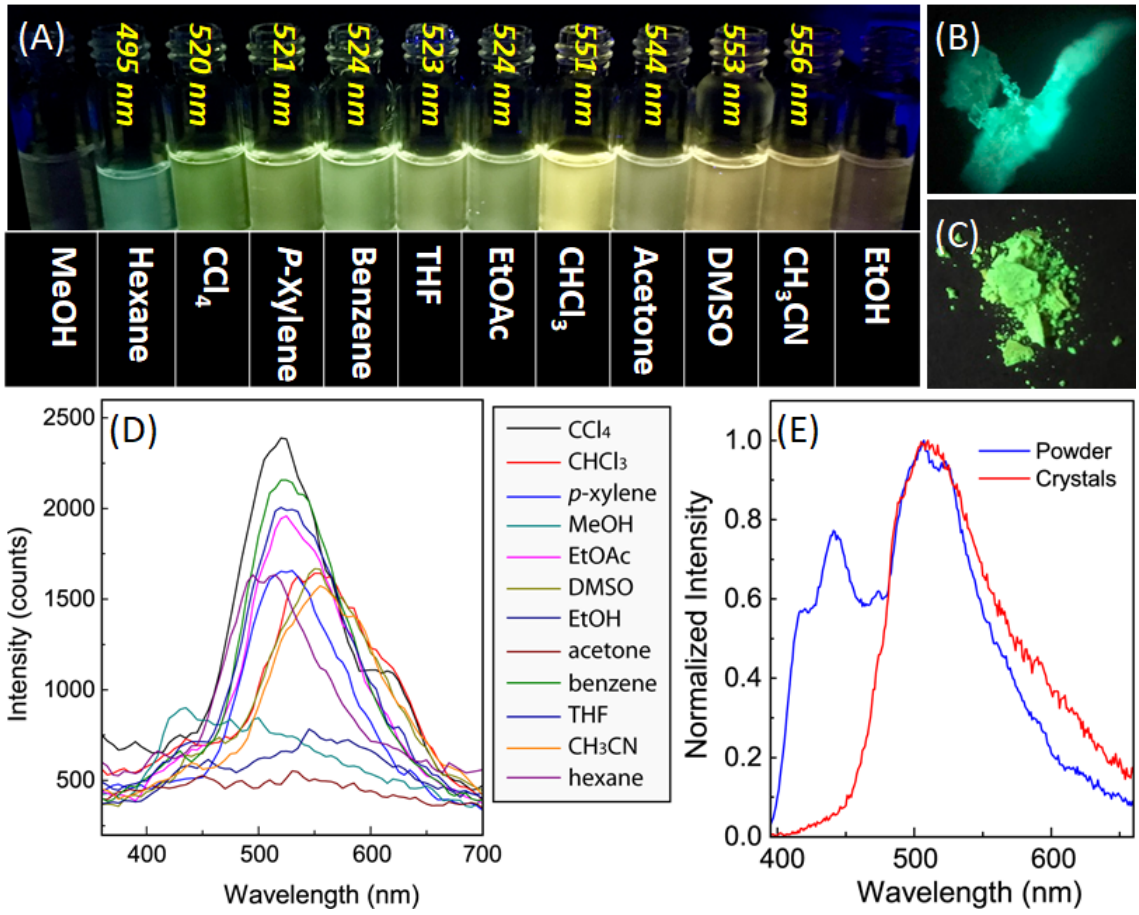

Figure 5.4: (A) Photographic images of **5-2b** (1.49×10^{-5} M) dissolved or suspended in different organic solvents (λ_{ex} values are indicated). (B) Photographic images of **5-2b** in crystalline form. (C) Photographic images of **5-2b** in powdery form. All samples were placed under irradiation with a UV lamp (365 nm). (D) Fluorescence spectra of **5-2b** (1.49×10^{-5} M) measured in various solvents (λ_{ex} = 313 nm). (E) Normalized fluorescence spectra of **5-2b** measured in crystalline and powdery forms (λ_{ex} = 350 nm).

fluorescence enhancement reached saturation after *ca.* 3,100 molar equivalents of TFA was added, while the λ_{ex} was observed to redshift to a moderate degree, from 513 nm to 530 nm, during the TFA titration. The relative fluorescence quantum

yield (Φ_F) of **5-2b** was determined to be 0.101 in CCl_4, and it increased to 0.340 after addition of excess TFA (3,100 equivalents).

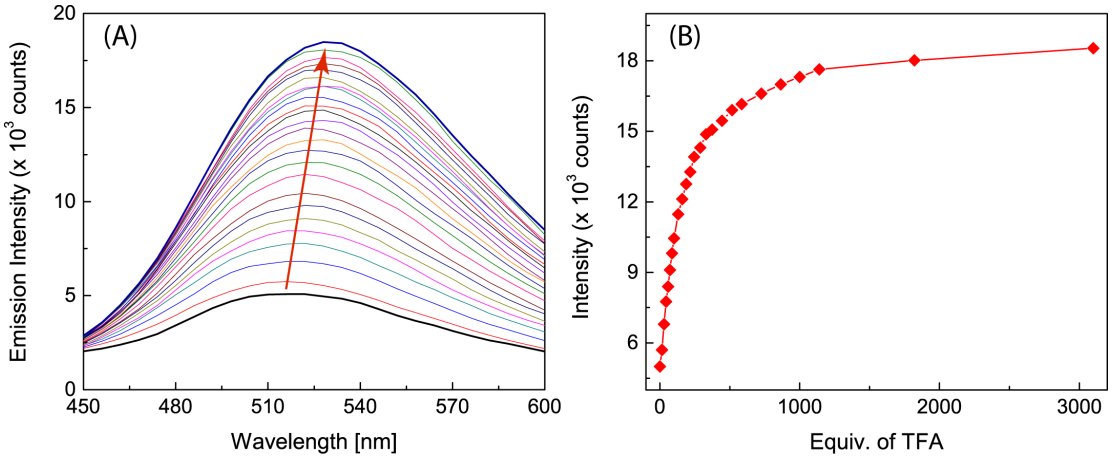

Figure 5.5: Fluorescence spectra of **5-2b** (1.49×10^{-4} M in CCl_4) in response to the addition of TFA from 0 to 3.10×10^3 molar equivalents. (B) Plot of maximum emission intensity against equivalents of TFA.

To understand the interacting between **5-2b** and TFA in the solution phase, ^{1}H NMR titration experiments were performed and the results are given in Figure 5.6. The aromatic proton signals exhibit varied degrees of shift with TFA addition, while the most significant changes can be noted in the downfield region of the spectrum. Herein the two doublets 9.63 ppm and 9.17 ppm are assigned to the aromatic protons at the 17 and 15 positions (referred to as H_{17} and H_{15}) according to DFT calculations (Figure S-21, Supporting Information). Upon addition of TFA, the imidazolyl nitrogen atom (N_{16}) is protonated since it is the most basic site in the molecule. The proposed protonation mode is also corroborated by the single-crystal structure of the complex of [**5-2b**·$(TFA)_2$] (shown in Figure S-23A, Supporting Information). Eventually, the protonation of **5-2b** with TFA leads to a substantial degree of upfield

shift of H_{17} (from 9.63 ppm to 8.95 ppm), while the signal of H_{15} is only moderately shifted from 9.17 ppm to 9.06 ppm. In the crystal structure of protonated **5-2b**, the newly formed imidazolium N-H group is much closer to H_{17} than to H_{15}. This accounts for the observation that the H_{17} signal is the most shifted after protonation. The X-ray packing diagram (Figure S-23B, Supporting Information) indicates that complexation of **5-2b** with TFA leads to highly ordered supramolecular assemblies. It is therefore reasonable to propose that addition of TFA to the solution of **5-2b** could also enhance intermolecular interactions, which facilitate excimer formation and increase fluorescence emission.

In summary, we have discovered a straightforward synthetic method to construct polycyclic aromatic structures based on 6*H*-phenanthro [4,5-*cde*] pyreno[4',5':4,5] imidazo[1,2-*a*]azepin-6-one. Interesting solvatofluorochromic, mechanofluorochromic, and acidochromic fluorescence properties were observed for this new class of pyrene-based organic fluorophores, and the origins of these fluorescence behaviors can be attributed to excimer/monomer equilibria. Our findings open a new avenue for the development of pyrene-based luminescent materials with potential applications in advanced molecular optoelectronics.

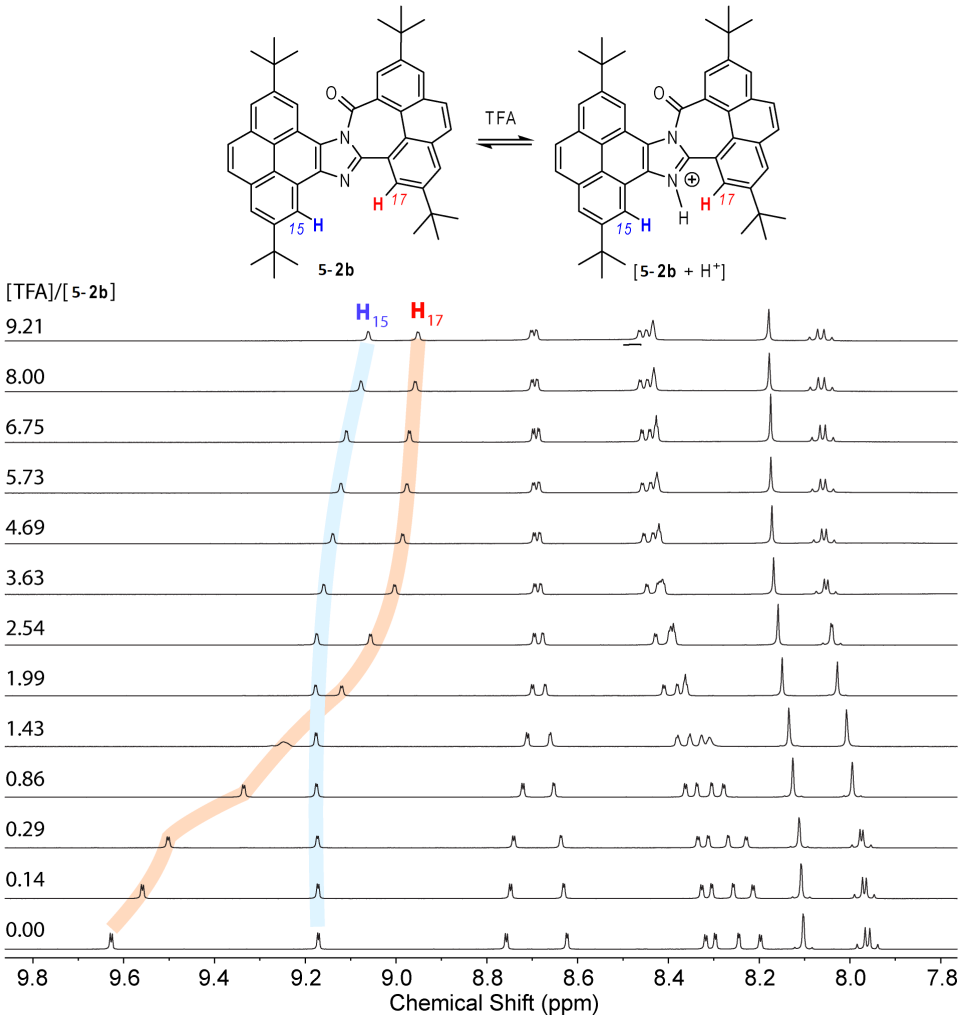

Figure 5.6: ^{1}H NMR spectra of **5-2b** (6.41×10^{-3} M in CD_2Cl_2) in response to the addition of TFA from 0 to 9.21 molar equivalents. Signals of protons at the 15 and 17 positions are highlighted.

Chapter 6

Conclusions

In this PhD thesis, four projects were successfully accomplished, in which novel π-conjugated oligomers, polymers, and polycyclic aromatic hydrocarbons (PAHs) were prepared through advanced organic synthesis and characterized by various spectroscopic techniques and electrochemical analysis. A large portion of the synthetic work in the first and second projects utilized the well-known Suzuki-Miyaura cross-coupling reaction as an efficient methodology to prepare functional molecular building blocks, based on which complex polymeric and macromolecular systems were constructed through stepwise synthesis. In addition, a phosphite-promoted olefination reaction was used as another important synthetic tool in this thesis to prepare various DTF derivatives. Synthetically, functionalization of DTF groups to a π-conjugated system can be readily achieved by reacting an aldehyde or ketone precursor with a 1,3-dithio-2-thione counterpart in the presence of trialkylphosphite (e.g., $P(OMe)_3$, $P(OEt)_3$) at elevated temperature, and the reaction yields were generally good. In the functionalization of pyrene-4,5-dione (K-region), however, this method gave a

relatively low yield (less than 10%). Alternatively, a two-step synthesis involving the Ramirez olefination reactions, followed by treatment with 1,3-dithio-2-thione under basic conditions was found to give a much better yield.

The unique electronic, redox, and structural properties of DTF and TTFV groups have allowed various new functional organic materials (oligomers, polymers, dendrimers, etc.) to be developed and applied in the fields of chemical sensors, molecular switches, nanoelectronic devices, and so on. In the last project described in this thesis, a novel self-condensation of pyrene is reported. This work contributes a new synthetic approach to pyrene-based functional organic fluorophores.

In terms of device application, a double-layer electropolymerization strategy was for the first time developed and tested in this thesis work (Chapter 2). The experimental results demonstrated the applicability of using fluorene-cored dendrimers that are functionalized with DTF end groups to produce highly sensitive and selective polymer thin film sensors for the detection of nitroaromtic explosives, such as TNT. The advantages of this double-layer method include easy preparation, high durability and tunability. It is envisioned that selective electrochemical thin film sensors would be attainable through this method by using other rationally designed DTF-functionalized building blocks as precursors for the electropolymerization. In addition to the fluorene-cored poly(DTF) derivatives, this thesis work also explored a new family of pyrene-cored multi-DTF derivatives (Chapter 3). The electronic and redox activity of these new compounds were found to show strong dependence on the substitution patterns of the DTF groups. Some of the multi-DTF-pyrene compounds can be electrochemically polymerized to form redox-active thin films. Their applicability in electrochemical devices is currently under investigation. The

observation that these compounds undergo facile hydrogen/deuterium exchange reactions under aicidic conditions present a potential approach to develop efficient deuterium traps that could be useful in isotope labelling.

Besides redox-active DTF derivatives, this thesis work also deals with new pyrene derivatives, particularly K-region functionalized pyrenes (Chapter 4). Three new pyrene derivatives were prepared through olefination reactions of pyrene-4,5-dione, which is a readily available precursor. The electronic and electrochemical redox properties of these pyrene derivatives were characterized and compared, while their molecular structural and crystalline packing properties were investigated by single-crystal X-ray analysis in conjunction with density functional theory (DFT) calculations. The findings disclosed in this work are beneficial to developing pyrene-based organic solid materials for advanced optoelectronic applications. Of particular note is the relatively narrow band gap of dithiole substituted pyrene may lead to further application in small-molecule semiconductors and related electronic devices.

In this thesis work, the most significant contribution to synthetic methodology is the self-condensation reaction of pyrene-4,5-dione (Chapter 5), which can be useful for the preparation π-extended pyrene-based organic fluorophores. Comparative studies showed that the rigid pyrene backbone plays a key role in the self-condensation reaction mechanism, while the observation of solvatochromic effects and the acidofluorometric behavior of these compounds points to their potential application in fluorescence sensing and bio-imaging.

Chapter 7

Future Work

In addition to the research projects described in Chapters 2 to 5, this PhD research has also investigated a range of π-conjugated molecules and oligomers, which are expected to possess novel electronic, photophysical, and electrochemical properties. Due to time limitation, these studies are either recently initiated or ongoing. Although the results of these projects are still premature, they have indeed shown promising potential and are therefore worth further investigation. This chapter provides a brief description of these preliminary studies, based on which future research directions are suggested.

Pyrenoimidazolyl-Functionalized Conjugated Oligomers and Dendrimers

The synthesis of 4,4'-((9*H*-fluoren-9-ylidene)methylene)dibenzaldehyde compound **7-1** was conducted through the Suzuki-Miyaura cross-coupling reaction in a good yield of 82%. In the next step, pyrene-4,5-dione **7-2** and dialdehyde **7-1** were mixed with

ammonium acetate in glacial acetic acid. The mixture was stirred and heated at 100°C for 3 h to undergo a condensation reaction, affording compound **7-3** in 80% yield (Scheme 7.1). The structure and purity of **7-3** have been confirmed by ^{1}H NMR analysis.

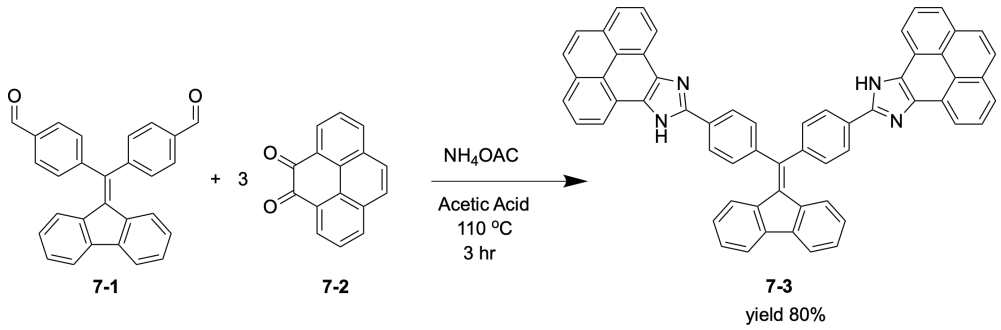

Scheme 7.1: The synthesis of fluorene-pyrenoimidazole **7-3**.

Under the same condensation conditions, the reaction between 2,7-bis(*t*-butyl)pyrene-4,5-dione (**7-4**) and compound (**7-1**) yielded a mono-condensation product **7-5** in 50% yield. This reaction certainly deserves further exploration to understand why only the mono-condensation product was isolated. The possibility to generate a double-condensation product may exist through tuning the reaction time, temperature and the ratios of starting materials. On the other hand, the aldehyde group in compound **7-5** presents new opportunities to attach other functional groups to generate more π-extended structures as well as bring about new optoelectronic properties. For the future work, it is suggested to focus on the functionalization of compound **7-5** (Scheme 7.2) with a DTF group through the olefination method. The resulting compound is anticipated to show redox-activity and may yield new TTFV derivatives with redox-sensitive fluorescence behavior.

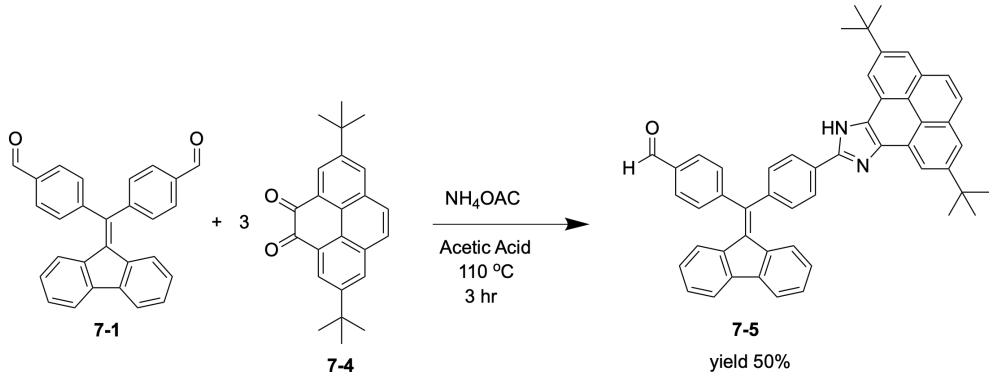

Scheme 7.2: The synthesis of fluorene-pyrenoimidazole **7-5**.

An anthraquinodimethane-cored tetraaldehyde **7-6** was prepared and then subjected to condensation with pyrene-4,5-dione (Scheme 7.3). The reaction yielded a tetrakis(pyrenoimidazolyl)-substituted compound **7-7** in a very good yield (82%). The molecular structure of **7-7** was confirmed by ^{1}H NMR analysis.

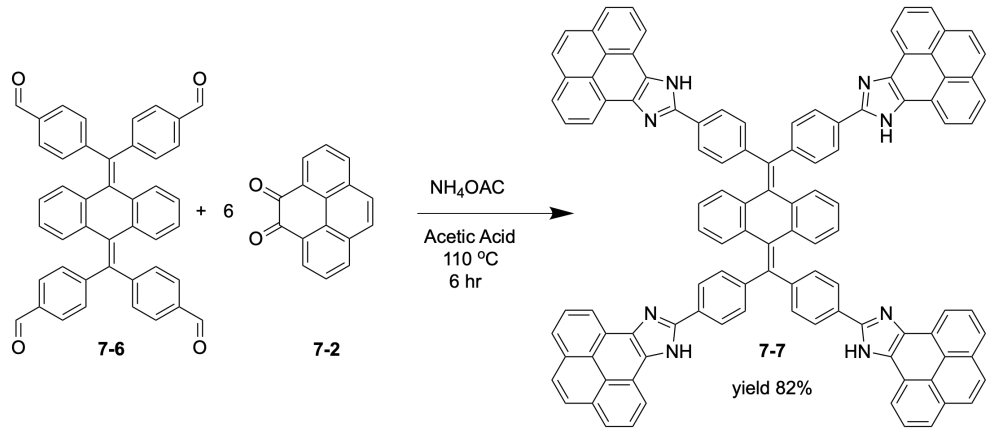

Scheme 7.3: The synthesis of pyrenoimidazolyl dendrimer **7-7**.

In an effort to develop pyrenoimidazolyl-functionalized dendrimers, compounds **7-8** and **7-9** were synthesized as outlined in Scheme 7.4. Although this work is only in the preliminary stages, however, it is envisioned that the pyrenoimidazolyl dendrimers derived from these compounds should show enhanced fluorescence and

intriguing solid-state packing properties. Hydrogen bonding interactions among the multiple imidazolyl units may dictate the formation of 3-dimensional supramolecular self-assemblies with defined cavity and/or microporosity beneficial for highly sensitive fluorescence sensing.

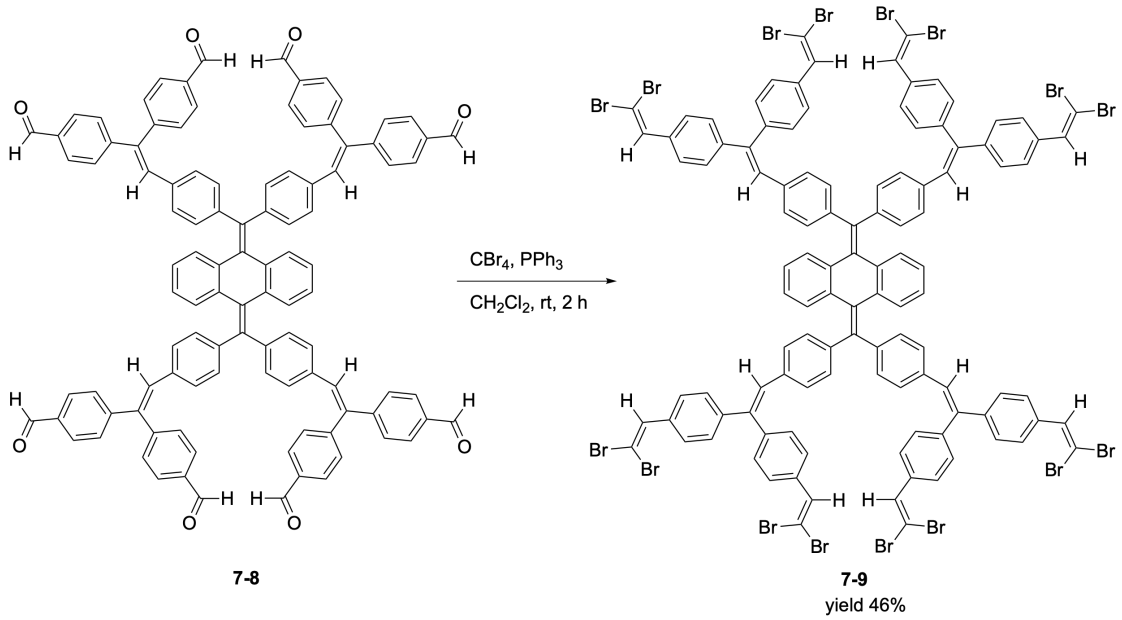

Scheme 7.4: The synthesis of hexadecabromide precursor **7-9**.

Synthesis of DTF-functionalized Ionic Liquids

In a recent collaborative project with Prof. Stockmann's group at the Department of Chemistry, Memorial University, a series of DTF-functionalized ionic liquids was targeted in order to investigate their electron transfer behavior with Au(III) on the surface of an electrode. To get this project underway, two DTF compounds with bromoalkyl tails (**7-15** and **7-16**) were prepared. They were synthesized through the steps described in Scheme 7.5 and Scheme 7.6.

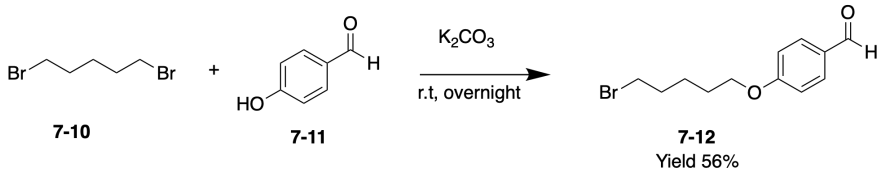

Scheme 7.5: The synthesis of compound **7-12**.

The bromo groups in the two DTF compounds are anticipated to provide synthetic handles, allowing imidazolium or phosphonium groups to be installed. The resulting ionic liquids are expected to induce the formation of gold nanoparticles through DTF reduction and to act as capping agents to stabilize the nanoparticles. Furthermore, the redox-properties of the DTF groups should enhance electron and charge transfers among gold nanoparticles, leading to appealing applications in nanoscale electronic devices. Continued synthesis and characterization of DTF-functionalized ionic liquids are expected to foster a fruitful interdisciplinary collaboration between the Stockmann and Zhao groups.

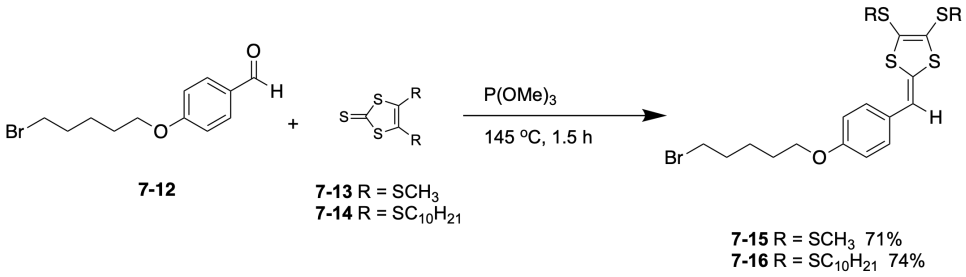

Scheme 7.6: The synthesis of DTF compounds **7-15** and **7-16**.

The ^{1}HNMR spectra of the above-mentioned new compounds are given in the Appendix.

Bibliography

[1] Bryce, M. R.; Murphy, L. C. Organic metals. *Nature* **1984**, 119–126.

[2] Jørgensen, T.; Hansen, T. K.; Becher, J. Tetrathiafulvalenes as building-blocks in supramolecular chemistry. *Chem. Soc. Rev.* **1994**, *23*, 41–51.

[3] Nielsen, M. B.; Lomholt, C.; Becher, J. Tetrathiafulvalenes as building blocks in supramolecular chemistry II. *Chem. Soc. Rev.* **2000**, *29*, 153–164.

[4] Bryce, M. R. Functionalised tetrathiafulvalenes: new applications as versatile π-electron systems in materials chemistry. *J. Mater. Chem.* **2000**, *10*, 589–598.

[5] Iyoda, M.; Hasegawa, M.; Miyake, Y. Bi-TTF, bis-TTF, and related TTF oligomers. *Chem. Rev.* **2004**, *104*, 5085–5114.

[6] Pérez, E. M.; Illescas, B. M.; Herranz, M. ; Martín, N. Supramolecular chemistry of π-extended analogues of TTF and carbon nanostructures. *New J. Chem.* **2009**, *33*, 228–234.

[7] Martín, N. Tetrathiafulvalene: the advent of organic metals. *Chem. Commun.* **2013**, *49*, 7025–7027.

[8] Bendikov, M.; Wudl, F.; Perepichka, D. F. Tetrathiafulvalenes, oligoacenenes, and their buckminsterfullerene derivatives: the brick and mortar of organic electronics. *Chem. Rev.* **2004**, *104*, 4891–4946.

[9] Wudl, F.; Smith, G. M.; Hufnagel, E. J. Bis-1,3-dithiolium chloride: an unusually stable organic radical cation. *J. Chem. Soc. D* **1970**, 1453–1454.

[10] Rovira, C. Bis(ethylenethio)tetrathiafulvalene (BET-TTF) and related dissymmetrical electron donors: from the molecule to functional molecular materials and devices (OFETs). *Chem. Rev.* **2004**, *104*, 5289–5318.

[11] Yamada, J.; Sugimoto, T. *TTF Chemistry: Fundamentals and Applications of Tetrathiafulvalene*; Springer Berlin Heidelberg, 2004.

[12] Canevet, D.; Sallé, M.; Zhang, G.; Zhang, D.; Zhu, D. Tetrathiafulvalene (TTF) derivatives: key building-blocks for switchable processes. *Chem. Commun.* **2009**, 2245–2269.

[13] Segura, J. L.; Martín, N. New Concepts in tetrathiafulvalene chemistry. *Angew. Chem. Int. Ed. 40*, 1372–1409.

[14] Blanchard, P.; Sallé, M.; Duguay, G.; Jubault, M.; Gorgues, A. 2-Mono or 2,3-Bis(hydroxymethyl)-6,7-ethylenedithio-tetrathiafulvalenes: New potential precursors of organic metals endowed with hydrogen bonds. *Tetrahedron Lett.* **1992**, *33*, 2685–2688.

[15] Carlier, R.; Hapiot, P.; Lorcy, D.; Robert, A.; Tallec, A. Electrosynthesis and

redox behavior of vinylogous TTF displaying strong conformational changes associated with electron transfers. *Electrochim. Acta* **2001**, *46*, 3269–3277.

[16] Logtenberg, H.; van der Velde, J. H. M.; de Mendoza, P.; Areephong, J.; Hjelm, J.; Feringa, B. L.; Browne, W. R. Electrochemical switching of conductance with diarylethene-based redox-active polymers. *J. Phys. Chem. C* **2012**, *116*, 24136–24142.

[17] Chen, G.; Mahmud, I.; Dawe, L. N.; Zhao, Y. Acetylenic phenyldithiafulvene: a versatile synthon for TTFV-Based macromolecules. *Org. Lett.* **2010**, *12*, 704–707.

[18] Solovyeva, V.; Keller, K.; Huth, M. Organic charge transfer phase formation in thin films of the BEDT-TTF/TCNQ donor–acceptor system. *Thin Solid Films* **2009**, *517*, 6671–6676.

[19] Massue, J.; Ghilane, J.; Bellec, N.; Lorcy, D.; Hapiot, P. Facile electrochemical generation of polyoxyethyl-vinylogous tetrathiafulvalene films. *Electrochem. Commun.* **2007**, *9*, 677–682.

[20] Simonsen, K. B.; Becher, J. Tetrathiafulvalene thiolates: important synthetic building blocks for macrocyclic and supramolecular chemistry. *Synlett* **1997**, 1211–1220.

[21] Bryce, M. R. Current trends in tetrathiafulvalene chemistry: towards increased dimensionality. *J. Mater. Chem.* **1995**, *5*, 1481–1496.

[22] Tseng, H.-R.; Vignon, S. A.; Stoddart, J. F. Toward chemically controlled nanoscale molecular machinery. *Angew. Chem. Int. Ed.* **2003**, *42*, 1491–1495.

[23] Batail, P. Introduction: molecular conductors. *Chem. Rev.* **2004**, *104*, 4887–4890.

[24] Sarhan, A. E.-W. A. Synthesis and applications of tetrathiafulvalenes and ferrocene-tetrathiafulvalenes and related compounds. *Tetrahedron* **2005**, *61*, 3889–3932.

[25] Kitamura, T.; Nakaso, S.; Mizoshita, N.; Tochigi, Y.; Shimomura, T.; Moriyama, M.; Ito, K.; Kato, T. Electroactive supramolecular self-assembled fibers comprised of doped tetrathiafulvalene-based gelators. *J. Am. Chem. Soc.* **2005**, *127*, 14769–14775.

[26] Zheng, Y. B.; Yang, Y.-W.; Jensen, L.; Fang, L.; Juluri, B. K.; Flood, A. H.; Weiss, P. S.; Stoddart, J. F.; Huang, T. J. Active molecular plasmonics: controlling plasmon resonances with molecular switches. *Nano Lett.* **2009**, *9*, 819–825.

[27] Bernhardt, P. V.; Moore, E. G. Functionalized macrocyclic compounds: potential sensors of small molecules and ions. *Austral. J. Chem.* **2003**, *56*, 239–258.

[28] Hansen, T. K.; Joergensen, T.; Stein, P. C.; Becher, J. Crown ether derivatives of tetrathiafulvalene. 1. *J. Org. Chem.* **1992**, *57*, 6403–6409.

[29] Johnston, B.; Goldenberg, L. M.; Bryce, M. R.; Kataky, R. A tetrathiafulvalene

derivative with an acyclic S4 domain as a voltammetric silver sensor. *J. Chem. Soc., Perkin Trans. 2* **2000**, 189–190.

[30] Lyskawa, J.; Le Derf, F.; Levillain, E.; Mazari, M.; Sallé, M.; Dubois, L.; Viel, P.; Bureau, C.; Palacin, S. Univocal demonstration of the electrochemically mediated binding of Pb^{2+} by a modified surface incorporating a TTF-Based redox-switchable ligand. *J. Am. Chem. Soc.* **2004**, *126*, 12194–12195.

[31] Zhao, B. T.; Blesa, M.-J.; Mercier, N.; Le Derf, F.; Sallé, M. Bis-calix[4]arenes bridged by an electroactive tetrathiafulvalene unit. *J. Org. Chem.* **2005**, *70*, 6254–6257.

[32] Blesa, M.-J.; Zhao, B.-T.; Allain, M.; Le Derf, F.; Sallé, M. Bis(calixcrown)tetrathiafulvalene receptors. *Chem. Eur. J.* **2006**, *12*, 1906–1914.

[33] Li, X.; Zhang, G.; Ma, H.; Zhang, D.; Li, J.; Zhu, D. 4,5-Dimethylthio-4'-[2-(9-anthryloxy)ethylthio]tetrathiafulvalene, a highly selective and sensitive chemiluminescence probe for singlet oxygen. *J. Am. Chem. Soc.* **2004**, *126*, 11543–11548.

[34] Zhang, G.; Li, X.; Ma, H.; Zhang, D.; Li, J.; Zhu, D. A selective and sensitive chemiluminescence reaction of 4,4'5'-bis[2-(9-anthryloxy) ethylthio] tetrathiafulvalene with singlet oxygen. *Chem. Commun.* **2004**, 2072–2073.

[35] Sies, H. Biochemistry of oxidative stress. *Angew. Chem. Int. Ed. Engl.* **1986**, *25*, 1058–1071.

[36] Devasagayam, T. P. A.; Kamat, J. P. Biological significance of singlet oxygen. *Indian J. Exp. Biol.* **2002**, *40*, 680—692.

[37] Wang, Z.; Zhang, D.; Zhu, D. A new saccharide sensor based on a tetrathiafulvalene-anthracene dyad with a boronic acid group. *J. Org. Chem.* **2005**, *70*, 5729–5732.

[38] Tan, W.; Wang, Z.; Zhang, D.; Zhu, D. A new Saccharides and nnucleosides sensor based on tetrathiafulvalene-anthracene dyad with two boronic acid groups. *Sensors* **2006**, *6*, 954–961.

[39] Zhang, Y.; Cai, L.-Z.; Wang, C.-Y.; Lai, G.-Q.; Shen, Y.-J. Synthesis and properties of a tetrathiafulvalene-perylene tetracarboxylic diimide-tetrathiafulvalene dyad. *New J. Chem.* **2008**, *32*, 1968–1973.

[40] Zhang, X.; Wang, C.; Lai, G.; Zhang, L.; Shen, Y. Conjugated ethynylene-fluorene polymers with electro-donating TTF as pendant groups: Synthesis, electrochemical, and spectroscopic properties. *New J. Chem.* **2010**, *34*, 318–324.

[41] Zhou, Y.; Zhang, D.; Zhu, L.; Shuai, Z.; Zhu, D. Binaphthalene molecules with tetrathiafulvalene units: CD spectrum modulation and new chiral molecular switches by reversible oxidation and reduction of tetrathiafulvalene units. *J. Org. Chem.* **2006**, *71*, 2123–2130.

[42] Setnička, V.; Urbanová, M.; Bouř, P.; Král, V.; Volka, K. Vibrational circular dichroism of 1,1‘-binaphthyl derivatives:experimental and theoretical study. *J. Phys. Chem. A* **2001**, *105*, 8931–8938.

[43] Nielsen, K. A.; Levillain, E.; Lynch, V. M.; Sessler, J. L.; Jeppesen, J. O. Tetrathiafulvalene porphyrins. *Chem. Eur. J.* **2009**, *15*, 506–516.

[44] Huang, T. J.; Brough, B.; Ho, C.-M.; Liu, Y.; Flood, A. H.; Bonvallet, P. A.; Tseng, H.-R.; Stoddart, J. F.; Baller, M.; Magonov, S. A nanomechanical device based on linear molecular motors. *Appl. Phys. Lett.* **2004**, *85*, 5391–5393.

[45] Nguyen, T. D.; Tseng, H.-R.; Celestre, P. C.; Flood, A. H.; Liu, Y.; Stoddart, J. F.; Zink, J. I. A reversible molecular valve. *PNAS* **2005**, *102*, 10029–10034.

[46] Kao, J.; Eyermann, C.; Southwick, E.; Leister, D. A systematic approach to calculate molecular properties of organosulfur compounds containing the carbon-sulfur (Csp^2-S) bond. *J. Am. Chem. Soc.* **1985**, *107*, 5323–5332.

[47] Benassi, R.; Taddei, F. Ground-state molecular stabilization of substituted ethylenes. A theoretical mo ab-initio thermochemical study. *J. Mol. Struct.: Theochem* **2001**, *572*, 169–183.

[48] Nielsen, M. B.; Sauer, S. P. On the aromaticity of tetrathiafulvalene cations. *Chem. Phys. Lett.* **2008**, *453*, 136–139.

[49] Brunetti, F. G.; López, J. L.; Atienza, C.; Martín, N. π-Extended TTF: a versatile molecule for organic electronics. *J. Mater. Chem.* **2012**, *22*, 4188–4205.

[50] Kirmse, W.; Horner, L. Über lichtreaktionen VIII. photolyse von 1.2.3-Thiodiazolen. *J. Lieb. Annal. der Chem.* **1958**, *614*, 4–18.

[51] Hartzler, H. D. 2-Benzylidene-1,3-dithioles. Remarkably rapid Wittig reaction. *J. Am. Chem. Soc.* **1971**, *93*, 4961–4962.

[52] Sato, M.; Gonnella, N. C.; Cava, M. P. Synthesis and reactions of (4,5-dicarbomethoxy-1,3-dithiolyl)tributylphosphonium tetrafluoroborate. *J. Org. Chem.* **1979**, *44*, 930–934.

[53] Christensen, C. A.; Batsanov, A. S.; Bryce, M. R. Thiolated π-extended tetrathiafulvalenes: versatile multifunctional π-systems. *J. Org. Chem.* **2007**, *72*, 1301–1308.

[54] Mizuno, M.; Cava, M. P. Organic metals. A study of the Hurtley-Smiles tetrathiafulvalene synthesis. *J. Org. Chem.* **1978**, *43*, 416–418.

[55] Gimbert, Y.; Moradpour, A.; Dive, G.; Dehareng, D.; Lahlil, K. A variable mechanism for the nucleophilic vinylic substitutions in a series of gem-dihalogenated alkenes by a bidentate sulfur nucleophile: an experimental and AM1 theoretical study. *J. Org. Chem.* **1993**, *58*, 4685–4690.

[56] Giguère, J.-B.; Morin, J.-F. Superextended tetrathiafulvalene: synthesis, optoelectronic properties, fullerenes complexation, and photooxidation study. *J. Org. Chem.* **2015**, *80*, 6767–6775.

[57] Broman, S. L.; Andersen, C. L.; Jousselin-Oba, T.; Mansø, M.; Hammerich, O.; Frigoli, M.; Nielsen, M. B. Tetraceno[2,1,12,11-opqra]tetracene-extended tetrathiafulvalene redox-controlled generation of a large PAH core. *Org. Biomol. Chem.* **2017**, *15*, 807–811.

[58] Parg, R. P.; Kilburn, J. D.; Ryan, T. G. A one-step synthesis of 1,3-dithiol-2-ylphosphonate esters from 1,3-dithiole-2-thiones. *Synthesis* **2002**, 195–198.

[59] Ohta, A.; Yamashita, Y. Oxidative intramolecular cyclization of 2,2'-bis(1,4-dithiafulven-6-yl)3,3'-bithienyls affording novel bis(1,3-dithiole) electron donors. *J. Chem. Soc., Chem. Commun.* **1995**, 1761–1762.

[60] Yamashita, Y.; Tomura, M.; Badruz Zaman, M. Synthesis and properties of novel tetrathiafulvalene vinylogues. *Chem. Commun.* **1998**, 1657–1658.

[61] Müller, H.; Salhi, F.; Divisia-Blohorn, B. Bis-substituted tetrathiapentalenes — novel building blocks for extended tetrathiafulvalenes and conducting polymers. *Tetrahedron Lett.* **1997**, *38*, 3215–3218.

[62] Massue, J.; Bellec, N.; Guerro, M.; Bergamini, J.-F.; Hapiot, P.; Lorcy, D. Crown ether vinylogous tetrathiafulvalene receptors: complexation interference on the molecular movements triggered by electron transfer. *J. Org. Chem.* **2007**, *72*, 4655–4662.

[63] Lakshmikantham, M. V.; Cava, M. P.; Carroll, P. J. Novel oxidative rearrangement of xylene-diylidenebis(4,5-dicarbomethoxy-1,3-dithiole). *J. Org. Chem.* **1984**, *49*, 726–728.

[64] Frère, P.; Gorgues, A.; Jubault, M.; Riou, A.; Gouriou, Y.; Roncali, J. Electrochemically induced intramolecular cyclization of 1,2-bis(1,4-dithiafulven-6-yl)benzenes. *Tetrahedron Lett.* **1994**, *35*, 1991–1994.

[65] Guerro, M.; Roisnel, T.; Pellon, P.; Lorcy, D.

Redox-active dithiafulvenyldiphenylphosphine as a mono- or bidentate ligand: intramolecular coupling reaction in the coordination sphere of a metal carbonyl fragment. *Inorg. Chem.* **2005**, *44*, 3347–3355.

[66] Guerro, M.; Pham, N. H.; Massue, J.; Bellec, N.; Lorcy, D. New redox active ligands involving a tetrathiafulvalene vinylogue backbone. *Tetrahedron* **2008**, *64*, 5285–5290.

[67] Gontier, E.; Bellec, N.; Brignou, P.; Gohier, A.; Guerro, M.; Roisnel, T.; Lorcy, D. Pyridyldithiafulvenes as precursors of coordination-driven self-assembled redox active macrocycle. *Org. Lett.* **2010**, *12*, 2386–2389.

[68] Benahmed-Gasmi, A.; Frère, P.; Roncali, J.; Elandaloussi, E.; Orduna, J.; Garin, J.; Jubault, M.; Gorgues, A. Oxidative dimerization of 2-(1,4-dithiafulven-6-yl)thiophenes: an alternative route towards extensively π-conjugated tetrathiafulvalene analogs. *Tetrahedron Lett.* **1995**, *36*, 2983–2986.

[69] Lorcy, D.; Carlier, R.; Robert, A.; Tallec, A.; Le Magueres, P.; Ouahab, L. Electrochemical synthesis of extended TTF. *J. Org. Chem.* **1995**, *60*, 2443–2447.

[70] Hascoat, P.; Lorcy, D.; Robert, A.; Carlier, R.; Tallec, A.; Boubekeur, K.; Batail, P. Formation of attractive π-redox cyclophanes. *J. Org. Chem.* **1997**, *62*, 6086–6089.

[71] Hapiot, P.; Lorcy, D.; Tallec, A.; Carlier, R.; Robert, A. Mechanism of dimerization of 1,4-dithiafulvenes into TTF vinylogues. *J. Phys. Chem.* **1996**, *100*, 14823–14827.

[72] F. Abdollahi, M.; Zhao, Y. Recent advances in dithiafulvenyl-functionalized organic conjugated materials. *New J. Chem.* **2020**, *44*, 4681–4693.

[73] Guerro, M.; Lorcy, D. A simple route to novel functionalized tetrathiafulvalene vinylogues. *Tetrahedron Lett.* **2005**, *46*, 5499–5502.

[74] Lakshmikantham, M. V.; Cava, M. P. Some novel transformations of 1,4-dithiafulvenes. *J. Org. Chem.* **1981**, *46*, 3246–3249.

[75] Sarhan, A. A. O.; Bolm, C. Iron(iii) chloride in oxidative C—C coupling reactions. *Chem. Soc. Rev.* **2009**, *38*, 2730–2744.

[76] Spies, H.; Gewald, K.; Mayer, R. Zur reaktion von natriumphenylacetylid mit schwefel oder selen und heterokumulenen. *J. Praktische Chem.* **1971**, *313*, 804–810.

[77] Mulla, K.; Zhao, Y. When dithiafulvenyl functionalized π-conjugated oligomers meet fullerenes and single-walled carbon nanotubes. *J. Mater. Chem. C* **2013**, *1*, 5116–5127.

[78] Fu, H.; Zhao, B.; Zhu, W. Elemental iodine mediated synthesis of thiadiazole-based dithiafulvalene donors via C(sp^2)–S formation. *Tetrahedron Lett.* **2019**, *60*, 124–128.

[79] Wang, Y.; Zhao, Y. Dithiafulvenyl-substituted phenylacetylene derivatives: synthesis and structure–property–reactivity relationships. *Org. Biomol. Chem.* **2015**, *13*, 9575–9579.

[80] Wang, C.; Flinn, C.; Zhao, Y. Intramolecular alkyne–dithiolium cycloaddition: a joint experimental and DFT mechanistic study. *RSC Adv.* **2017**, *7*, 36623–36631.

[81] Alévêque, O.; Leriche, P.; Cocherel, N.; Frère, P.; Cravino, A.; Roncali, J. Star-shaped conjugated systems derived from dithiafulvenyl-derivatized triphenylamines as active materials for organic solar cells. *Solar Energy Mater. Solar Cells* **2008**, *92*, 1170–1174.

[82] Guo, K.; Yan, K.; Lu, X.; Qiu, Y.; Liu, Z.; Sun, J.; Yan, F.; Guo, W.; Yang, S. dithiafulvenyl unit as a new donor for high-efficiency dye-sensitized solar cells: synthesis and demonstration of a family of metal-free organic sensitizers. *Org. Lett.* **2012**, *14*, 2214–2217.

[83] Wu, Y.; Zhang, Q.; Li, J.; Tian, X.; Li, D.; Lu, X.; Xu, B.; Wu, Y.; Guo, K. Regulation of dithiafulvene-based molecular shape and aggregation on TiO_2 for high efficiency dye-sensitized solar cells. *J. Mater. Chem. C* **2019**, *7*, 1974–1981.

[84] Wu, M.; Li, J.; Zhang, R.; Tian, X.; Han, Z.; Lu, X.; Guo, K.; Liu, Z.; Wang, Z. Synthesis and properties of dithiafulvenyl functionalized spiro(fluorene-9,9'-xanthene) molecules. *Org. Lett.* **2018**, *20*, 780–783.

[85] Bumm, L.; Arnold, J.; Cygan, M.; Dunbar, T.; Burgin, T.; Jones, L. Are single molecular wires conducting? *Science* **1996**, *271*, 1705–1707.

[86] Yaliraki, S.; Kemp, M.; Ratner, M. A. Conductance of molecular wires: influence of molecule- electrode binding. *J. Am. Chem. Soc.* **1999**, *121*, 3428–3434.

[87] Leary, E.; La Rosa, A.; González, M. T.; Rubio-Bollinger, G.; Agraït, N.; Martín, N. Incorporating single molecules into electrical circuits. The role of the chemical anchoring group. *Chem. Soc. Rev.* **2015**, *44*, 920–942.

[88] Perrin, M. L.; Burzurí, E.; van der Zant, H. S. J. Single-molecule transistors. *Chem. Soc. Rev.* **2015**, *44*, 902–919.

[89] Xiang, D.; Wang, X.; Jia, C.; Lee, T.; Guo, X. Molecular-scale electronics: from concept to function. *Chem. Rev.* **2016**, *116*, 4318–4440.

[90] Sørensen, J. K.; Vestergaard, M.; Kadziola, A.; Kilså, K.; Nielsen, M. B. Synthesis of oligo(phenyleneethynylene)-tetrathiafulvalene cruciforms for molecular electronics. *Org. Lett.* **2006**, *8*, 1173–1176.

[91] Vestergaard, M.; Jennum, K.; Sørensen, J. K.; Kilså, K.; Nielsen, M. B. Synthesis and characterization of cruciform-conjugated molecules based on tetrathiafulvalene. *J. Org. Chem.* **2008**, *73*, 3175–3183.

[92] Jennum, K.; Vestergaard, M.; Pedersen, A. H.; Fock, J.; Jensen, J.; Santella, M.; Led, J. J.; Kilså, K.; Bjørnholm, T.; Nielsen, M. B. Synthesis of oligo (phenyleneethynylene)s with vertically disposed tetrathiafulvalene units. *Synthesis* **2011**, 539–548.

[93] Jennum, K.; Nielsen, M. B. Tetrathiafulvalene-based cruciform molecules. *Chem. Lett.* **2011**, *40*, 662–667.

[94] Schou, S. S.; Parker, C. R.; Lincke, K.; Jennum, K.; Vibenholt, J.; Kadziola, A.;

Nielsen, M. B. On the phosphite-mediated synthesis of dithiafulvenes and π-extended tetrathiafulvalenes. *Synlett* **2013**, *24*, 231–235.

[95] Wei, Z. et al. Molecular heterojunctions of oligo(phenylene ethynylene)s with linear to cruciform framework. *Adv. Funct. Mater.* **2015**, *25*, 1700–1708.

[96] Parker, C. R. et al. A comprehensive study of extended tetrathiafulvalene cruciform molecules for molecular electronics: synthesis and electrical transport measurements. *J. Am. Chem. Soc.* **2014**, *136*, 16497–16507.

[97] Lissau, H.; Frisenda, R.; Olsen, S. T.; Jevric, M.; Parker, C. R.; Kadziola, A.; Hansen, T.; van der Zant, H. S. J.; Brøndsted Nielsen, M.; Mikkelsen, K. V. Tracking molecular resonance forms of donor-acceptor push-pull molecules by single-molecule conductance experiments. *Nature Commun.* **2015**, *6*, 10233–10240.

[98] Khadem, M.; Walsh, J. C.; Bodwell, G. J.; Zhao, Y. A macrocyclization of 1,8-Bis(dithiafulvenyl)pyrenes. *Org. Lett.* **2016**, *18*, 2403–2406.

[99] Khadem, M.; Zhao, Y. Multivalent dithiafulvenyl functionalization of dendritic oligo(phenylene vinylene)s with an anthraquinodimethane core. *Chem. Commun.* **2017**, *53*, 1821–1824.

[100] Iijima, S. Growth of carbon nanotubes. *Mater. Sci. Eng.: B* **1993**, *19*, 172–180.

[101] Yamabe, T.; Fukui, K.; Tanaka, K. *The science and technology of carbon nanotubes*; Elsevier, 1999.

[102] Bethune, D.; Kiang, C. H.; De Vries, M.; Gorman, G.; Savoy, R.; Vazquez, J.; Beyers, R. Cobalt-catalysed growth of carbon nanotubes with single-atomic-layer walls. *Nature* **1993**, *363*, 605–607.

[103] Dresselhaus, G.; Riichiro, S., et al. *Physical properties of carbon nanotubes*; World scientific, 1998.

[104] Endo, M.; Iijima, S.; Dresselhaus, M. S. *Carbon nanotubes*; Elsevier, 2013.

[105] Ebbesen, T. W. *Carbon nanotubes: preparation and properties*; CRC press, 1996.

[106] Fong, D.; Adronov, A. Recent developments in the selective dispersion of single-walled carbon nanotubes using conjugated polymers. *Chem. Sci.* **2017**, *8*, 7292–7305.

[107] Wang, H.; Mei, J.; Liu, P.; Schmidt, K.; Jiménez-Osés, G.; Osuna, S.; Fang, L.; Tassone, C. J.; Zoombelt, A. P.; Sokolov, A. N., et al. Scalable and selective dispersion of semiconducting arc-discharged carbon nanotubes by dithiafulvalene/thiophene copolymers for thin film transistors. *ACS Nano* **2013**, *7*, 2659–2668.

[108] Liang, S.; Chen, G.; Peddle, J.; Zhao, Y. Reversible dispersion and releasing of single-walled carbon nanotubes by a stimuli-responsive TTFV-phenylacetylene polymer. *Chem. Commun.* **2012**, *48*, 3100–3102.

[109] Liang, S.; Chen, G.; Zhao, Y. Conformationally switchable TTFV-phenylacetylene polymers: synthesis, properties, and supramolecular

interactions with single-walled carbon nanotubes. *J. Mater. Chem. C* **2013**, *1*, 5477–5490.

[110] Liang, S.; Zhao, Y.; Adronov, A. Selective and reversible noncovalent functionalization of single-walled carbon nanotubes by a pH-Responsive vinylogous tetrathiafulvalene–fluorene copolymer. *J. Am. Chem. Soc.* **2014**, *136*, 970–977.

[111] Liang, S.; Subrahmanyam, A. V.; Khadem, M.; Zhao, Y.; Adronov, A. Selective dispersion of single-walled carbon nanotubes with electron-rich fluorene-based copolymers. *RSC Adv.* **2016**, *6*, 25733–25740.

[112] Khadem, M.; Zhao, Y. Tetrathiafulvalene vinylogue-fluorene co-oligomers: synthesis, properties, and supramoleclar interactions with carbon nanotubes. *J. Org. Chem.* **2015**, *80*, 7419–7429.

[113] Khan, M. Z. H.; Alrawashdeh, A. I.; Aljohani, S.; Zhao, Y.; Lagowski, J. B. DFT investigation of the interaction between single-walled carbon nanotubes and fluorene-based conjugated oligomers. *Phys. Chem. Chem. Phys.* **2017**, *19*, 28071–28082.

[114] Aljohani, S.; Alrawashdeh, A. I.; Khan, M. Z. H.; Zhao, Y.; Lagowski, J. B. Dispersion of single-walled carbon nanotubes with oligo(p-phenylene ethynylene)s: a DFT study. *J. Phys. Chem. C.* **2017**, *121*, 4692–4702.

[115] Alrawashdeh, A. I.; Lagowski, J. B. The role of the solvent and the size of the

nanotube in the non-covalent dispersion of carbon nanotubes with short organic oligomers a DFT study. *RSC Adv.* **2018**, *8*, 30520–30529.

[116] Daniel, M.-C.; Astruc, D. Gold nanoparticles: assembly, supramolecular chemistry, quantum-size-related properties, and applications toward biology, catalysis, and nanotechnology. *Chem. Rev.* **2004**, *104*, 293–346.

[117] Zhou, Y.; Itoh, H.; Uemura, T.; Naka, K.; Chujo, Y. Preparation of π-conjugated polymer-protected gold nanoparticles in stable colloidal form. *Chem. Commun.* **2001**, 613–614.

[118] Zhou, Y.; Itoh, H.; Uemura, T.; Naka, K.; Chujo, Y. Synthesis of novel stable nanometer-sized metal (M = Pd, Au, Pt) colloids protected by a π-conjugated polymer. *Langmuir* **2002**, *18*, 277–283.

[119] Adows, H.; Zhao, Y. Redox interactions of Au(iii) with carboxylated dithiafulvenes and tetrathiafulvalene analogues in polar organic media. *Chem. Commun.* **2016**, *52*, 13101–13104.

[120] Moreno-Mañas, M.; Pleixats, R.; Andreu, R.; Garín, J.; Orduna, J.; Villacampa, B.; Levillain, E.; Sallé, M. The first 1,3-dithiol-2-ylidene donor–π–acceptor chromophores containing an azine spacer: synthesis, electrochemical and nonlinear optical properties. *J. Mater. Chem.* **2001**, *11*, 374–380.

[121] Andreu, R.; Aramburo, J.; Cerdán, M. A.; Garín, J.; Orduna, J.; Villacampa, B. Highly polarized dithiafulvenes: synthesis and nonlinear optical properties. *Tetrahedron Lett.* **2006**, *47*, 661–664.

[122] Alías, S.; Andreu, R.; Blesa, M. J.; Franco, S.; Garín, J.; Gragera, A.; Orduna, J.; Romero, P.; Villacampa, B.; Allain, M. Synthesis, structure, and optical properties of 1,4-dithiafulvene-based nonlinear optic-phores. *J. Org. Chem.* **2007**, *72*, 6440–6446.

[123] Zhou, P.; Wan, Z.; Liu, Y.; Jia, C.; Weng, X.; Xie, J.; Deng, L. Synthesis and electrochromic properties of a novel conducting polymer film based on dithiafulvenyl-triphenylamine-di(N-carbazole). *Electrochim. Acta* **2016**, *190*, 1015–1024.

[124] Guo, K.; Yang, J.; Shi, X.; Lu, X.; Cheng, J.; Wu, Y.; Guo, Y.; Wang, H. A π-extended tetrathiafulvene derivative: Synthesis and photoluminescence properties. *Mater. Chem. Phys.* **2014**, *146*, 193–197.

[125] Laurent, A. Pyrene from coal tar. *Ann. Chim. Phys* **1837**, *66*, 136–137.

[126] Vollmann, H.; Becker, H.; Corell, M.; Streeck, H. Beiträge zur kenntnis des pyrens und seiner derivate. *J. Lieb. Annal. Chem.* **1937**, *531*, 1–159.

[127] Altschuler, L.; Berliner, E. Rates of bromination of polynuclear aromatic hydrocarbons1. *J. Am. Chem. Soc.* **1966**, *88*, 5837–5845.

[128] Dewar, M. J. S.; Dennington, R. D. DEWAR-PI study of electrophilic substitution in selected polycyclic fluoranthene hydrocarbons. *J. Am. Chem. Soc.* **1989**, *111*, 3804–3808.

[129] Hites, R. A.; Simonsick Jr, W. Calculated molecular properties of polycyclic aromatic hydrocarbons. **1987**,

[130] Miyazawa, A.; Yamato, T.; Tashiro, M. Preparation of 4-alkyl-2, 7-di-tert.-butylpyrene from pyrene. *ChemInform* **1990**, *21*, 381–384.

[131] Coventry, D. N.; Batsanov, A. S.; Goeta, A. E.; Howard, J. A. K.; Marder, T. B.; Perutz, R. N. Selective Ir-catalysed borylation of polycyclic aromatic hydrocarbons: structures of naphthalene-2,6-bis(boronate), pyrene-2,7-bis(boronate) and perylene-2,5,8,11-tetra(boronate) esters. *Chem. Commun.* **2005**, 2172–2174.

[132] Oberender, F. G.; Dixon, J. A. Osmium and ruthenium tetroxide-catalyzed oxidations of pyrene1. *J. Org. Chem.* **1959**, *24*, 1226–1229.

[133] Stille, J.; Mainen, E. Thermally stable ladder polyquinoxalines. *Macromolecules* **1968**, *1*, 36–42.

[134] Young, E. R.; Funk, R. L. A practical synthesis of pyrene-4,5-dione. *J. Org. Chem.* **1998**, *63*, 9995–9996.

[135] Cho, H.; Harvey, R. G. Synthesis of "K-region" quinones and arene oxides of polycyclic aromatic hydrocarbons. *Tetrahedron Lett.* **1974**, *15*, 1491–1494.

[136] Walsh, J. C.; Williams, K.-L. M.; Lungerich, D.; Bodwell, G. J. Synthesis of pyrene-4,5-dione on a 15 g Scale. *Eur. J. Org. Chem.* **2016**, 5933–5936.

[137] Figueira-Duarte, T. M.; Müllen, K. Pyrene-based materials for organic electronics. *Chem. Rev.* **2011**, *111*, 7260–7314.

[138] Zoephel, L.; Enkelmann, V.; Muellen, K. Tuning the HOMO-LUMO gap of

pyrene effectively via donor-acceptor substitution: positions 4, 5 versus 9, 10. *Org. Lett.* **2013**, *15*, 804–807.

[139] Merz, J.; Fink, J.; Friedrich, A.; Krummenacher, I.; Al Mamari, H. H.; Lorenzen, S.; Haehnel, M.; Eichhorn, A.; Moos, M.; Holzapfel, M., et al. Pyrene molecular orbital shuffle-controlling excited state and redox properties by changing the nature of the frontier orbitals. *Chem. Eur. J.* **2017**, *23*, 13164–13180.

[140] Förster, T.; Kasper, K. Ein konzentrationsumschlag der fluoreszenz des pyrens. *Elektrochem.* **1955**, *59*, 976–980.

[141] Winnik, F. M. Photophysics of preassociated pyrenes in aqueous polymer solutions and in other organized media. *Chem. Rev.* **1993**, *93*, 587–614.

[142] Winnik, M. A.; Winnik, F. M. *Structure-property relations in polymers*; Chapter 18, pp 485–505.

[143] Goedeweeck, M.; Van der Auweraer, M.; De Schryver, F. C. Molecular dynamics of a peptide chain, studied by intramolecular excimer formation. *J. Am. Chem. Soc.* **1985**, *107*, 2334–2341.

[144] Hammarström, P.; Kalman, B.; Jonsson, B.-H.; Carlsson, U. Pyrene excimer fluorescence as a proximity probe for investigation of residual structure in the unfolded state of human carbonic anhydrase II. *FEBS lett.* **1997**, *420*, 63–68.

[145] Sahoo, D.; Weers, P. M.; Ryan, R. O.; Narayanaswami, V. Lipid-triggered

conformational switch of apolipophorin III helix bundle to an extended helix organization. *J. Mol. Biol.* **2002**, *321*, 201–214.

[146] Sahoo, D.; Narayanaswami, V.; Kay, C. M.; Ryan, R. O. Pyrene excimer fluorescence: a spatially sensitive probe to monitor lipid-induced helical rearrangement of apolipophorin III. *Biochem.* **2000**, *39*, 6594–6601.

[147] Paris, P. L.; Langenhan, J. M.; Kool, E. T. Probing DNA sequences in solution with a monomer-excimer fluorescence color change. *Nucleic Acids Res.* **1998**, *26*, 3789–3793.

[148] Lewis, F. D.; Zhang, Y.; Letsinger, R. L. Bispyrenyl excimer fluorescence: a sensitive oligonucleotide probe. *J. Am. Chem. Soc.* **1997**, *119*, 5451–5452.

[149] Yamana, K.; Iwai, T.; Ohtani, Y.; Sato, S.; Nakamura, M.; Nakano, H. Bis-pyrene-labeled oligonucleotides: sequence specificity of excimer and monomer fluorescence changes upon hybridization with DNA. *Bioconjugate Chem.* **2002**, *13*, 1266–1273.

[150] Yamana, K.; Takei, M.; Nakano, H. Synthesis of oligonucleotide derivatives containing pyrene labeled glycerol linkers: Enhhanced excimer fluorescence on binding to a complementary DNA sequence. *Tetrahedron Lett.* **1997**, *38*, 6051–6054.

[151] Tong, G.; Lawlor, J. M.; Tregear, G. W.; Haralambidis, J. Oligonucleotide-polyamide hybrid molecules containing multiple pyrene residues exhibit significant excimer fluorescence. *J. Am. Chem. Soc.* **1995**, *117*, 12151–12158.

[152] Birks, J.; Braga, C.; Lumb, M. Excimer fluorescence VI. benzene, toluene, p-xylene and mesitylene. *Proceed. Royal Soc. London A.* **1965**, *283*, 83–99.

[153] Templer, R. H.; Castle, S. J.; Curran, A. R.; Rumbles, G.; Klug, D. R. Sensing isothermal changes in the lateral pressure in model membranes using di-pyrenyl phosphatidylcholine. *Faraday Discuss.* **1999**, *111*, 41–53.

[154] Chang, J.; Lee, C.-P.; Kumar, D.; Chen, P.-W.; Lin, L.-Y.; Thomas, K. J.; Ho, K.-C. Co-sensitization promoted light harvesting for organic dye-sensitized solar cells using unsymmetrical squaraine dye and novel pyrenoimidazole-based dye. *J. Power Sources* **2013**, *240*, 779–785.

[155] Peng, Y.-X.; Dai, Y.; Wang, N.; Huang, W. Symmetrical fluorescent oligothiophene and benzene centered bispyrenoimidazole derivatives with double n-dodecyl chains showing high thermal stability. *Tetrahedron Lett.* **2014**, *55*, 5984–5987.

[156] Jadhav, T.; Dhokale, B.; Mobin, S. M.; Misra, R. Aggregation induced emission and mechanochromism in pyrenoimidazoles. *J. Mater. Chem. C* **2015**, *3*, 9981–9988.

[157] Shan, T.; Liu, Y.; Tang, X.; Bai, Q.; Gao, Y.; Gao, Z.; Li, J.; Deng, J.; Yang, B.; Lu, P.; Ma, Y. Highly efficient deep blue organic light-emitting diodes based on imidazole: significantly enhanced performance by effective energy transfer with negligible efficiency roll-off. *ACS Appl. Mater. Interf.* **2016**, *8*, 28771–28779.

[158] Tabasi, Z. A.; Younes, E. A.; Walsh, J. C.; Thompson, D. W.; Bodwell, G. J.;

Zhao, Y. Pyrenoimidazolyl-benzaldehyde fluorophores: synthesis, properties, and sensing function for fluoride anions. *ACS Omega* **2018**, *3*, 16387–16397.

[159] Moore, A. J.; Bryce, M. R. New vinylogous tetrathiafulvalene (TTF) π-electron donors. *Tetrahedron Lett.* **1992**, *33*, 1373–1376.

[160] Zhao, Y.; Chen, G.; Mulla, K.; Mahmud, I.; Liang, S.; Dongare, P.; Thompson, D. W.; Dawe, L. N.; Bouzan, S. Tetrathiafulvalene vinylogues as versatile building blocks for new organic materials. *Pure Appl. Chem.* **2012**, *84*, 1005–1025.

[161] Miao, W.; Ge, C.; Parajuli, S.; Shi, J.; Jing, X. *Trace Analysis with Nanomaterials*; Wiley-Blackwell, 2010; Chapter 7, pp 161–189.

[162] Hu, Z.; Deibert, B. J.; Li, J. Luminescent metal-organic frameworks for chemical sensing and explosive detection. *Chem. Soc. Rev.* **2014**, *43*, 5815–5840.

[163] Salinas, Y.; Martínez-Máñez, R.; Marcos, M. D.; Sancenón, F.; Costero, A. M.; Parra, M.; Gil, S. Optical chemosensors and reagents to detect explosives. *Chem. Soc. Rev.* **2012**, *41*, 1261–1296.

[164] Won, W. D.; Disalvo, L. H.; Ng, J. Toxicity and mutagenicity of 2, 4,-6-trinitrotoluene and its microbial metabolites. *Appl. Environ. Microbiol.* **1976**, *31*, 576–580.

[165] Van Beelen, P.; Burris, D. R. Reduction of the explosive 2, 4, 6-trinitrotoluene by enzymes from aquatic sediments. *Environ. Toxicol. Chem.* **1995**, *14*, 2115–2123.

[166] Reifenrath, W. G.; Kammen, H. O.; Palmer, W. G.; Major, M. M.; Leach, G. J. Percutaneous absorption of explosives and related compounds: an empirical model of bioavailability of organic nitro compounds from soil. *Toxicol. Appl. Pharmacol.* **2002**, *182*, 160–168.

[167] Adamia, G.; Ghoghoberidze, M.; Graves, D.; Khatisashvili, G.; Kvesitadze, G.; Lomidze, E.; Ugrekhelidze, D.; Zaalishvili, G. Absorption, distribution, and transformation of TNT in higher plants. *Ecotoxicol. Environ. Safety* **2006**, *64*, 136–145.

[168] Van Dillewijn, P.; Couselo, J. L.; Corredoira, E.; Delgado, A.; Wittich, R.-M.; Ballester, A.; Ramos, J. L. Bioremediation of 2, 4, 6-trinitrotoluene by bacterial nitroreductase expressing transgenic aspen. *Environ. Sci. Technol.* **2008**, *42*, 7405–7410.

[169] Wang, J. *Counterterrorist detection techniques of explosives*; Elsevier, 2007; pp 91–107.

[170] Tang, L.; Feng, H.; Cheng, J.; Li, J. Uniform and rich-wrinkled electrophoretic deposited graphene film: a robust electrochemical platform for TNT sensing. *Chem. Commun.* **2010**, *46*, 5882–5884.

[171] Chen, G.; Mahmud, I.; Dawe, L. N.; Daniels, L. M.; Zhao, Y. Synthesis and properties of conjugated oligoyne-centered π-extended tetrathiafulvalene analogues and related macromolecular systems. *J. Org. Chem.* **2011**, *76*, 2701–2715.

[172] Palma-Cando, A.; Scherf, U. Electrogenerated thin films of microporous polymer networks with remarkably increased electrochemical response to nitroaromatic analytes. *ACS Appl. Mater. Interf.* **2015**, *7*, 11127–11133.

[173] Kartha, K. K.; Sandeep, A.; Nair, V. C.; Takeuchi, M.; Ajayaghosh, A. A carbazole-fluorene molecular hybrid for quantitative detection of TNT using a combined fluorescence and quartz crystal microbalance method. *Phys. Chem. Chem. Phys.* **2014**, *16*, 18896–18901.

[174] Feng, L.-J.; Guo, J.-W.; Zhong, X.; Sun, Z.-Y. Fluorescent microporous polymeric microsphere: porosity, adsorption performance, and TNT sensing. *J. Macromol. Sci., Part A* **2014**, *51*, 706–711.

[175] Räupke, A.; Palma-Cando, A.; Shkura, E.; Teckhausen, P.; Polywka, A.; Görrn, P.; Scherf, U.; Riedl, T. Highly sensitive gas-phase explosive detection by luminescent microporous polymer networks. *Sci. Rep.* **2016**, *6*, 29118.

[176] Zhang, Q.; Yu, S.; Wang, Q.; Xiao, Q.; Yue, Y.; Ren, S. Fluorene-based conjugated microporous polymers: preparation and chemical sensing application. *Macromol. Rapid Commun.* **2017**, *38*, 1700445.

[177] Suga, T.; Ohshiro, H.; Sugita, S.; Oyaizu, K.; Nishide, H. Emerging N-type redox-active radical polymer for a totally organic polymer-based rechargeable battery. *Adv. Mater.* **2009**, *21*, 1627–1630.

[178] Reiss, P.; Couderc, E.; De Girolamo, J.; Pron, A. Conjugated polymers/semiconductor nanocrystals hybrid materials-preparation, electrical transport properties and applications. *Nanoscale* **2011**, *3*, 446–489.

[179] Rivnay, J.; Owens, R. M.; Malliaras, G. G. The rise of organic bioelectronics. *Chem. Mater.* **2014**, *26*, 679–685.

[180] Burgess, M.; Moore, J. S.; Rodríguez-López, J. Redox active polymers as soluble nanomaterials for energy storage. *Acc. Chem. Res.* **2016**, *49*, 2649–2657.

[181] Muench, S.; Wild, A.; Friebe, C.; Häupler, B.; Janoschka, T.; Schubert, U. S. Polymer-based organic batteries. *Chem. Rev.* **2016**, *116*, 9438–9484.

[182] Kim, J.; Kim, J. H.; Ariga, K. Redox-active polymers for energy storage nanoarchitectonics. *Joule* **2017**, *1*, 739–768.

[183] Venkataramana, G.; Dongare, P.; Dawe, L. N.; Thompson, D. W.; Zhao, Y.; Bodwell, G. J. 1, 8-Pyrenylene-ethynylene macrocycles. *Org. Lett.* **2011**, *13*, 2240–2243.

[184] Younes, E. A.; Williams, K.-L. M.; Walsh, J. C.; Schneider, C. M.; Bodwell, G. J.; Zhao, Y. A TTFV-pyrene-based copolymer: synthesis, redox properties, and aggregation behaviour. *RSC Adv.* **2015**, *5*, 23952–23956.

[185] Wan, S.; Guo, J.; Kim, J.; Ihee, H.; Jiang, D. A belt-shaped, blue luminescent, and semiconducting covalent organic framework. *Angew. Chem. Int. Ed.* **2008**, *47*, 8826–8830.

[186] Lin, G.; Ding, H.; Yuan, D.; Wang, B.; Wang, C. A pyrene-based, fluorescent three-dimensional covalent organic framework. *J. Am. Chem. Soc.* **2016**, *138*, 3302–3305.

[187] Stegbauer, L.; Zech, S.; Savasci, G.; Banerjee, T.; Podjaski, F.; Schwinghammer, K.; Ochsenfeld, C.; Lotsch, B. V. Tailor-made photoconductive pyrene-based covalent organic frameworks for visible-light driven hydrogen generation. *Adv. Energy Mater.* **2018**, *8*, 1703278.

[188] Qin, J.-H.; Huang, Y.-D.; Zhao, Y.; Yang, X.-G.; Li, F.-F.; Wang, C.; Ma, L.-F. Highly dense packing of chromophoric linkers achievable in a pyrene-based metal-organic framework for photoelectric response. *Inorg. Chem.* **2019**, *58*, 15013–15016.

[189] Knapp, J. G.; Zhang, X.; Elkin, T.; Wolfsberg, L. E.; Hanna, S. L.; Son, F. A.; Scott, B. L.; Farha, O. K. Single crystal structure and photocatalytic behavior of grafted uranyl on the Zr-node of a pyrene-based metal-organic framework. *CrystEngComm* **2020**, *22*, 2097–2102.

[190] Martínez, R.; Ratera, I.; Tárraga, A.; Molina, P.; Veciana, J. A simple and robust reversible redox-fluorescence molecular switch based on a 1, 4-disubstituted azine with ferrocene and pyrene units. *Chem. Commun.* **2006**, 3809–3811.

[191] Barathi, P.; Senthil Kumar, A. Electrochemical conversion of unreactive pyrene to highly redox-active 1,2-quinone derivatives on a carbon nanotube-modified gold electrode surface and its selective hydrogen peroxide sensing. *Langmuir* **2013**, *29*, 10617–10623.

[192] Bandyopadhyay, S.; Singh, C.; Jash, P.; Hussain, M. W.; Paul, A.; Patra, A.

Redox-active, pyrene-based pristine porous organic polymers for efficient energy storage with exceptional cyclic stability. *Chem. Commun.* **2018**, *54*, 6796–6799.

[193] Shahrokhi, F.; Zhao, Y. A tetrathiafulvalene vinylogue-based double-layer polymer thin film as a highly sensitive and selective TNT sensor. *New J. Chem.* **2019**, *43*, 5277–5281.

[194] Salami, F.; Zhao, Y. Synthesis and characterization of bis(dithiafulvenyl)-substituted fluorenones and fluorenylidene-1,3-dithioles. *New J. Chem.* **2020**, *44*, 9179–9189.

[195] Mizoshita, N.; Goto, Y.; Maegawa, Y.; Tani, T.; Inagaki, S. Tetraphenylpyrene-bridged periodic mesostructured organosilica films with efficient visible-light emission. *Chem. Mater.* **2010**, *22*, 2548–2554.

[196] Auras, F.; Ascherl, L.; Hakimioun, A. H.; Margraf, J. T.; Hanusch, F. C.; Reuter, S.; Bessinger, D.; Döblinger, M.; Hettstedt, C.; Karaghiosoff, K., et al. Synchronized offset stacking: a concept for growing large-domain and highly crystalline 2D covalent organic frameworks. *J. Am. Chem. Soc.* **2016**, *138*, 16703–16710.

[197] Gupta, S. K.; Kaleeswaran, D.; Nandi, S.; Vaidhyanathan, R.; Murugavel, R. Bulky isopropyl group loaded tetraaryl pyrene based azo-linked covalent organic polymer for nitroaromatics sensing and CO_2 adsorption. *ACS Omega* **2017**, *2*, 3572–3582.

[198] Jin, E.; Li, J.; Geng, K.; Jiang, Q.; Xu, H.; Xu, Q.; Jiang, D. Designed synthesis

of stable light-emitting two-dimensional sp^2 carbon-conjugated covalent organic frameworks. *Nature Commun.* **2018**, *9*, 1–10.

[199] Ascherl, L.; Evans, E. W.; Hennemann, M.; Di Nuzzo, D.; Hufnagel, A. G.; Beetz, M.; Friend, R. H.; Clark, T.; Bein, T.; Auras, F. Solvatochromic covalent organic frameworks. *Nature Commun.* **2018**, *9*, 1–8.

[200] Matsumoto, A.; Suzuki, M.; Kuzuhara, D.; Yuasa, J.; Kawai, T.; Aratani, N.; Yamada, H. A kinetically protected pyrene: molecular design, bright blue emission in the crystalline state and aromaticity relocation in its dicationic species. *Chem. Commun.* **2014**, *50*, 10956–10958.

[201] Vyas, V. S.; Lindeman, S. V.; Rathore, R. Photophysical properties of 1, 3, 6, 8-tetraarylpyrenes and their cation radicals. *J. Photochem. Photobiol. A: Chem.* **2019**, *375*, 209–218.

[202] Natarajan, P.; Bajpai, A.; Venugo, P.; Moorthy, J. N. Pseudopolymorphism of a highly adaptable tetraarylpyrene host that exhibits abundant solid-state guest inclusion. *Cryst. Growth Des.* **2012**, *12*, 6134–6143.

[203] Bajpai, A.; Natarajan, P.; Venugopalan, P.; Moorthy, J. N. Crystal engineering: lattice inclusion based on O–H··· O hydrogen-bonded self-assembly and guest-induced structural mimicry. *J. Org. Chem.* **2012**, *77*, 7858–7865.

[204] Moorthy, J. N.; Natarajan, P.; Krishna, M. S.; Nagarajaiah, H.; Venugopalan, P. Isomorphous three-component crystals (pseudopolymorphs of binary cocrystals) based on lattice inclusion of guests with a sterically-rigidified tetraarylpyrene host. *CrystEngComm* **2015**, *17*, 5307–5314.

[205] Maeda, H.; Suzuki, T.; Segi, M. Effects of substituents in silyl groups on the absorption, fluorescence and structural properties of 1,3,6,8-tetrasilylpyrenes. *Photochem. Photobiol. Sci.* **2018**, *17*, 781–792.

[206] Christensen, C. A.; Batsanov, A. S.; Bryce, M. R. Thiolated π-extended tetrathiafulvalenes: Versatile multifunctional π-systems. *J. Org. Chem.* **2007**, *72*, 1301–1308.

[207] Woolridge, K.; Goncalves, L. C.; Bouzan, S.; Chen, G.; Zhao, Y. Aryl-substituted dithiafulvenes: synthesis, electronic properties, and redox reactivity. *Tetrahedron Lett.* **2014**, *55*, 6362–6366.

[208] Dolomanov, O. V.; Bourhis, L. J.; Gildea, R. J.; Howard, J. A.; Puschmann, H. OLEX2: a complete structure solution, refinement and analysis program. *J. Appl. Cryst.* **2009**, *42*, 339–341.

[209] Sheldrick, G. M. *SHELXT* – Integrated space-group and crystal-structure determination. *Acta Cryst. A* **2015**, *C71*, 3–8.

[210] Bhunia, S.; Das, S. K.; Jana, R.; Peter, S. C.; Bhattacharya, S.; Addicoat, M.; Bhaumik, A.; Pradhan, A. Electrochemical stimuli-driven facile metal-Free hydrogen evolution from pyrene-porphyrin-based crystalline covalent organic framework. *ACS Appl. Mater. Interf.* **2017**, *9*, 23843–23851.

[211] Manandhar, E.; Wallace, K. J. Host-guest chemistry of pyrene-based molecular receptors. *Inorg. Chim. Acta* **2012**, *381*, 15–43.

[212] Gong, Y.; Zhan, X.; Li, Q.; Li, Z. Progress of pyrene-based organic

semiconductor in organic field effect transistors. *Sci. China Chem.* **2016**, *59*, 1623–1631.

[213] Vanga, M.; Lalancette, R. A.; Jäkle, F. Controlling the optoelectronic properties of pyrene by regioselective lewis base-directed electrophilic aromatic borylation. *Chem. Eur. J.* **2019**, *25*, 10133–10140.

[214] Ozaki, K.; Kawasumi, K.; Shibata, M.; Ito, H.; Itami, K. One-shot K-region-selective annulative π-extension for nanographene synthesis and functionalization. *Nature Commun.* **2015**, *6*, 1–8.

[215] Feng, X.; Hu, J.-Y.; Redshaw, C.; Yamato, T. Functionalization of pyrene to prepare luminescent materials-typical examples of synthetic methodology. *Chem. Eur. J.* **2016**, *22*, 11898–11916.

[216] Harvey, R. G.; Goh, S. H.; Cortez, C. K-region oxides and related oxidized metabolites of carcinogenic aromatic hydrocarbons. *J. Am. Chem. Soc.* **1975**, *97*, 3468–3479.

[217] Hu, J.; Zhang, D.; Harris, F. W. Ruthenium (III) chloride catalyzed oxidation of pyrene and 2,7-disubstitued pyrenes: An efficient, one-step synthesis of pyrene-4,5-diones and pyrene-4,5,9,10-tetraones. *J. Org. Chem.* **2005**, *70*, 707–708.

[218] Tabasi, Z. A.; Walsh, J. C.; Bodwell, G. J.; Thompson, D. W.; Zhao, Y. Crystal engineering and photophysical properties of phenyl-pyrenoimidazole systems. *Cryst. Growth Des.* **2020**, *20*, 1681–1693.

[219] Desai, N.; McKelvie, N.; Ramirez, F. A new synthesis of 1, 1-dibromoölefins via

phosphine-dibromomethylenes. The reaction of triphenylphosphine with carbon tetrabromide. *J. Am. Chem. Soc.* **1962**, *84*, 1745–1747.

[220] Frampton, C.; Knight, K.; Shankland, N.; Shankland, K. Single-crystal X-ray diffraction analysis of pyrene II at 93 K. *J. Mol. Struct.* **2000**, *520*, 29–32.

[221] Costa, J. C.; Taveira, R. J.; Lima, C. F.; Mendes, A.; Santos, L. M. Optical band gaps of organic semiconductor materials. *Opt. Mater.* **2016**, *58*, 51–60.

[222] Ángyán, J.; Kucsman, Á.; Poirier, R.; Csizmadia, I. Intramolecular sulfur-oxygen interaction: An ab initio conformational study of (Z)-3-fluorothio-2-propenal. *J. Mol. Struct.: Theochem* **1985**, *123*, 189–201.

[223] Burling, F. T.; Goldstein, B. M. Computational studies of nonbonded sulfur-oxygen and selenium-oxygen interactions in the thiazole and selenazole nucleosides. *J. Am. Chem. Soc.* **1992**, *114*, 2313–2320.

[224] Si, M. K.; Lo, R.; Ganguly, B. The origin and magnitude of intramolecular quasi-cyclic S–O and S–S interactions revisited: A computational study. *Chem. Phys. Lett.* **2015**, *631*, 6–11.

[225] Conboy, G.; Spencer, H. J.; Angioni, E.; Kanibolotsky, A. L.; Findlay, N. J.; Coles, S. J.; Wilson, C.; Pitak, M. B.; Risko, C.; Coropceanu, V., et al. To bend or not to bend-are heteroatom interactions within conjugated molecules effective in dictating conformation and planarity? *Mater. Horiz.* **2016**, *3*, 333–339.

[226] Hudson, B. M.; Nguyen, E.; Tantillo, D. J. The influence of intramolecular

sulfur-lone pair interactions on small-molecule drug design and receptor binding. *Org. Biomol. Chem.* **2016**, *14*, 3975–3980.

[227] Pascoe, D. J.; Ling, K. B.; Cockroft, S. L. The origin of chalcogen-bonding interactions. *J. Am. Chem. Soc.* **2017**, *139*, 15160–15167.

[228] Vogel, L.; Wonner, P.; Huber, S. M. Chalcogen bonding: An overview. *Angew. Chem. Int. Ed.* **2019**, *58*, 1880–1891.

[229] Scilabra, P.; Terraneo, G.; Resnati, G. The chalcogen bond in crystalline solids: A world parallel to halogen bond. *Acc. Chem. Res.* **2019**, *52*, 1313–1324.

[230] Johnson, E. R.; Keinan, S.; Mori-Sánchez, P.; Contreras-García, J.; Cohen, A. J.; Yang, W. Revealing noncovalent interactions. *J. Am. Chem. Soc.* **2010**, *132*, 6498–6506.

[231] Spackman, M. A.; Jayatilaka, D. Hirshfeld surface analysis. *CrystEngComm* **2009**, *11*, 19–32.

[232] Chen, G.; Dawe, L.; Wang, L.; Zhao, Y. Planar acetylene-expanded TTFAQ analogues. *Org. Lett.* **2009**, *11*, 2736–2739.

[233] Sheldrick, G. M. SHELXT-Integrated space-group and crystal-structure determination. *Acta Cryst.* **2015**, *A71*, 3–8.

[234] Sheldrick, G. M. Crystal structure refinement with SHELXL. *Acta Cryst.* **2015**, *C71*, 3–8.

[235] Frisch, M. J. et al. Gaussian 16 Revision C.01. 2016; Gaussian Inc. Wallingford CT.

[236] Yanai, T.; Tew, D. P.; Handy, N. C. A new hybrid exchange-correlation functional using the Coulomb-attenuating method (CAM-B3LYP). *Chem. Phys. Lett.* **2004**, *393*, 51–57.

[237] Marenich, A. V.; Cramer, C. J.; Truhlar, D. G. Universal solvation model based on solute electron density and on a continuum model of the solvent defined by the bulk dielectric constant and atomic surface tensions. *J. Phys. Chem. B* **2009**, *113*, 6378–6396.

[238] Zhao, Y.; Truhlar, D. G. The M06 suite of density functionals for main group thermochemistry, thermochemical kinetics, noncovalent interactions, excited states, and transition elements: two new functionals and systematic testing of four M06-class functionals and 12 other functionals. *Theor. Chem. Acc.* **2008**, *120*, 215–241.

[239] Weigend, F.; Ahlrichs, R. Balanced basis sets of split valence, triple zeta valence and quadruple zeta valence quality for H to Rn: Design and assessment of accuracy. *Phys. Chem. Chem. Phys.* **2005**, *7*, 3297–3305.

[240] Lu, T.; Chen, F. Multiwfn: a multifunctional wavefunction analyzer. *J. Comput. Chem.* **2012**, *33*, 580–592.

[241] Wolff, S.; Grimwood, D.; McKinnon, J.; Turner, M.; Jayatilaka, D.; Spackman, M. CrystalExplorer (Version 3.1). *University of Western Australia* **2012**,

[242] Humphrey, W.; Dalke, A.; Schulten, K., et al. VMD: visual molecular dynamics. *J. Mol. Graph.* **1996**, *14*, 33–38.

[243] Li, J.; Chen, S.; Wang, Z.; Zhang, Q. Pyrene-fused acenes and azaacenes: synthesis and applications. *Chem. Rec.* **2016**, *16*, 1518–1530.

[244] Mateo-Alonso, A. Pyrene-fused pyrazaacenes: from small molecules to nanoribbons. *Chem. Soc. Rev.* **2014**, *43*, 6311–6324.

[245] Casas-Solvas, J. M.; Howgego, J. D.; Davis, A. P. Synthesis of substituted pyrenes by indirect methods. *Org. Biomol. Chem.* **2014**, *12*, 212–232.

[246] Zöphel, L.; Enkelmann, V.; Rieger, R.; Müllen, K. Saddle Shaped Hexaaryl [a,c,fg,j,l,op] tetracenes from 4,5,9,10-tetrafunctionalized pyrenes. *Org. Lett.* **2011**, *13*, 4506–4509.

[247] Rao, H. S. P.; Vijjapu, S. Synthesis and photochromic properties of benzofuran-phenanthrene and benzofuran-pyrene hybrids. *RSC Adv.* **2014**, *4*, 25747–25758.

[248] Fan, Q.; Liu, Y.; Xiao, M.; Tan, H.; Wang, Y.; Su, W.; Yu, D.; Yang, R.; Zhu, W. Donor-acceptor copolymers based on benzo(1,2-b:4,5-b') dithiophene and pyrene-fused phenazine for high-performance polymer solar cells. *Org. Electr.* **2014**, *15*, 3375–3383.

[249] Gu, P.-Y.; Zhang, J.; Long, G.; Wang, Z.; Zhang, Q. Solution-processable thiadiazoloquinoxaline-based donor-acceptor small molecules for thin-film transistors. *J. Chem. Mater. C* **2016**, *4*, 3809–3814.

[250] Liu, Y.; Bai, Q.; Li, J.; Zhang, S.; Zhang, C.; Lu, F.; Yang, B.; Lu, P. Efficient pyrene-imidazole derivatives for organic light-emitting diodes. *RSC Adv.* **2016**, *6*, 17239–17245.

[251] Karthik, S.; Ajantha, J.; Nagaraja, C.; Easwaramoorthi, S.; Gandhi, T. Synthesis and photophysics of extended π-conjugated systems of substituted 10-aryl-pyrenoimidazoles. *Org. Biomol. Chem.* **2016**, *14*, 10255–10266.

[252] Mardanya, S.; Karmakar, S.; Mondal, D.; Baitalik, S. An imidazolyl-pyrenoimidazole conjugate as a cyanide sensor and a set-reset memorized sequential logic device. *Dalton Trans.* **2015**, *44*, 15994–16012.

[253] Emery, F. S.; Maria do Carmo, F.; de Simone, C. A.; Malta, V. R.; da Silva Junior, E. N.; Pinto, A. V. Complex diazaazulenones from the reaction of ortho-naphthoquinones with ammonium acetate. *Synlett* **2010**, 1931–1934.

[254] Lantos, I. Reaction of phenanthrenequinone with ammonium acetate. *J. Org. Chem.* **1975**, *40*, 1641–1642.

[255] Biegger, P.; Schaffroth, M.; Brödner, K.; Tverskoy, O.; Rominger, F.; Bunz, U. H. Bisalkynylated 3,6-diiminocyclohexa-1,4-diene-1,4-diamine. *Chem. Commun.* **2015**, *51*, 14844–14847.

[256] Förster, T. Excimers. *Angew. Chem. Int. Ed. Engl.* **1969**, *8*, 333–343.

Appendix I

Supporting Information for Chapter 2

A Tetrathiafulvalene Vinylogue-based Double-Layer Polymer Thin Film as a Highly Sensitive and Selective TNT Sensor

https://doi.org/10.1039/C8NJ06467A

Table of Content

1. Experimental

1.1 General

Chemicals were purchased from commercial suppliers and used directly without purification. All reactions were conducted in standard, dry glassware. Evaporation and concentration were carried out with a rotary evaporator. Flash column chromatography was performed with 240-400 mesh silica gel, and thin-layer chromatography (TLC) was carried out with silica gel F254 covered on plastic sheets and visualized by UV light. Melting points (m.p.) were measured using an SRS OptiMelt melting point apparatus and are uncorrected. ^{1}H and ^{13}C NMR spectra were measured on a Bruker Avance III 300 MHz multinuclear spectrometer. Chemical shifts (δ) are reported in ppm downfield relative to the signals of the internal reference $SiMe_4$ or residual solvents ($CHCl_3$: δ_H = 7.24 ppm, δ_C = 77.2 ppm; CH_2Cl_2: δ_H = 5.32 ppm, δ_C = 54.0 ppm). Coupling constants (*J*) are given in Hz. Infrared spectra (IR) were recorded on a Bruker Alfa spectrometer. MALDI-TOF MS analysis was performed on Bruker 9.4T Apex-Qe FTICR system. High-resolution APPI-TOF MS analysis was done on a GCT premier Micromass Technologies instrument. UV-Vis absorption spectra were measured on a Cary 6000i spectrophotometer. Surface topography of polymer thin films was visualized by using a New View 8000 3D optical surface profiler (Zygo Corporation) and FEI MLA 650F scanning electron microscope (SEM). Samples for SEM imaging were subjected to Au sputter coating before analysis.

Cyclic voltammetric (CV) and differential pulse voltammetric (DPV) analyses were carried out in a standard three-electrode setup controlled by a BASi Epsilon potentiostat. Experimental conditions were set up as follows. CV analysis: glassy carbon or indium tin oxide (ITO) coated glass as the working electrode, Pt wire as the counter electrode, Ag/AgCl as the reference electrode, scan rate = 100 mV/s. DPV analysis: glassy carbon as the working electrode, Pt wire as the counter electrode, Ag/AgCl as the reference electrode, step E = 4 mV, pulse width = 50 ms, pulse period = 200 ms, scan rate = 20 mV/s. All samples were measured in CH_2Cl_2 using Bu_4NBF_4 as electrolyte.

1.2 Synthetic procedures

4,4'-((9*H*-Fluoren-9-ylidene)methylene)dibenzaldehyde (5)

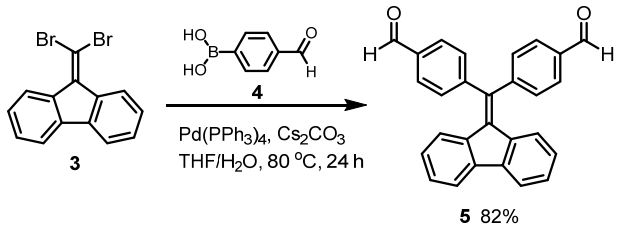

9-(Dibromomethylene)-9*H*-fluorene (**3**) (0.500 g, 1.489 mmol), 4-formylphenylboronic acid (**4**) (0.665 g, 4.46 mmol), cesium carbonate (2.418 g, 7.440 mmol), THF (25 mL), and deionized water (10 mL) were added to 50 mL round-bottomed flask. The mixture was bubbled with N_2 flow for 5 min, and then $Pd(PPh_3)_4$ (0.172 g, 0.148 mmol) was added. The reaction mixture was stirred under N_2 and heated at reflux 24 h. The reaction mixture was next cooled down to room temperature, poured into a separatory funnel including water, and extracted twice with CH_2Cl_2. The organic layers were combined and dried over $MgSO_4$. After filtration and concentration

under gentle heating and reduced pressure, the resulting residue was subjected to silica gel column chromatography (hexanes/EtOAc, 9:1) to give pure compound **5** (0.471 g, 1.219 mmol, 82%) as a yellow crystalline solid. m.p.: 199–202 °C; IR (neat): 3054, 2833, 2735, 1692, 1596, 1562, 1432, 1202, 1164 cm^{-1}; ^1H NMR (300 MHz, CD_2Cl_2): δ 10.07 (s, 2H), 7.95 (d, *J* = 8.4 Hz, 4H), 7.72–7.67 (m, 2H), 7.57 (d, *J* = 8.1 Hz, 4H), 7.27 (td, *J* = 7.5, 1.0 Hz, 2H), 6.95 – 6.88 (m, 2H), 6.58 (dt, *J* = 7.9, 0.8 Hz, 2H) ppm; ^{13}C NMR (75 MHz, CD_2Cl_2): δ 192.02, 148.53, 142.04, 141.25, 138.23, 136.57, 136.41, 130.77, 130.67, 128.99, 127.15, 125.44, 119.94 ppm; HRMS (APPI-TOF, positive mode): *m/z* calcd for $C_{28}H_{18}O_2$ $[M]^+$ 386.1307, found 386.1295. X-ray.

9-(Bis(4-(2,2-dibromovinyl)phenyl)methylene)-9*H*-fluorene (6)

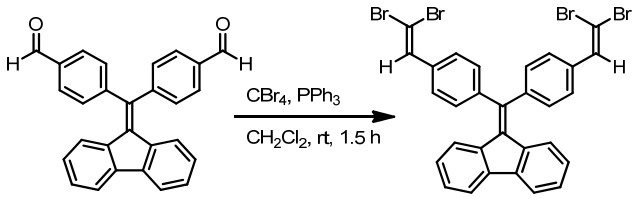

5 **6** 92%

Compound **5** (1.043 g, 2.699 mmol), CBr_4 (4.470 g, 13.51 mmol), PPh_3 (5.663 g, 21.62 mmol), CH_2Cl (50 mL) were added to a 100 mL round-bottomed flask. The reaction mixture was stirred at room temperature for 1.5 hours and then subjected to vacuum filtration. The solids collected were extracted with CH_2Cl_2 and the organic layers were combined and concentrated under reduced pressure. The resulting residue was subjected to silica gel column chromatography (hexanes/CH_2Cl_2, 4:1) to give pure compound **6** (1.734 g, 2.484 mmol, 92%) as a pale yellow solid. m.p.: 213–216 °C; IR (neat): 3019, 1595, 1500, 1439, 1402, 1256, 1113, 1018, 785, 765 cm^{-1}; ^1H NMR (300 MHz, $CDCl_3$): δ 7.72 (d, *J* = 7.5 Hz, 2H), 7.65 (d, *J* = 8.2 Hz, 4H), 7.57 (s, 2H), 7.40 (d, *J* = 8.3 Hz, 4H), 7.32–7.24 (m, 2H), 7.00–6.93 (m, 2H), 6.70 (d, *J* = 7.9 Hz, 2H) ppm; ^{13}C NMR (75 MHz, $CDCl_3$): δ 143.68, 142.86, 140.75, 138.51, 136.50, 135.36, 135.23, 130.22, 129.03, 128.14, 126.68, 125.01, 119.54, 90.31 ppm; HRMS (APPI-TOF, positive mode): *m/z* calcd for $C_{48}H_{29}Br_8$ $[M + H]^+$ 693.8123, found 693.8142.

2,2'-((((9*H*-Fluoren-9-ylidene)methylene)bis(4,1-phenylene))bis(methaneylylidene))bis(4,5-bis(methylthio)-1,3-dithiole) (9a)

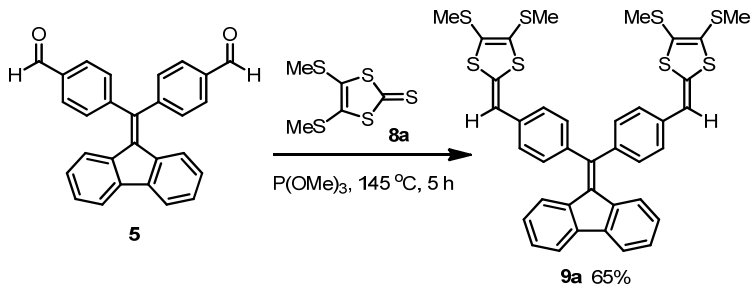

5 **9a** 65%

Compound **5** (0.151 g, 0.391 mmol), 4,5-bis(methylthio)-1,3-dithiole-2-thione (**8a**) (0.265 g, 1.173 mmol), and $P(OMe)_3$ (15 mL) were added to a 100 mL round-bottomed flask. The flask was placed in an oil bath heated at 145 °C and kept in it for 5 h. After that, the reaction mixture was subjected to under vacuum distillation at the same temperature to remove unreacted $P(OMe)_3$. The residue was subjected to silica gel column chromatography (hexanes/EtOAc, 7:3)

to give pure compound **9a** (0.189 g, 0.254 mmol, 65%) as a deep-orange oil. Caution: the product is quite sensitive to air and light, and it needs to be stored in a fridge immediately after purification to prevent significant decomposition. IR (neat): 3054, 3021, 2990, 2918, 2852, 1567, 1540, 1502, 1443, 1314, 1184 cm^{-1}; ^1H NMR (300 MHz, CD_2Cl_2): δ 7.71 (d, *J* = 7.3 Hz, 2H), 7.38–7.32 (m, 4H), 7.30–7.21 (m, 6H), 6.94 (td, *J* = 7.7, 1.2 Hz, 2H), 6.77 (d, *J* = 7.9 Hz, 2H), 6.57 (s, 2H), 2.45 (s, 6H), 2.43 (s, 6H) ppm; ^{13}C NMR (75 MHz, CD_2Cl_2): δ 145.45, 140.84, 140.69, 139.32, 136.91, 134.77, 133.98, 131.08, 128.11, 128.01, 127.51, 126.94, 125.33, 125.00, 119.79, 114.48, 19.40, 19.31 ppm; HRMS (APPI-TOF, positive mode): *m/z* calcd for $C_{74}H_{102}S_8$ $[M]^+$ 1246.5747, found 1246.5708.

2,2'-((((9*H*-Fluoren-9-ylidene)methylene)bis(4,1-phenylene))bis(methaneylylidene))bis(4,5-bis(decylthio)-1,3-dithiole) (9b)

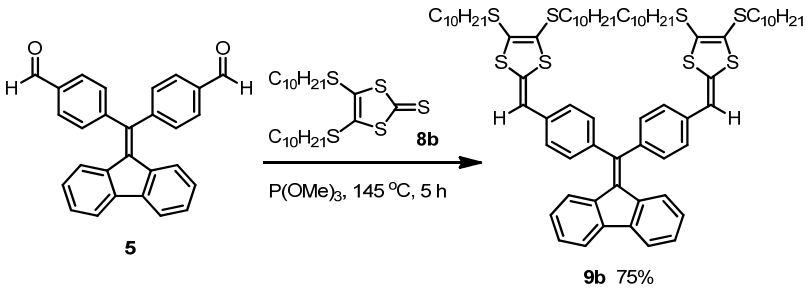

Compound **5** (0.151 g, 0.391 mmol), 4,5-bis(decylthio)-1,3-dithiole-2-thione (**8b**) (0.561 g, 1.173 mmol), and $P(OMe)_3$ (15 mL) were added to a 100 mL round-bottomed flask. The flask was placed in an oil bath heated at 145 °C and kept in it for 5 h. After that, the reaction mixture was subjected to under vacuum distillation at the same temperature to remove unreacted $P(OMe)_3$. The residue was subjected to silica gel column chromatography (hexanes/EtOAc, 98:2) to give pure compound **9b** (0.366 g, 0.293 mmol, 75%) as a deep-orange oil. Caution: the product is quite sensitive to air and light, and it needs to be stored in a fridge immediately after purification to prevent significant decomposition. IR (neat): 3054, 3021, 2920, 2850, 1566, 1540, 1501, 1442, 1184 cm^{-1}; ^1H NMR (300 MHz, CD_2Cl_2): δ 7.72 (d, *J* = 7.5 Hz, 2H), 7.35 (d, *J* = 8.4 Hz, 4H), 7.32–7.20 (m, 6H), 6.97–6.90 (m, 2H), 6.79 (d, *J* = 7.9 Hz, 2H), 6.56 (s, 2H), 2.85 (td, *J* = 7.3, 2.5 Hz, 8H), 1.72–1.59 (m, 8H), 1.36–1.19 (m, 56H), 0.96–0.81 (m, 12H) ppm; ^{13}C NMR (75 MHz, CD_2Cl_2) δ 145.17, 140.52, 140.24, 139.02, 136.66, 134.42, 134.02, 130.81, 127.94, 127.75, 127.13, 126.59, 125.22, 125.02, 119.45, 113.70, 36.35, 36.27, 32.19, 32.17, 29.84, 29.82, 29.61, 29.60, 29.42, 22.97, 22.96, 14.19 ppm; HRMS (APPI-TOF, positive mode): *m/z* calcd for $C_{74}H_{102}S_8$ $[M]^+$ 1246.5747, found 1246.5708.

4,4',4'',4'''-((((9*H*-Fluoren-9-ylidene)methylene)bis(4,1-phenylene))bis(ethene-2,1,1-riyl))tetrabenzaldehyde (7)

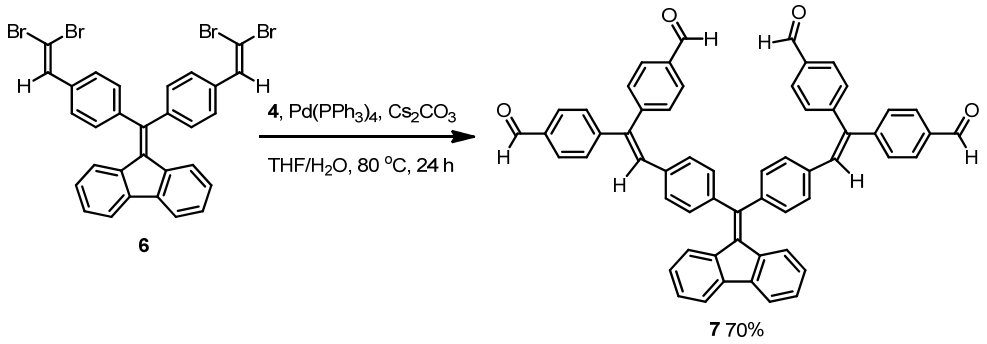

Compound **6** (0.642 g, 0.919 mmol), 4-formylphenylboronic acid (**4**) (0.685 g, 4.599 mmol), cesium carbonate (2.989 g, 9.197 mmol), THF (50 mL), and deionized water (15 mL) were added to 250 mL round-bottomed flask. The mixture was bubbled with N_2 flow for 5 min and then $Pd(PPh_3)_4$ (0.212 g, 0.184 mmol) was added. The reaction mixture was stirred under N_2 and heated at reflux 24 h. The mixture was next cooled down to room temperature, poured into a separatory funnel containing water, and extracted twice with CH_2Cl_2. The organic layers were combined and dried over $MgSO_4$. After filtration and concentration under gentle heating and reduced pressure, the resulting residue was subjected to silica gel column chromatography (hexanes/EtOAc, 4:1) to give pure compound **7** (0.514 g, 0.643 mmol, 70%) as a yellow crystalline solid. m.p.: 255 □ (dec.); IR (neat): 3043, 3023, 2922, 2823, 2733, 1694, 1598, 1562, 1385, 1303, 1205, 1164 cm^{-1}; ^1H NMR (300 MHz, CD_2Cl_2): δ 10.02 (s, 2H), 10.01 (s, 2H), 7.90–7.83 (m, 8H), 7.67 (d, J = 7.3 Hz, 2H), 7.50–7.43 (m, 8H), 7.27–7.22 (m, 4H), 7.15–7.07 (m, 8H), 6.97–6.92 (m, 2H), 6.60 (d, J = 7.9 Hz, 2H) ppm; ^{13}C NMR (75 MHz, CD_2Cl_2): δ 192.17, 192.07, 148.68, 146.67, 144.62, 142.52, 141.74, 140.97, 138.94, 137.11, 136.47, 136.28, 135.24, 131.80, 131.73, 130.75, 130.68, 130.27, 130.23, 128.65, 128.42, 126.87, 125.35, 119.86 ppm; HRMS (APPI-TOF, positive mode): *m/z* calcd for $C_{58}H_{38}O_4$ $[M]^+$ 798.2770, found 798.2743.

2,2',2'',2'''-((((((9*H*-Fluoren-9-ylidene)methylene)bis(4,1-phenylene))bis(ethene-2,1,1-triyl))tetrakis(benzene-4,1-diyl))tetrakis(methaneylylidene))tetrakis(4,5-bis(decylthio)-1,3-dithiole) (2)

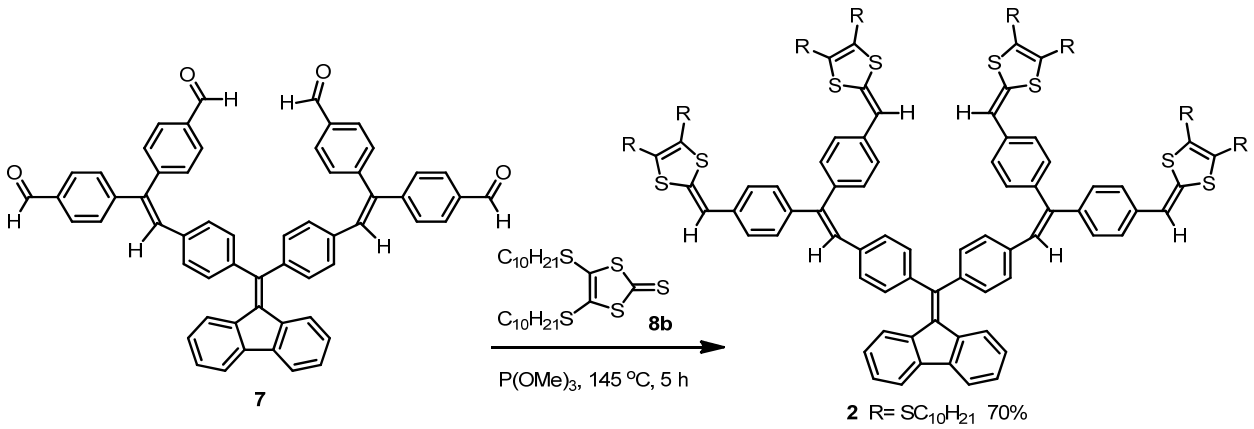

Compound **7** (0.103 g, 0.129 mmol), **8b** (0.370 g, 0.774 mmol), and $P(OMe)_3$ (6 mL) were added to a 50 mL round-bottomed flask. The flask was placed in an oil bath heated at 145 °C and kept

in it for 5 h. After that, the reaction mixture was subjected to under vacuum distillation at the same temperature to remove unreacted $P(OMe)_3$. The residue was subjected to silica gel column chromatography (hexanes/EtOAc, 98:2) to give pure compound **2** (0.228 g, 0.090 mmol, 70%) as a deep-orange oil. Caution: the product is quite sensitive to air and light, and it needs to be stored in a fridge immediately after purification to prevent significant decomposition. IR (neat): 3022, 2920, 2850, 1567, 1542, 1504, 1462, 1412, 1018 cm^{-1}; ^1H NMR (300 MHz, CD_2Cl_2): δ 7.67 (d, *J* = 7.5 Hz, 2H), 7.34 (d, *J* = 8.5 Hz, 4H), 7.27–7.15 (m, 14H), 7.12–7.04 (m, 10H), 7.00–6.93 (m, 2H), 6.67 (d, *J* = 7.9 Hz, 2H), 6.48 (s, 4H), 2.89–2.73 (m, 16H), 1.62 (dq, *J* = 16.8, 9.1, 8.2 Hz, 16H), 1.25 (d, *J* = 14.1 Hz, 112H), 0.91–0.84 (m, 24H) ppm; ^{13}C NMR (75 MHz, CD_2Cl_2): δ 145.42, 143.01, 141.49, 140.71, 139.01, 138.17, 137.87, 136.17, 136.07, 134.57, 133.30, 133.25, 131.10, 130.31, 129.94, 128.20, 128.14, 127.99, 127.82, 127.37, 126.98, 126.74, 125.30, 125.19, 119.57, 114.12, 36.51, 36.44, 32.35, 30.31, 30.29, 30.18, 30.13, 30.01, 29.98, 29.77, 29.58, 28.98, 28.95, 28.92, 23.13, 14.35 ppm; MS (MALDI-TOF, positive mode, DCTB as matrix): *m/z* calcd for $C_{150}H_{206}S_{16}O$ $[M + O]^+$ 2535.16, found 2535.15.

1,2-Bis(4,5-bis(methylthio)-1,3-dithiol-2-ylidene)-1,2-bis(4-((4-((4,5-bis(methylthio)-1,3-dithiol-2-ylidene)methyl)phenyl)(9*H*-fluoren-9-ylidene)methyl)phenyl)ethane (10)

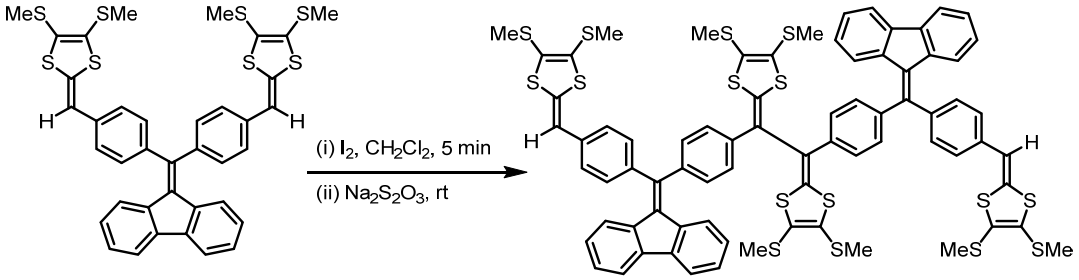

9a **10** 20%

Compound **9a** (0.050 g, 0.067 mmol), iodine (0.051 g, 0.20 mmol), and CH_2Cl_2 (10 mL) were added to a 100 mL round-bottom flask. The reaction mixture was stirred under N_2 at room temperature for 5 min. Then 60 mL of the aqueous solution of saturated $Na_2S_2O_3$ was added to the reaction and the mixture was kept stirring for another 15 min. The mixture was poured into a separatory funnel, and the aqueous layer was separated and extracted with CH_2Cl_2 twice. The organic layers were combined and dried over $MgSO_4$. After filtration and concentration under gentle heating and reduced pressure, the resulting residue was subjected to silica gel column chromatography (hexanes/CH_2Cl_2, 7:3) to give compound **10** (0.019 g, 0.013 mmol, 20%) as a red semi-solid. IR (neat): 3054, 3022, 2918, 2851, 1565, 1537, 1501, 1443, 1427, 1185, 967 cm^{-1}; ^1H NMR (300 MHz, CD_2Cl_2): δ 7.72–7.68 (m, 4H), 7.56–7.51 (m, 3H), 7.39–7.34 (m, 8H), 7.31–7.16 (m, 10H), 6.98–6.91 (m, 3H), 6.89–6.81 (m, 2H), 6.78 (d, *J* = 7.9 Hz, 2H), 6.66 (d, *J* = 7.9 Hz, 2H), 6.57 (s, 2H), 2.45 (s, 6H), 2.44 (s, 6H), 2.42 (s, 6H), 2.41 (s, 6H) ppm; HRMS (APPI-TOF, positive mode): *m/z* calcd for $C_{76}H_{58}S_{16}$ $[M]^+$ 1482.0070, found 1482.0091.

2. NMR Spectra for New Compounds

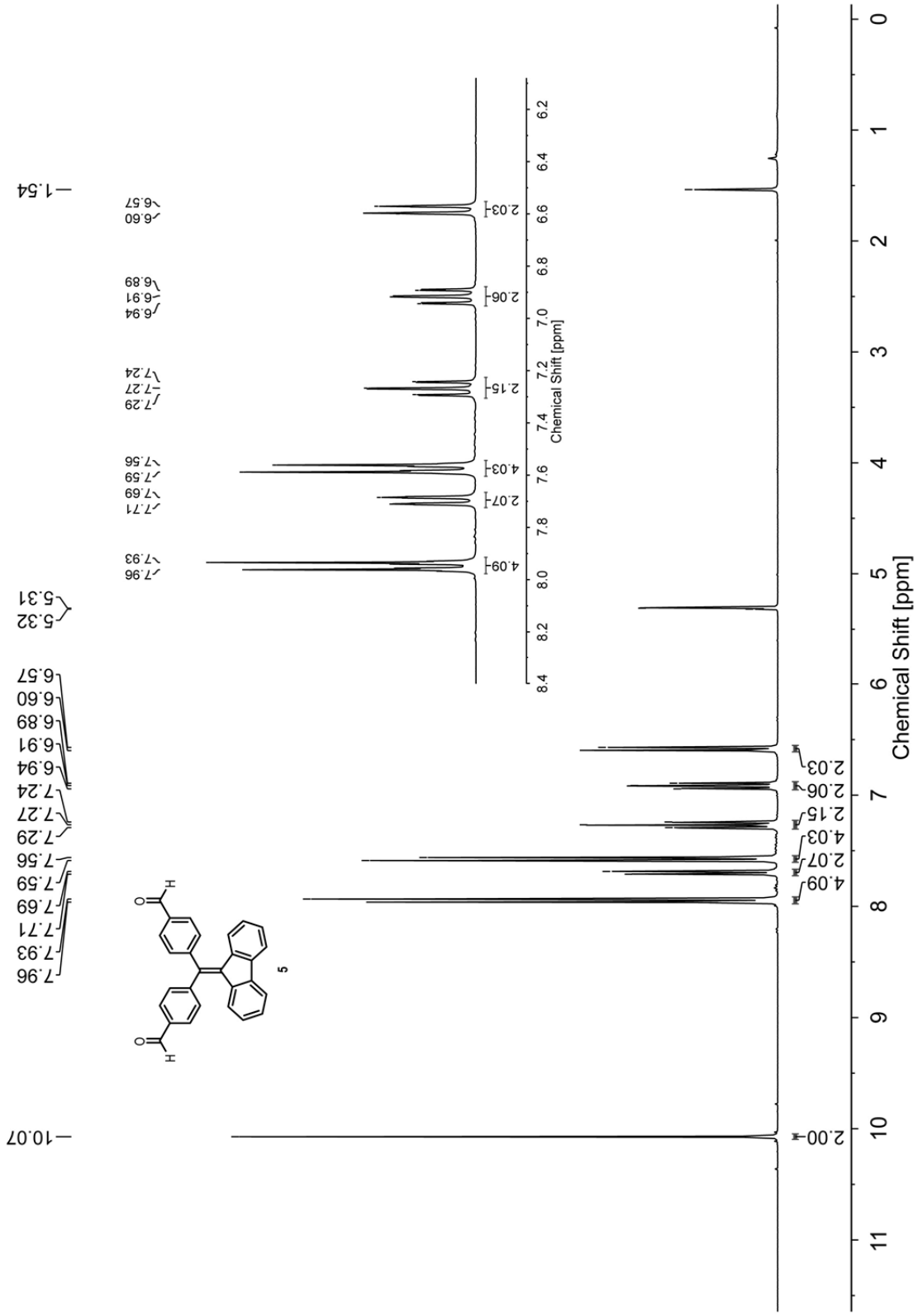

Fig. S-1 ^{1}H NMR (300 MHz, CD_2Cl_2) spectrum of compound **5**.

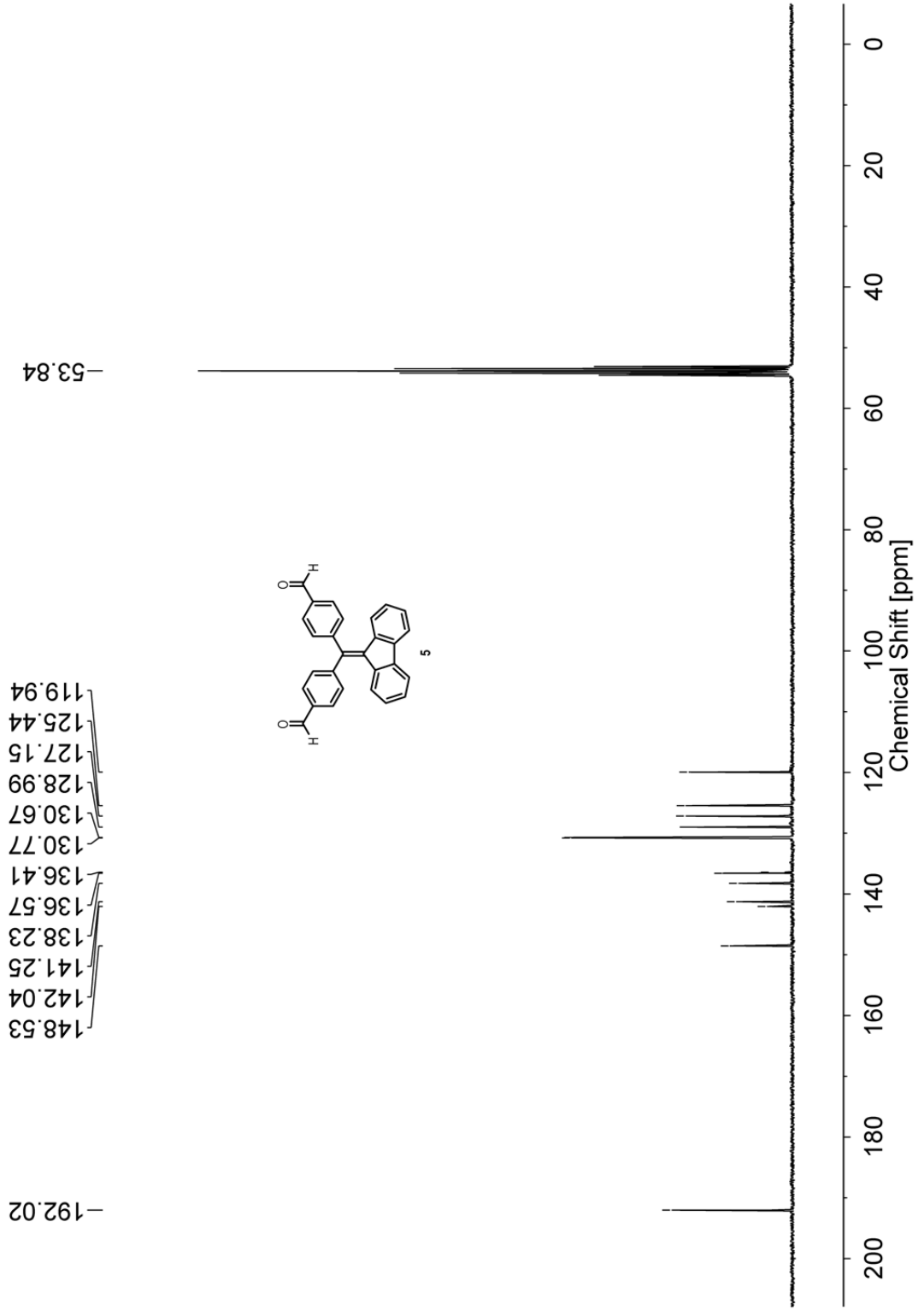

Fig. S-2 ^{13}C NMR (75 MHz, CD_2Cl_2) spectrum of compound **5**.

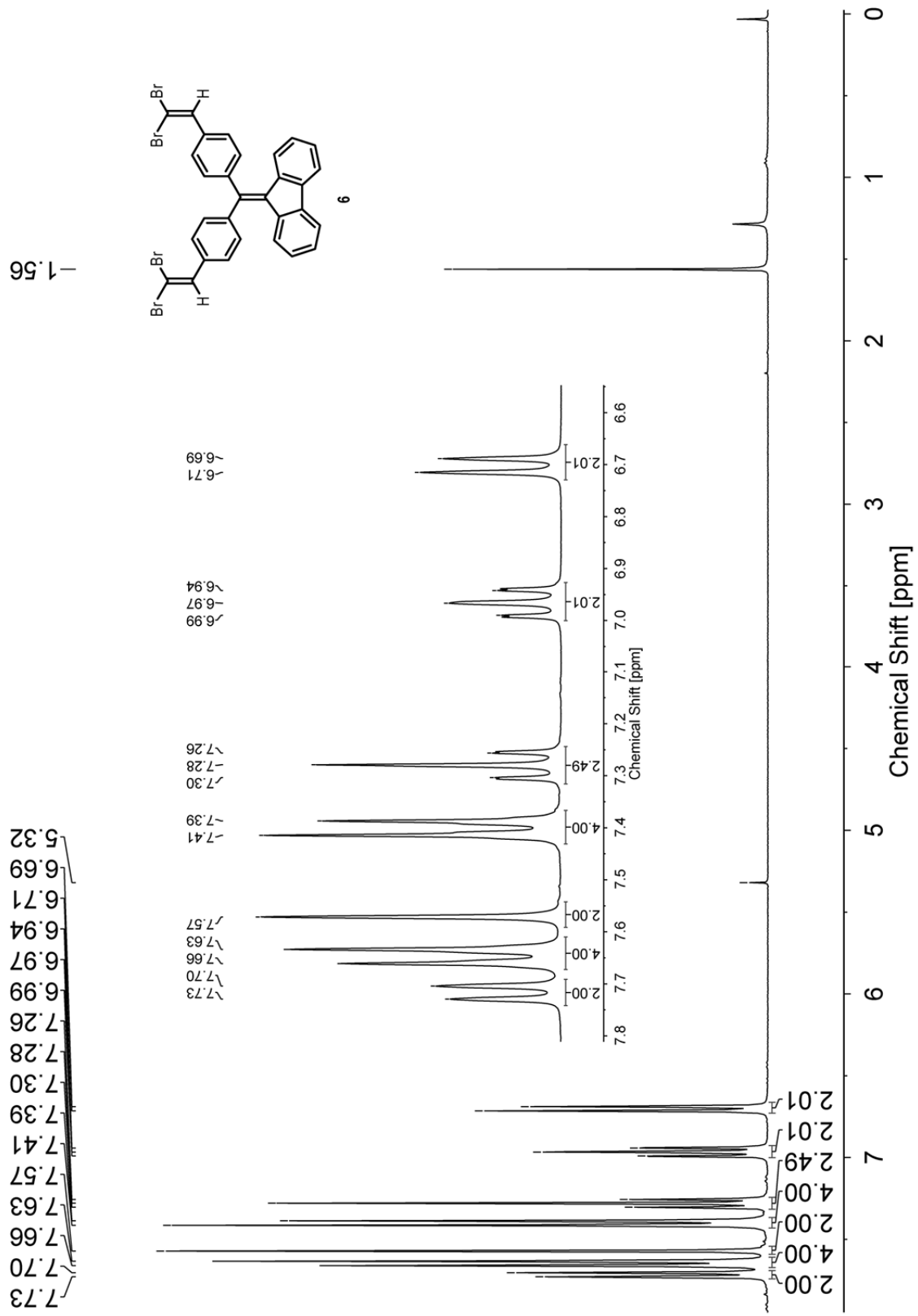

Fig. S-3 ^{1}H NMR (300 MHz, $CDCl_3$) spectrum of compound **6**.

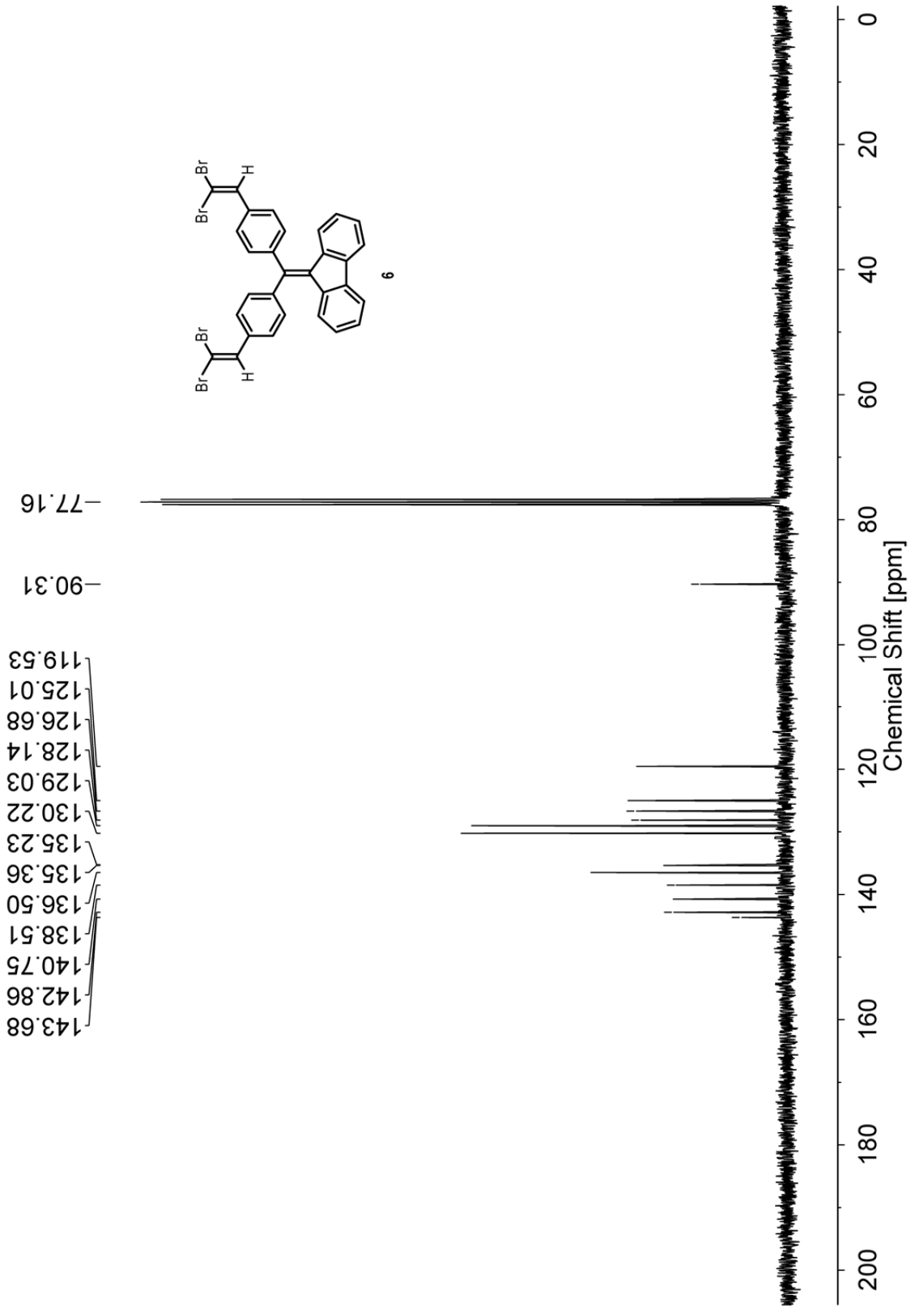

Fig. S-4 ^{13}C NMR (75 MHz, $CDCl_3$) spectrum of compound **6**.

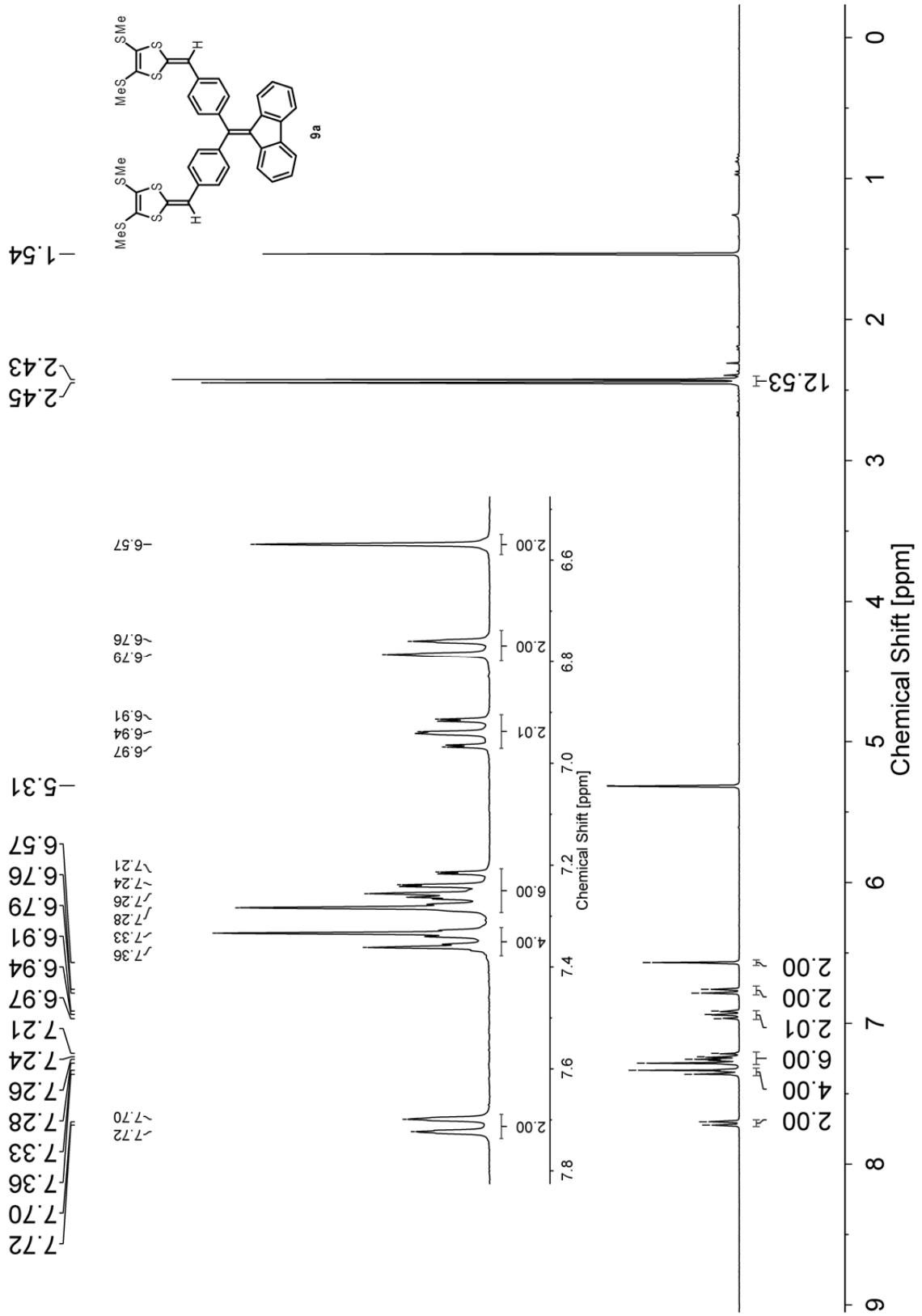

Fig. S-5 ^{1}H NMR (300 MHz, CD_2Cl_2) spectrum of compound **9a**.

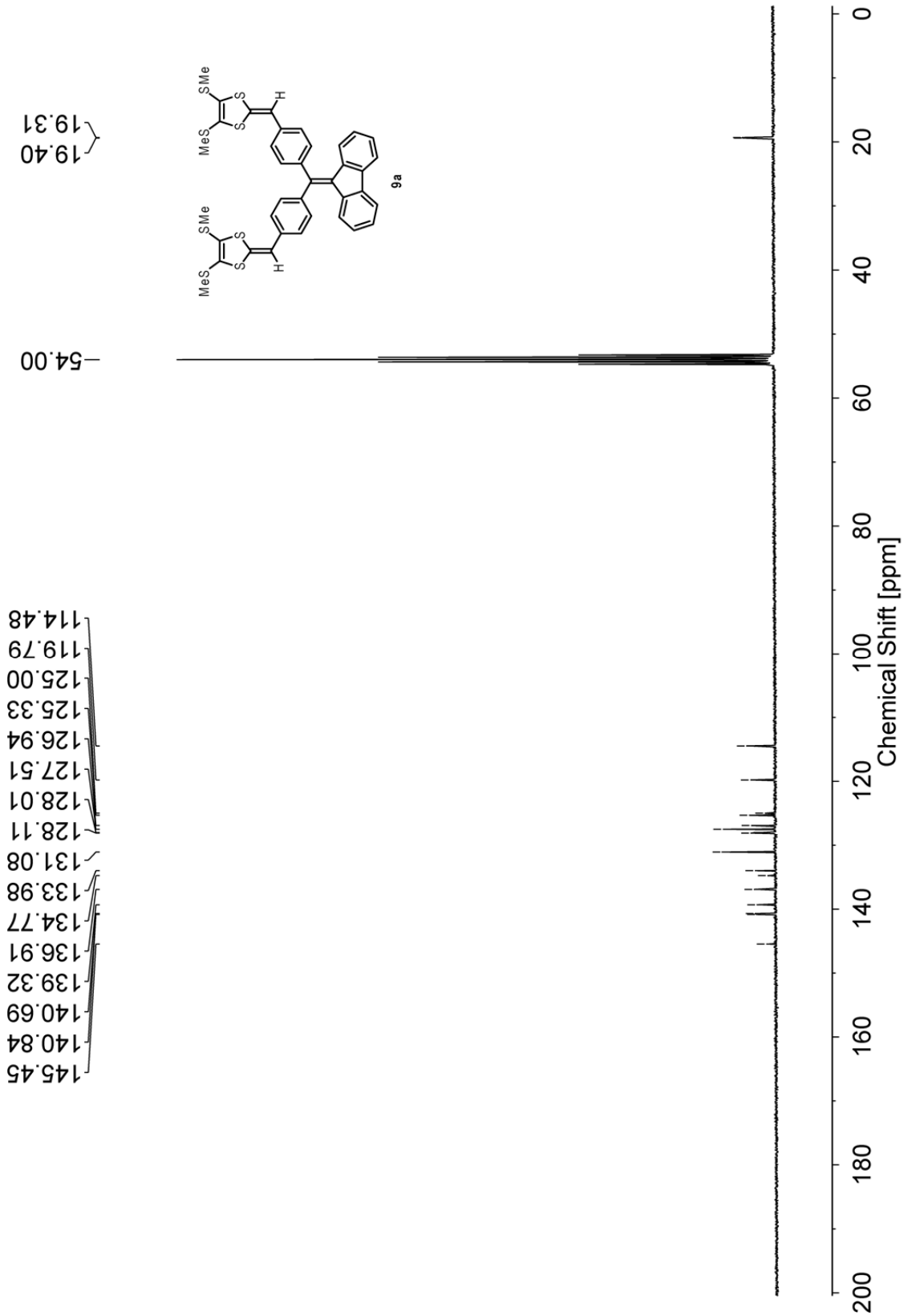

Fig. S-6 ^{13}C NMR (75 MHz, CD_2Cl_2) spectrum of compound **9a**.

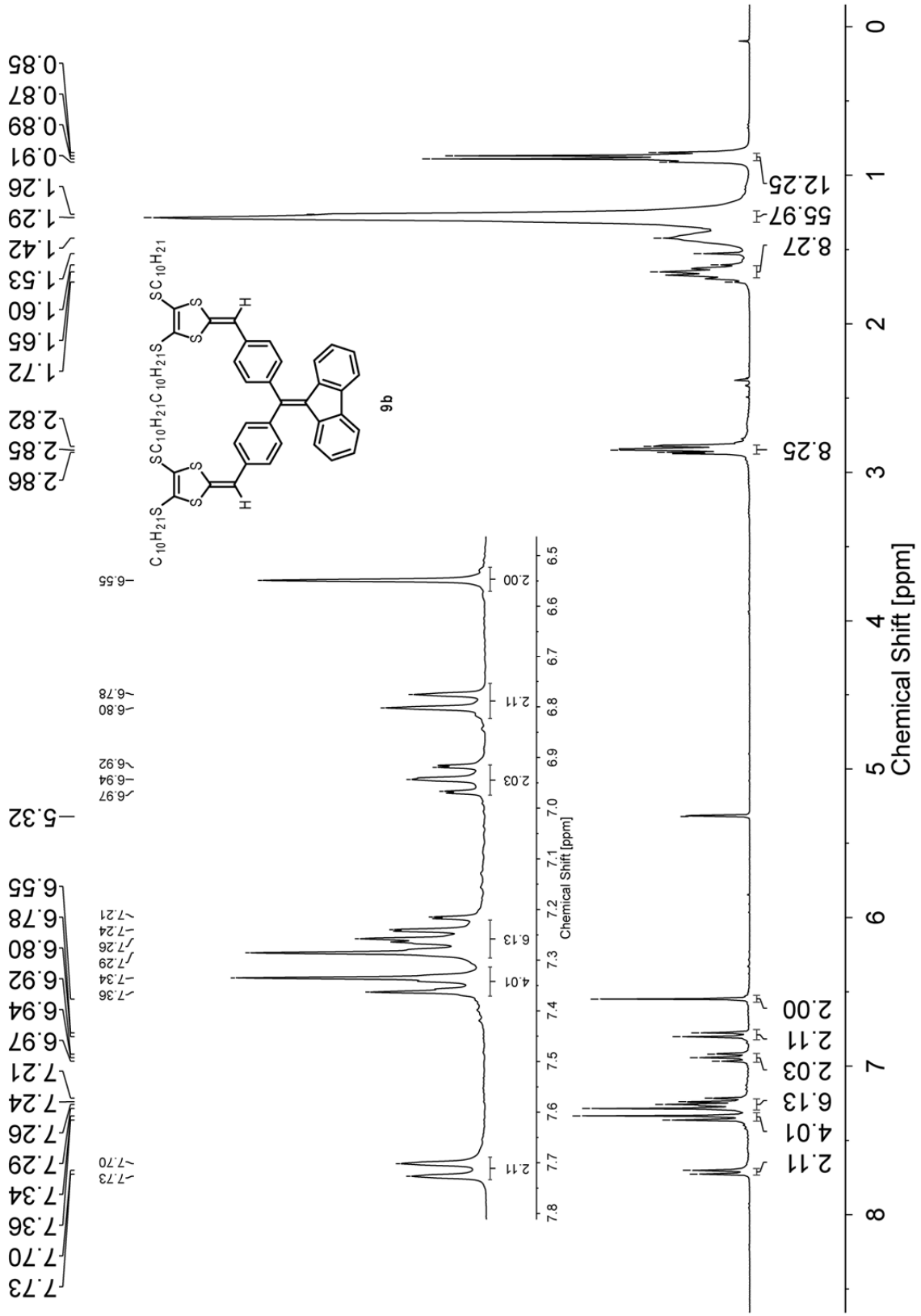

Fig. S-7 ^{1}H NMR (300 MHz, CD_2Cl_2) spectrum of compound **9b**.

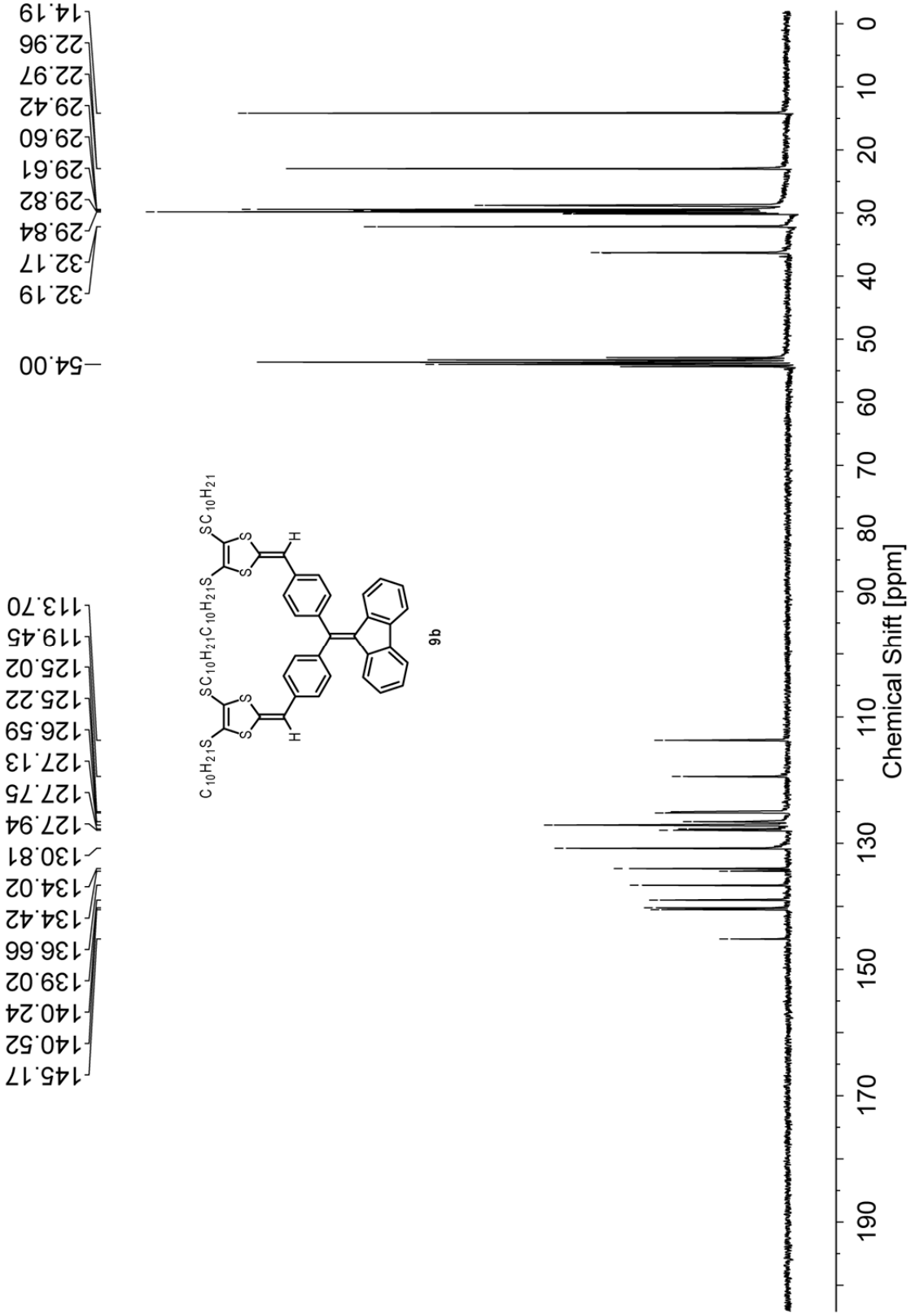

Fig. S-8 ^{13}C NMR (75 MHz, CD_2Cl_2) spectrum of compound **9b**.

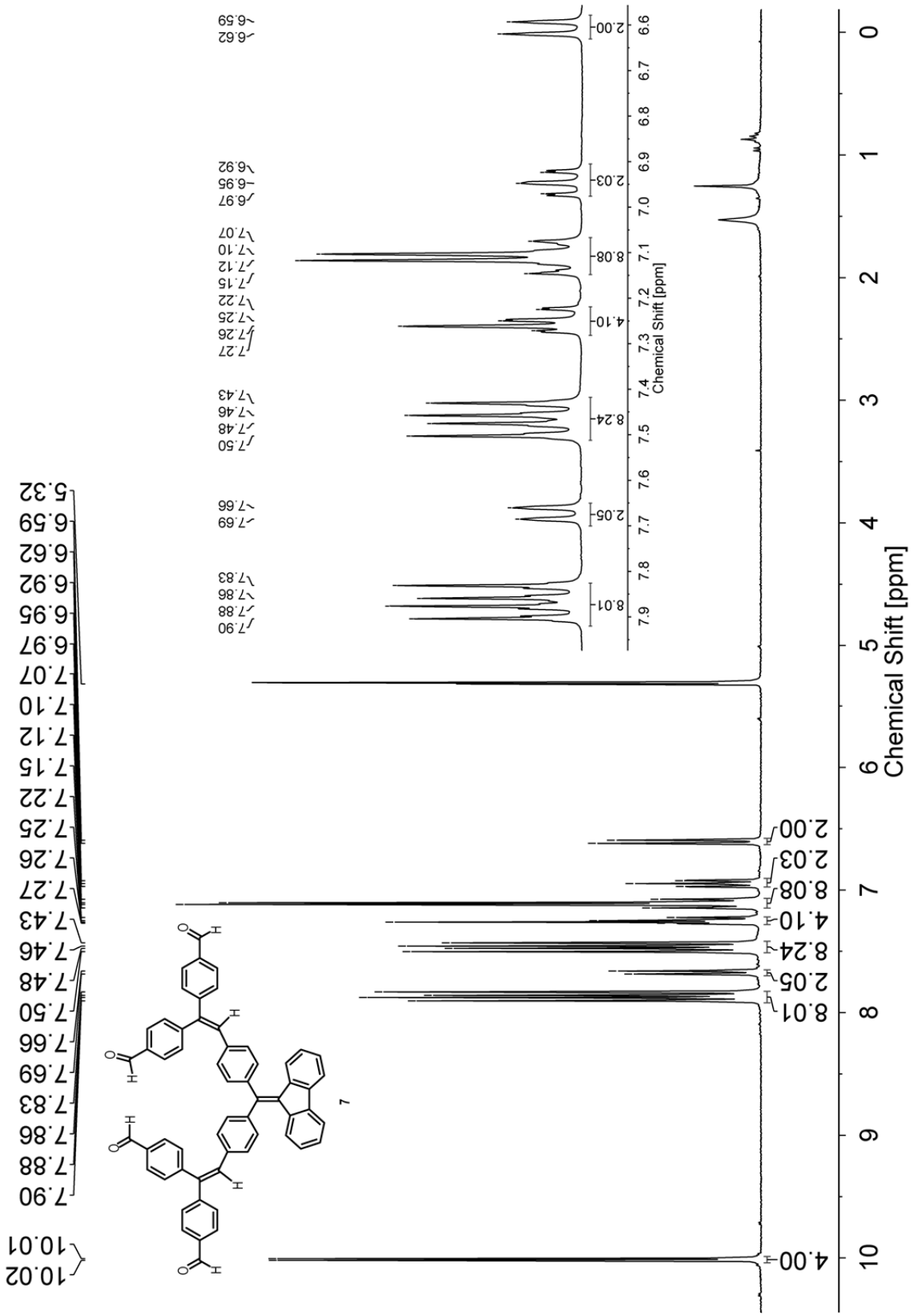

Fig. S-9 ^{1}H NMR (300 MHz, CD_2Cl_2) spectrum of compound **7**.

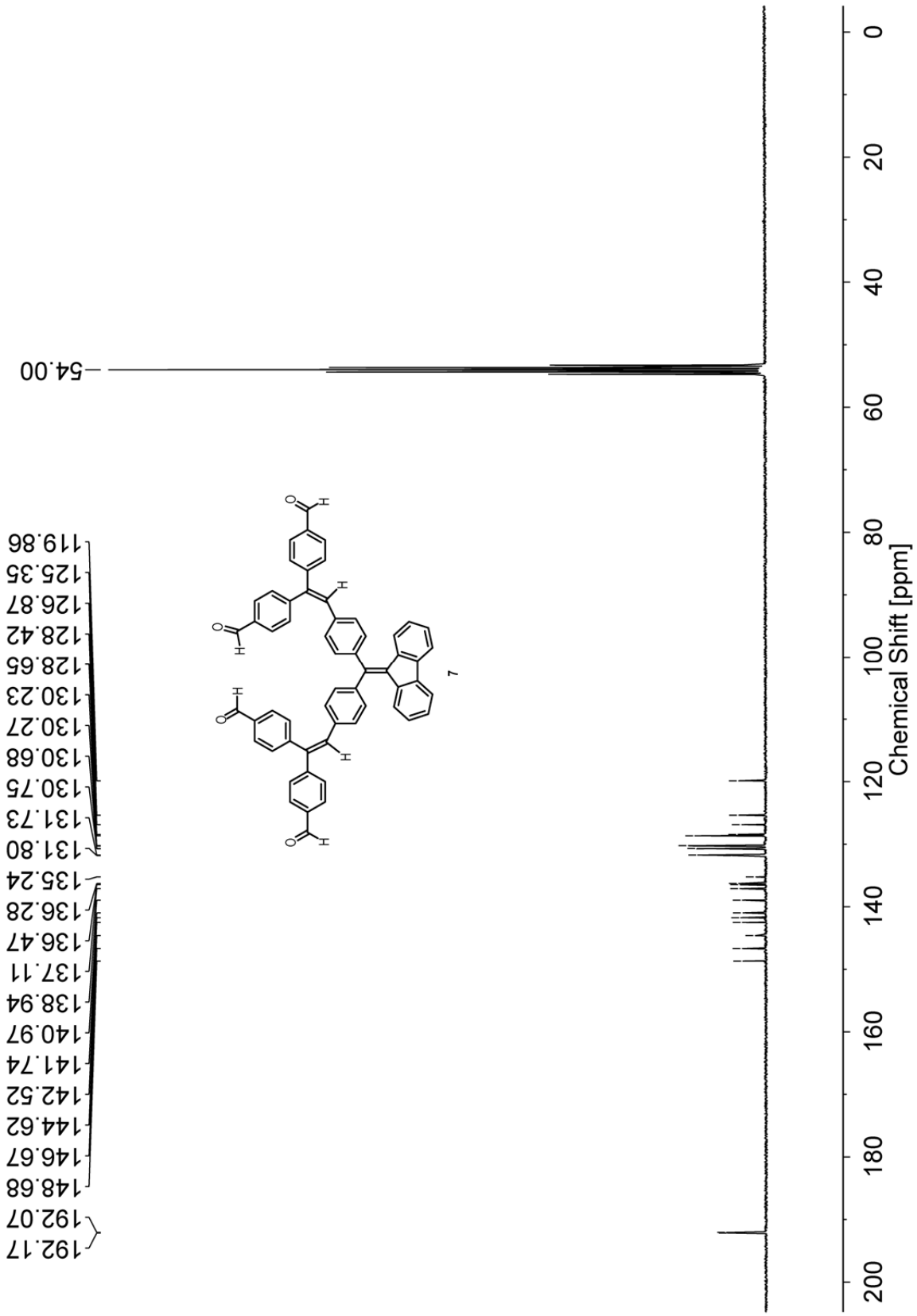

Fig. S-10 ^{13}C NMR (75 MHz, CD_2Cl_2) spectrum of compound **7**.

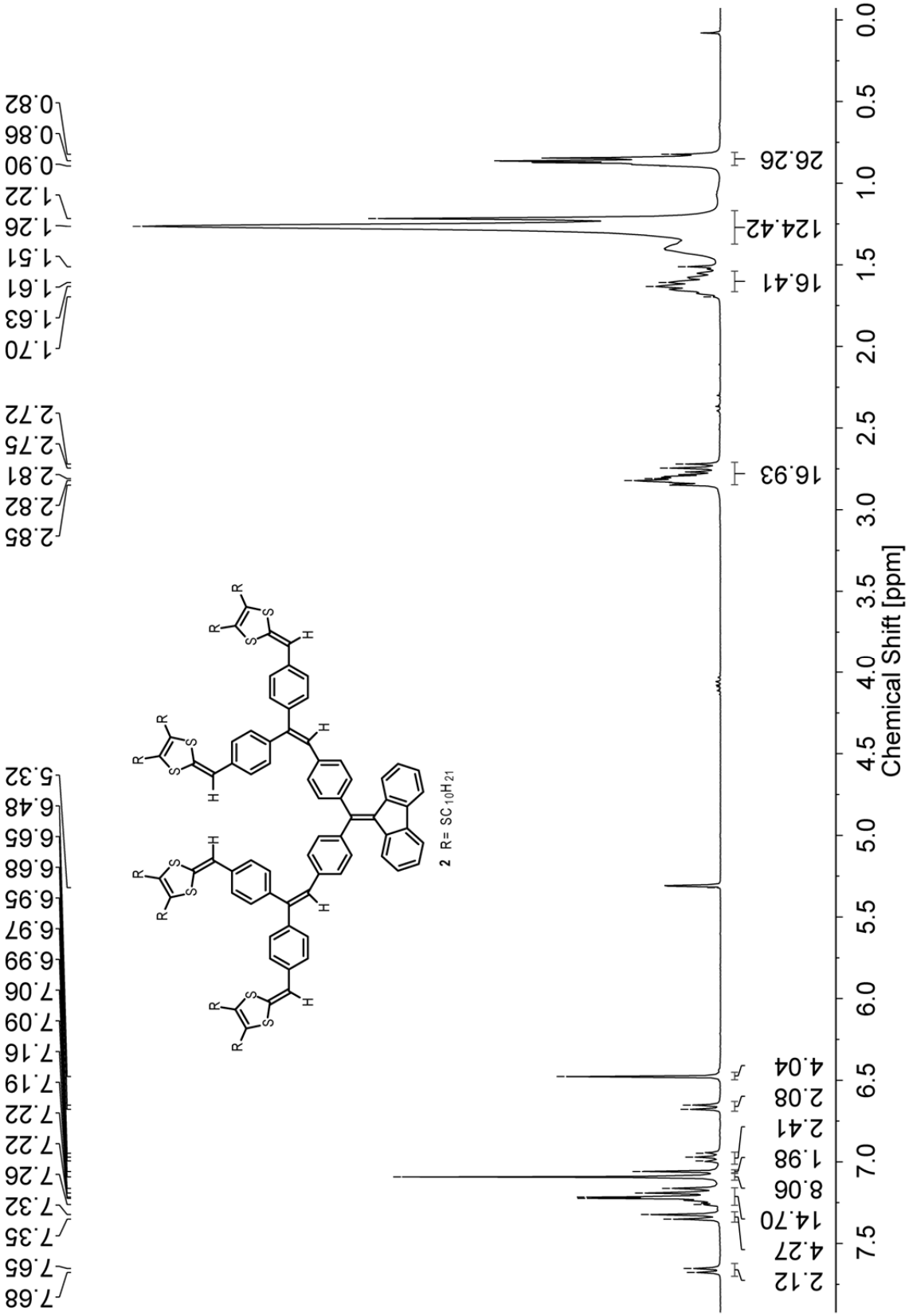

Fig. S-11 ^{1}H NMR (300 MHz, CD_2Cl_2) spectrum of compound **2**.

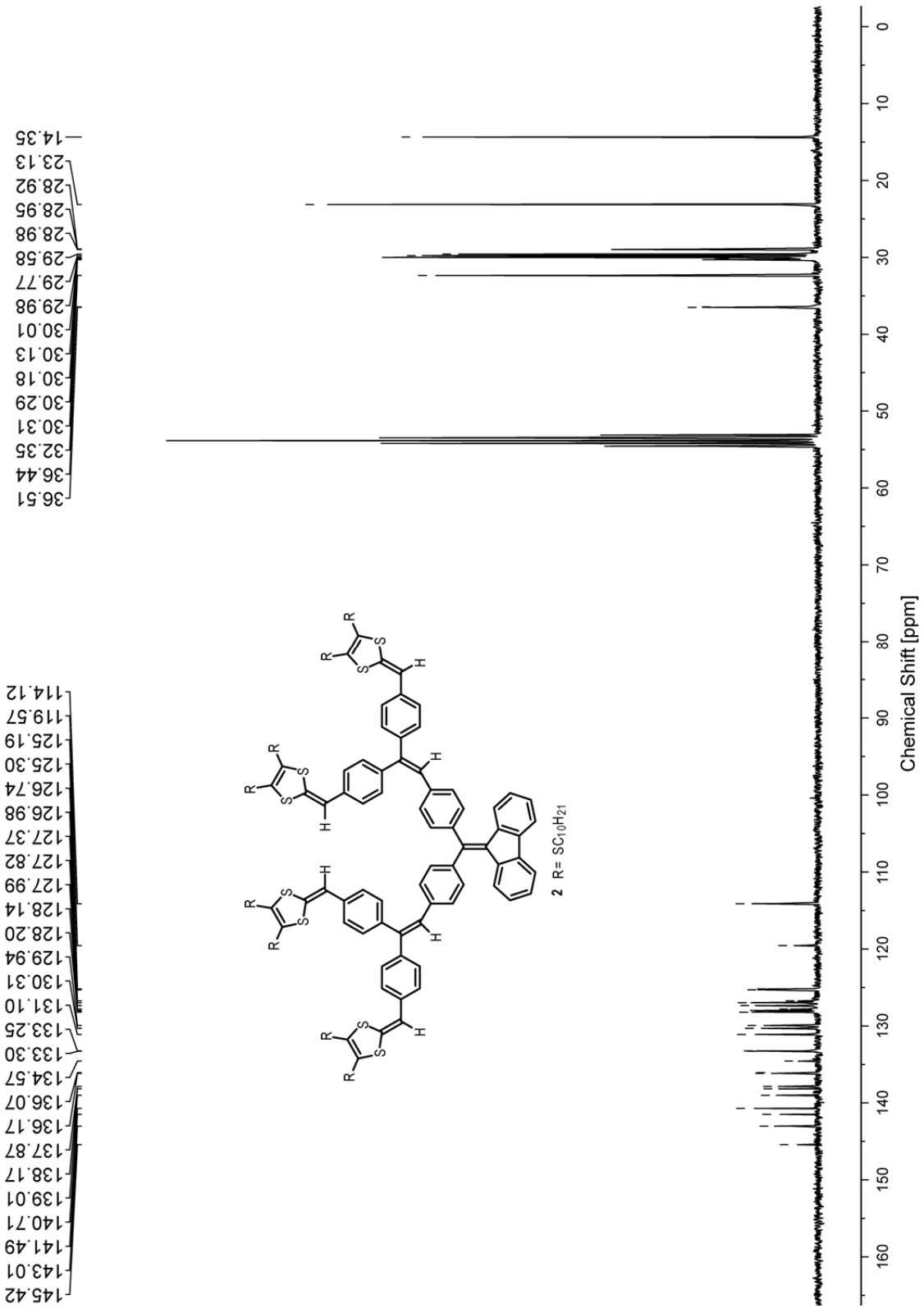

Fig. S-12 ^{13}C NMR (75 MHz, CD_2Cl_2) spectrum of compound **2**.

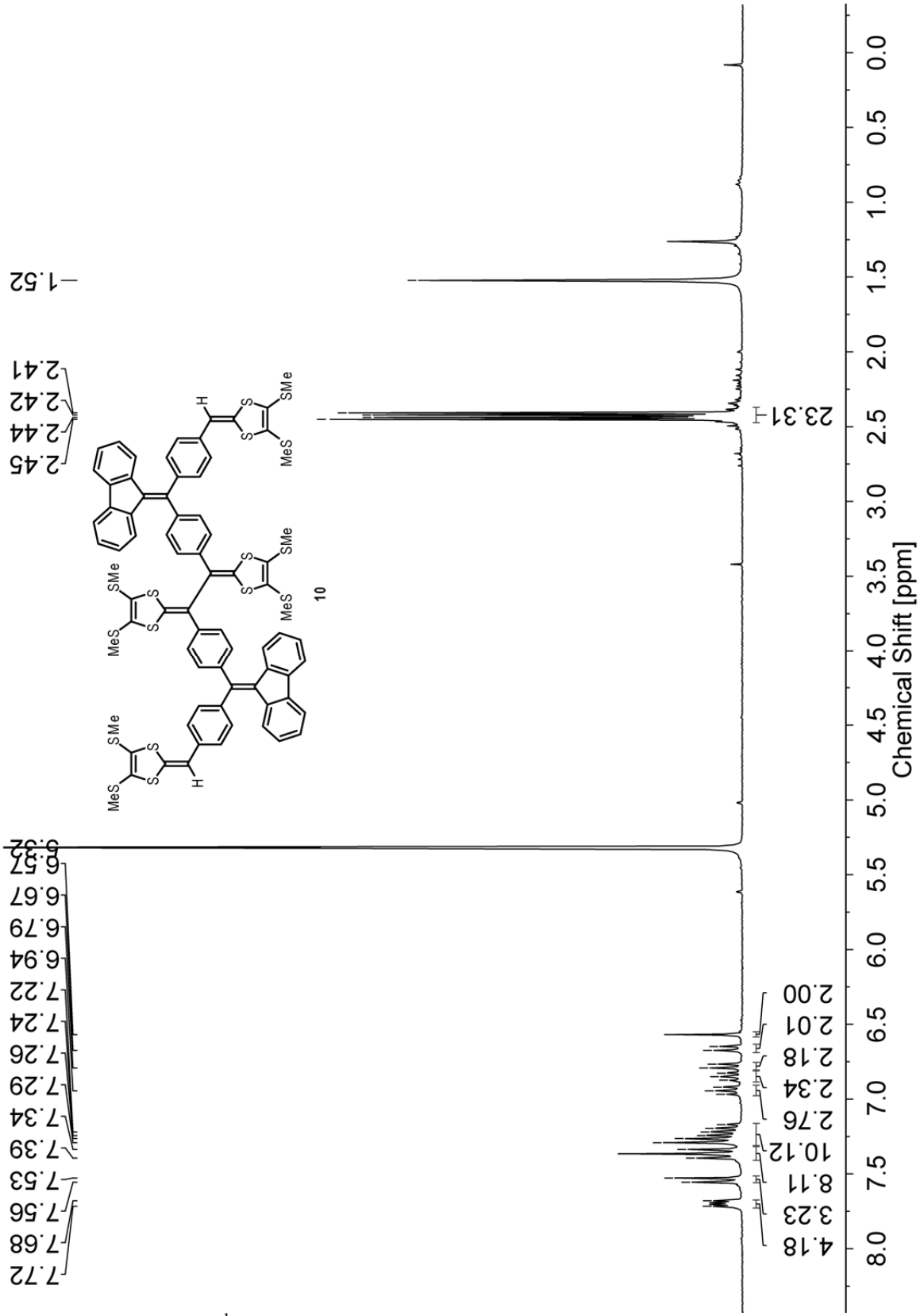

Fig. S-13 ^{1}H NMR (300 MHz, CD_2Cl_2) spectrum of compound **10**.

3. Detailed Results of UV-Vis Titration Experiments

Solutions of compounds **9a** and **2** in $CHCl_3$ were subjected to titrations with nitrobenzene, 2,4-dinitrotoluene (DNT), and 2,4,6-trinitrotoluene (TNT), respectively. Detailed results are summarized in the following figure. Attempts to extract binding constants from the titration data, however, were not successful due to poor spectral fitting.

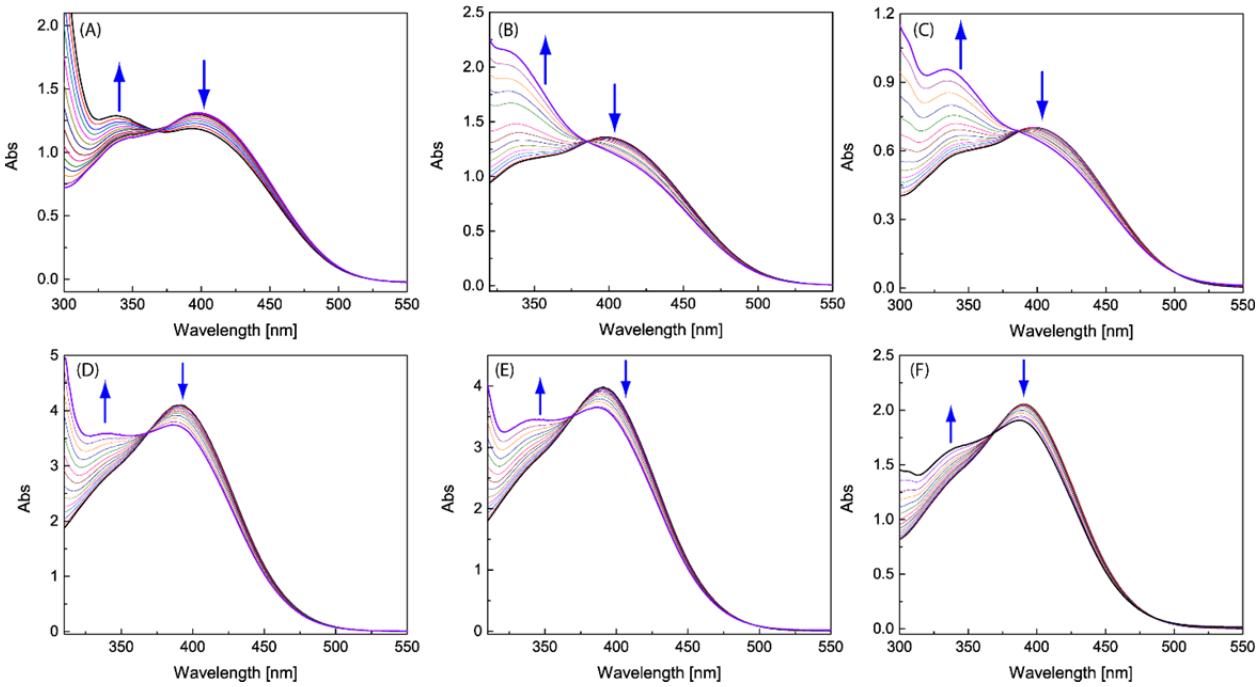

Fig. S-14 (A) UV-Vis titration results of compound **9b** (4.00×10^{-5} M in $CHCl_3$, 298 K) with nitrobenzene (from 0 to 27.4 molar equiv). (B) UV-Vis titration results of compound **9b** (4.00×10^{-5} M in $CHCl_3$, 298 K) with 2,4-dinitrotoluene (from 0 to 11.6 molar equiv). (C) UV-Vis titration results of compound **9b** (2.00×10^{-5} M in $CHCl_3$, 298 K) with 2,4,6-trinitrotoluene (from 0 to 7.43 molar equiv). (D) UV-Vis titration results of compound **2** (3.97×10^{-5} M in $CHCl_3$, 298 K) with nitrobenzene (from 0 to 27.1 molar equiv). (E) UV-Vis titration results of compound **2** UV-Vis titration results of compound **2** (3.97×10^{-5} M in $CHCl_3$, 298 K) 2,4-dinitrotoluene (from 0 to 11.7 molar equiv). (F) UV-Vis titration results of compound **2** UV-Vis titration results of compound **2** (1.98×10^{-5} M in $CHCl_3$, 298 K) 2,4,6-trinitrotoluene (from 0 to 7.5 molar equiv).

4. Detailed Results of Differential Pulse Voltammetric Titrations

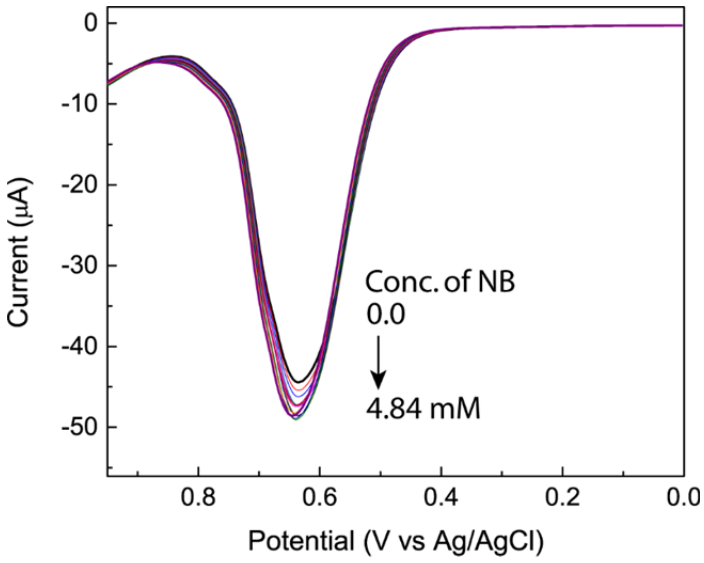

Fig. S-15 DPV profiles showing the responses of **poly-1** thin film (deposited on glassy carbon) to nitrobenzene (NB) at varied concentrations. Experimental conditions: solvent: CH_2Cl_2; electrolyte: Bu_4NBF_4 (0.1 M); reference electrode: Ag/AgCl; counter electrode: Pt wire. Step E: 4 ms; pulse with: 50 ms; pulse amplitude: 50 mV; pulse period: 200 ms; scan rate: 20 mV s^{-1}.

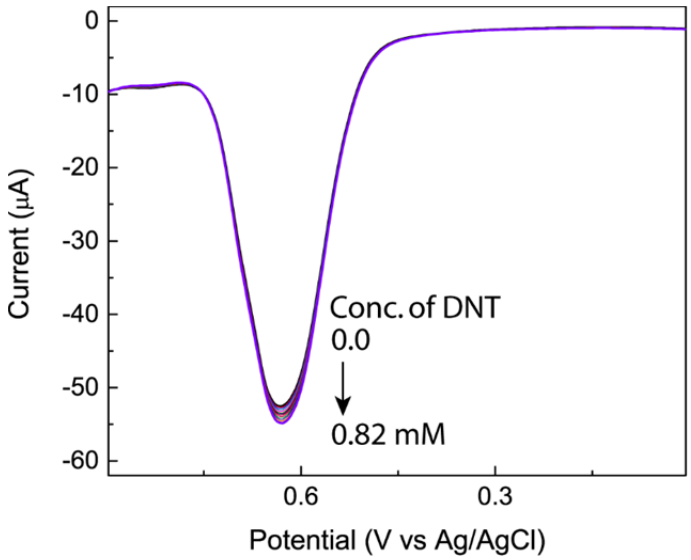

Fig. S-16 DPV profiles showing the responses of **poly-1** thin film (deposited on glassy carbon) to 2,4-dinitrotoluene (DNT) at varied concentrations. Experimental conditions: solvent: CH_2Cl_2; electrolyte: Bu_4NBF_4 (0.1 M); reference electrode: Ag/AgCl; counter electrode: Pt wire. Step E: 4 ms; pulse with: 50 ms; pulse amplitude: 50 mV; pulse period: 200 ms; scan rate: 20 mV s^{-1}.

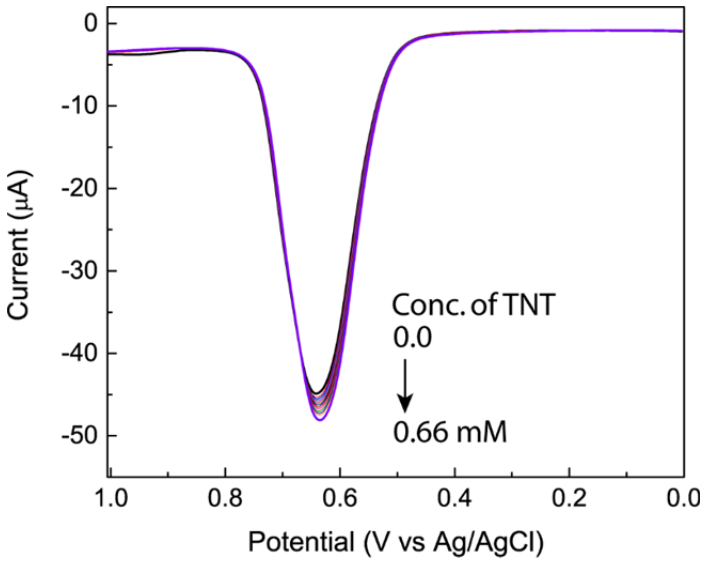

Fig. S-17 DPV profiles showing the responses of **poly-1** thin film (deposited on glassy carbon) to 2,4,6-trinitrotoluene (TNT) at varied concentrations. Experimental conditions: solvent: CH_2Cl_2; electrolyte: Bu_4NBF_4 (0.1 M); reference electrode: Ag/AgCl; counter electrode: Pt wire. Step E: 4 ms; pulse with: 50 ms; pulse amplitude: 50 mV; pulse period: 200 ms; scan rate: 20 mV s^{-1}.

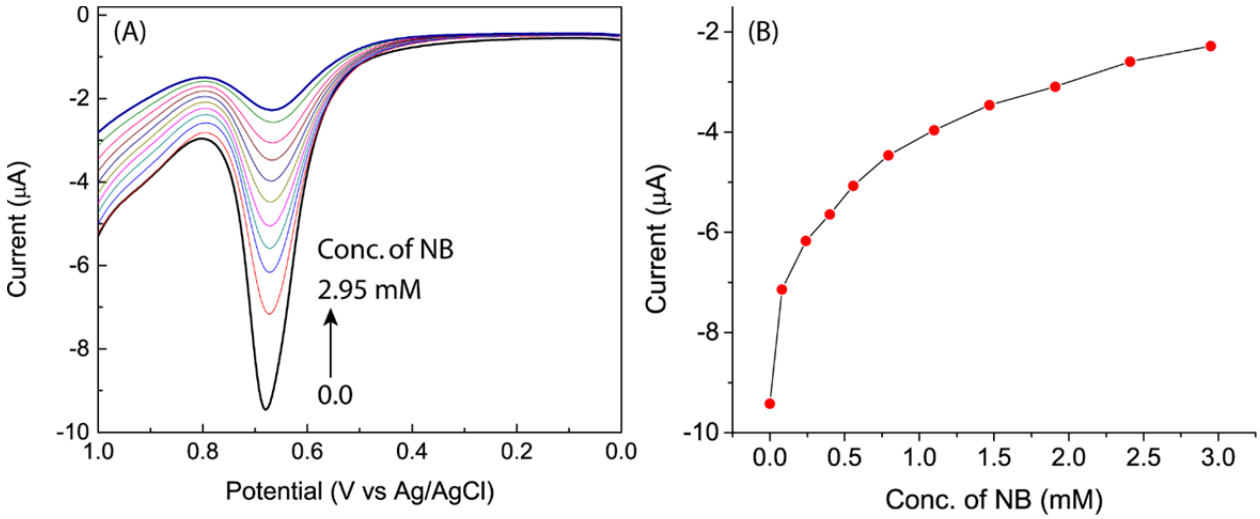

Fig. S-18 (A) DPV profiles showing the responses of **poly-2** thin film (deposited on glassy carbon) to nitrobenzene (NB) at varied concentrations. Experimental conditions: solvent: CH_2Cl_2; electrolyte: Bu_4NBF_4 (0.1 M); reference electrode: Ag/AgCl; counter electrode: Pt wire. Step E: 4 ms; pulse with: 50 ms; pulse amplitude: 50 mV; pulse period: 200 ms; scan rate: 20 mV s^{-1}. (B) Plot of DPV peak current against the concentration of nitrobenzene (NB).

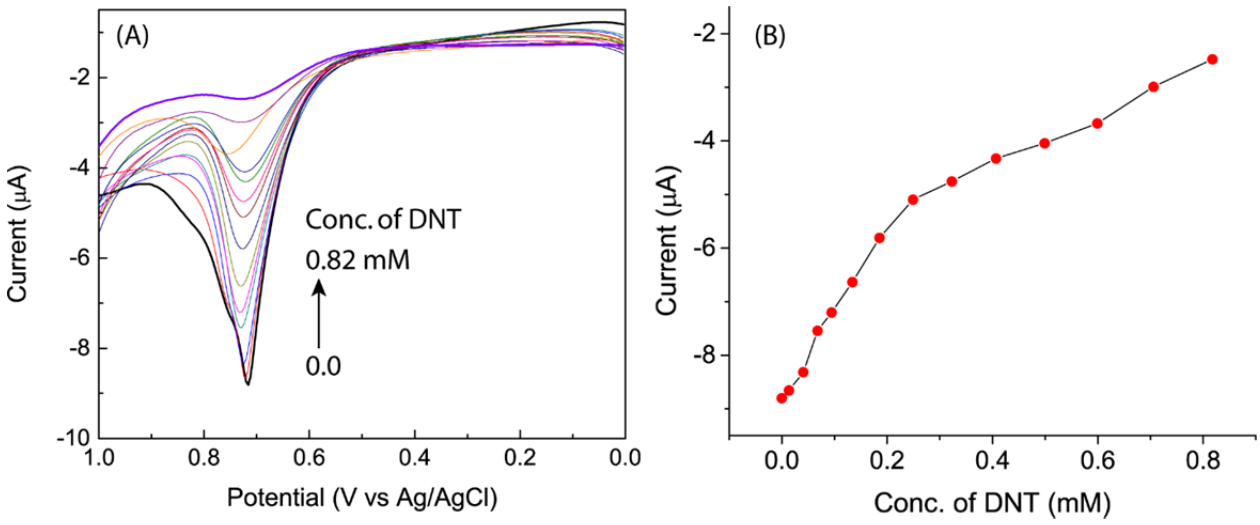

Fig. S-19 (A) DPV profiles showing the responses of **poly-2** thin film (deposited on glassy carbon) to 2,4-dinitrotoluene (DNT) at varied concentrations. Experimental conditions: solvent: CH_2Cl_2; electrolyte: Bu_4NBF_4 (0.1 M); reference electrode: Ag/AgCl; counter electrode: Pt wire. Step E: 4 ms; pulse with: 50 ms; pulse amplitude: 50 mV; pulse period: 200 ms; scan rate: 20 mV s^{-1}. (B) Plot of DPV peak current against the concentration of 2,4-dinitrotoluene (DNT).

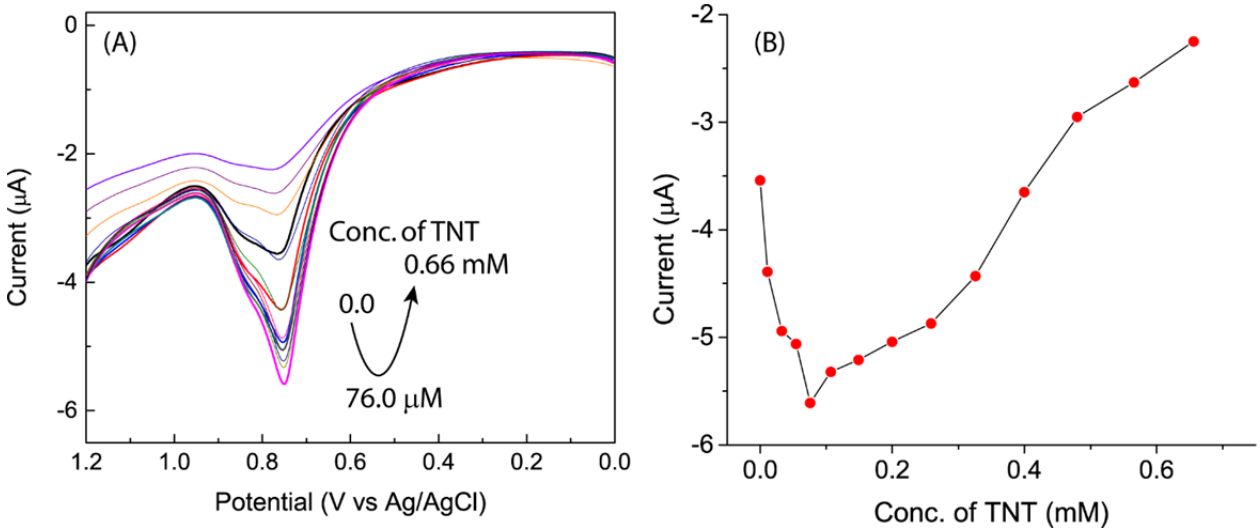

Fig. S-20 (A) DPV profiles showing the responses of **poly-2** thin film (deposited on glassy carbon) to 2,4,6-trinitrotoluene (TNT) at varied concentrations. Experimental conditions: solvent: CH_2Cl_2; electrolyte: Bu_4NBF_4 (0.1 M); reference electrode: Ag/AgCl; counter electrode:

Pt wire. Step E: 4 ms; pulse with: 50 ms; pulse amplitude: 50 mV; pulse period: 200 ms; scan rate: 20 mV s^{-1}. (B) Plot of DPV peak current against the concentration of 2,4,6-trinitrotoluene (TNT).

5. Optical Profiling and SEM Images of Polymer Films

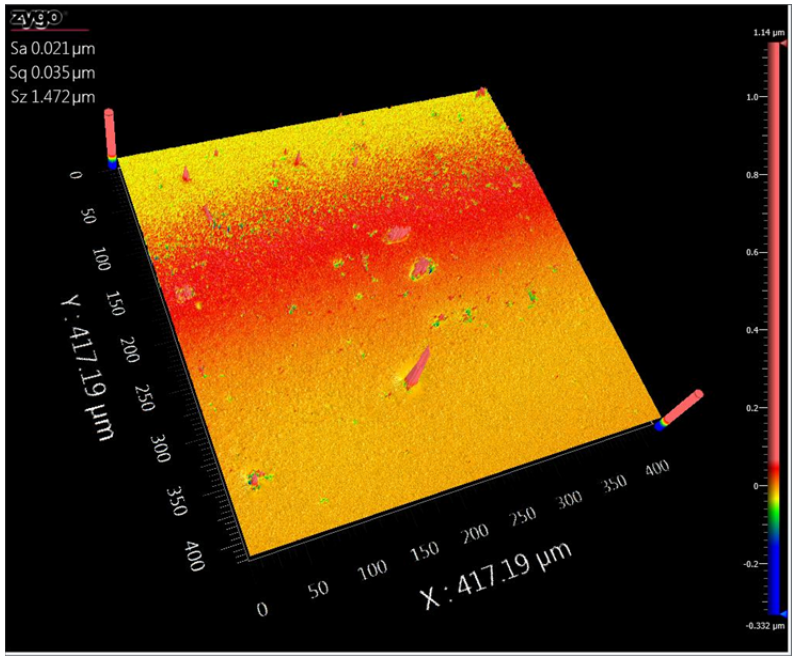

Fig. S-21 Surface morphology of the thin film of **poly-1** electrochemically deposited on an ITO substrate.

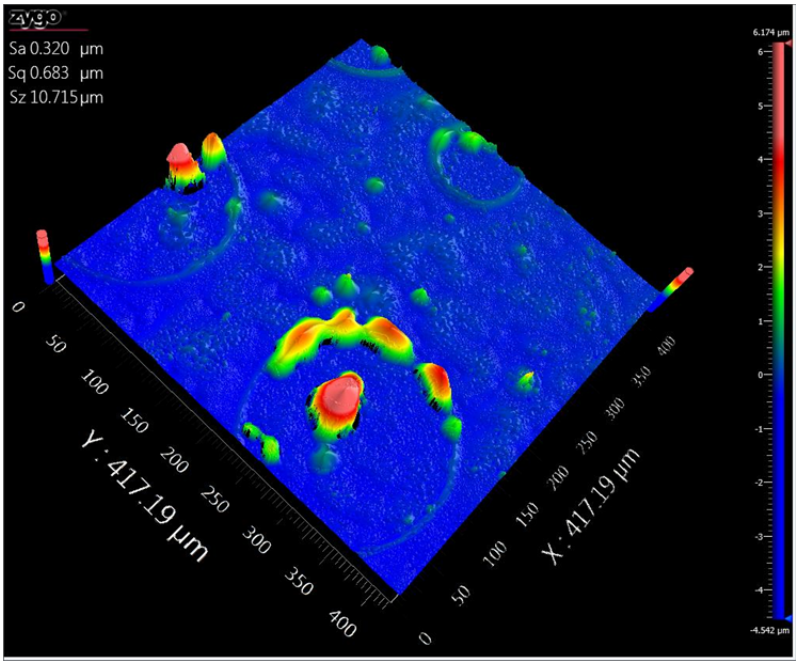

Fig. S-22 Surface morphology of the thin film of **poly-2** electrochemically deposited on an ITO substrate.

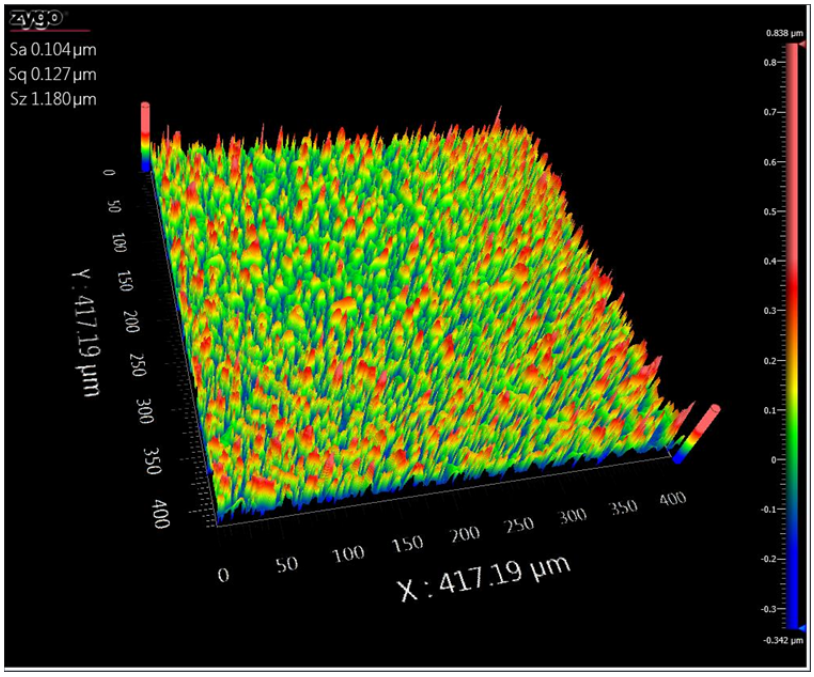

(A)

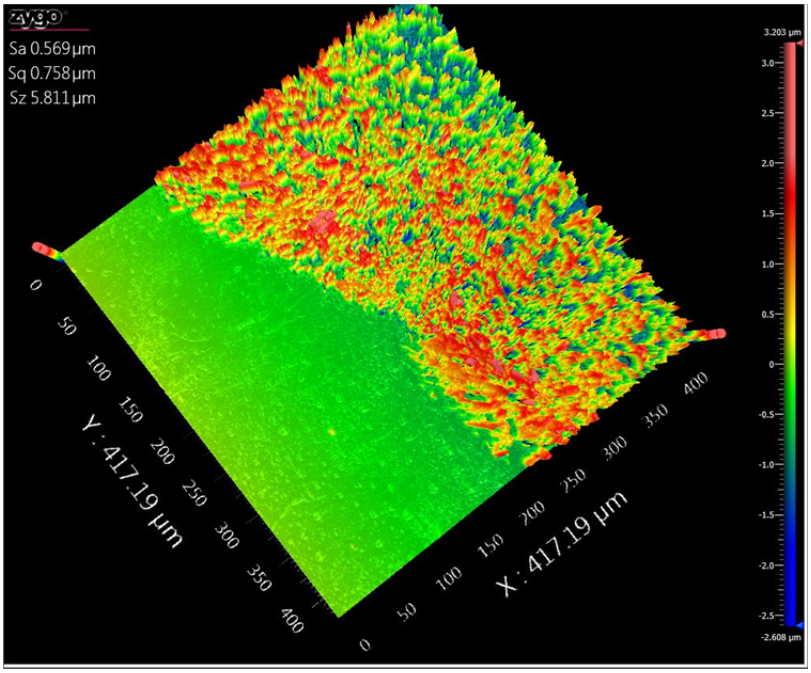

(B)

Fig. S-23 Optical profiling images for the surface morphology of the double-layer thin film of **poly-2**|**poly-1** on an ITO substrate. (A) Scanned in the central area of the film, and (B) scanned on the edge of the film.

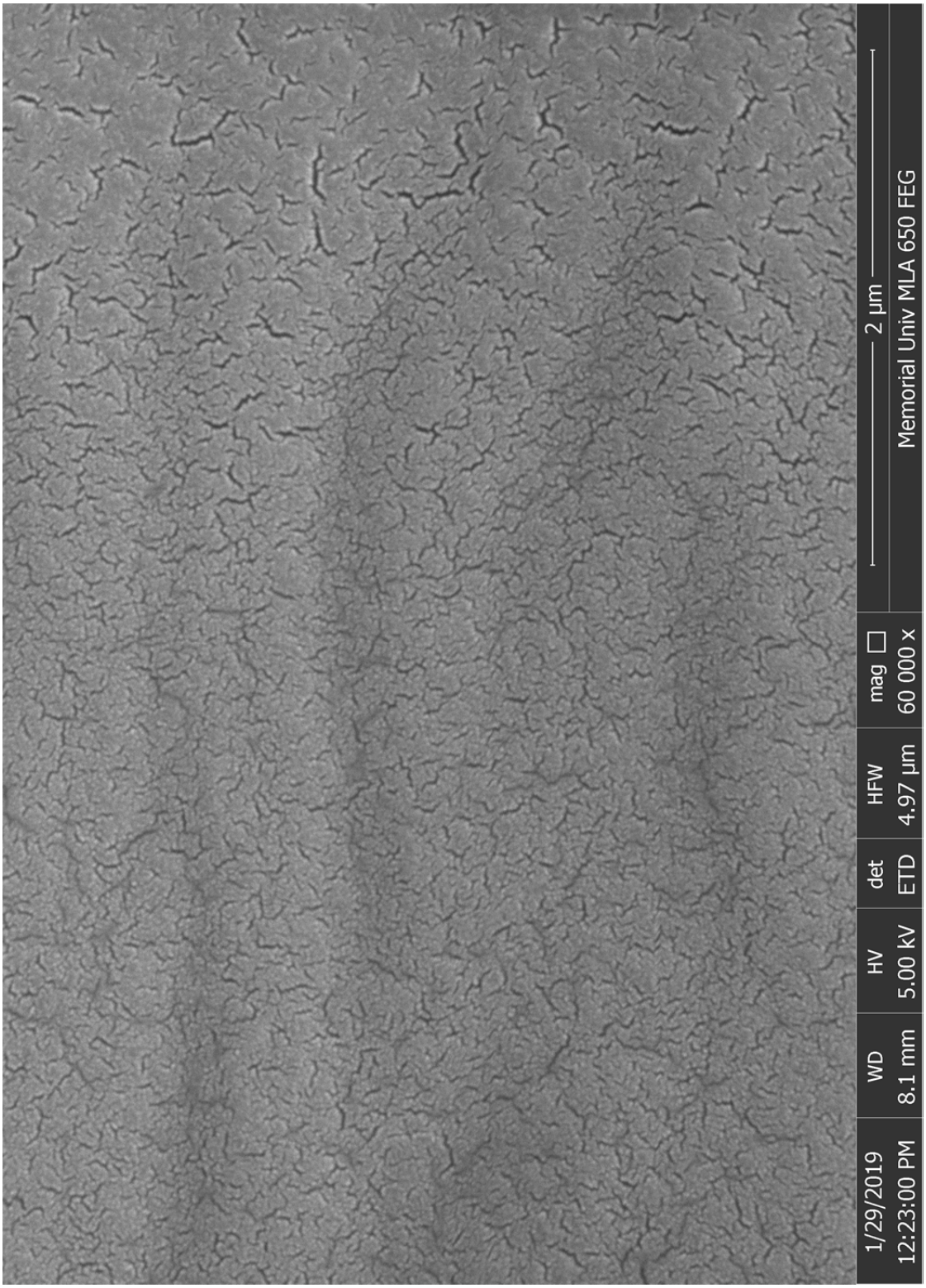

Fig. S-24 SEM image of the surface of the double-layer thin film of **poly-2**|**poly-1** on an ITO substrate.

Appendix II

Supporting Information for Chapter 3

Redox-active Dithiafulvenyl-functionalized 1,3,6,8-Tetraphenylpyrene Derivatives: Synthesis, Spectroscopic, and Electrochemical Redox Properties

Table of Content

1. NMR Spectra for New Compounds

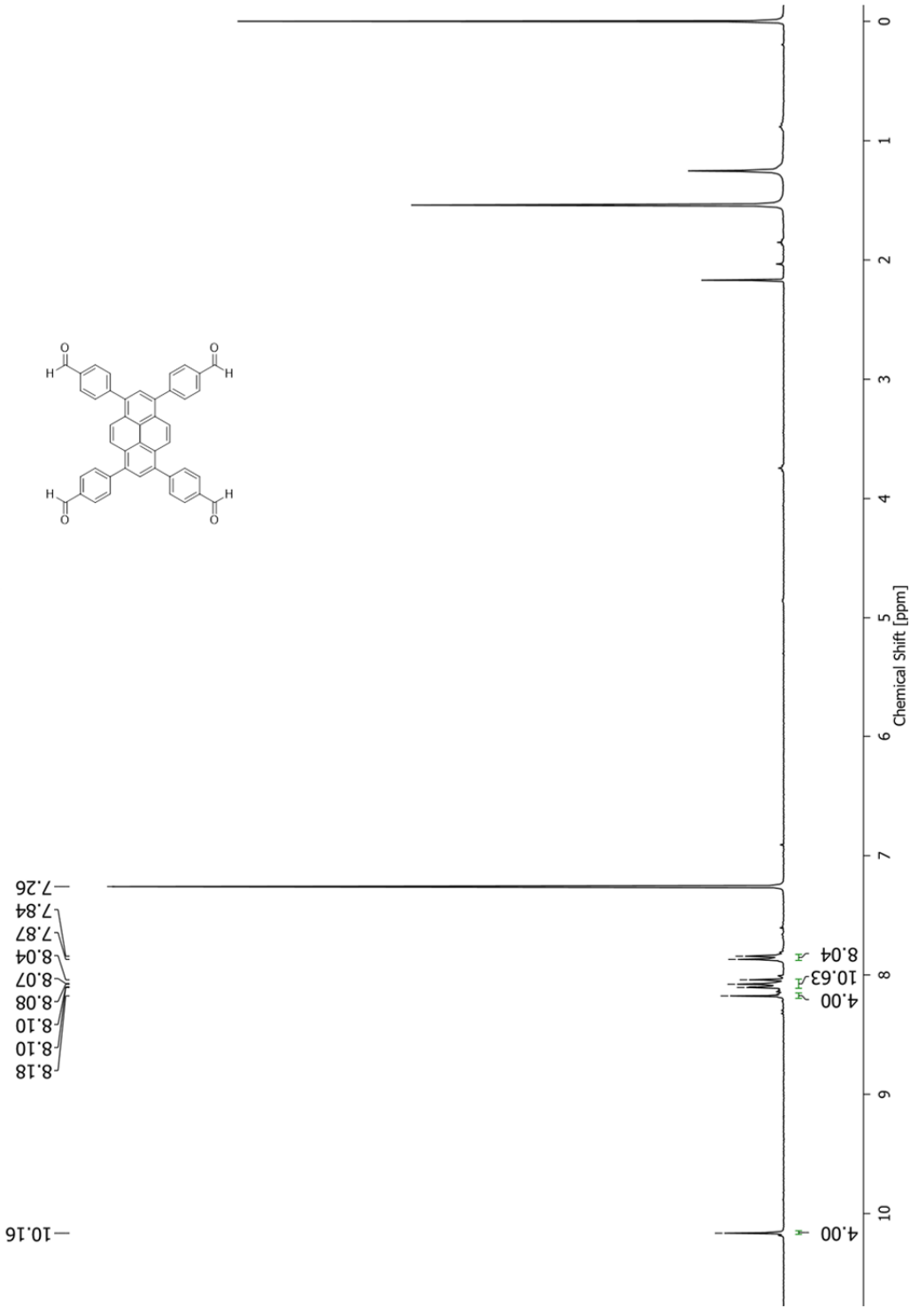

Fig. S-1 ^{1}H NMR (300 MHz, $CDCl_3$) of compound **5a**.

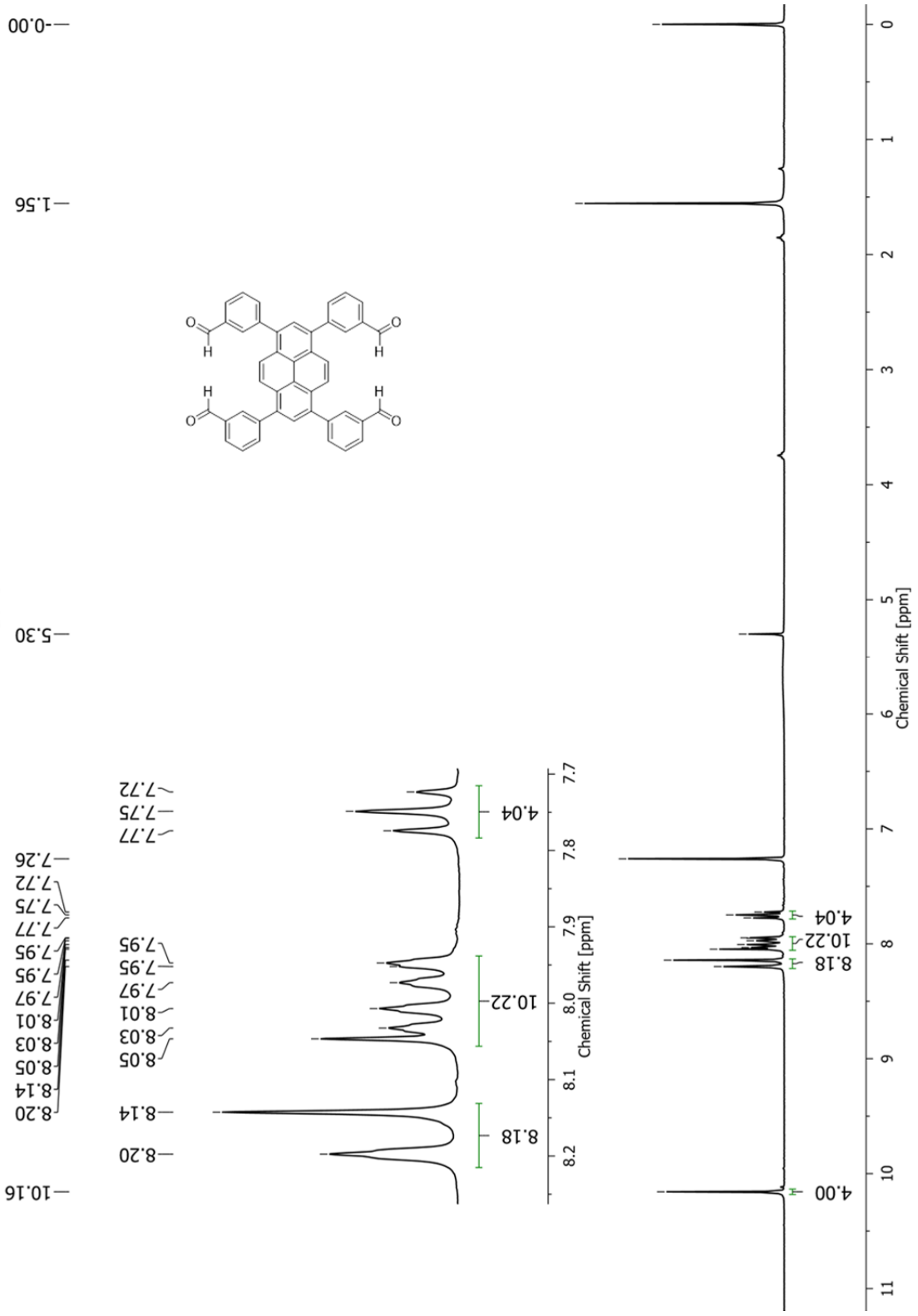

Fig. S-2 ^{1}H NMR (300 MHz, $CDCl_3$) of compound **5b**.

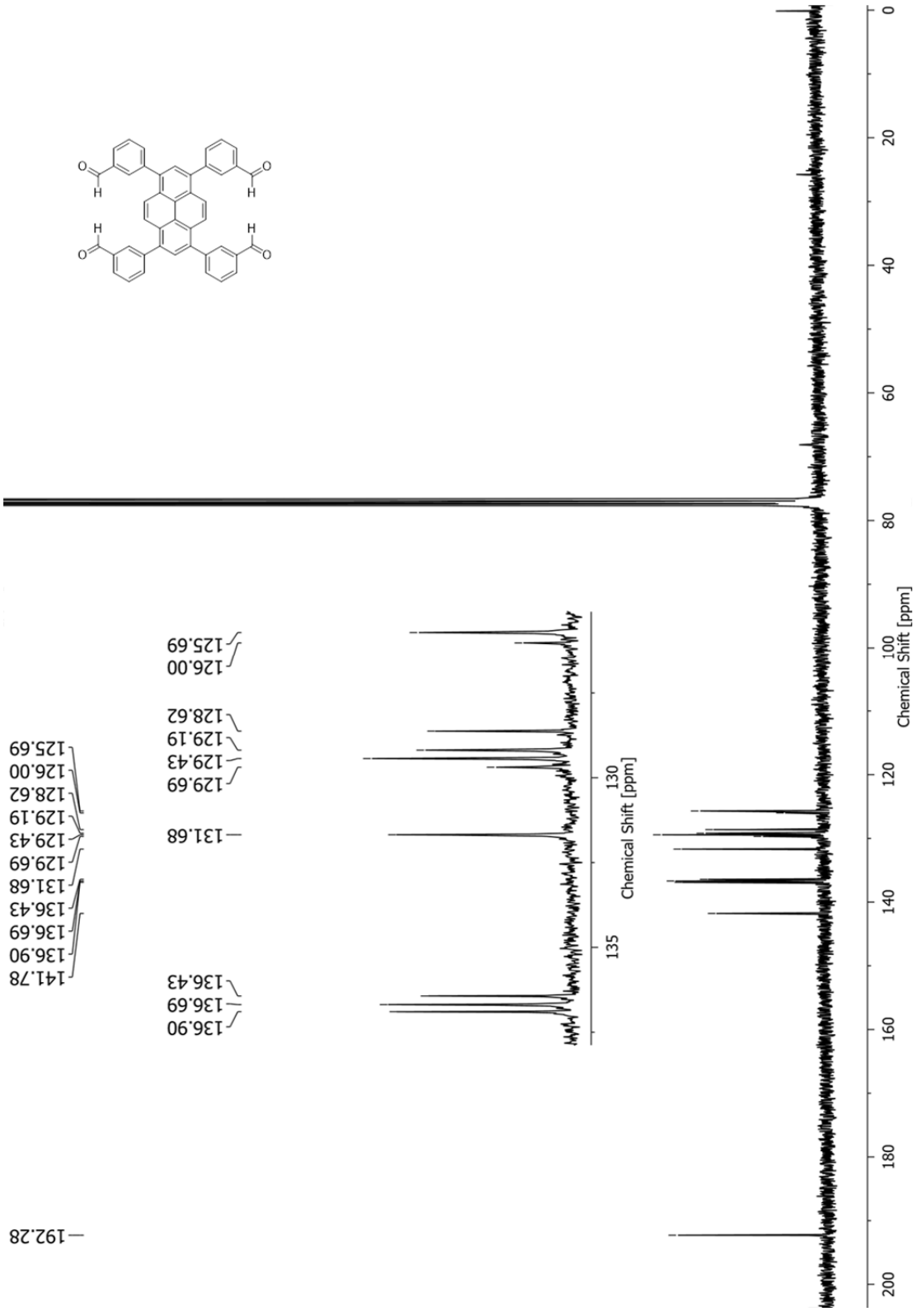

Fig. S-3 ^{13}C NMR (75 MHz, $CDCl_3$) of compound **5b**.

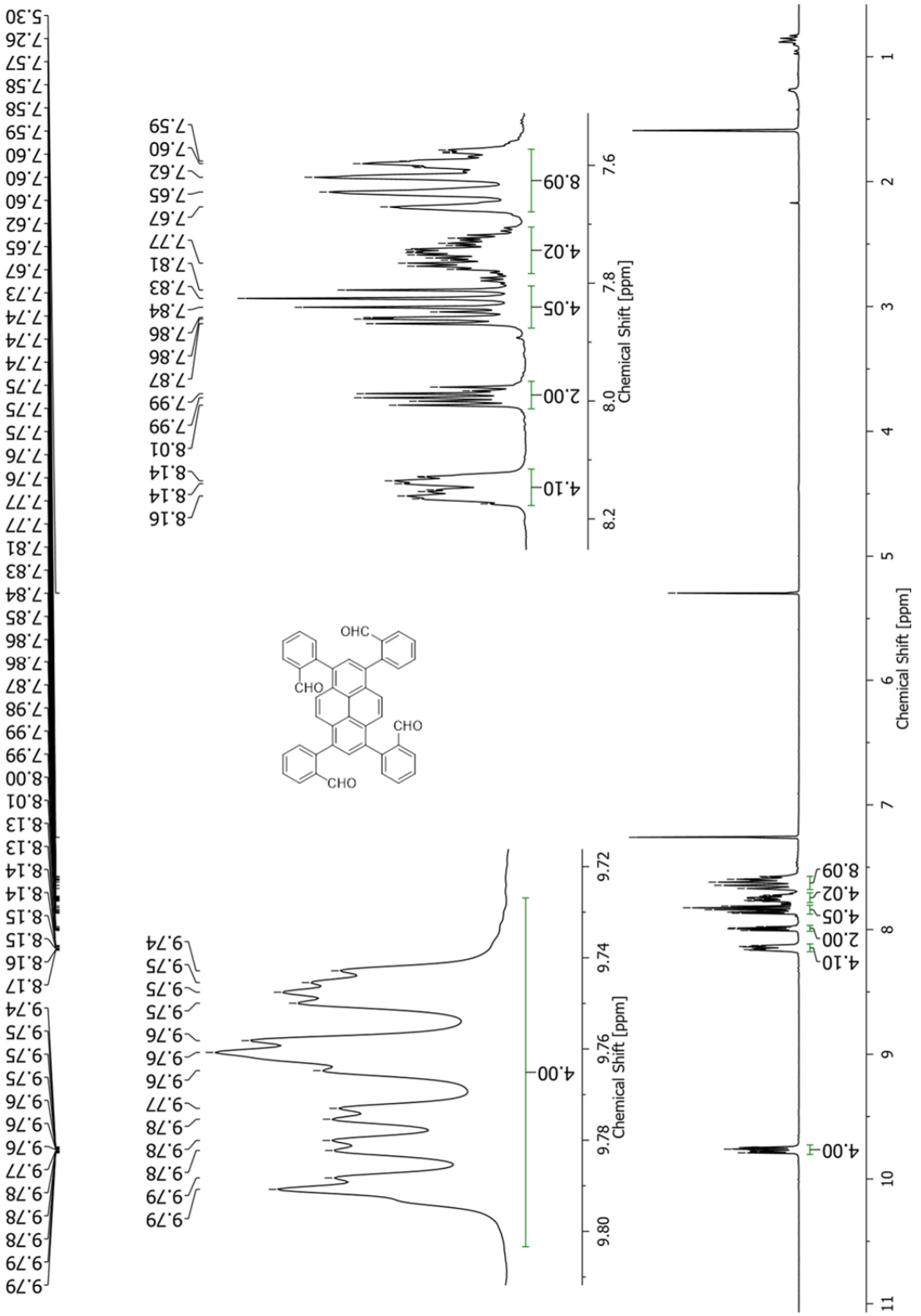

Fig. S-4 ^{1}H NMR (300 MHz, $CDCl_3$) of compound **5c**.

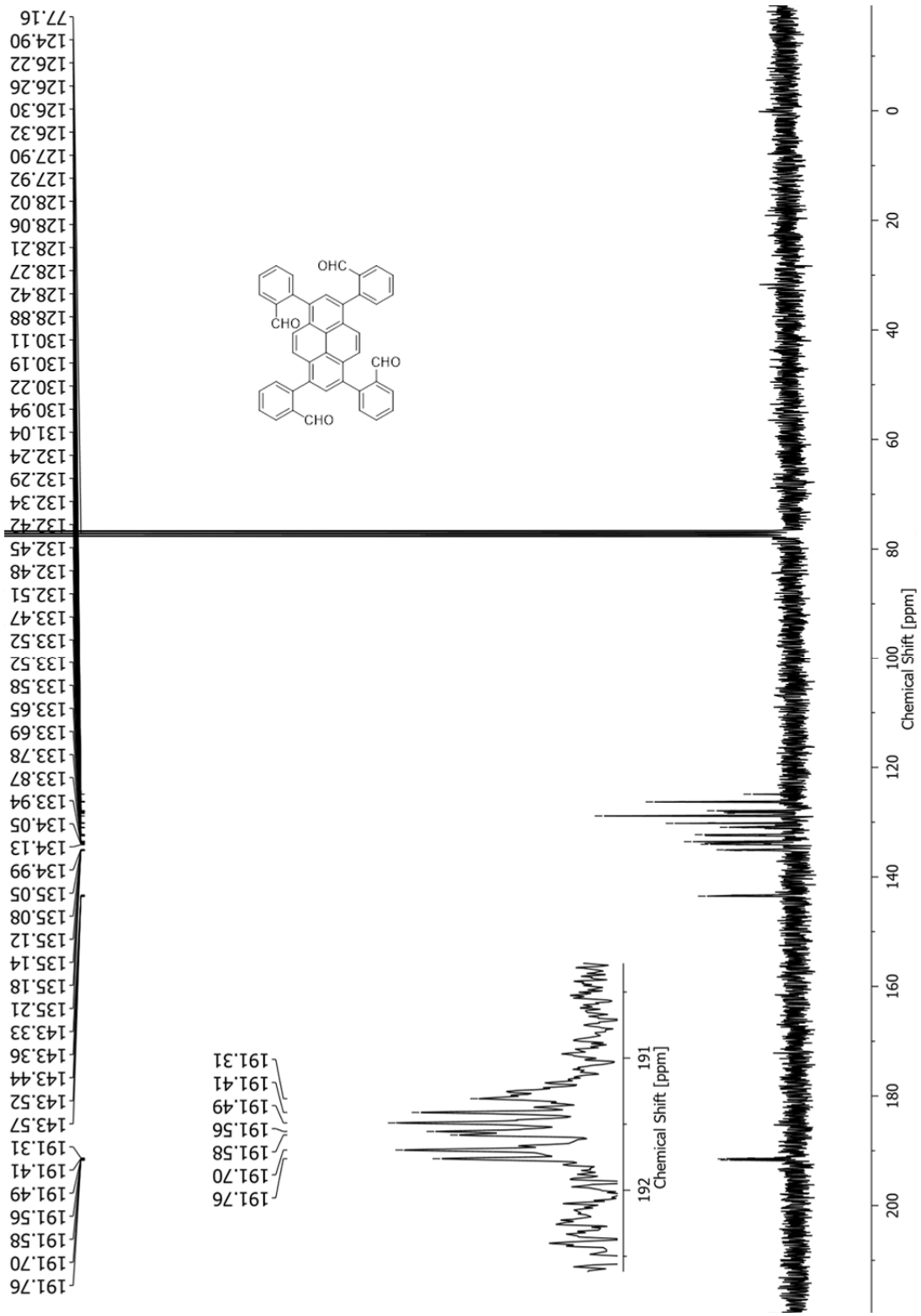

Fig. S-5 ^{13}C NMR (75 MHz, $CDCl_3$) of compound **5c**.

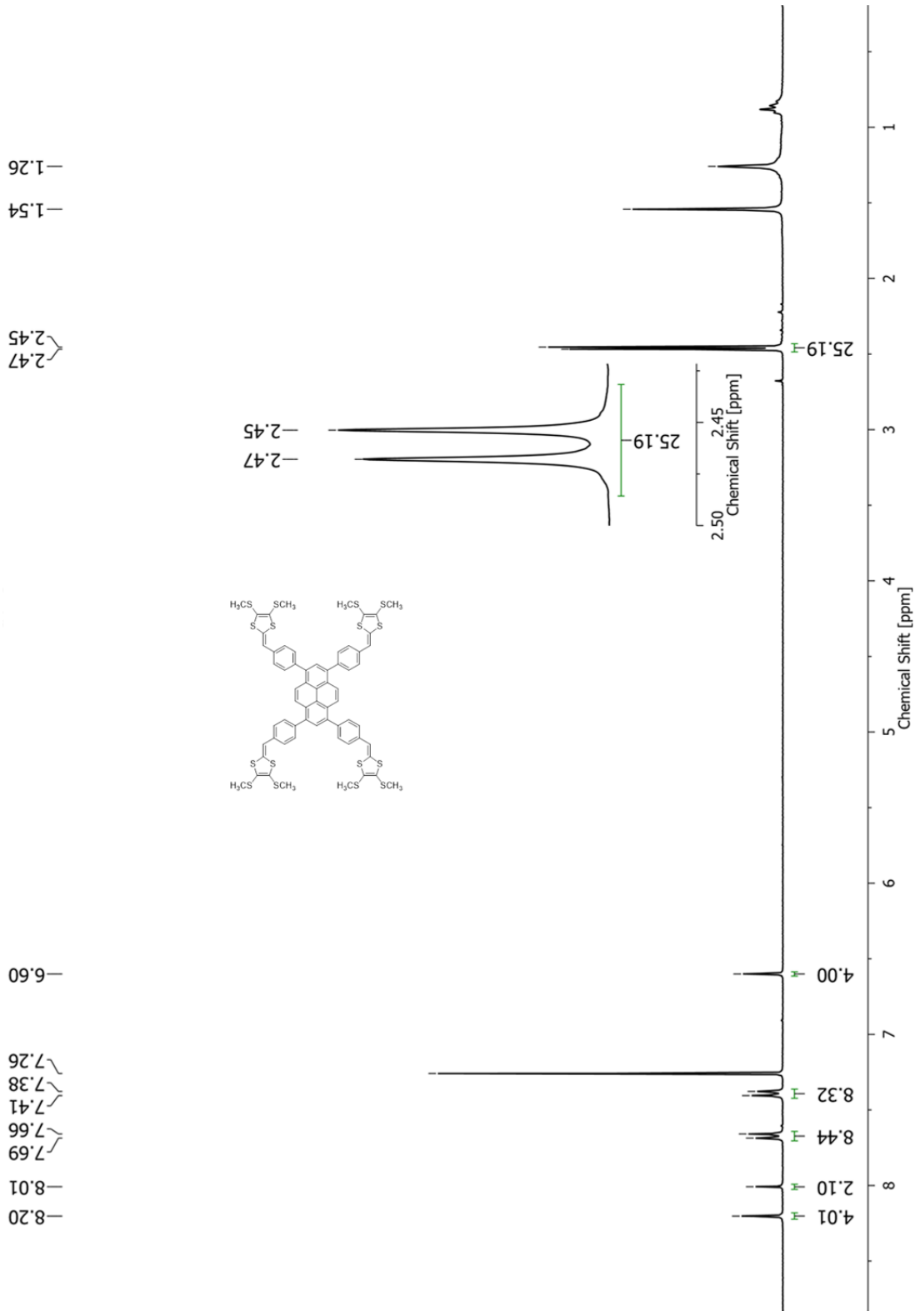

Fig. S-6 ^{1}H NMR (300 MHz, $CDCl_3$) of compound **7a**.

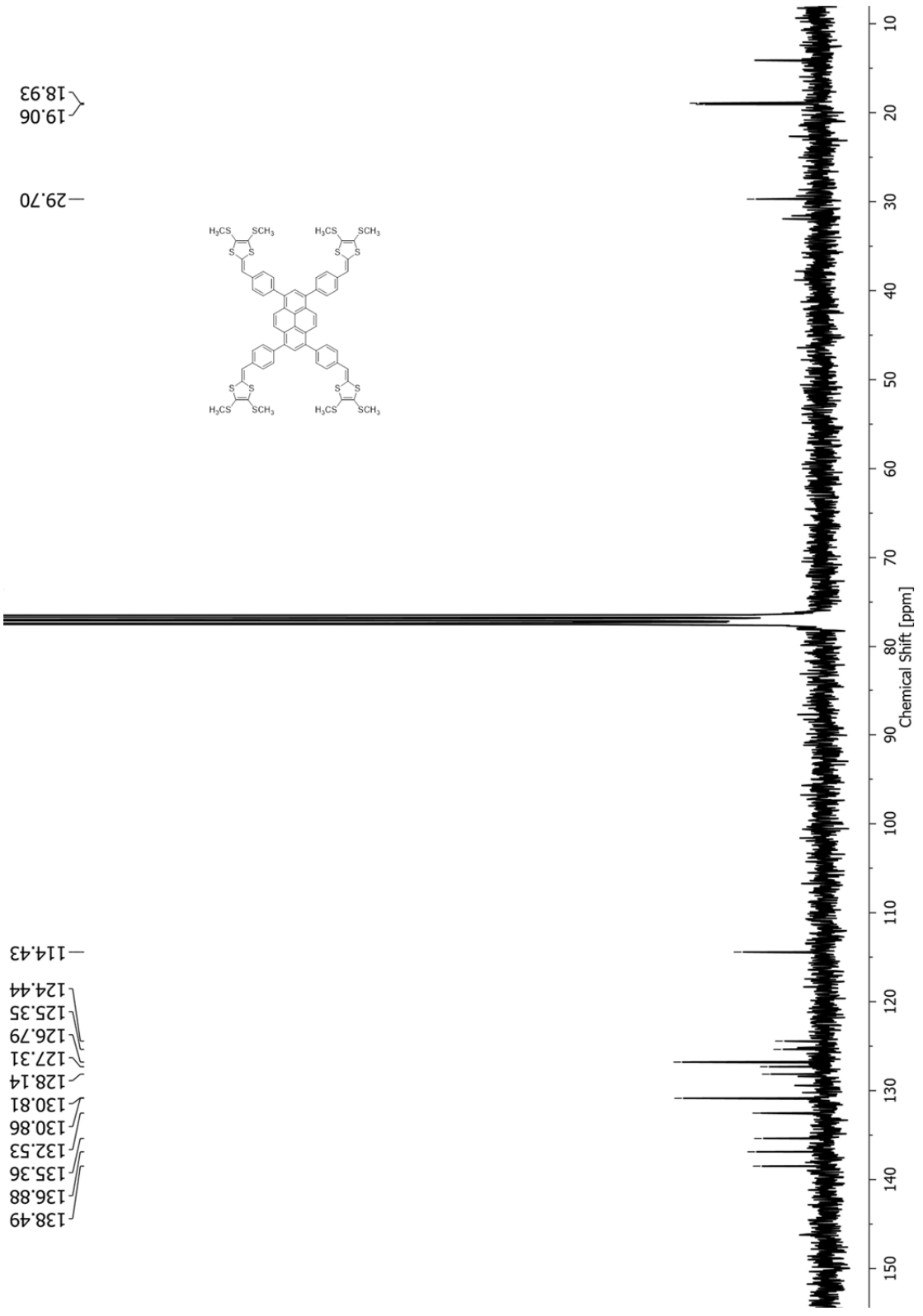

Fig. S-7 ^{13}C NMR (75 MHz, $CDCl_3$) of compound **7a**.

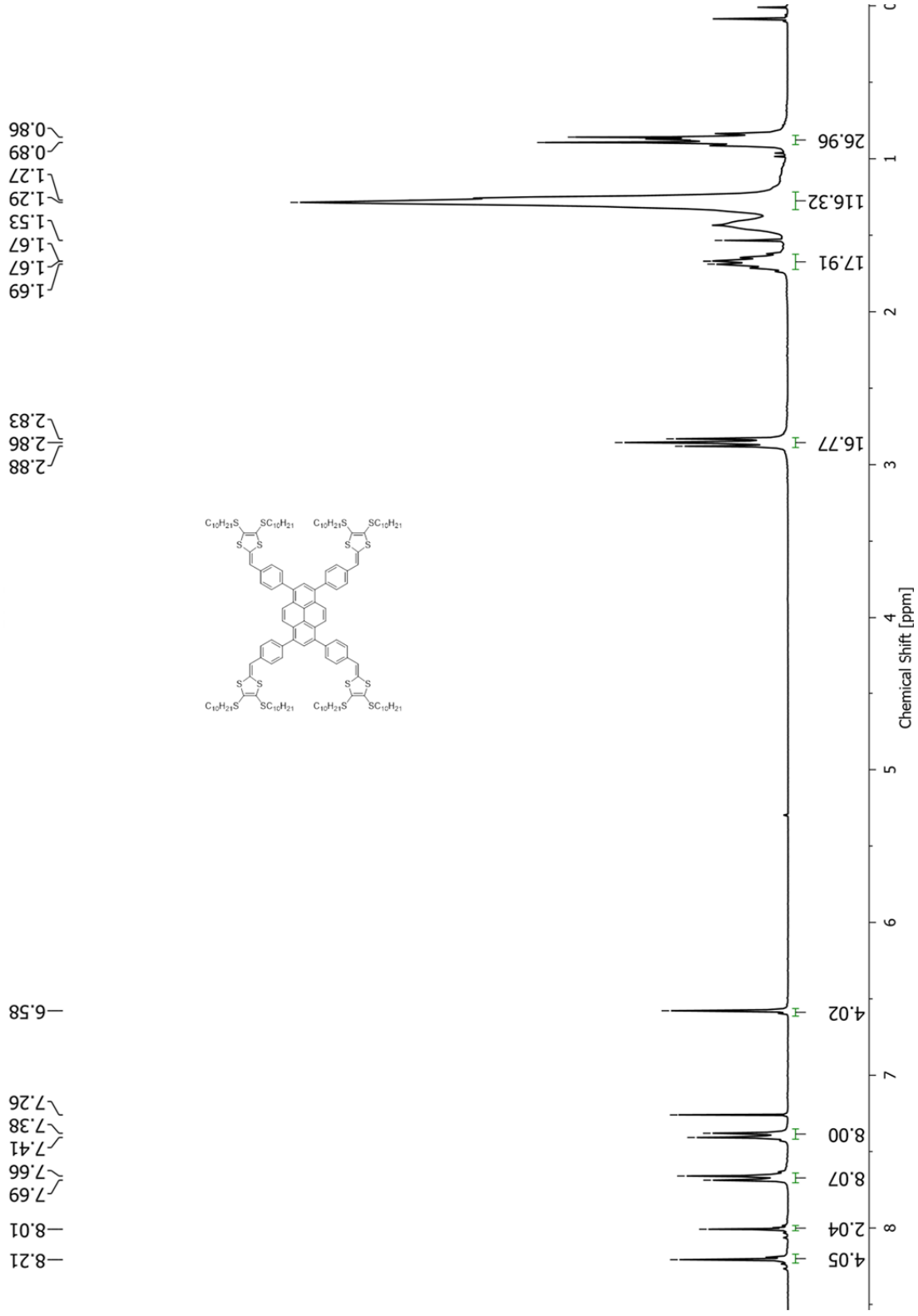

Fig. S-8 ^{1}H NMR (300 MHz, $CDCl_3$) of compound **7b**.

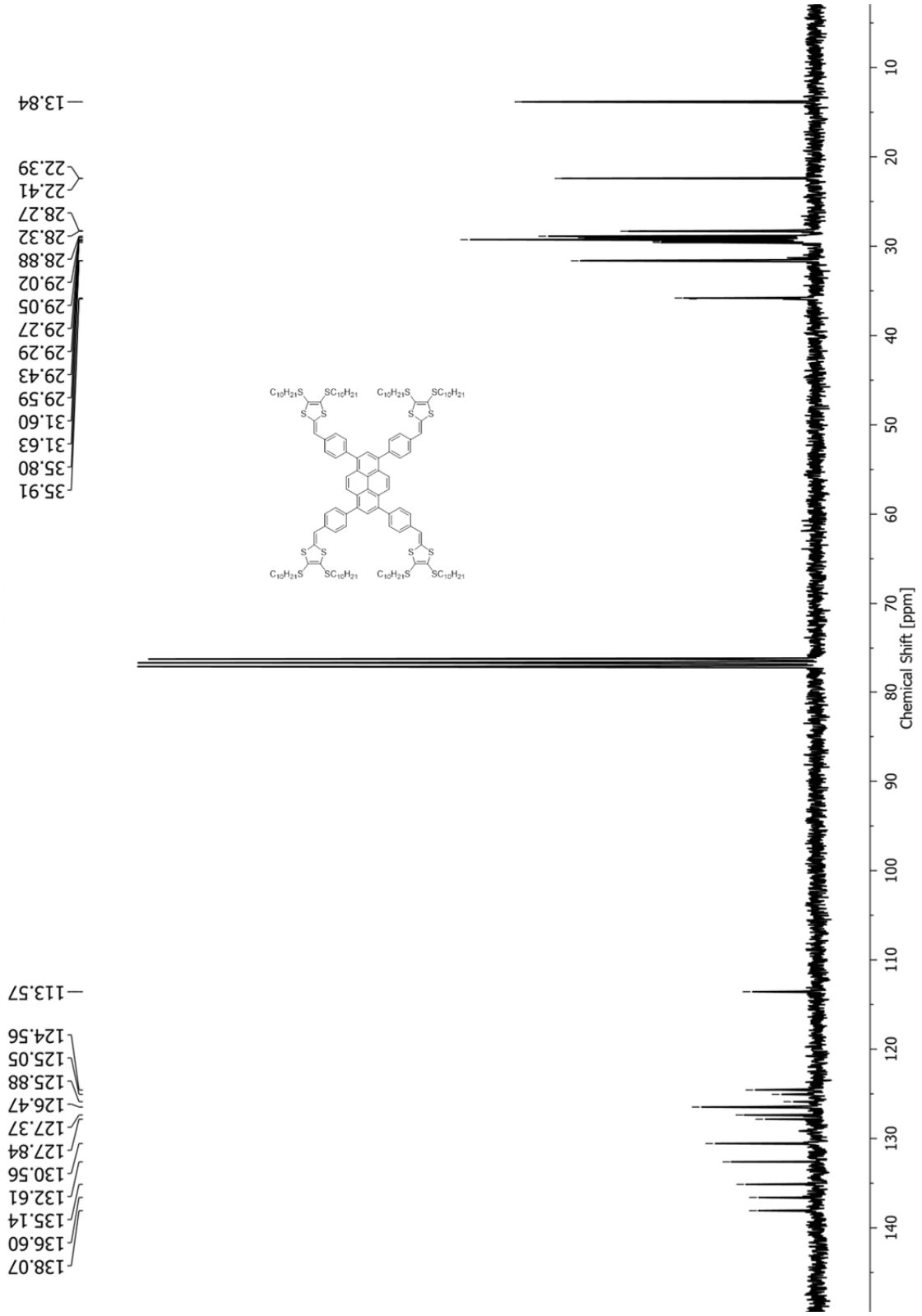

Fig. S-9 ^{13}C NMR (75 MHz, $CDCl_3$) of compound **7b**.

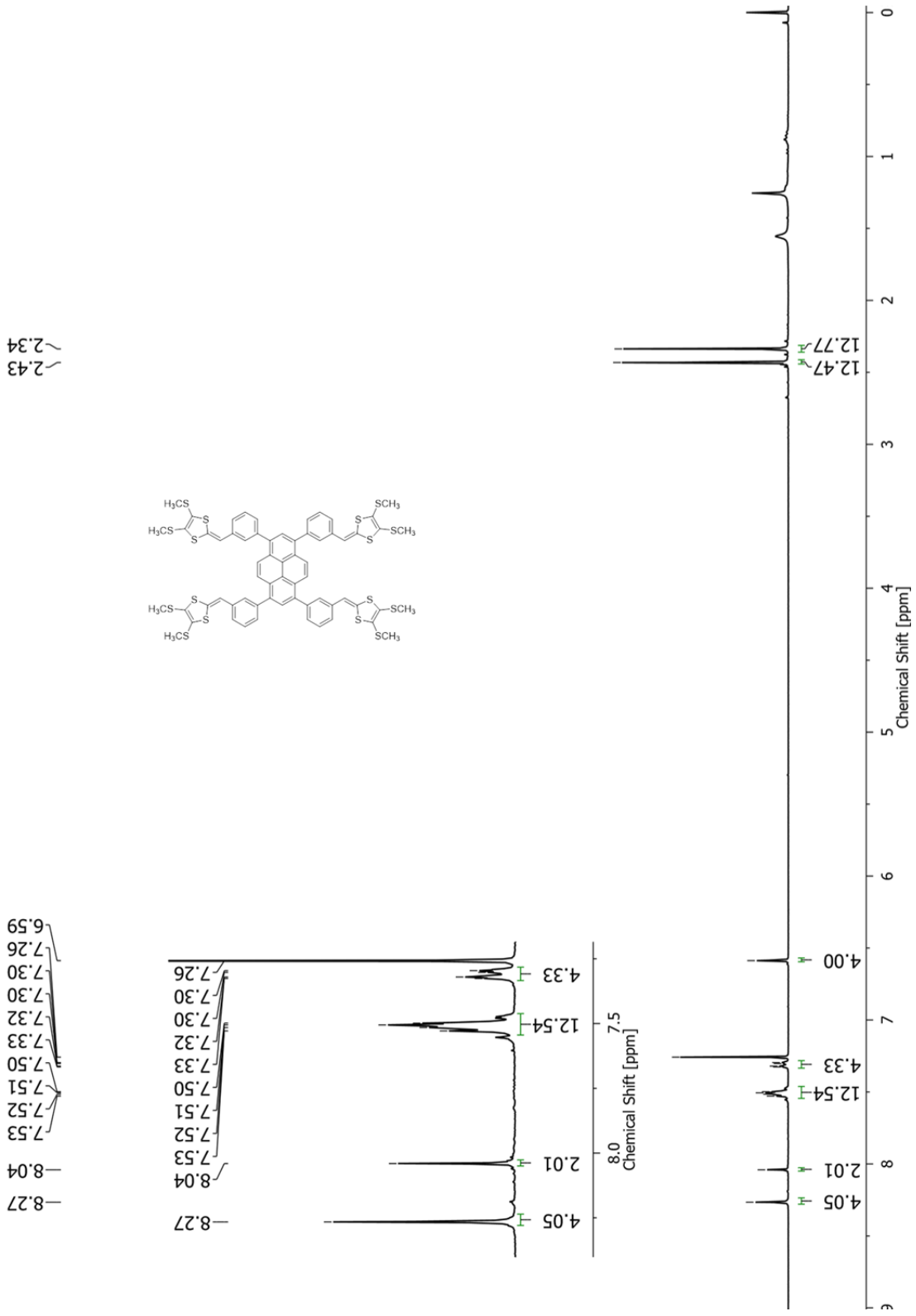

Fig. S-10 ^{1}H NMR (300 MHz, $CDCl_3$) of compound **8a**.

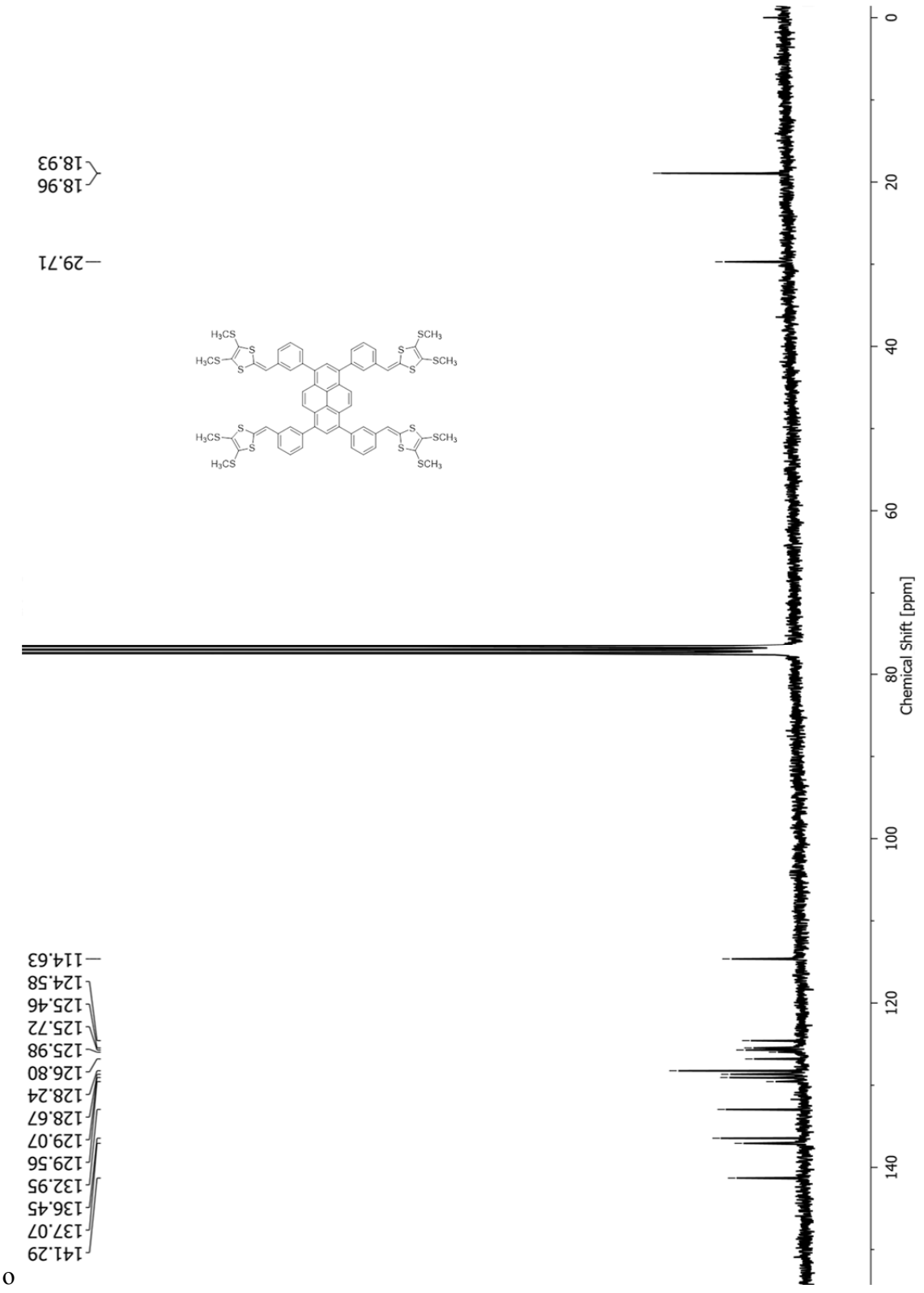

Fig. S-11 ^{13}C NMR (75 MHz, $CDCl_3$) of compound **8a**.

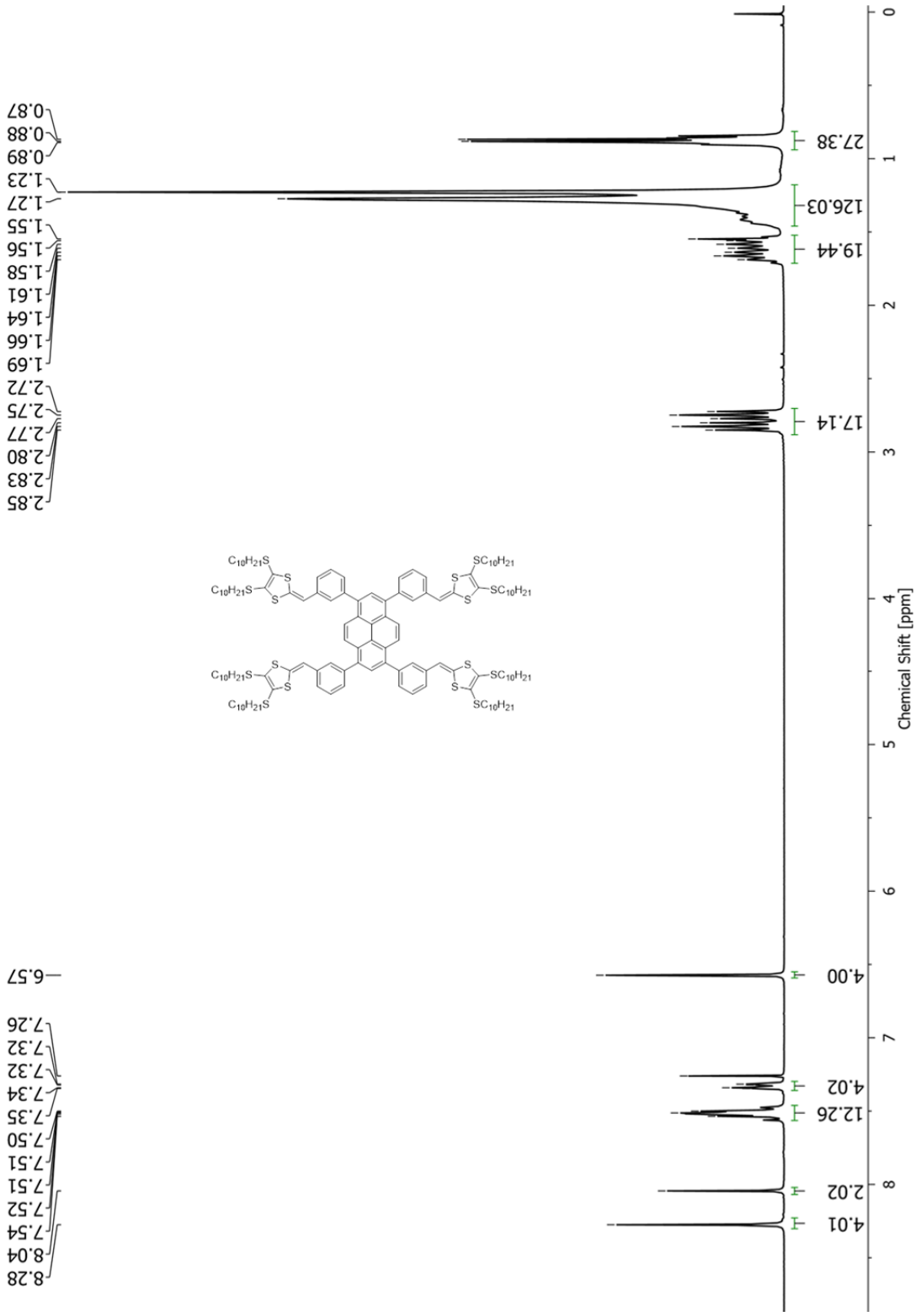

Fig. S-12 ^{1}H NMR (300 MHz, $CDCl_3$) of compound **8b**.

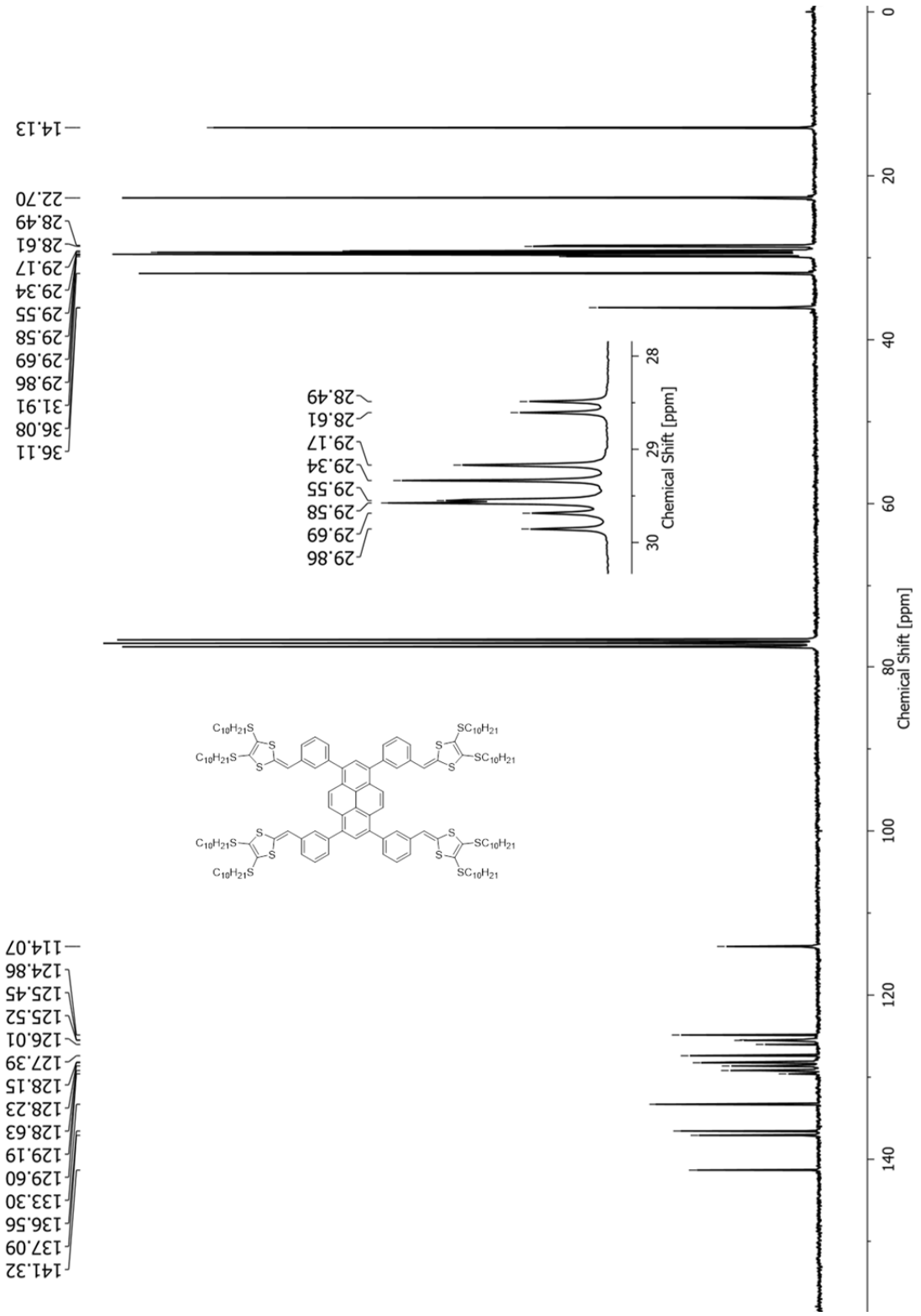

Fig. S-13 ^{1}H NMR (300 MHz, $CDCl_3$) of compound **8b**.

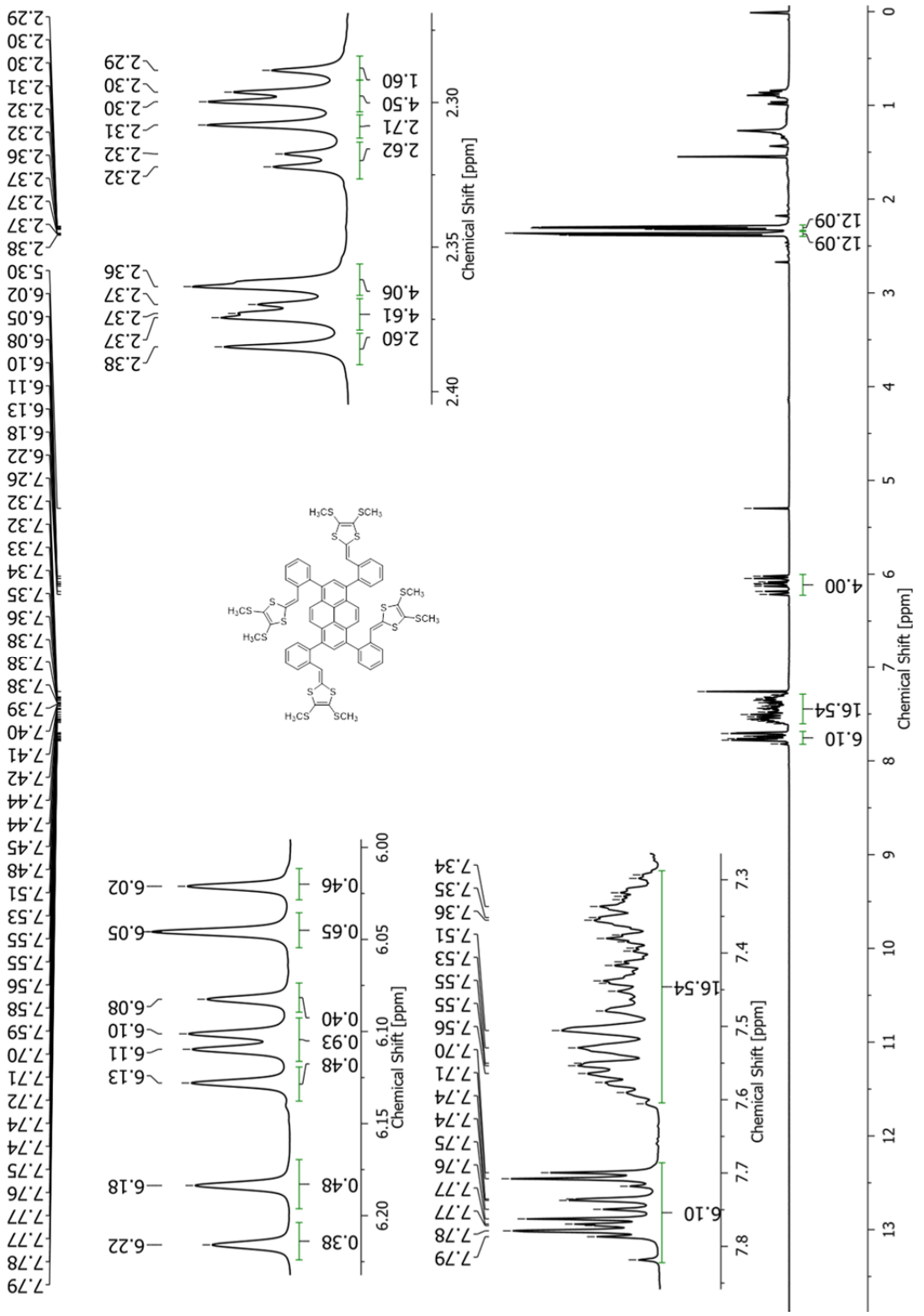

Fig. S-14 ^{1}H NMR (300 MHz, $CDCl_3$) of compound **9a**.

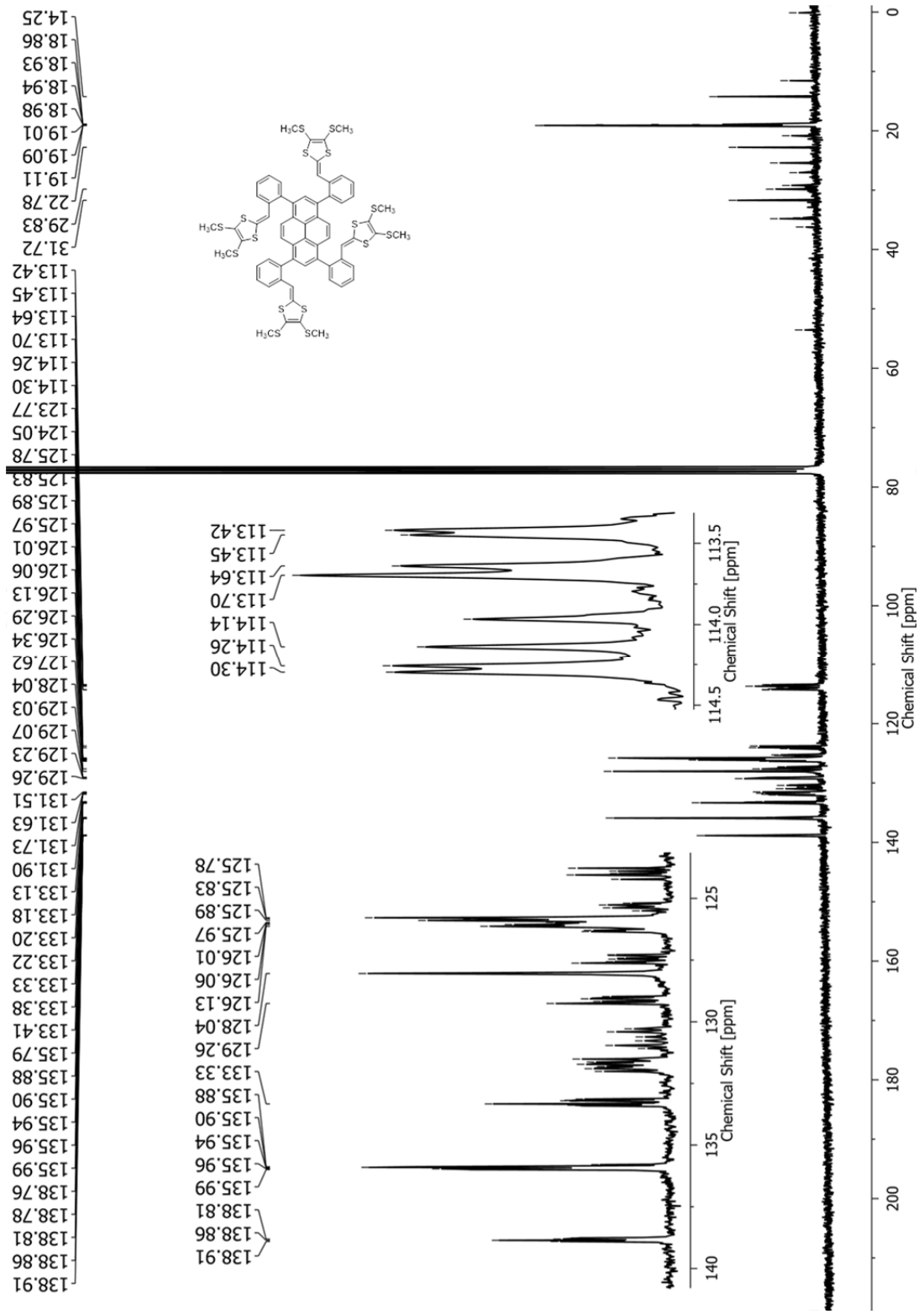

Fig. S-15 ^{13}C NMR (75 MHz, $CDCl_3$) of compound **9a**.

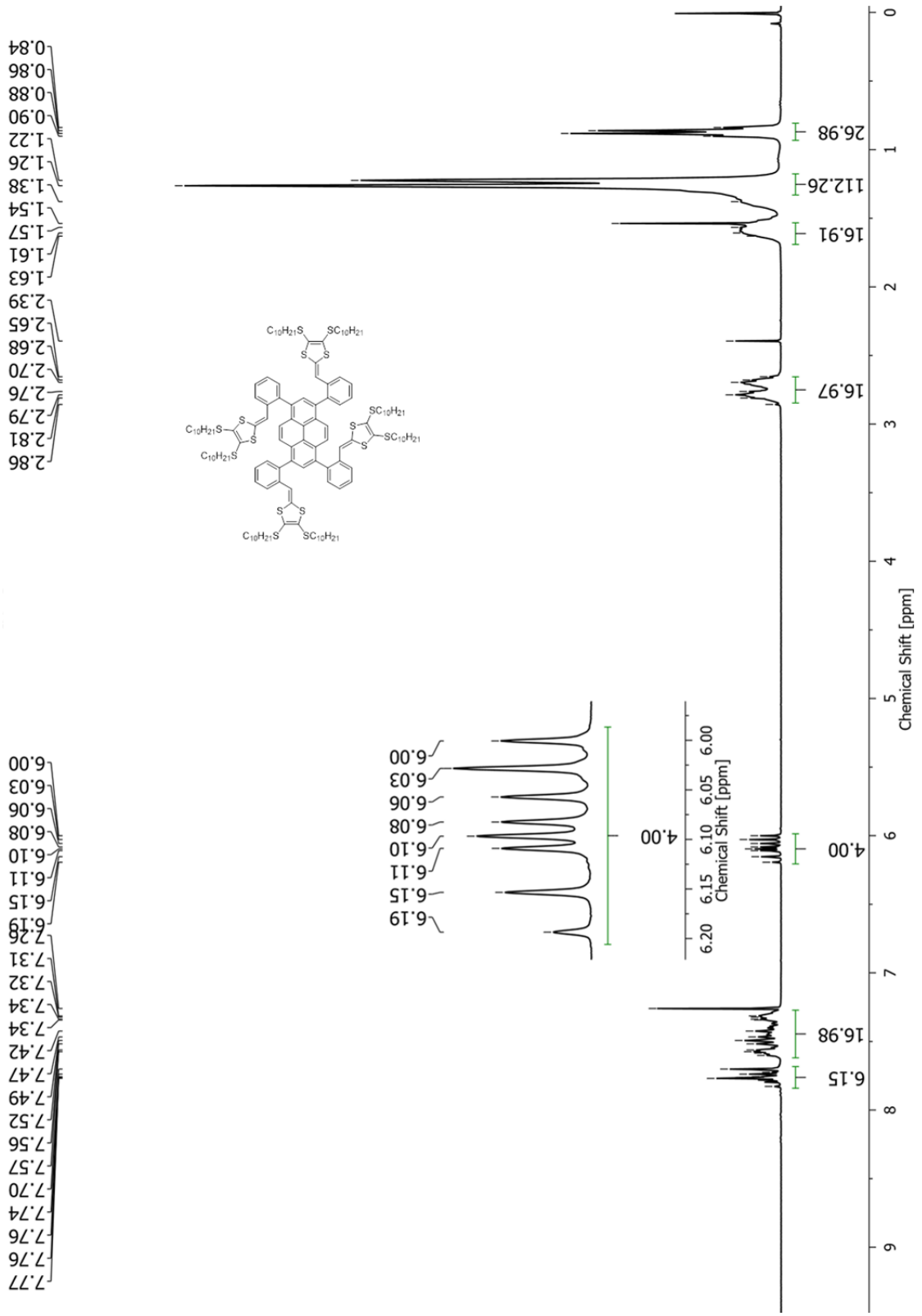

Fig. S-16 ^{1}H NMR (300 MHz, $CDCl_3$) of compound **9b**.

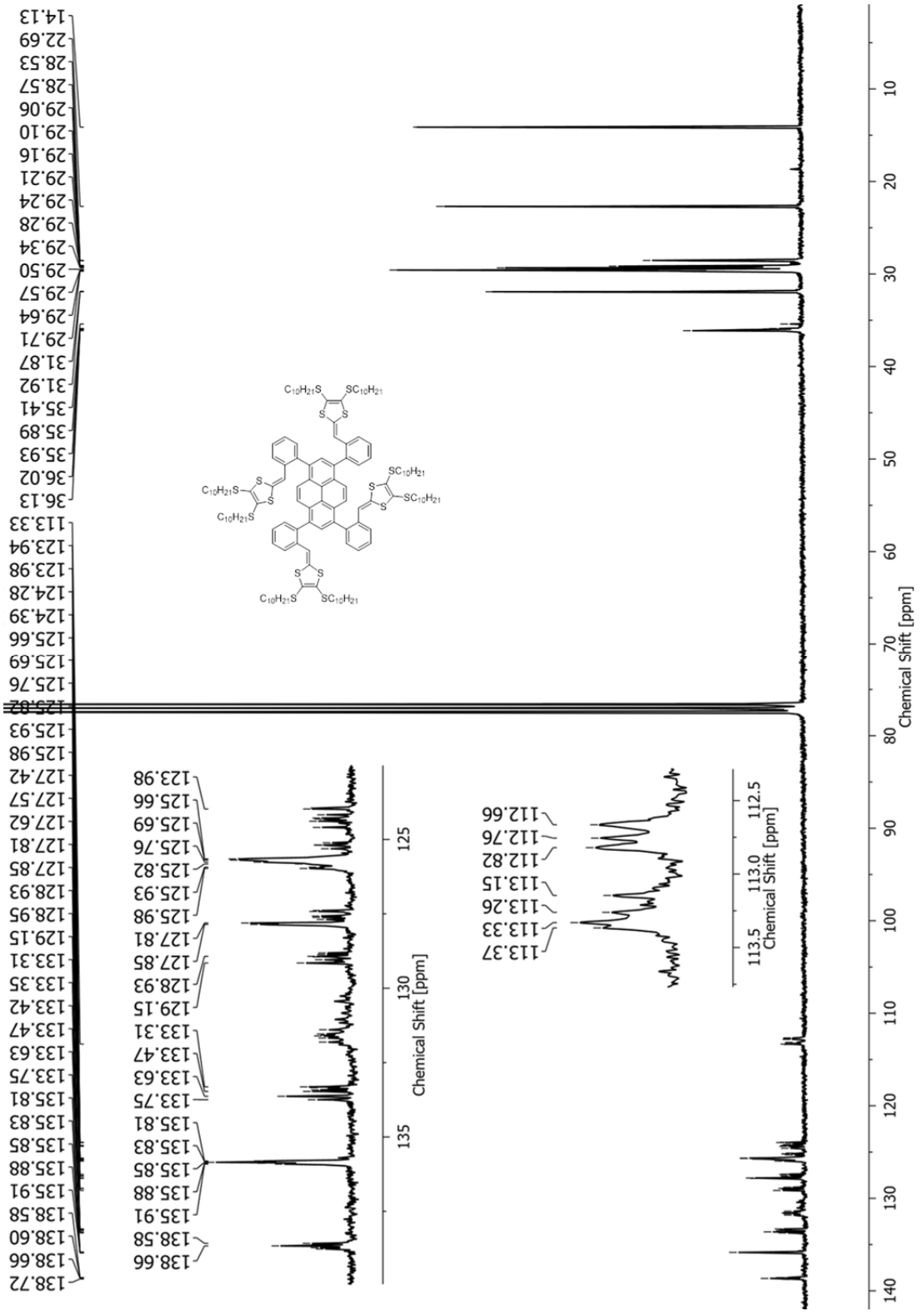

Fig. S-17 ^{13}C NMR (75 MHz, $CDCl_3$) of compound **9b**.

Appendix III

Supporting Information for Chapter 4

Synthesis and Comparative Studies of K-region Functionalized Pyrene Derivatives

Table of Content

3. NMR Spectra for New Compounds

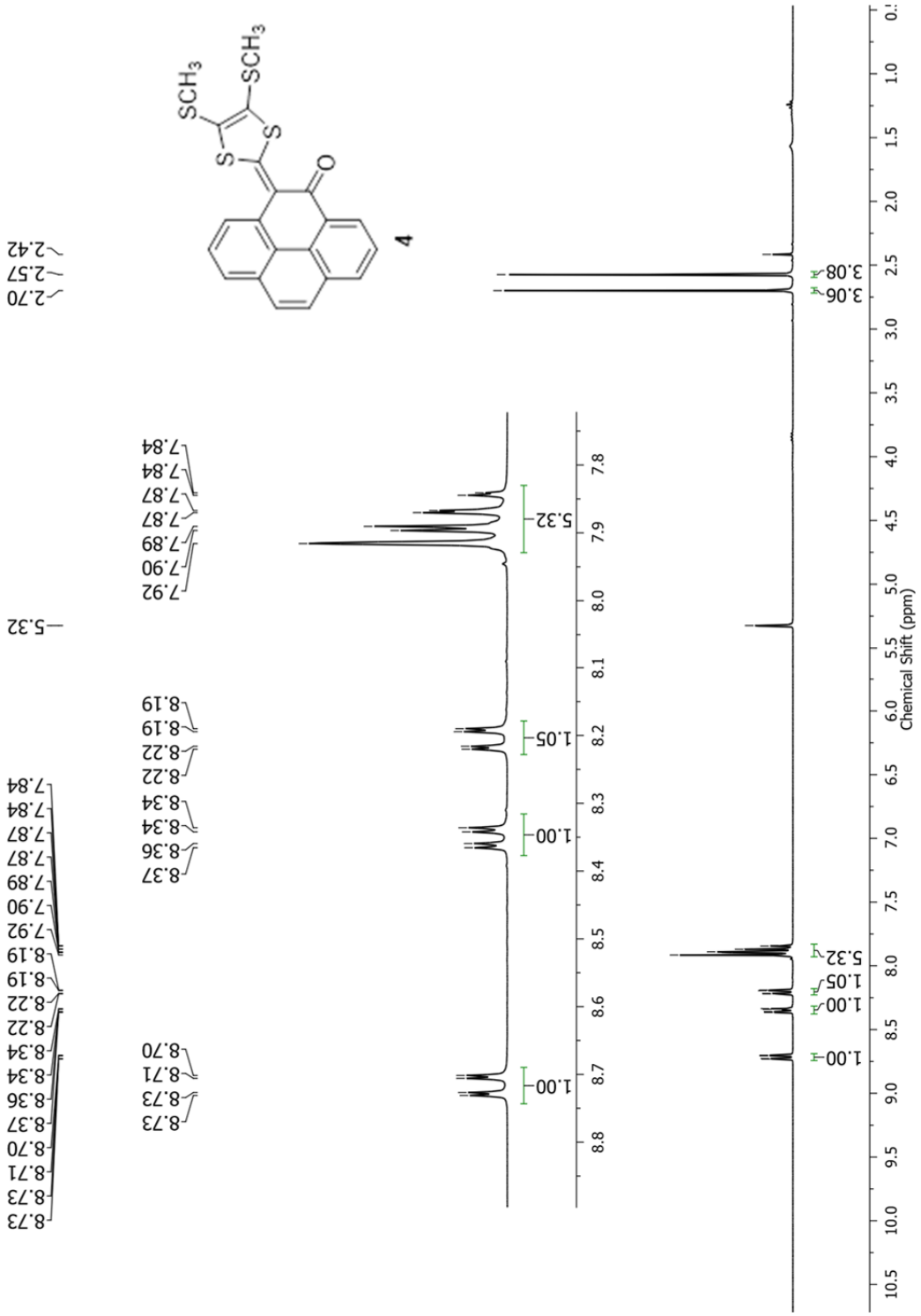

Fig. S-1 ^{1}H NMR (300 MHz, CD_2Cl_2) of compound **4**.

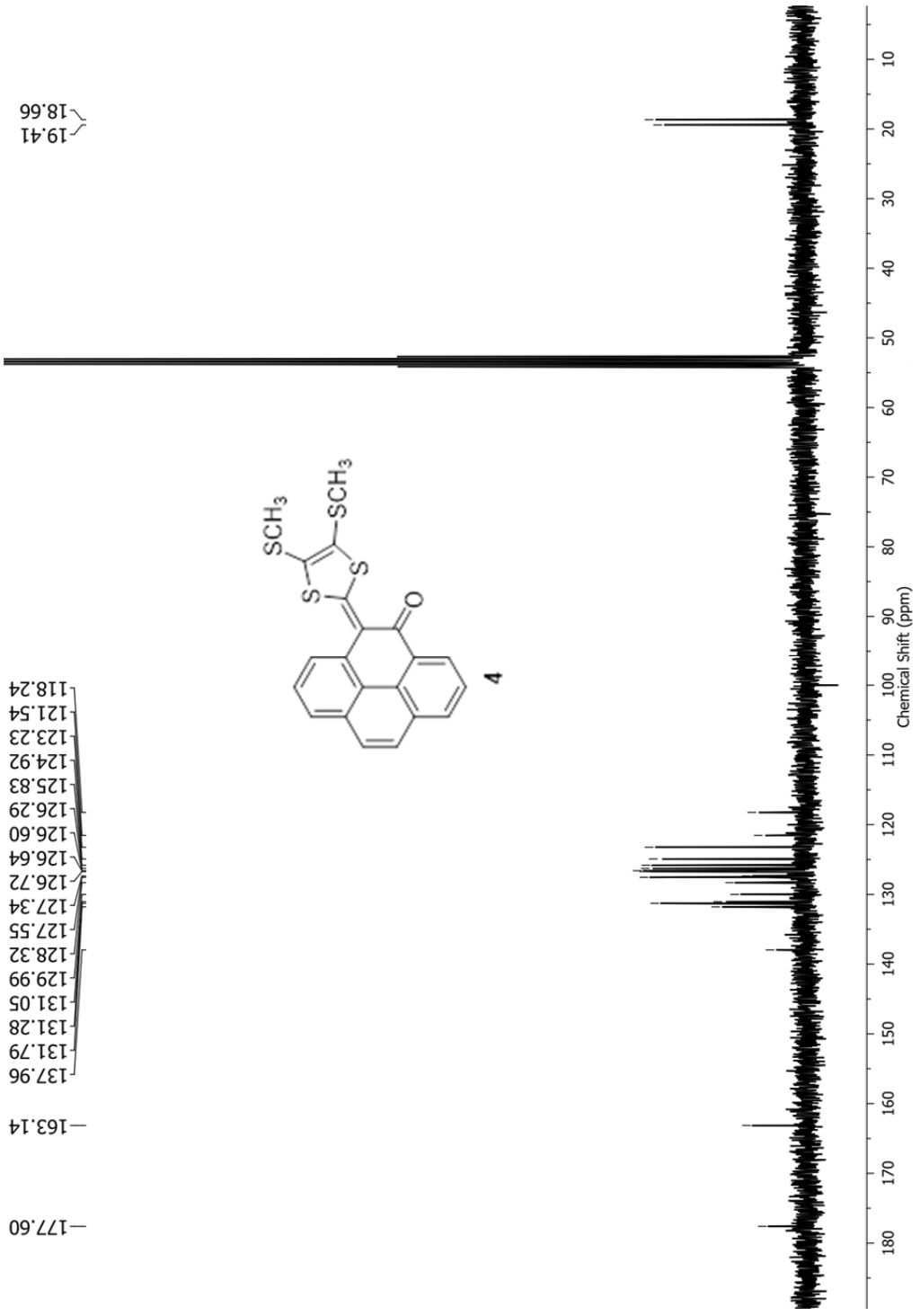

Fig. S-2 ^{13}C NMR (75 MHz, CD_2Cl_2) of compound **4**.

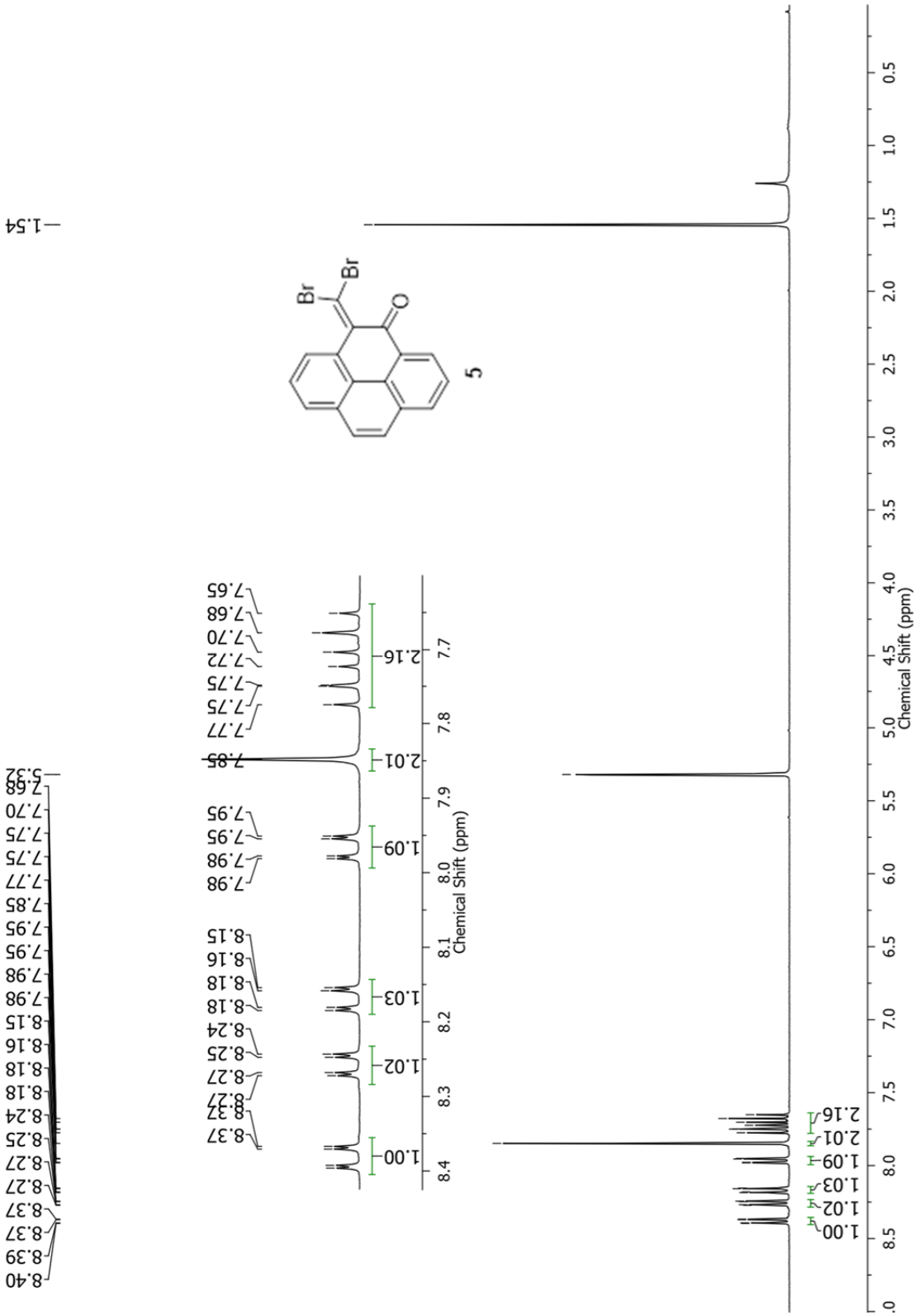

Fig. S-3 ^{1}H NMR (300 MHz, CD_2Cl_2) of compound **5**.

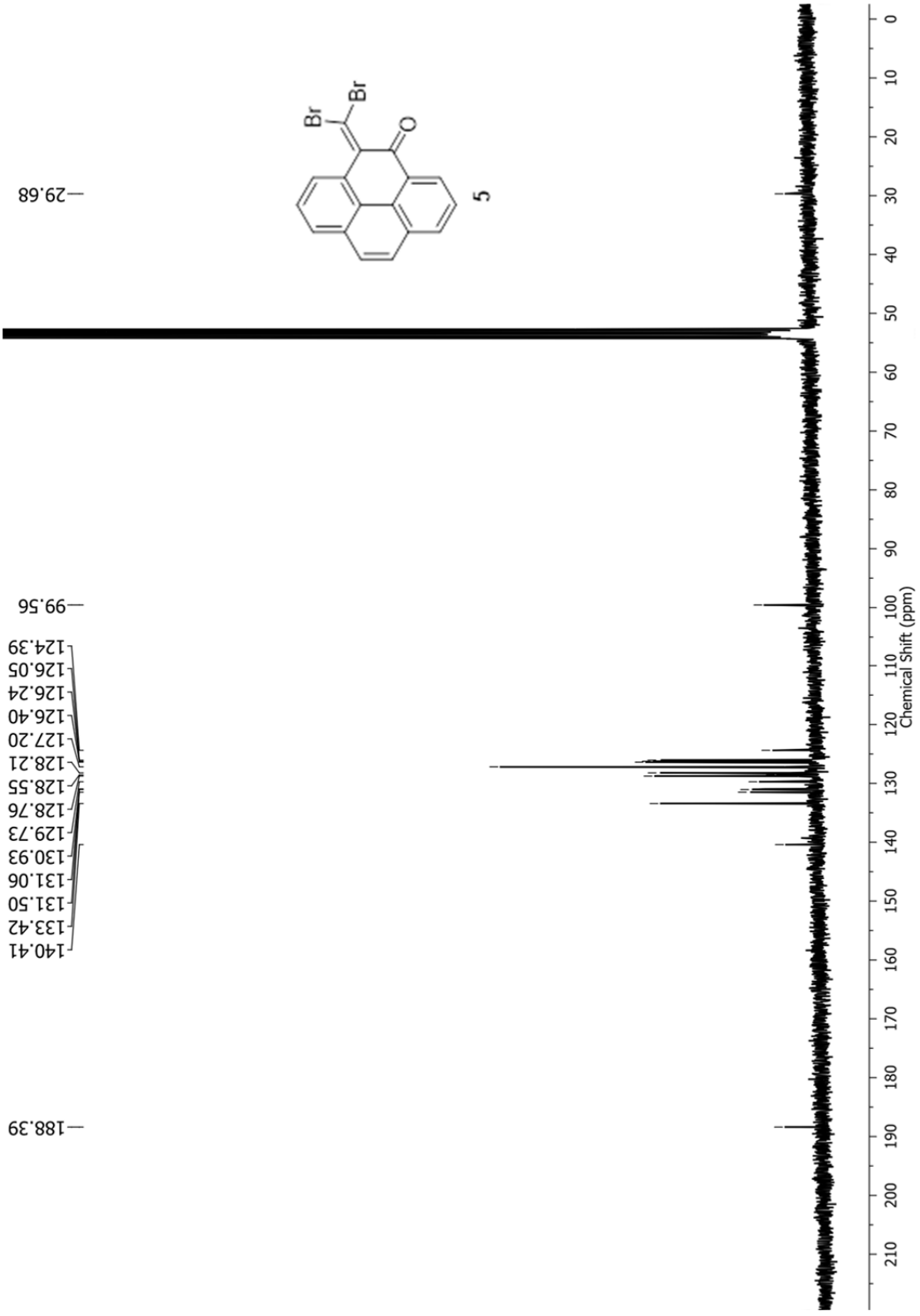

Fig. S-4 ^{13}C NMR (75 MHz, CD_2Cl_2) of compound **5**.

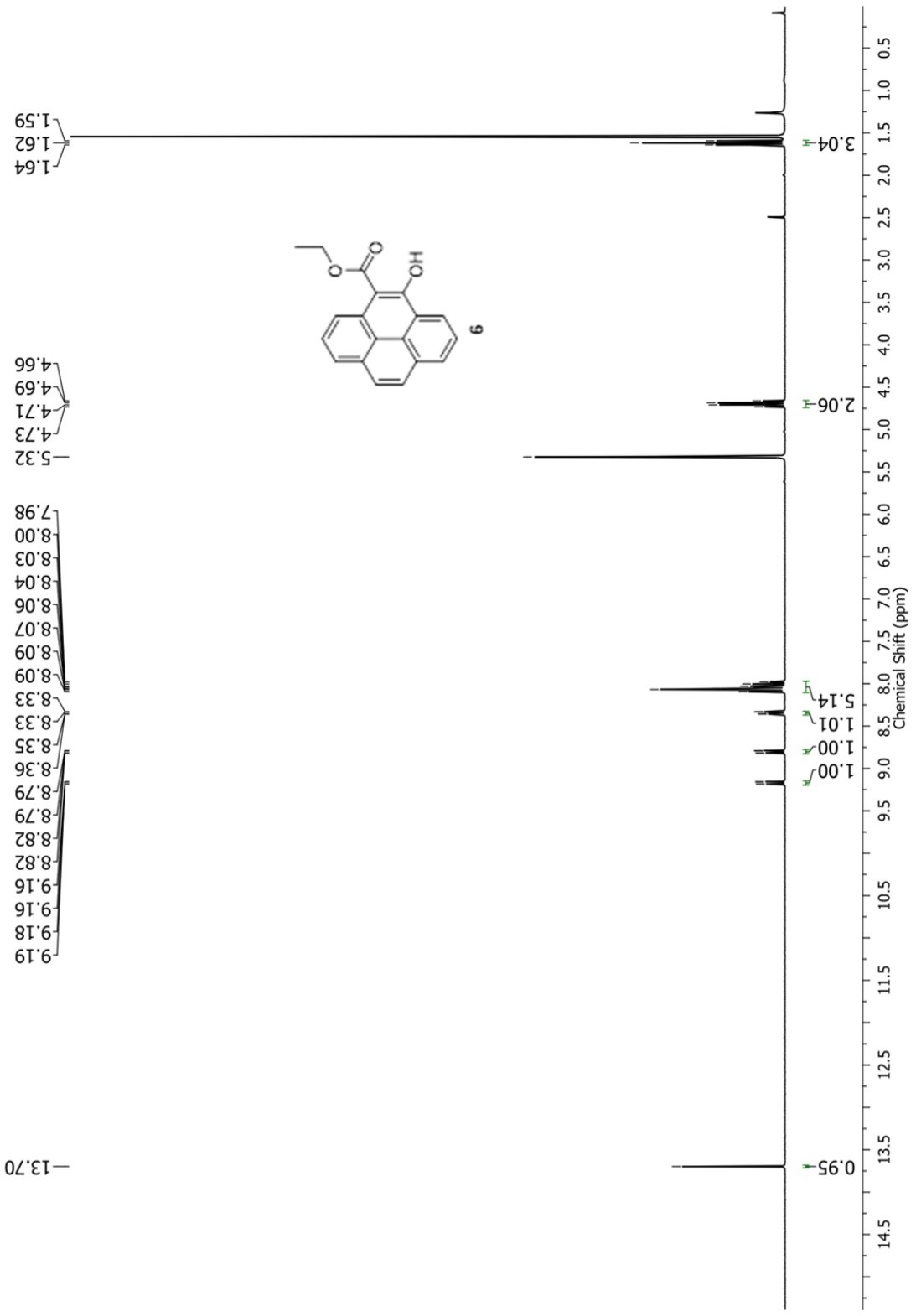

Fig. S-5 ^{1}H NMR (300 MHz, CD_2Cl_2) of compound **6**.

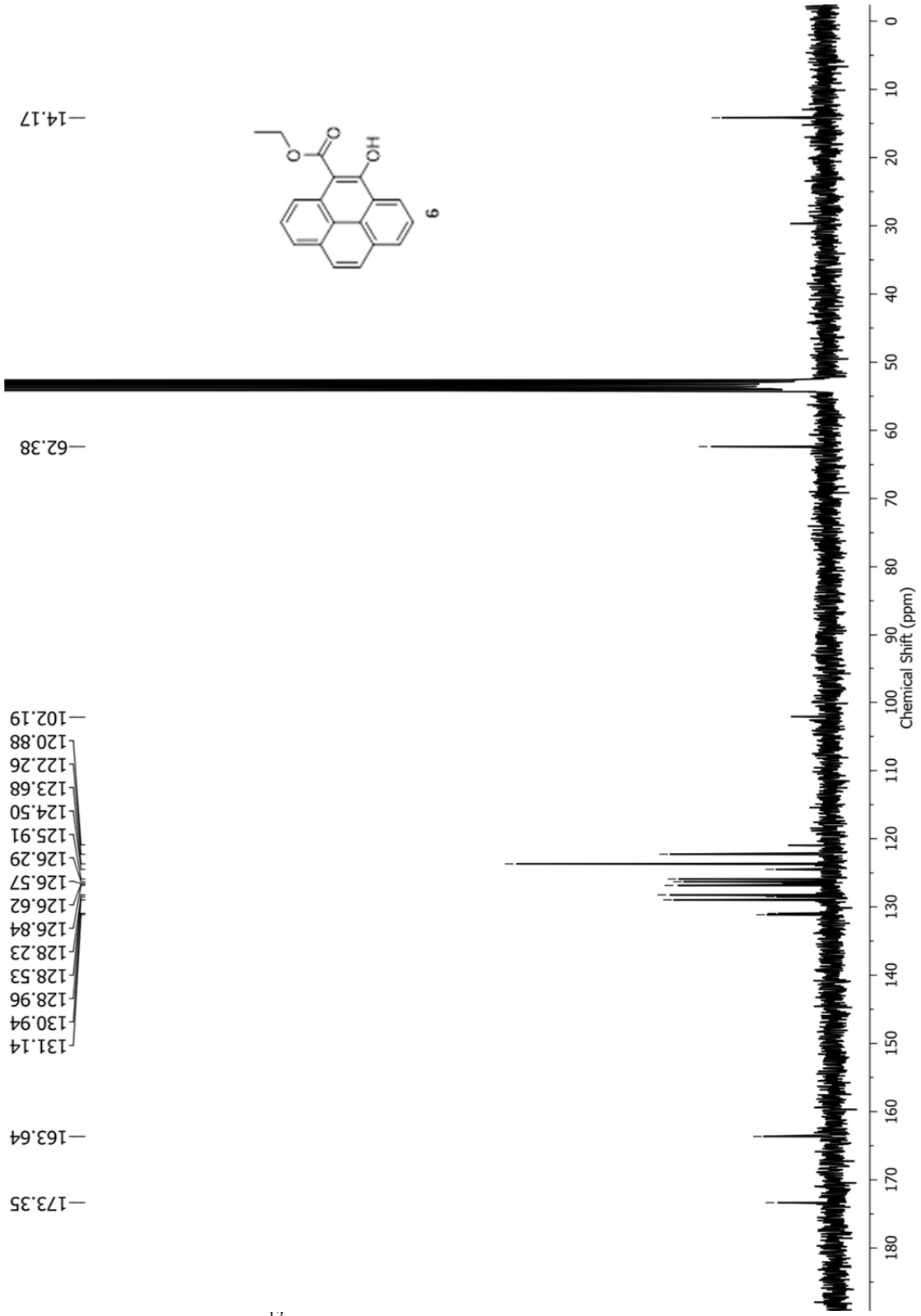

Fig. S-6 ^{13}C NMR (75 MHz, CD_2Cl_2) of compound **6**.

2. Optimization of the Synthesis of 4

Table S-1 Optimization of the synthetic conditions for compound **4**

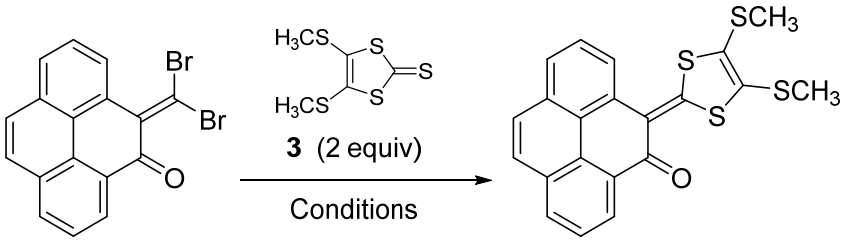

5 **4**

Entry	Solvent	Base	Temperature	Time	Yield
1	EtOH	KOH (10 eq)	80 °C	45 min	45%
2	EtOH	KOH (4 eq)	80 °C	45 min	45%
3	EtOH	KOH (2 eq)	80 °C	45 min	10%
4	EtOH	NH_4OH (4 eq)	80 °C	45 min	trace
5	EtOH	Pyridine (4 eq)	80 °C	45 min	0%
6	EtOH	Imidazole (4 eq)	80 °C	45 min	0
7	EtOH	Bu_4NOH	80 °C	45 min	35%
8	Dioxane	Bu_4NOH	80 °C	45 min	0%
9	THF/water	KOH (4 eq)	80 °C	45 min	0%
10	DMF	KOH (4 eq)	80 °C	45 min	0%
11	EtOH	KOH (4 eq)	rt	45 min	32%
12	EtOH	KOH (4 eq)	120 °C	45 min	40%
13	EtOH	KOH (4 eq)	80 °C	10 min	25%

3. Crystal Data and Refinement of 4-6

Table S-2 Crystal data and structure refinement of **4**

Empirical formula	$C_{21}H_{14}OS_4$
Formula weight	410.56
Temperature/K	100(2)
Crystal system	monoclinic
Space group	$P2_1/c$
a/Å	5.15876(6)
b/Å	20.4115(3)
c/Å	16.5822(2)
β/°	96.4856(12)
Volume/Å^3	1734.90(4)
Z	4
ρ_{calc}g/cm^3	1.572
μ/mm^{-1}	5.091
F(000)	848.0
Crystal size/mm^3	0.193 × 0.04 × 0.034
Radiation	Cu $K\alpha$ (λ = 1.54184)
2θ range for data collection/°	6.894 to 154.812
Index ranges	$-6 \le h \le 6$, $-25 \le k \le 25$, $-16 \le l \le 20$
Reflections collected	42353
Independent reflections	3667 [R_{int} = 0.0638, R_{sigma} = 0.0255]
Data/restraints/parameters	3667/0/237
Goodness-of-fit on F^2	1.032
Final R indexes [I>=2σ (I)]	R_1 = 0.0391, wR_2 = 0.1045
Final R indexes [all data]	R_1 = 0.0427, wR_2 = 0.1067
Largest diff. peak/hole / e Å^{-3}	0.61/-0.35

Table S-3 Crystal data and structure refinement of **5**

Empirical formula	$C_{17}H_8Br_2O$
Formula weight	388.05
Temperature/K	100(2)
Crystal system	monoclinic
Space group	$P2_1/c$
a/Å	3.88283(4)
b/Å	18.75250(17)
c/Å	17.4959(2)
β/°	92.4372(10)
Volume/Å^3	1272.77(2)
Z	4
ρ_{calc}g/cm^3	2.025
μ/mm^{-1}	7.994
F(000)	752.0
Crystal size/mm^3	0.12 × 0.06 × 0.05
Radiation	Cu $K\alpha$ (λ = 1.54184)
2θ range for data collection/°	6.914 to 154.478
Index ranges	$-4 \le h \le 4$, $-23 \le k \le 20$, $-22 \le l \le 21$
Reflections collected	16339
Independent reflections	2654 [R_{int} = 0.0565, R_{sigma} = 0.0330]
Data/restraints/parameters	2654/0/181
Goodness-of-fit on F^2	1.088
Final R indexes [I>=2σ (I)]	R_1 = 0.0277, wR_2 = 0.0720
Final R indexes [all data]	R_1 = 0.0303, wR_2 = 0.0736
Largest diff. peak/hole / e Å^{-3}	0.43/-0.56

Table S-4 Crystal data and structure refinement of **6**

Empirical formula	$C_{19}H_{14}O_3$
Formula weight	290.30
Temperature/K	100(2)
Crystal system	monoclinic
Space group	$P2_1/c$
a/Å	14.9879(7)
b/Å	4.96700(10)
c/Å	18.9991(7)
β/°	105.932(4)
Volume/Å^3	1360.06(9)
Z	4
ρ_{calc}g/cm^3	1.418
μ/mm^{-1}	0.773
F(000)	608.0
Crystal size/mm^3	0.2 × 0.1 × 0.05
Radiation	Cu $K\alpha$ (λ = 1.54184)
2θ range for data collection/°	6.132 to 154.814
Index ranges	$-18 \le h \le 18$, $-6 \le k \le 5$, $-24 \le l \le 23$
Reflections collected	17708
Independent reflections	2855 [R_{int} = 0.0450, R_{sigma} = 0.0302]
Data/restraints/parameters	2855/0/201
Goodness-of-fit on F^2	1.081
Final R indexes [I>=2σ (I)]	R_1 = 0.0641, wR_2 = 0.1896
Final R indexes [all data]	R_1 = 0.0710, wR_2 = 0.1968
Largest diff. peak/hole / e Å^{-3}	0.47/-0.25

4. Results of TD-DFT Calculations of 4-6

Table S-5 Summary of vertical electronic transition properties of **4** computed at the TD-CAM-B3LYP/6-311+G(d,p) level of theory

Wavelength (nm)	***f***	**MO Contributions**
416.2	0.5839	HOMO→LUMO (93%)
331.8	0.0047	H-5→LUMO (61%), H-1→LUMO (17%)
325.0	0.0355	H-5→LUMO (11%), H-1→LUMO (45%), HOMO→L+1 (17%)
316.5	0.0228	H-2→LUMO (66%)
295.8	0.2926	H-1→LUMO (26%), HOMO→L+1 (51%)
284.6	0.0921	H-2→LUMO (12%), H-2→L+1 (23%), H-1→L+2 (11%), HOMO→L+2 (22%)
277.1	0.0425	HOMO→L+4 (26%), HOMO→L+5 (38%)
269.6	0.0168	H-3→LUMO (22%), H-1→L+1 (35%)
265.9	0.1874	H-3→LUMO (18%), HOMOvL+3 (30%), HOMO→L+5 (10%)
262.1	0.1973	H-3→LUMO (18%), H-1→L+1 (14%), HOMO→L+2 (33%)
250.8	0.0426	HOMO→L+3 (16%), HOMO→L+4 (17%)
248.4	0.0501	H-4→LUMO (11%), H-2→L+1 (13%), HOMO→L+4 (12%)
245.9	0.0194	H-4→LUMO (13%), HOMO→L+4 (17%), HOMO→L+6 (15%), HOMO→L+9 (14%)
242.3	0.0645	H-4→LUMO (43%)
238.3	0.1028	H-6→LUMO (36%), H-2→L+2 (10%), HOMO→L+8 (17%)
230.3	0.3358	H-2→L+1 (16%), H-2→L+2 (20%), H-1→L+1 (10%), H-1→L+2 (31%)
228.0	0.0175	HOMO→L+6 (10%), HOMO→L+7 (26%)
225.2	0.1466	H-6→LUMO (33%), HOMO→L+8 (25%)
223.9	0.0107	HOMO→L+6 (10%), HOMO→L+10 (27%)
220.6	0.7142	H-3→L+2 (10%), H-2→L+2 (33%), H-1→L+2 (20%)

Table S-6 Summary of vertical electronic transition properties of **5** computed at the TD-CAM-B3LYP/6-311+G(d,p) level of theory

Wavelength (nm)	***f***	**MO Contributions**
367.0	0.1078	H-3→LUMO (15%), HOMO→LUMO (69%)
331.8	0.0565	H-3→LUMO (33%), H-1→LUMO (26%), HOMO→LUMO (23%)
326.4	0.0191	H-3→LUMO (21%), H-1→LUMO (62%)
285.4	0.2405	H-2→LUMO (26%), H-1→L+1 (33%), HOMO→L+1 (10%), HOMO→L+3 (14%)
279.1	0.3073	HOMO→L+1 (76%)
269.2	0.0202	H-2→LUMO (65%), H-1→L+1 (13%)
254.2	0.0119	H-2→L+2 (19%), HOMO→L+2 (40%)
250.1	0.0181	H-4→LUMO (45%), H-3→LUMO (12%)
242.2	0.0659	H-5→LUMO (50%), H-1→L+1 (12%), HOMO→L+3 (11%)
235.6	0.4185	H-5→LUMO (12%), H-4→LUMO (12%), H-2→L+1 (11%), H-1→L+1 (17%), HOMO→L+3 (28%)
228.0	0.0479	H-5→L+2 (13%), H-3→L+2 (28%), H-1→L+2 (14%)
226.4	0.7095	H-1→L+3 (45%)
223.3	0.0974	H-2→L+1 (11%), HOMO→L+4 (13%), HOMO→L+5 (11%)
216.2	0.0403	H-2→L+1 (29%), HOMO→L+5 (13%)
215.7	0.1164	H-2→L+1 (21%), HOMO→L+6 (20%)
210.9	0.102	H-6→LUMO (36%), HOMO→L+4 (16%), HOMO→L+5 (12%)
210.1	0.0442	H-7→LUMO (15%), H-6→LUMO (11%), HOMO→L+4 (12%), HOMO→L+5 (24%)
209.5	0.019	H-7→LUMO (12%), H-3→L+1 (21%), HOMO→L+6 (10%)
208.7	0.0063	H-7→LUMO (33%), H-3→L+1 (23%)
205.9	0.0358	H-1→L+2 (17%), H-1→L+4 (11%)

Table S-7 Summary of vertical electronic transition properties of **6** computed at the TD-CAM-B3LYP/6-311+G(d,p) level of theory

Wavelength (nm)	***f***	**MO Contributions**
339.8	0.3977	HOMO→LUMO (87%)
314.3	0.058	H-1→LUMO (47%), HOMO→L+1 (38%)
279.3	0.1269	H-2→LUMO (11%), HOMO→L+1 (26%), HOMO→L+2 (52%)
265.3	0.2693	H-2→LUMO (29%), H-1→LUMO (38%), HOMO→L+1 (24%)
254.7	0.2393	H-2→LUMO (51%), HOMO→L+2 (23%)
241.7	0.3014	H-1→L+1 (56%), HOMO→L+4 (17%)
230.1	0.0003	H-4→LUMO (59%), H-4→L+1 (12%), H-4→L+2 (15%)
226.7	0.2459	H-1→L+1 (19%), HOMO→L+4 (56%)
223.9	0.0059	HOMO→L+3 (73%)
221.7	0.4278	H-2→L+1 (10%), H-1→L+2 (59%)
216.7	0.1791	H-3→LUMO (75%)
213.2	0.0584	H-2→L+1 (31%), H-1→L+4 (19%), HOMO→L+4 (12%)
206.4	0.2326	H-2→L+1 (12%), H-2→L+2 (41%)
205.6	0.0076	HOMO→L+5 (28%), HOMO→L+6 (47%)
202.0	0.0011	HOMO→L+5 (39%), HOMO→L+6 (38%)
201.5	0.01	H-3→L+1 (13%), H-2→L+1 (18%), H-2→L+2 (12%), H-1→L+2 (14%), HOMO→L+11 (21%)
192.3	0.0107	H-1→L+3 (57%)
192.0	0.0692	H-5→LUMO (16%), H-3→L+1 (10%), H-1→L+3 (10%), HOMO→L+11 (34%)
190.1	0.0247	HOMO→L+9 (73%)
189.7	0.3996	H-3→L+1 (12%), H-2→L+2 (20%), H-1→L+4 (37%), HOMO→L+11(11%)

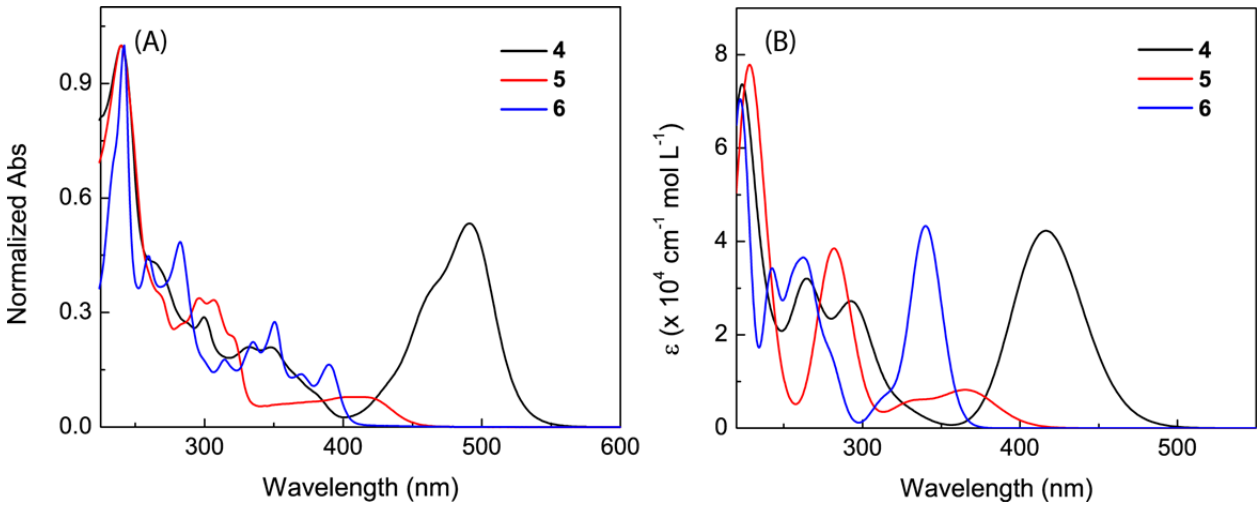

Fig. S-7 Comparison of (A) experimental and (B) TD-DFT calculated UV-Vis spectra for **4-6**.

Table S-8 Summary of experimental UV-Vis absorption data for **4-6**

Entry	UV-Vis absorption λ_{max} / nm (ε / mol^{-1} L cm^{-1})	E_{opt} (eV)
4	488 (3.64×10^3), 346 (1.31×10^3), 329 (sh, 1.38×10^3), 297 (1.85×10^3), 237 (6.75×10^3)	2.35
5	418 (sh, 5.11×10^2), 320 (1.46×10^3), 307 (2.08×10^3), 296 (2.09×10^3), 239 (6.36×10^3)	2.75
6	389 (7.98×10^2), 370 (6.74×10^2), 350 (1.37×10^3), 334, (1.11×10^3), 313(8.63×10^2), 282 (2.39×10^3), 258 (2.21×10^3), 241 (5.00×10^3)	3.07

5. Molecular Orbital Properties of 4-6

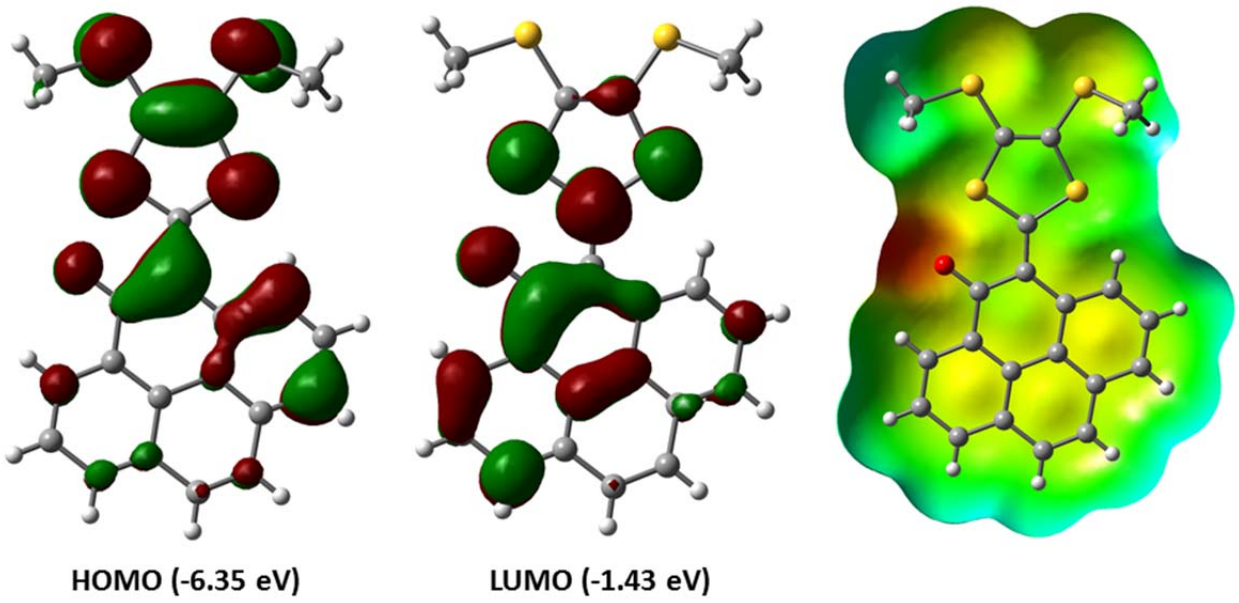

Fig. S-8 Plots of frontier molecular orbitals and electrostatic potential map of **4** calculated at the M06-2X/Def2-SVP level.

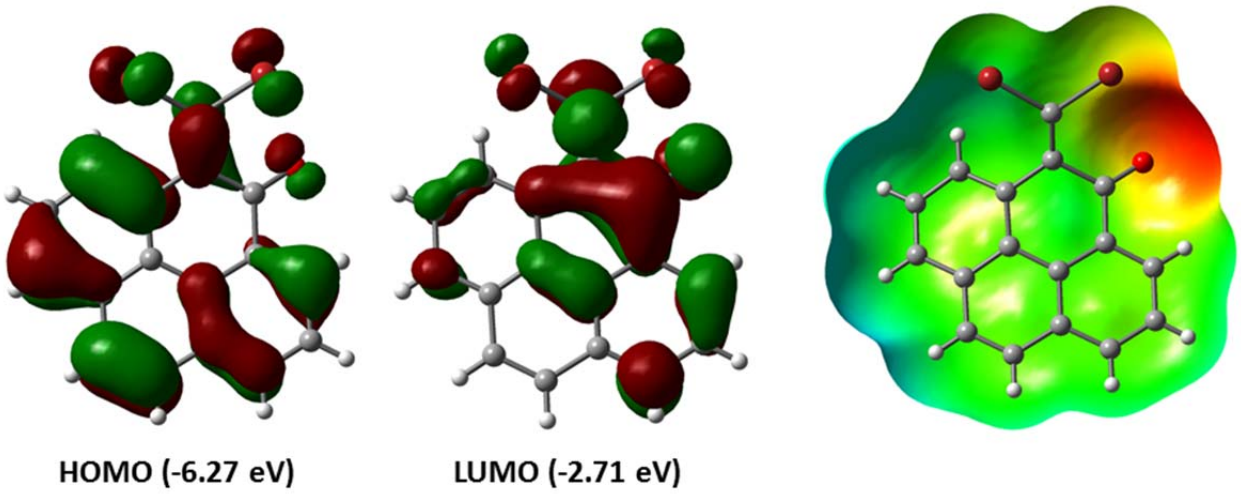

Fig. S-9 Plots of frontier molecular orbitals and electrostatic potential map of **5** calculated at the M06-2X/Def2-SVP level.

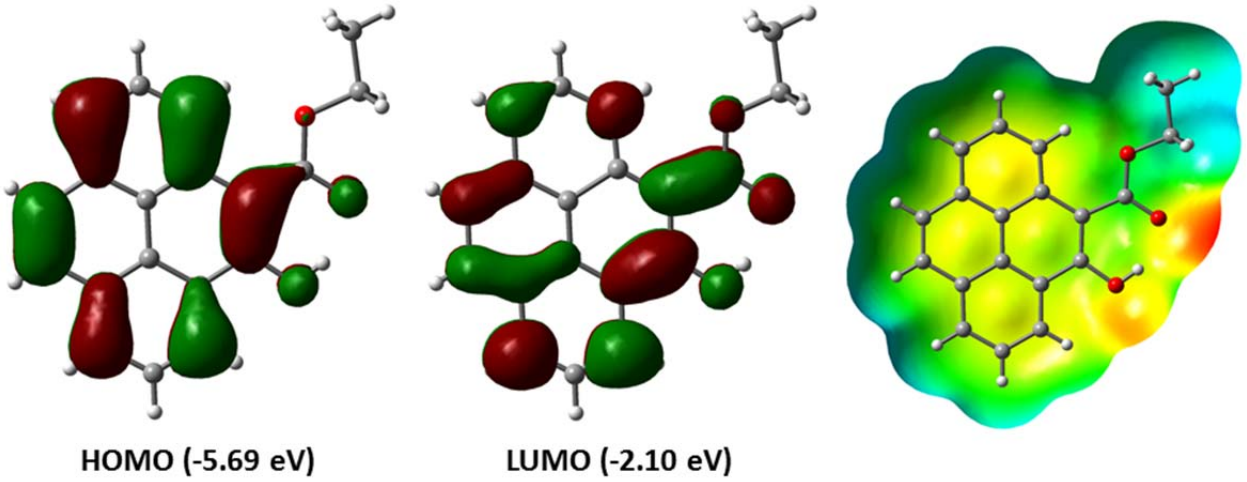

Fig. S-10 Plots of frontier molecular orbitals and electrostatic potential map of **6** calculated at the M06-2X/Def2-SVP level.

6. Results of QTAIM Analysis of 4-6

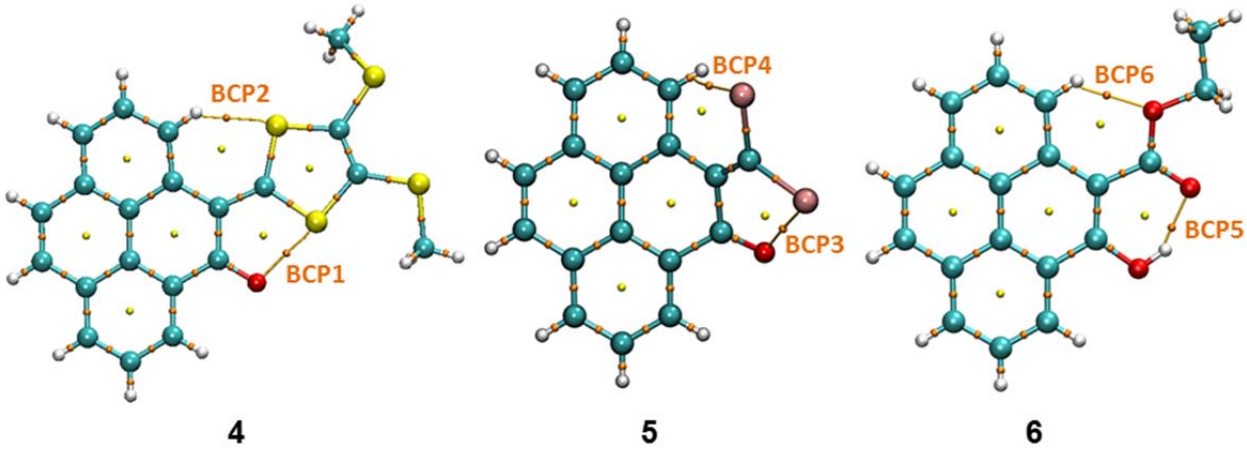

	Type	ρ (a.u.)	$\nabla^2\rho$ (a.u.)	H(r) (a.u.)	ELF	ε
BCP1	(3,-1)	0.0418	0.146	0.001495	0.145	0.150
BCP2	(3,-1)	0.0215	0.0716	0.00120	0.0760	0.0948
BCP3	(3,-1)	0.0165	0.0528	0.000791	0.0580	0.119
BCP4	(3,-1)	0.0129	0.0502	0.002229	0.0375	1.072
BCP5	(3,-1)	0.0444	0.188	0.00238	0.113	0.0187
BCP6	(3,-1)	0.0213	0.0871	0.00190	0.0529	0.0342

Fig. S-11 Molecular topological graphs obtained from QTAIM analysis for compound **4** computed at M06-2X/Def2-SVP level of theory.

Appendix IV

Supporting Information for Chapter 5

Self-Condensation of Pyrene-4,5-dione: An Approach to Generate Functional Organic Fluorophores

https://doi.org/10.1021/acs.orglett.9b03297

Table of Content

1. Experimental

1.1 General

Chemicals were purchased from commercial suppliers and used directly without purification. All reactions were conducted in standard glassware. Evaporation and concentration were carried out with a rotary evaporator. Flash column chromatography was performed with 240-400 mesh silica gel, and thin-layer chromatography (TLC) was carried out with silica gel F254 covered on plastic sheets and visualized by UV light. Melting points (m.p.) were measured using an SRS OptiMelt melting point apparatus and are uncorrected. ^{1}H and ^{13}C NMR spectra were measured on a Bruker Avance III 300 MHz and Bruker Avance 500 MHz multinuclear spectrometer. Chemical shifts (δ) are reported in ppm downfield relative to the signals of the internal reference $SiMe_4$ or residual solvents ($CHCl_3$: δ_H = 7.24 ppm, δ_C = 77.2 ppm; CH_2Cl_2: δ_H = 5.32 ppm, δ_C = 54.0 ppm). Coupling constants (*J*) are given in Hz. Infrared spectra (IR) were recorded on a Bruker Alfa spectrometer. MALDI-TOF MS analysis was performed on Bruker 9.4T Apex-Qe FTICR system. High-resolution APPI-TOF MS analysis was done on a GCT premier Micromass Technologies instrument. UV-Vis absorption spectra were measured on a Cary 6000i spectrophotometer. Fluorescence spectra were measured on a Photon Technology International (PTI) QuantaMaster spectrofluorometer. Relative fluorescence quantum yields (ϕ_F) in solution were determined following reported procedures[1] using quninine sulfate (ϕ_F = 0.546) as the standard.

Single crystal X-ray diffraction analysis was conducted on a Bruker PLATFORM/APEX II CCD diffractometer equipped with a Cu-*K*α (1.54178 Å) source. The crystal structures were solved and refined with the SHELXT software package.

Density functional theory (DFT) calculations were performed using the Gaussian 16 software package. Geometry optimization was done at the M06-2X/6-31G(d) level and the optimized geometries were further confirmed by frequency calculations at the same level of theory as energy minima (zero imaginary frequency) or transition state (one imaginary frequency). NMR calculations were carried out using the Gauge-Independent Atomic Orbital (GIAO) method at the B3LYP/6-31+G(2d,p) level of theory with the solvent effect (methylene chloride) taken into account by the polarizable continuum model (PCM).

1.2 Synthesis

6*H*-phenanthro[4,5-*cde*]pyreno[4',5':4,5]imidazo[1,2-*a*]azepin-6-one (2a)

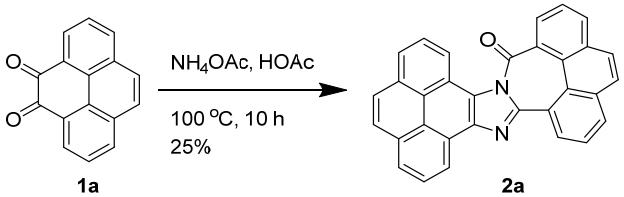

1a **2a**

Pyrene-4,5-dione (**1a**) (0.090 g, 0.387 mmol), ammonium acetate (0.239 g, 3.103 mmol), and glacial acetic acid (99.7%, 5 mL) were added to a 50 mL round-bottomed flask. The reaction

[1] Williams, A. T. R.; Winfield, S. A.; Miller, J. N. *Analyst*, **1983**, *108*, 1067–1071; Miller, J. N. in *Standards in Flourescence Spectrometry. Techniques in Visible and Ultraviolet Spectometry*, *Vol 2*., Miller, J. N., Ed.; Springer, Dordrecht, 1981, pp 68–78.

mixture was stirred and heated at 100 °C for 10 h. Next, the reaction mixture was cooled down to room temperature. The resulting yellow solid was collected by suction filtration and washed sequentially with a saturated aqueous $NaHCO_3$ solution, water, and acetone. The resulting residue was washed with CH_2Cl_2 (2 mL) to give compound **2a** (0.043 g, 0.097 mmol, 25%) as a yellow solid. m.p. > 386.1 °C (dec); IR (neat): 2958, 2921, 2851, 1692, 1622, 1586, 1464, 1337, 1320, 1255, 1151, 823, 717 cm^{-1}; ^1H NMR (300 MHz, $CDCl_3$): δ 9.52 (dd, *J* = 7.7, 1.5 Hz, 1H), 9.16 (dd, *J* = 7.5, 1.2 Hz, 1H), 8.74 (dd, *J* = 7.5, 1.5 Hz, 1H), 8.61–8.56 (m, 1H), 8.34 (dd, *J* = 7.9, 1.6 Hz, 1H), 8.30–7.95 (m, 11H); Meaningful ^{13}C NMR spectrum could not be obtained due to limited solubility; HRMS (APPI-TOF, positive mode) *m/z* calcd for $C_{32}H_{16}N_2O$ 444.1263, found 444.1273 $[M + H]^+$.

4,9,14,18-Tetra-*tert*-butyl-6*H*-phenanthro[4,5-*cde*]pyreno[4',5':4,5]imidazo[1,2-*a*]azepin-6-one (2b)

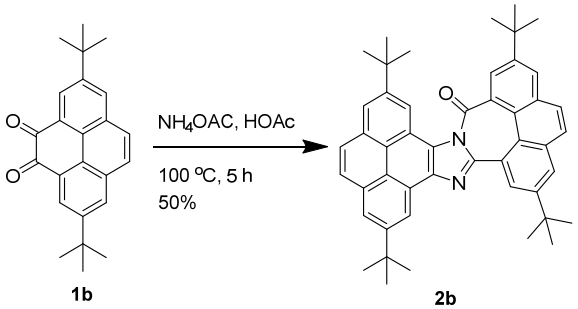

1b **2b**

2,7-Di-*tert*-butylpyrene-4,5-dione (**1b**) (0.344 g, 1.00 mmol), ammonium acetate (0.616 g, 8.00 mmol), and glacial acetic acid (99.7%, 5 mL) were added to a 50 mL round-bottomed flask. The reaction mixture was stirred and heated at 100 °C for 5 h. Next, the reaction mixture was cooled down to room temperature and then poured into a separatory funnel including water. The mixture was extracted twice with CH_2Cl_2. The combined organic layer was washed twice with a saturated aqueous $NaHCO_3$ solution. The organic layer was dried over $MgSO_4$, filtered, and concentrated *in vacuo*. The resulting residue was subjected to silica gel column chromatography (hexanes/ CH_2Cl_2, 80:20) to give pure compound **2b** (0.219 g, 0.327 mmol, 50%) as a yellow crystalline solid. m.p. > 254.6 °C (dec.); IR (neat): 3051, 2950, 2901, 2863, 1696, 1605, 1472, 1433, 1393, 1262, 1204, 1073, 891 cm^{-1}; ^1H NMR (300 MHz, CD_2Cl_2): δ 9.63 (d, *J* = 2.3 Hz, 1H), 9.18 (d, *J* = 1.9 Hz, 1H), 8.76 (d, *J* = 2.3 Hz, 1H), 8.64 (d, *J* = 1.8 Hz, 1H), 8.34 (d, *J* = 2.3 Hz, 1H), 8.31 (d, *J* = 2.0 Hz, 1H), 8.26 (d, *J* = 1.8 Hz, 1H), 8.21 (d, *J* = 2.3 Hz, 1H), 8.11 (s, 2H), 7.97 (s, 1H), 7.97 (s, 1H), 1.73 (s, 9H), 1.69 (s, 9H) 1.67 (s, 9H) 1.63 (s, 9H); ^{13}C NMR (75 MHz, CD_2Cl_2): δ 171.76, 150.24, 150.08, 149.86, 149.43, 148.22, 140.93, 133.74, 133.47, 132.77, 131.83, 131.42, 130.18, 129.44, 128.99, 128.56, 128.12, 127.93, 127.67, 127.60, 127.08, 125.54, 125.14, 124.37, 123.71, 122.66, 122.02, 121.90, 121.87, 121.41, 118.41, 117.79, 35.53, 35.39, 35.04, 34.97, 31.88, 31.74, 31.17, 31.08; HRMS (APPI-TOF, positive mode) *m/z* calcd for $C_{48}H_{48}N_2O$ 668.3767, found 668.3783 $[M + H]^+$. X-ray.

14,18-Di-*tert*-butyl-6H-phenanthro[4,5-*cde*]pyreno[4',5':4,5]imidazo[1,2-*a*]azepin-6-one (2c)

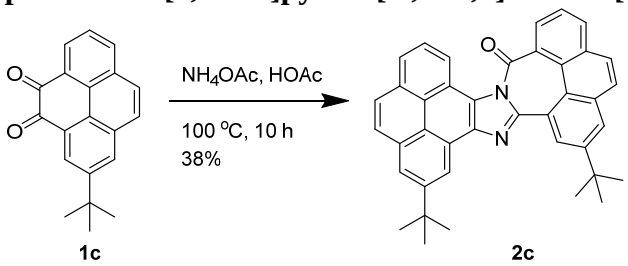

2-(*tert*-Butyl)pyrene-4,5-dione (**1c**) (0.060 g, 0.208 mmol), ammonium acetate (0.128 g, 1.664 mmol), and glacial acetic acid (99.7%, 5 mL) were added to a 50 mL round-bottomed flask. The reaction mixture was stirred and heated at 100 °C for 10 h. Next, the reaction mixture was cooled down to room temperature and then poured into a separatory funnel including water. The mixture was extracted twice with CH_2Cl_2. The combined organic layer was washed twice with a saturated aqueous $NaHCO_3$ solution. The organic layer was dried over $MgSO_4$, filtered, and concentration *in vacuo*. The resulting residue was subjected to silica gel column chromatography (hexanes/CH_2Cl_2/EtOAC, 80:20:3) to give pure compound **2c** (0.044 g, 0.076 mmol, 38%) as a yellow crystalline solid: m.p. 246.3–247.9 °C. IR (neat): 3051, 2950, 2902, 2863, 1687, 1602, 1567, 1475, 1316, 1261, 1202, 1055, 891 cm^{-1}; ^1H NMR (300 MHz, CD_2Cl_2): δ 9.62 (d, J = 2.3 Hz, 1H), 9.23 (d, J = 2.0 Hz, 1H), 8.70 (dd, J = 7.5, 1.5 Hz, 1H), 8.53 (dd, J = 7.9, 1.1 Hz, 1H), 8.36–8.32 (m, 2H), 8.24–8.20 (m, 2H), 8.14–8.08 (m, 3H), 8.02–7.93 (m, 3H), 1.69 (s, 9H), 1.67 (s, 9H); ^{13}C NMR (75 MHz, CD_2Cl_2): δ 171.89, 151.21, 150.71, 150.40, 141.52, 134.45, 134.32, 133.77, 133.45, 132.59, 132.17, 131.30, 130.35, 129.86, 128.77, 128.34, 128.28, 127.95, 127.37, 127.22, 126.31, 125.96, 125.87, 125.50, 125.02, 124.30, 123.45, 122.48, 122.32, 121.03, 118.52, 35.97, 35.63, 32.26, 31.70; HRMS (APPI-TOF, positive mode) *m/z* calcd for $C_{40}H_{32}N_2O$ 556.2514, found 556.2512 $[M + H]^+$. X-ray.

4,18-Di-*tert*-butyl-6*H*-phenanthro[4,5-*cde*]phenanthro[9',10':4,5]imidazo[1,2-*a*]azepin-6-one (5)

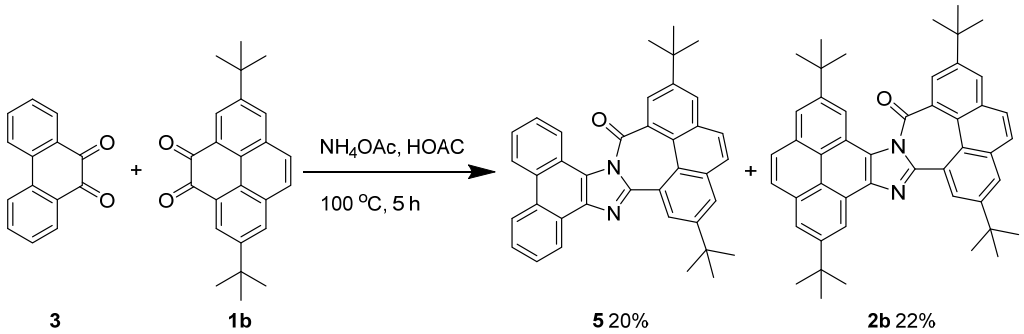

2,7-Di-*tert*-butylpyrene-4,5-dione (**1b**) (0.050 g, 0.17 mmol), phenanthrene-9,10-dione (**3**) (0.050 g, 0.24 mmol), ammonium acetate (0.107 g, 1.392 mmol), and glacial acetic acid (99.7%, 5 mL) were added to a 50 mL round-bottomed flask. The reaction mixture was stirred and heated at 100 °C for 5 h. Next, the mixture was cooled down to room temperature and then poured into a separatory funnel including water. The mixture was extracted twice with CH_2Cl_2. The combined organic layer washed twice with a saturated aqueous $NaHCO_3$ solution. The organic layer was dried over $MgSO_4$, filtered, and concentrated *in vacuo*. The resulting residue was

subjected to silica gel column chromatography (hexanes/CH_2Cl_2, 80:20) to give pure compound **5** (0.018 g, 0.035 mmol, 20%) and compound **2b** (0.022 g, 0.032 mmol, 22%). Both products appeared as yellow crystalline solids. Compound **5**: m.p. > 251.2 °C (dec.); IR (neat): 3058, 2952, 2924, 2855, 1687, 1608, 1567, 1478, 1362, 1261, 1224, 1076, 888 cm^{-1}; ^1H NMR (300 MHz, CD_2Cl_2): δ 9.56 (d, *J* = 2.3 Hz, 1H), 8.92 (m, 1H), 8.86 (m, 1H), 8.78 (m, 1H), 8.67 (d, *J* = 2.3 Hz, 1H), 8.30 (d, *J* = 2.3 Hz, 1H), 8.27 (m, 1H), 8.18 (d, *J* = 2.3 Hz, 1H), 7.94 (d, *J* = 1.1 Hz, 2H), 7.82–7.67 (m, 4H), 1.63 (s, 9H), 1.61 (s, 9H); ^{13}C NMR (75 MHz, CD_2Cl_2): δ 172.11, 150.76, 150.72, 150.45, 140.86, 134.31, 134.00, 133.05, 130.77, 130.72, 130.39, 130.07, 129.52, 129.39, 128.72, 128.27, 127.88, 127.32, 127.06, 126.91, 126.17, 125.99, 124.92, 124.70, 124.24, 123.94, 123.91, 123.81, 123.52, 35.55, 31.68, 31.61, 30.28; HRMS (APPI-TOF, positive mode) *m/z* calcd for $C_{38}H_{32}N_2O$ 532.2515, found 532.2526 $[M + H]^+$. X-ray.

2'-(1*H*-phenanthro[9,10-*d*]imidazol-2-yl)-[1,1'-biphenyl]-2-carboxylic acid (4)

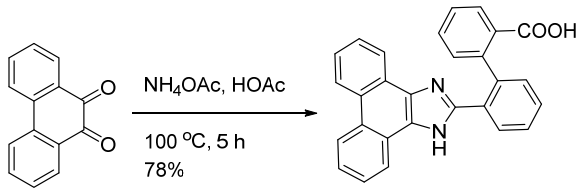

3 **4**

Phenanthrene-9,10-dione (**3**) (0.200 g, 0.960 mmol), ammonium acetate (0.592 g, 7.684 mmol), and glacial acetic acid (99.7%, 10 mL) were added to a 50 mL round-bottomed flask. The reaction mixture was stirred and heated at 100 °C for 5 h. Next, the mixture was cooled down to room temperature and kept at this temperature for 2 days. Compound **4** (0.310 g, 0.749 mmol, 78%) was collected as a pale yellow solid after vacuum filtration and solvent rinsing. The structure of **4** was confirmed by ^1H NMR, which is consistent with the data reported by Lantos [see, *J. Org. Chem*. **1975**, *40*, 1641–1642].

2. NMR Spectra for New Compounds

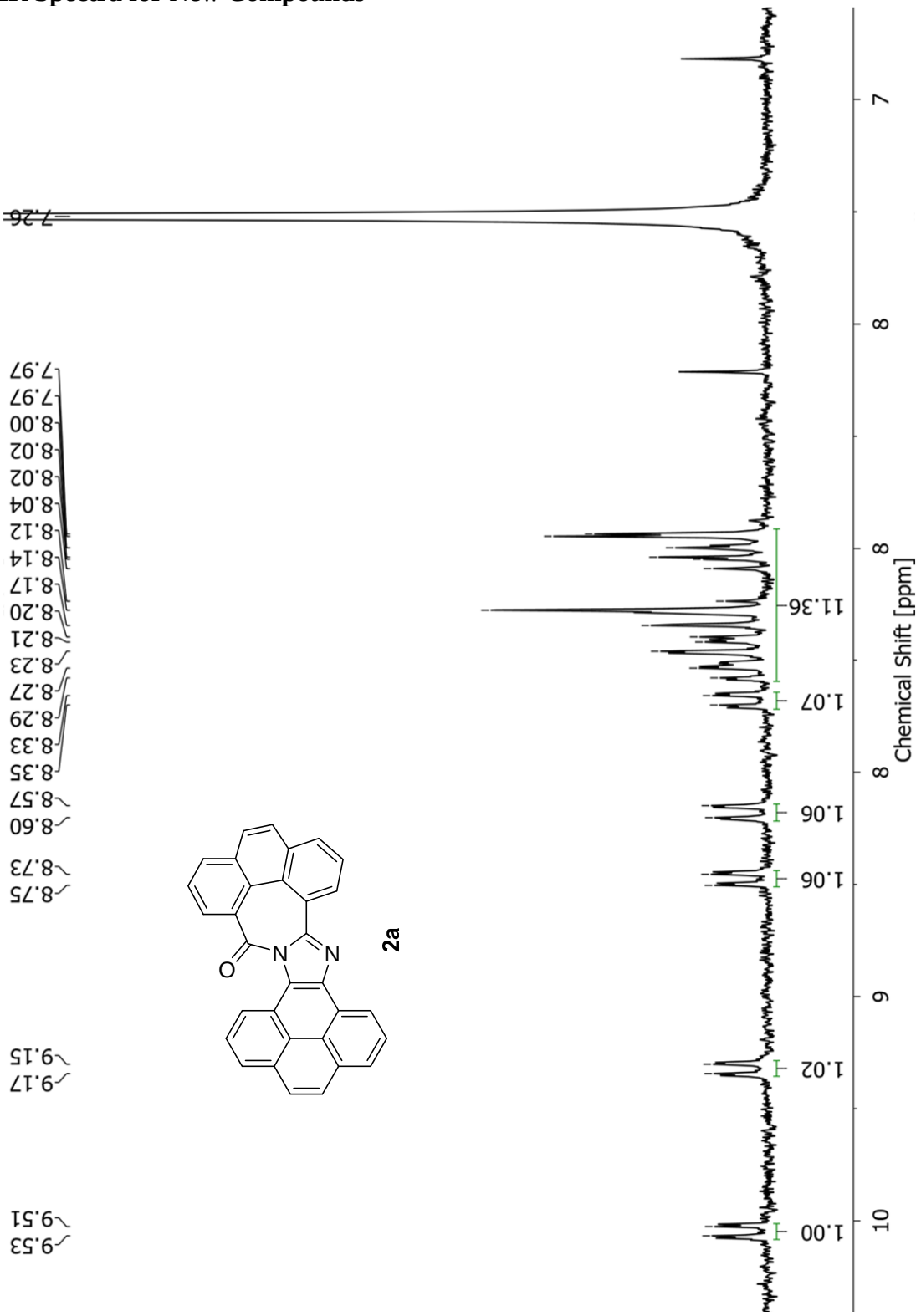

Fig. S-1 ^{1}H NMR (300 MHz, CD_2Cl_2) of compound **2a**.

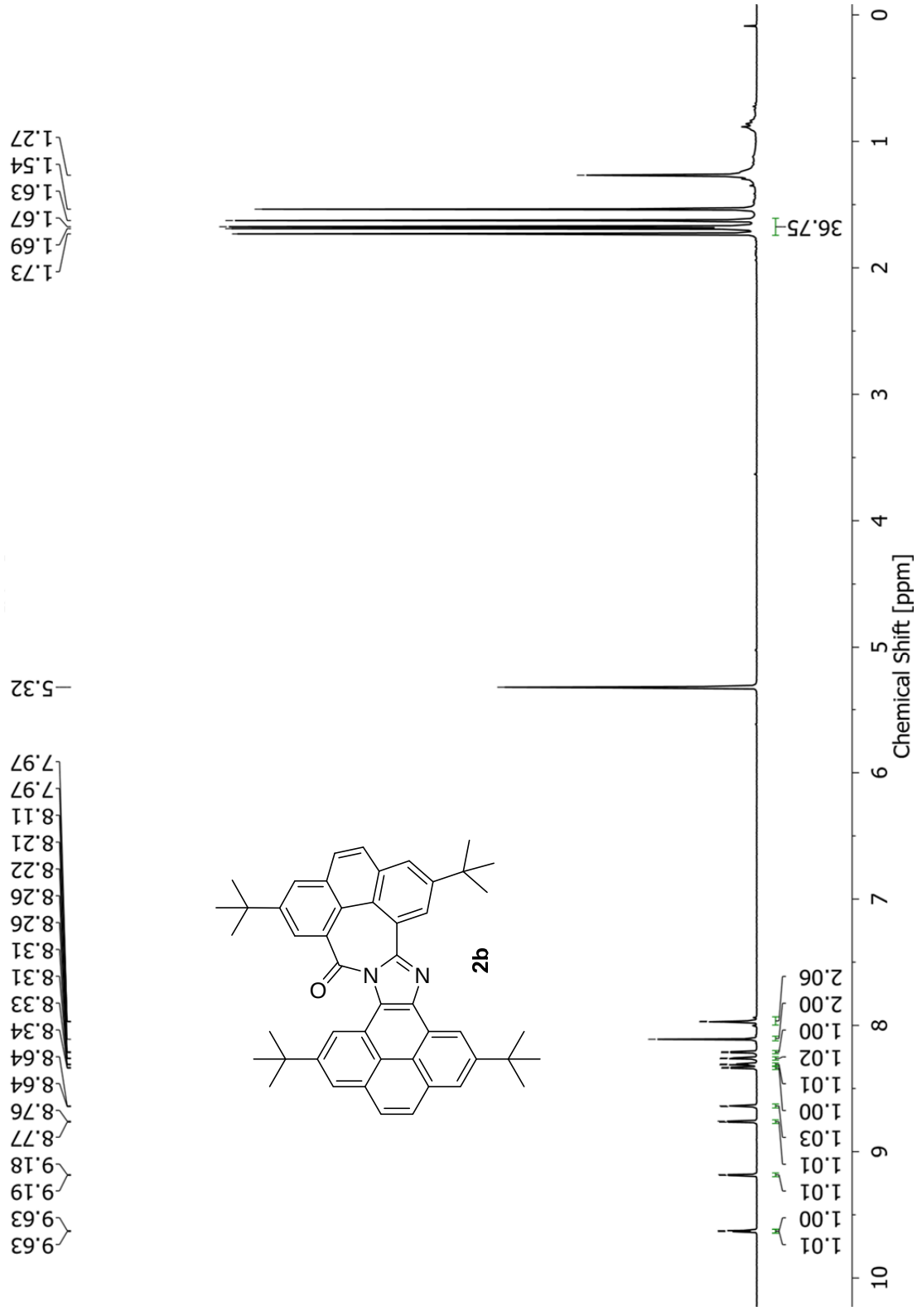

Fig. S-2 ^{1}H NMR (300 MHz, CD_2Cl_2) of compound **2b**.

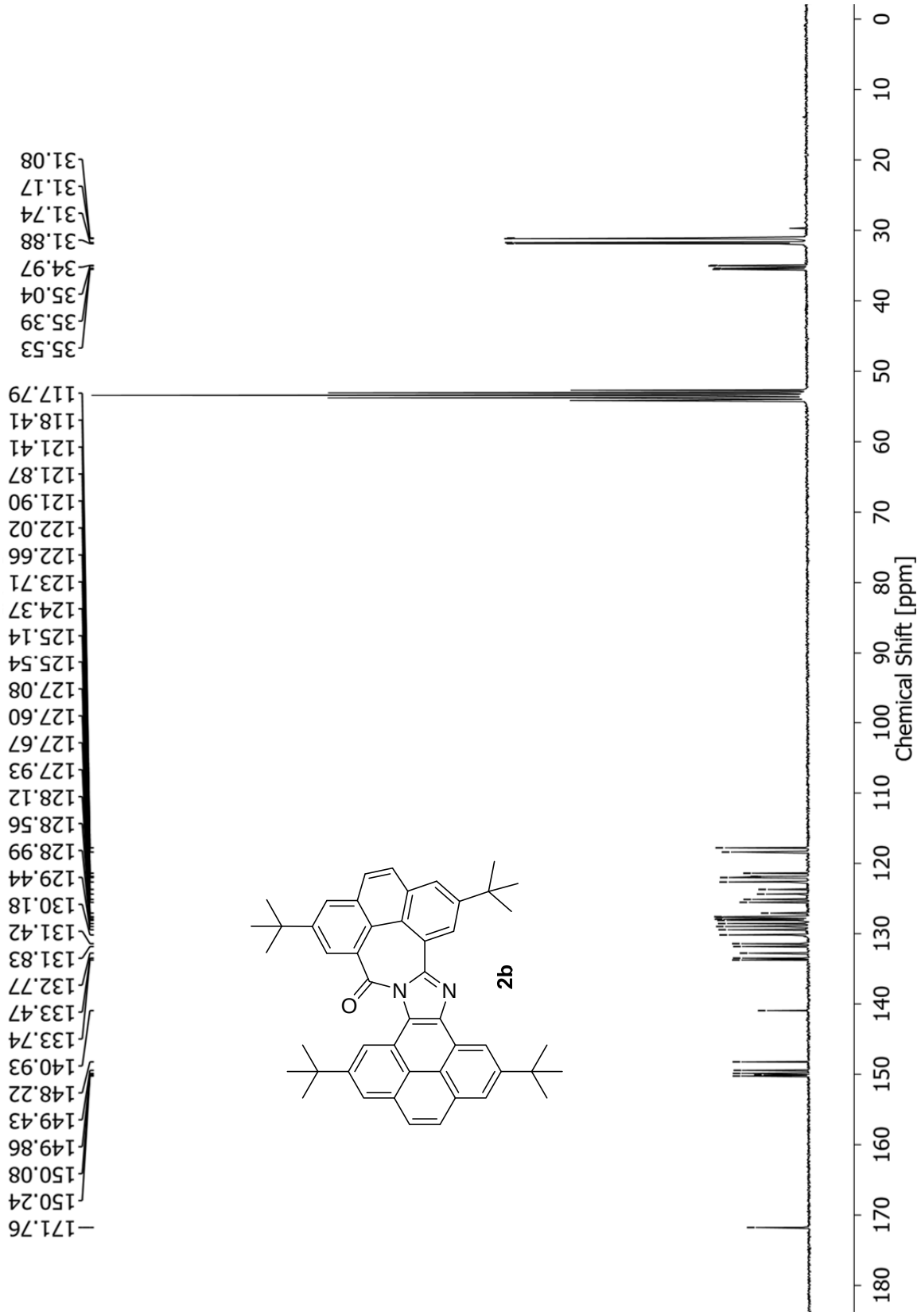

Fig. S-3 ^{13}C NMR (75 MHz, CD_2Cl_2) of compound **2b**.

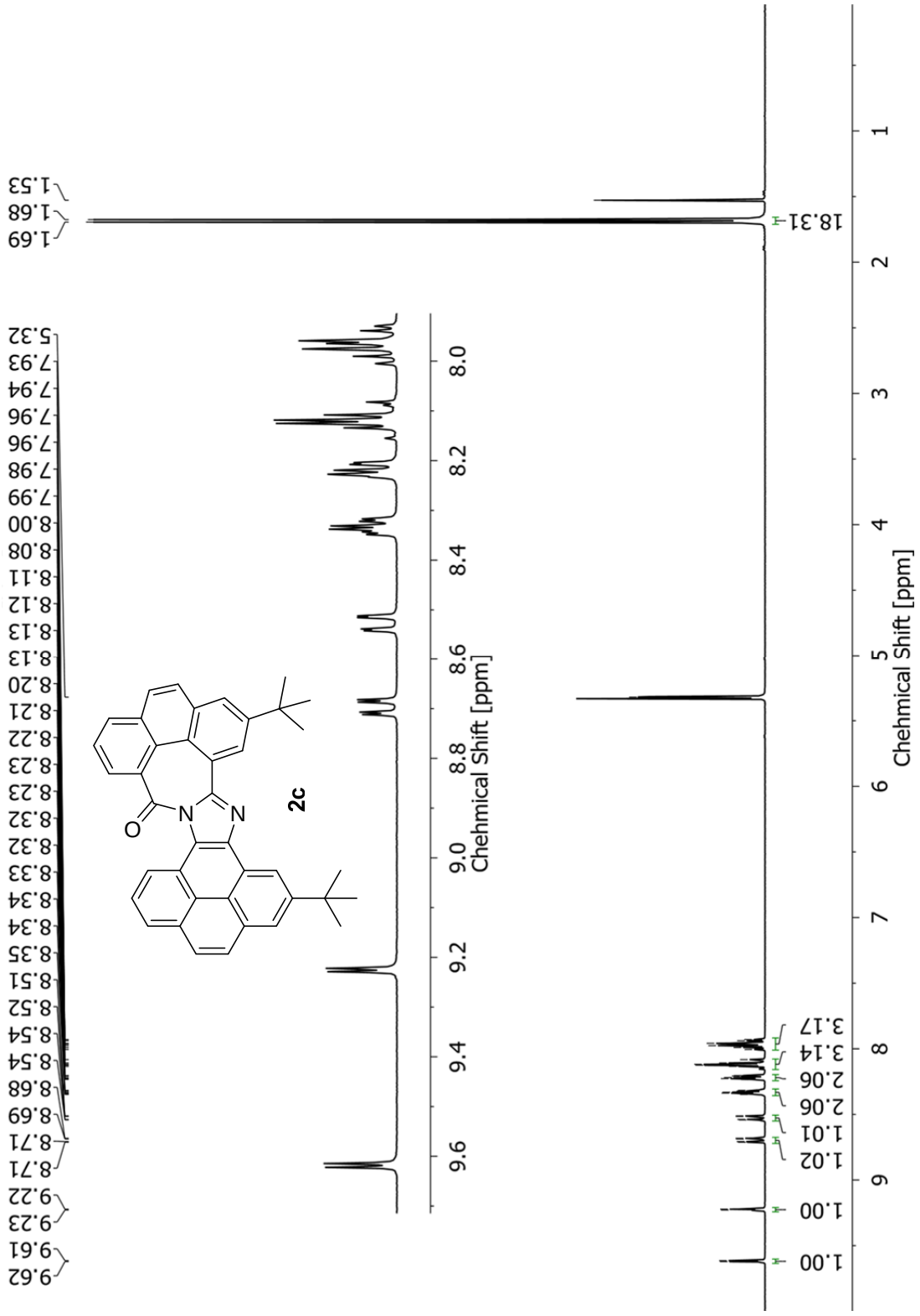

Fig. S-4 ^{1}H NMR (300 MHz, CD_2Cl_2) of compound **2c**.

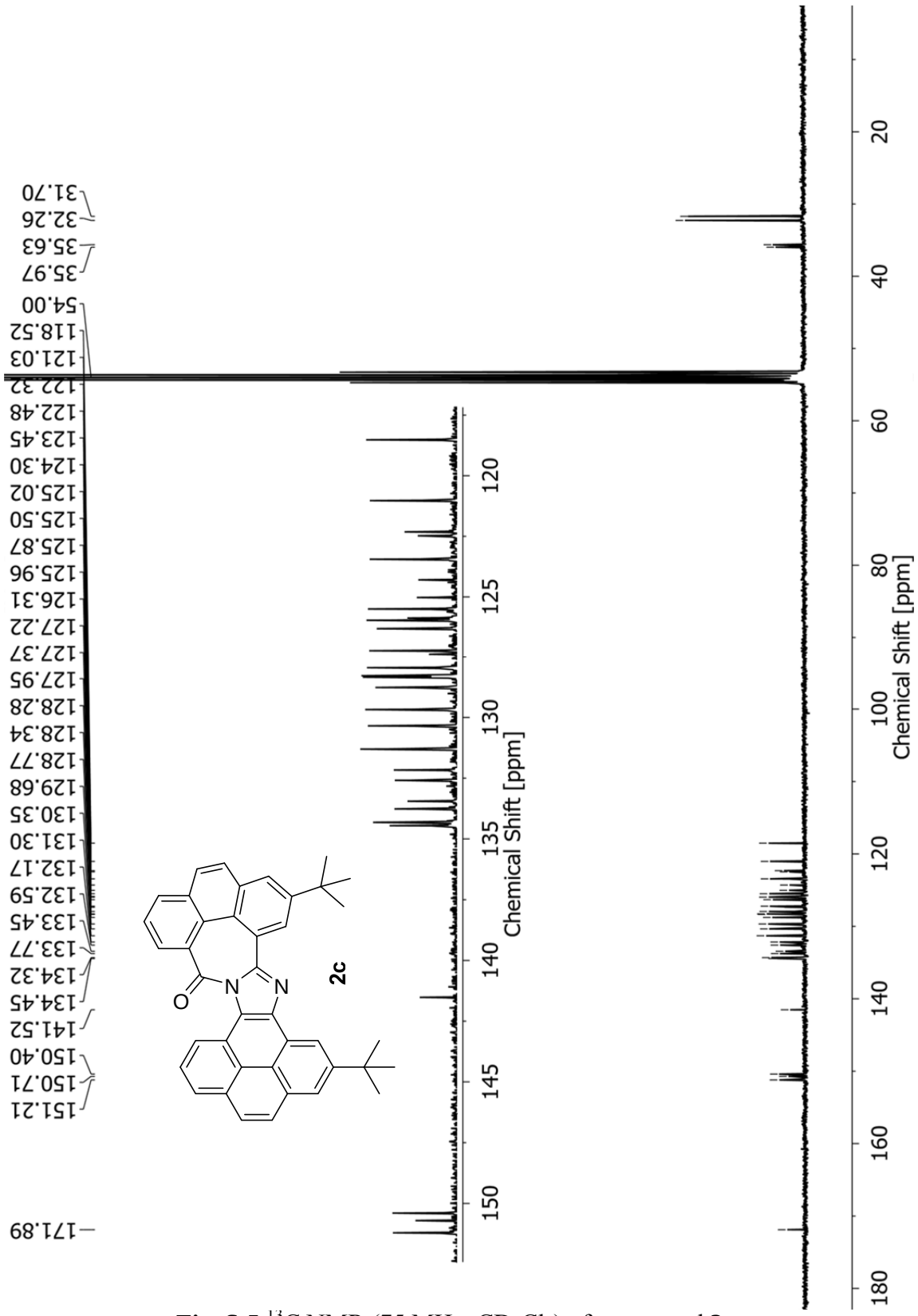

Fig. S-5 ^{13}C NMR (75 MHz, CD_2Cl_2) of compound **2c**.

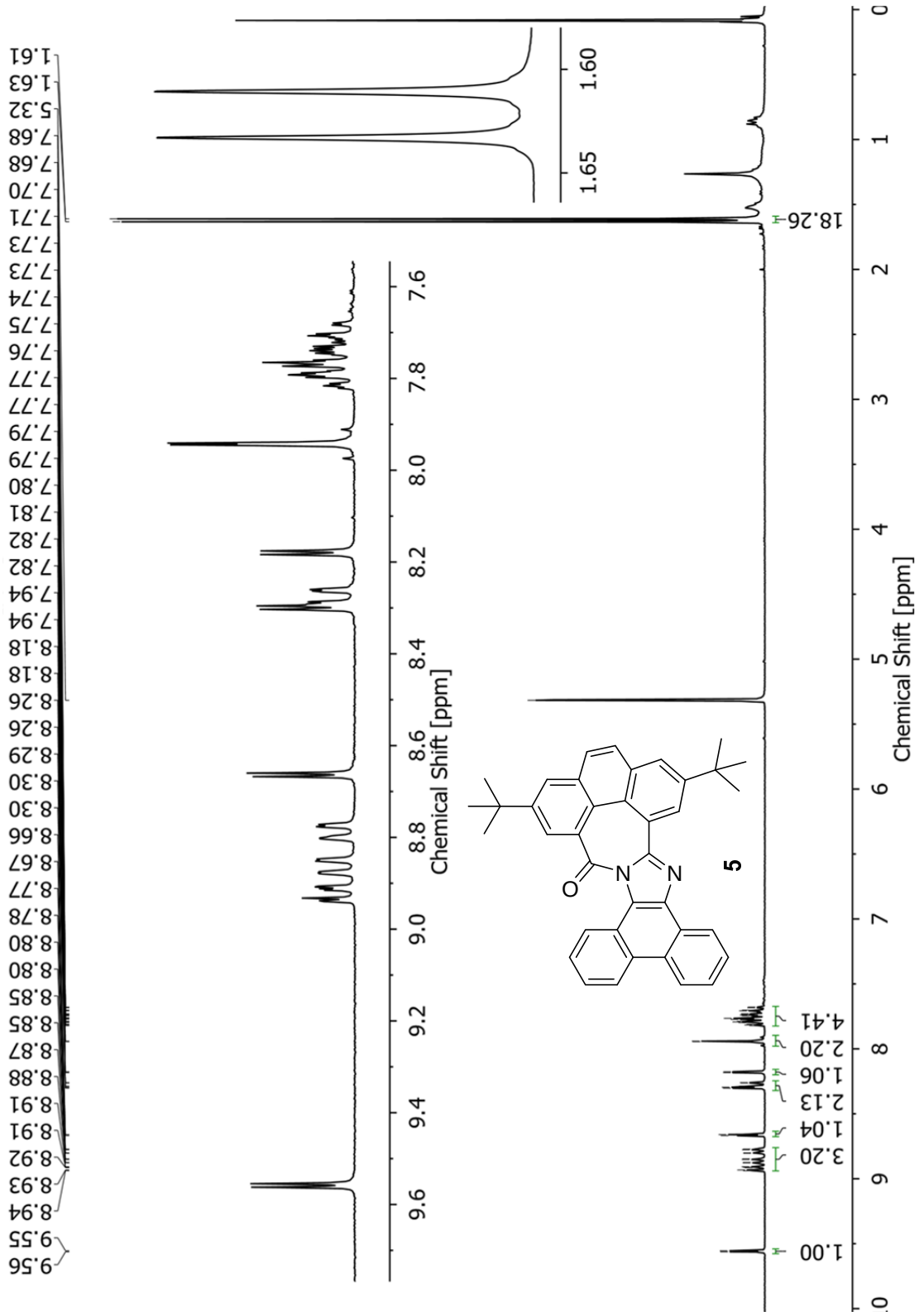

Fig. S-6 ^{1}H NMR (300 MHz, CD_2Cl_2) of compound **5**.

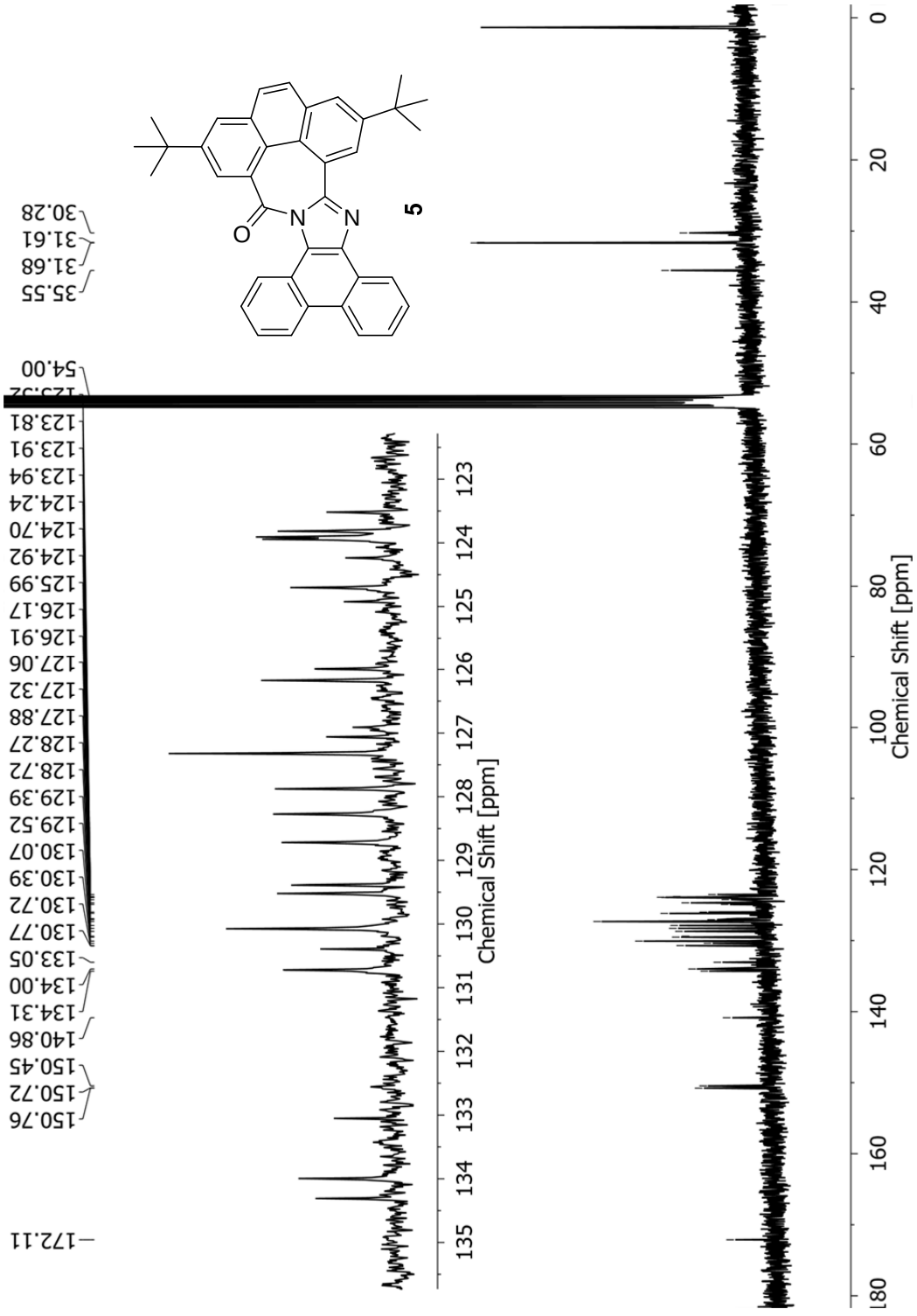

Fig. S-7 ^{13}C NMR (75 MHz, CD_2Cl_2) of compound **5**.

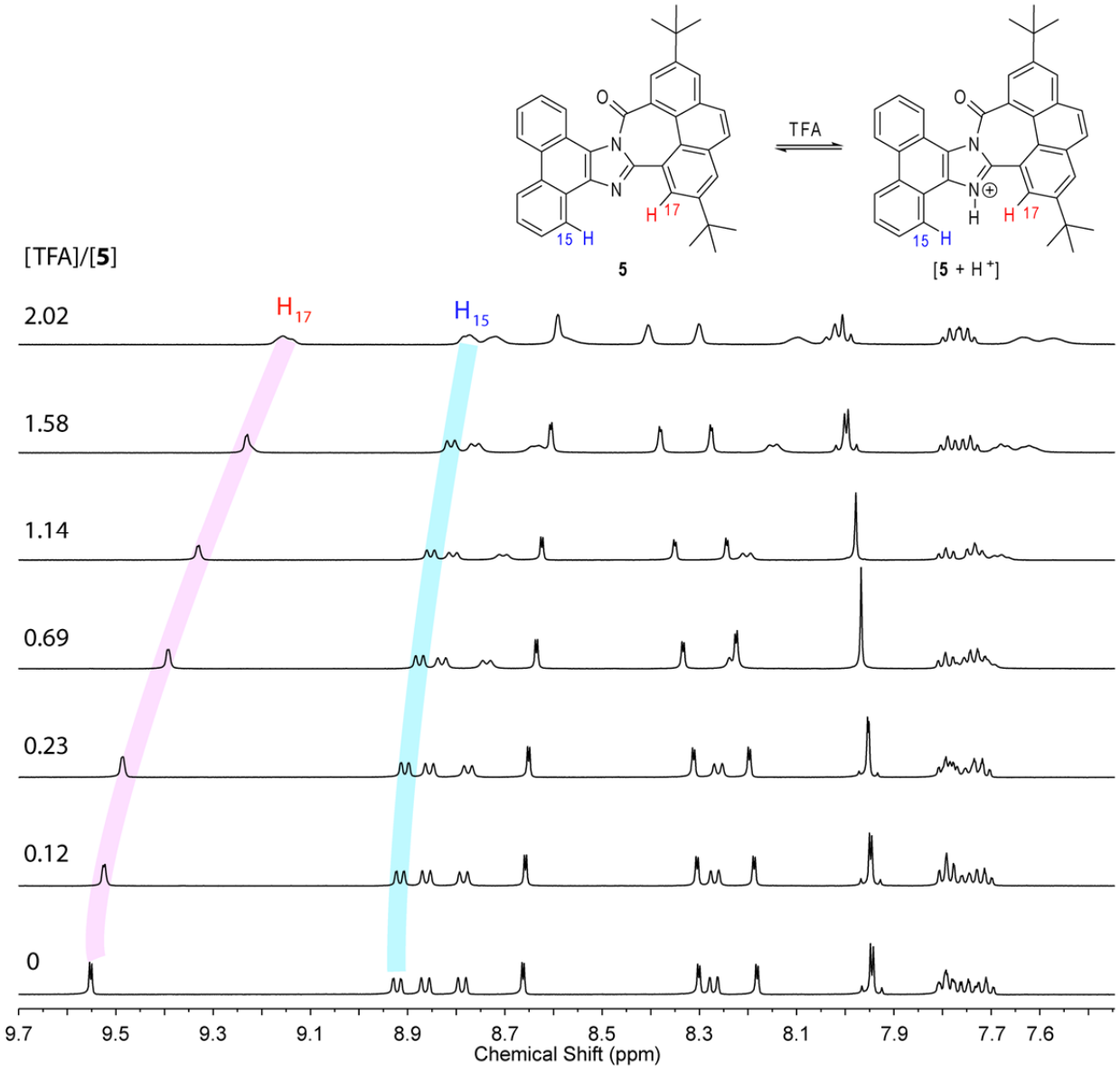

Fig. S-8 ^{1}H NMR spectra of **5** (8.04×10^{-3} M in CD_2Cl_2) in response to the addition of TFA from 0 to 2.02 molar equivalents.

3. UV-Vis Spectroscopic Data

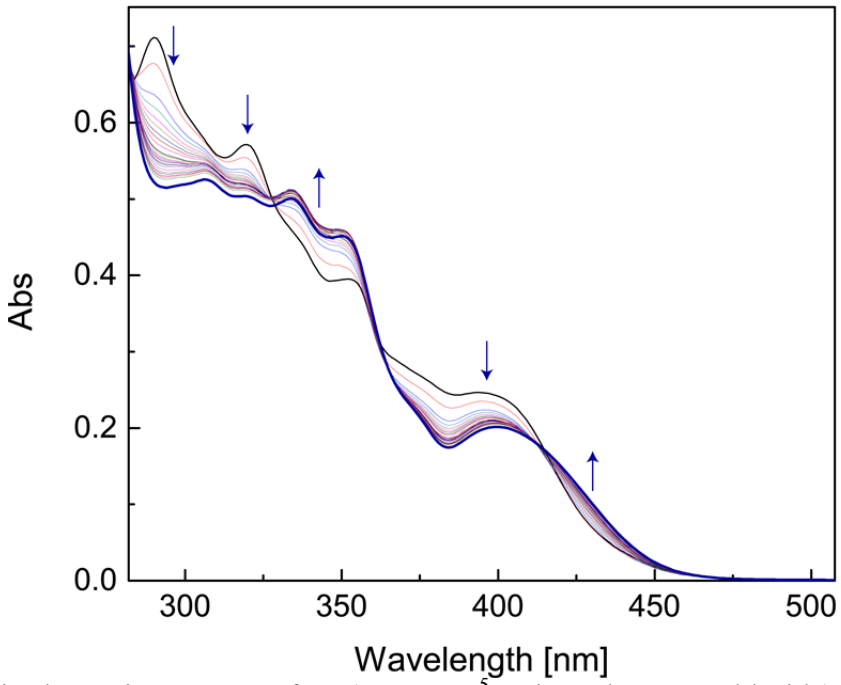

Fig. S-9. UV-Vis absorption spectra of **2b** (1.49×10^{-5} M in carbon tetrachloride) in response to the addition of TFA from 0 to 3.10×10^{3} molar equivalents. Arrows indicate the trend of change.

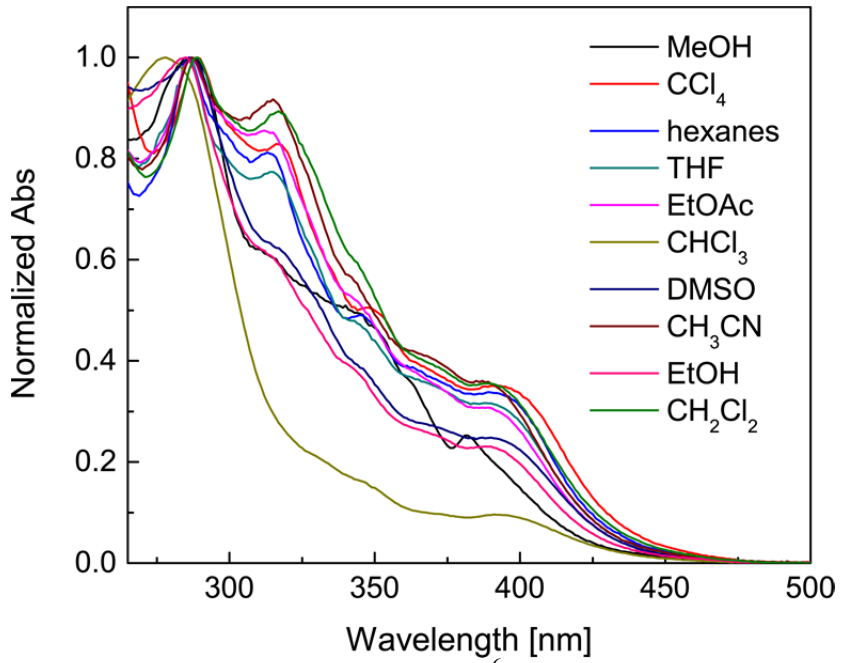

Fig. S-10 UV-Vis absorption spectra of **2c** (8.98×10^{-6} M) measured in different organic solvents (all spectra are normalized).

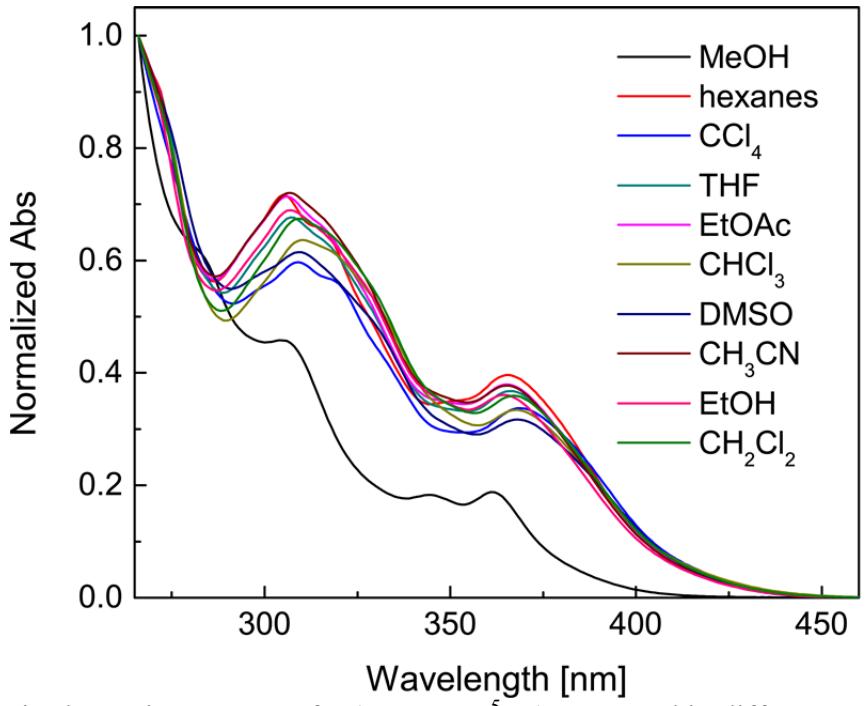

Fig. S-11 UV-Vis absorption spectra of **5** (1.87×10^{-5} M) measured in different organic solvents (all spectra are normalized).

Table S-1 Summary of UV-Vis Absorption and Fluorescence Data of Compound **2b**

Solvent	UV-Vis absorption λ_{max} /nm (ε / mol^{-1} L cm^{-1})	Fluorescence λ_{em} /nm
EtOH	395 (6.98×10^3), 345 (sh, 1.32×10^4), 316 (1.75×10^4), 288 (2.03×10^4)	**
CH_3CN	394 (4.97×10^3), 317 (1.25×10^4), 288 (1.38×10^4)	551
DMSO	394 (9.861×10^3), 320 (2.33×10^4), 290 (2.72×10^4)	553
Acetone	395 (1.42×10^4), 372 (sh, 1.66×10^4), 345 (2.57×10^4)	544
$CHCl_3$	401 (1.37×10^4), 349 (3.01×10^4), 334 (3.42×10^4), 278 (4.64×10^4)	551
EtOAc	393 (2.07×10^4), 345 (sh, 3.58×10^4), 316 (5.10×10^4), 288 (5.88×10^4)	524

THF	395 (6.98×10^3), 348 (sh, 3.10×10^4), 318 (4.42×10^4), 289 (5.19×10^4)	523
Benzene	395 (1.87×10^4), 349 (3.17×10^4), 318 (4.31×10^4), 289 (5.54×10^4)	524
p-Xylene	396 (1.98×10^4), 348 (sh, 3.37×10^4), 318 (4.52×10^4)	521
CCl_4	401 (1.65×10^4), 353 (2.66×10^4), 319 (3.87×10^4), 290 (4.78×10^4)	520
Hexane	399 (1.96×10^4), 348 (3.29×10^4), 316 (4.76×10^4), 287 (5.86×10^4)	495, 514
MeOH	382 (3.18×10^3), 347 (7.11×10^3), 291 (1.38×10^4), 244 (2.76×10^4)	**

** Too weak to be determined accurately

Table S-2 Summary of UV-Vis Absorption Data of Compound **2c**

Solvent	UV-Vis absorption λ_{max} /nm (ε / mol^{-1} L cm^{-1})
EtOH	390 (2.61×10^3), 284 (1.12×10^4)
CH_3CN	389 (3.02×10^3), 315 (7.34×10^3), 285 (8.03×10^3)
DMSO	391 (2.76×10^3), 345 (sh, 4.46×10^3), 316 (sh, 7.16×10^3), 285 (1.16×10^4)
Acetone	391 (2.23×10^3)
$CHCl_3$	395 (2.26×10^3), 278 (2.44×10^4)
EtOAc	390 (6.74×10^3), 343 (sh, 8.63×10^3), 313 (1.16×10^4), 286 (1.30×10^4)
THF	395 (2.64×10^3), 345 (sh, 4.17×10^3), 314 (6.81×10^3), 286 (8.76×10^3)
Benzene	395 (2.68×10^3), 348 (sh, 4.31×10^3), 284 (2.15×10^4)
p-Xylene	392 (2.78×10^3), 347 (sh, 4.50×10^3), 316 (7.54×10^3)
CCl_4	395 (2.75×10^3), 350 (sh, 4.03×10^4), 316 (6.50×10^3), 288 (8.00×10^4)
Hexane	393 (2.73×10^3), 346 (sh, 3.93×10^3), 313 (6.44×10^3), 283 (7.80×10^3)
MeOH	382 (2.12×10^3), 346 (sh, 4.19×10^3), 285 (8.29×10^3)

Table S-3 Summary of UV-Vis Absorption Data of Compound **5**

Solvent	UV-Vis absorption λ_{max} /nm (ε / mol^{-1} L cm^{-1})
EtOH	366 (1.19×10^4), 307 (2.27×10^4), 251 (5.63×10^4)
CH_3CN	365 (1.32×10^4), 305 (2.47×10^4), 249 (5.82×10^4)

DMSO	368 (1.27×10^4), 308 (2.46×10^4), 255 (5.34×10^4)
Acetone	365 (2.49×10^4)
$CHCl_3$	368 (1.26×10^4), 310 (2.40×10^4), 252 (5.67×10^4)
EtOAc	366 (1.57×10^4), 306 (2.81×10^4), 250 (6.43×10^4)
THF	354 (1.65×10^4), 297 (2.70×10^4), 245 (6.02×10^4)
Benzene	369 (1.28×10^4), 308 (2.29×10^4), 274 (3.78×10^4)
p-Xylene	368 (1.27×10^4), 319 (2.13×10^4), 308 (2.30×10^4)
CCl_4	369 (1.26×10^4), 318 (sh, 2.13×10^4), 308 (2.24×10^4), 255 (5.13×10^4)
Hexane	367 (1.41×10^4), 315 (sh, 2.37×10^4), 305 (2.58×10^4), 249 (6.53×10^4)
MeOH	362 (8.17×10^3), 305 (2.04×10^4), 282 (sh 2.75×10^4), 258 (6.25×10^4)

4. Photographic Images

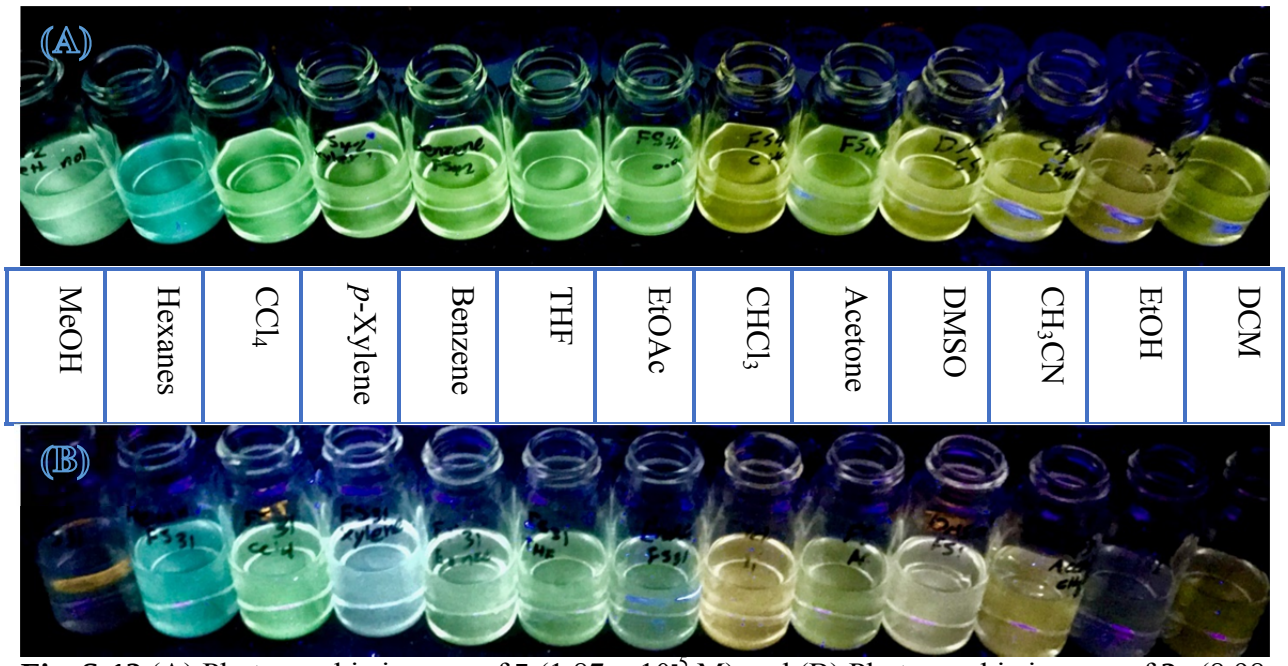

Fig. S-12 (A) Photographic images of **5** (1.87×10^{-5} M) and (B) Photographic images of **2c** (8.98×10^{-6} M) dissolved or suspended in different organic solvents.

5. Cyclic Voltammetric Data of 2b

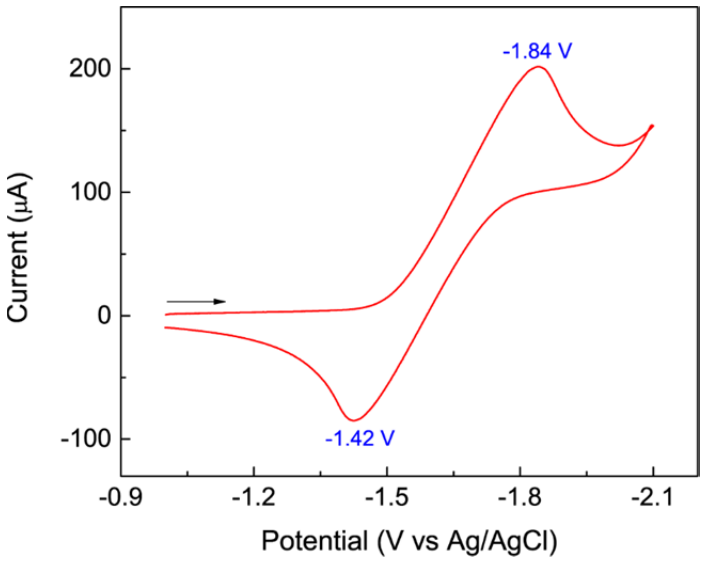

Fig. S-13 Cyclic voltammogram of **2b** measured in CH_2Cl_2 at room temperature. Experimental conditions: Bu_4NBF_4 as electrolyte, glassy carbon as working electrode, Pt wire as counter electrode, Ag/AgCl as reference electrode, scan rate = 200 mV/s.

5. Detailed Results of DFT Calculations

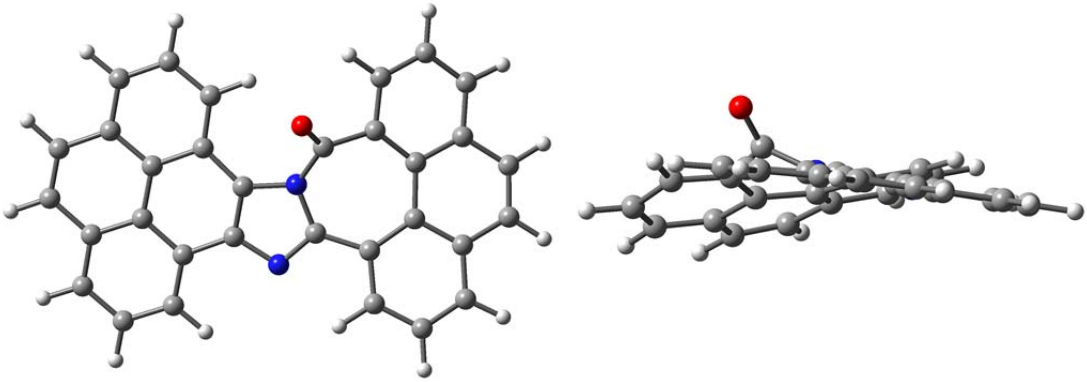

Fig. S-14 Optimized geometry of compound **2a** calculated at the M06-2X/6-31G(d) level (top view and side view).

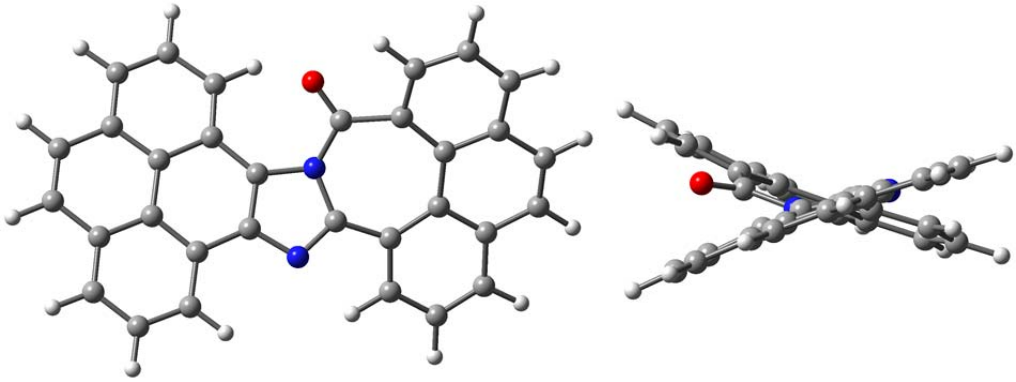

Fig. S-15 Transition state of compound **2a** calculated at the M06-2X/6-31G(d) level (top view and side view). Imaginary frequency = *i*21.63 cm^{-1}.

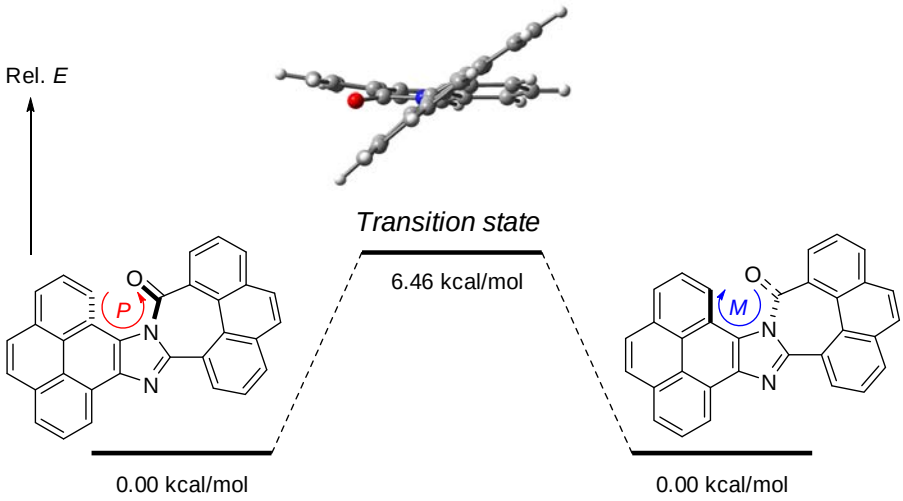

Fig. S-16 Energy profile for the epimerization process of **2a** calculated at the M06-2X/6-31G(d) level.

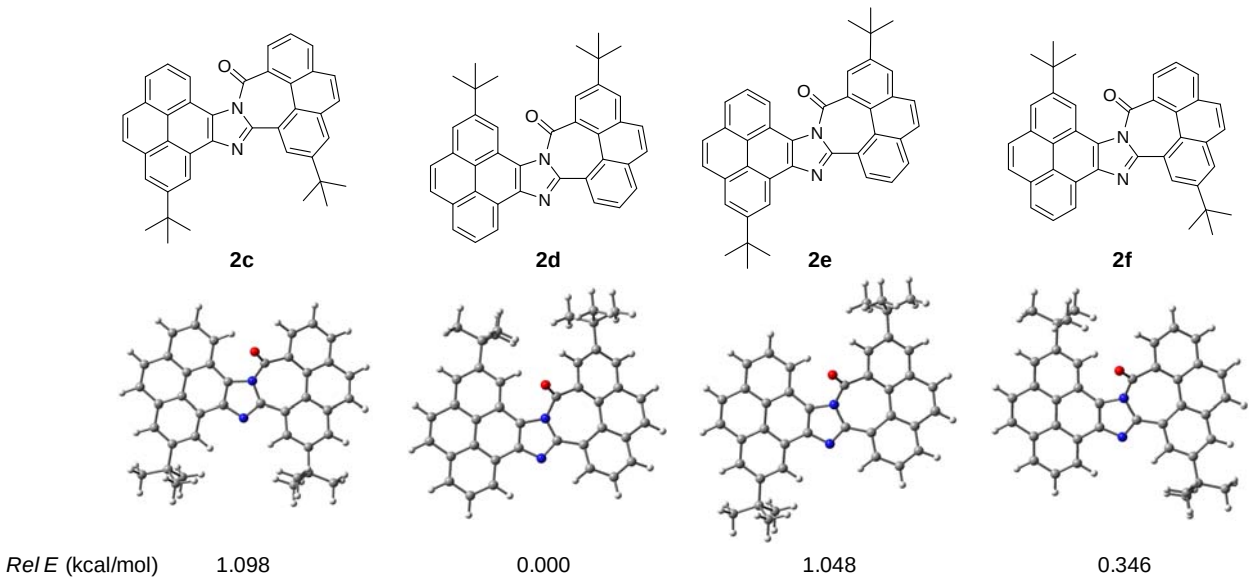

Fig. S-17 Structures, optimized geometries, and relative energies of compounds **2c**–**f** calculated at the M06-2X/6-31G(d) level.

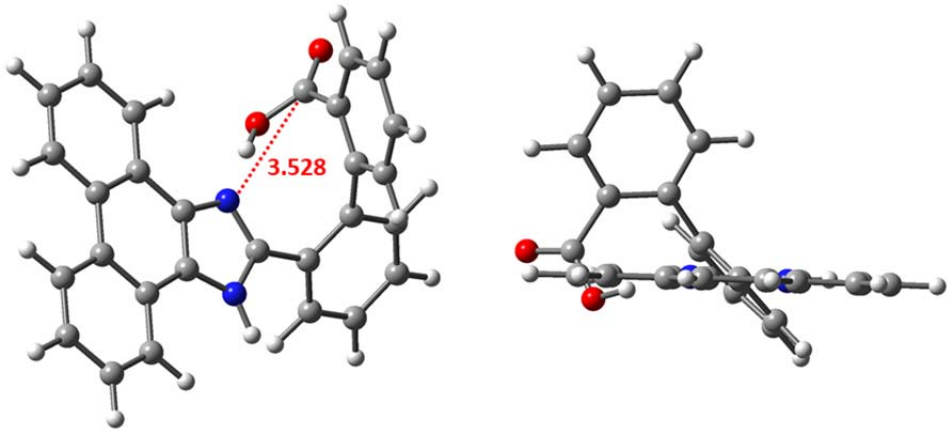

Fig. S-18 Optimized geometry of compound **4** calculated at the M06-2X/6-31G(d) level. The distance between imidazolyl N and carbonyl C atoms is indicated (in Å).

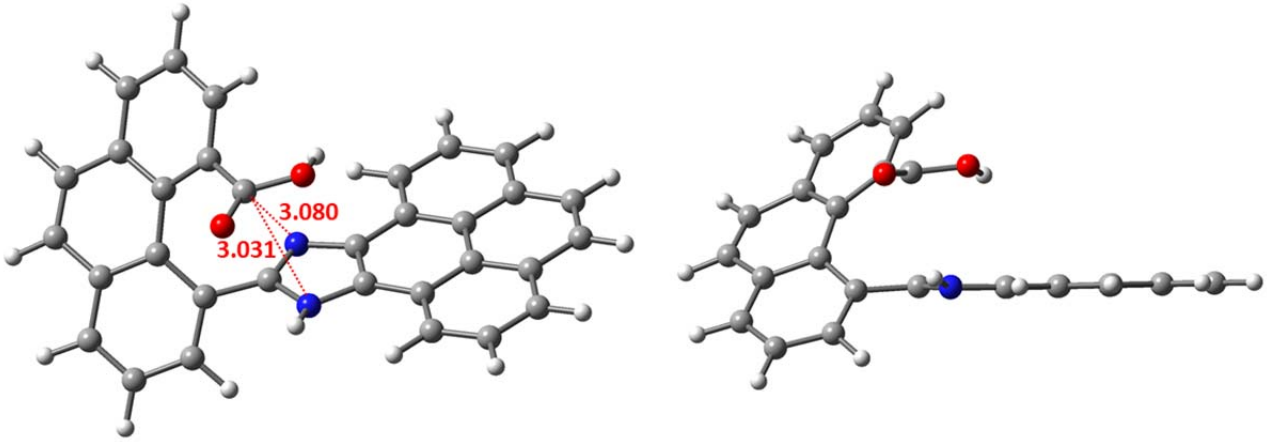

Fig. S-19 Optimized geometry of intermediate **IM-5** calculated at the M06-2X/6-31G(d) level. The distances between imidazolyl N and carbonyl C atoms are indicated (in Å).

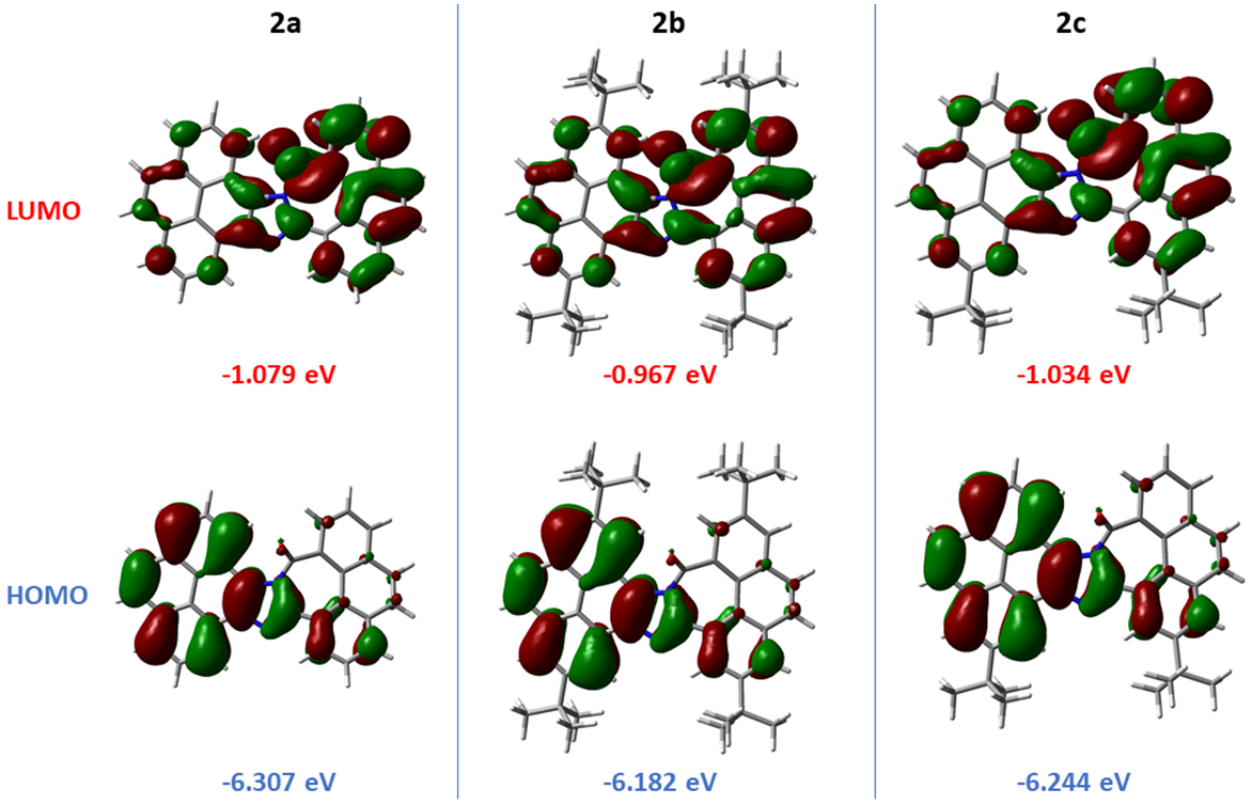

Fig. S-20 Plots and energies of frontier molecular orbitals for **2a-c** calculated at the M06-2X/6-31G(d) level.

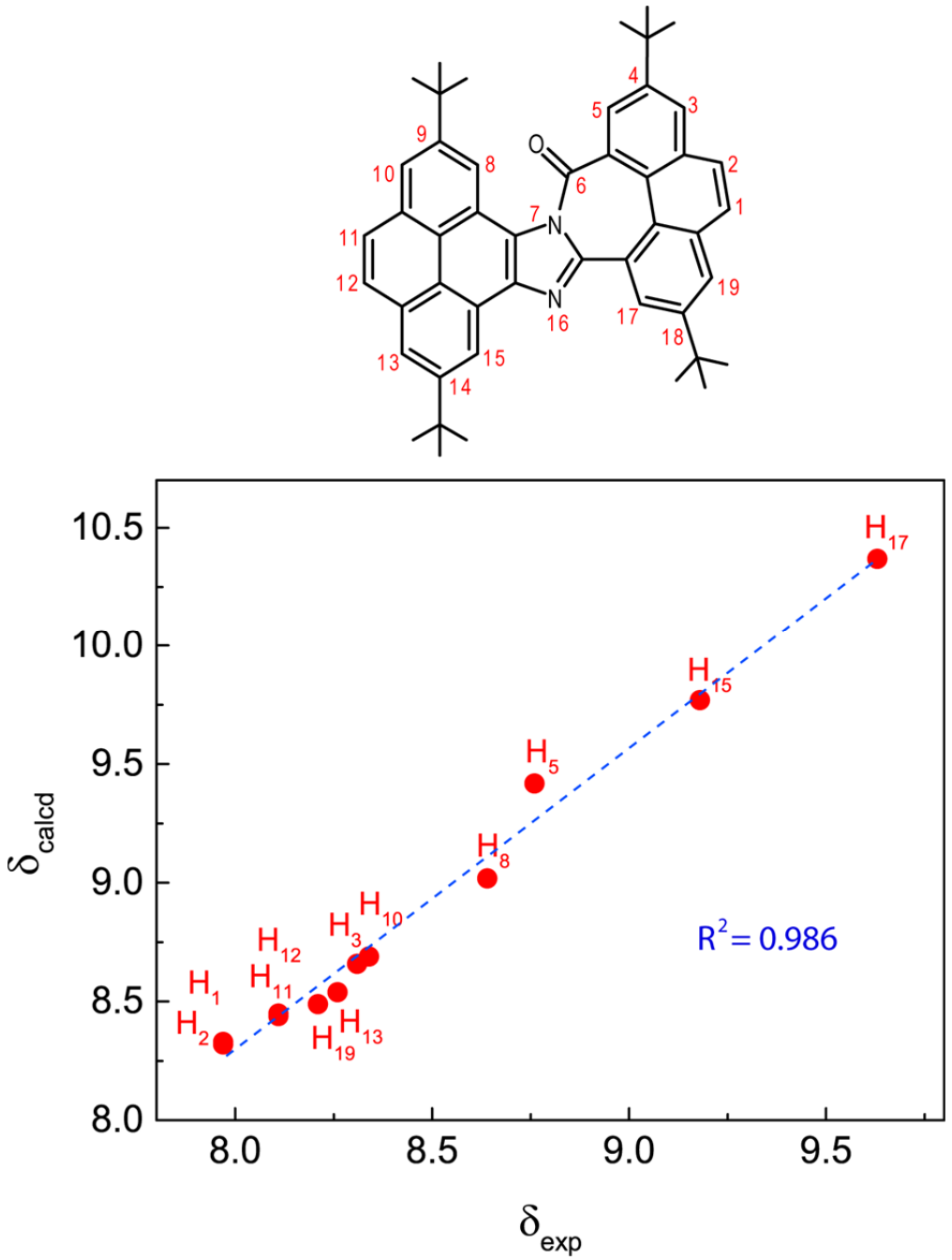

Fig. S-21 Correlation of DFT calculated and experimental observed chemical shifts for the aromatic protons in compound **2b**.

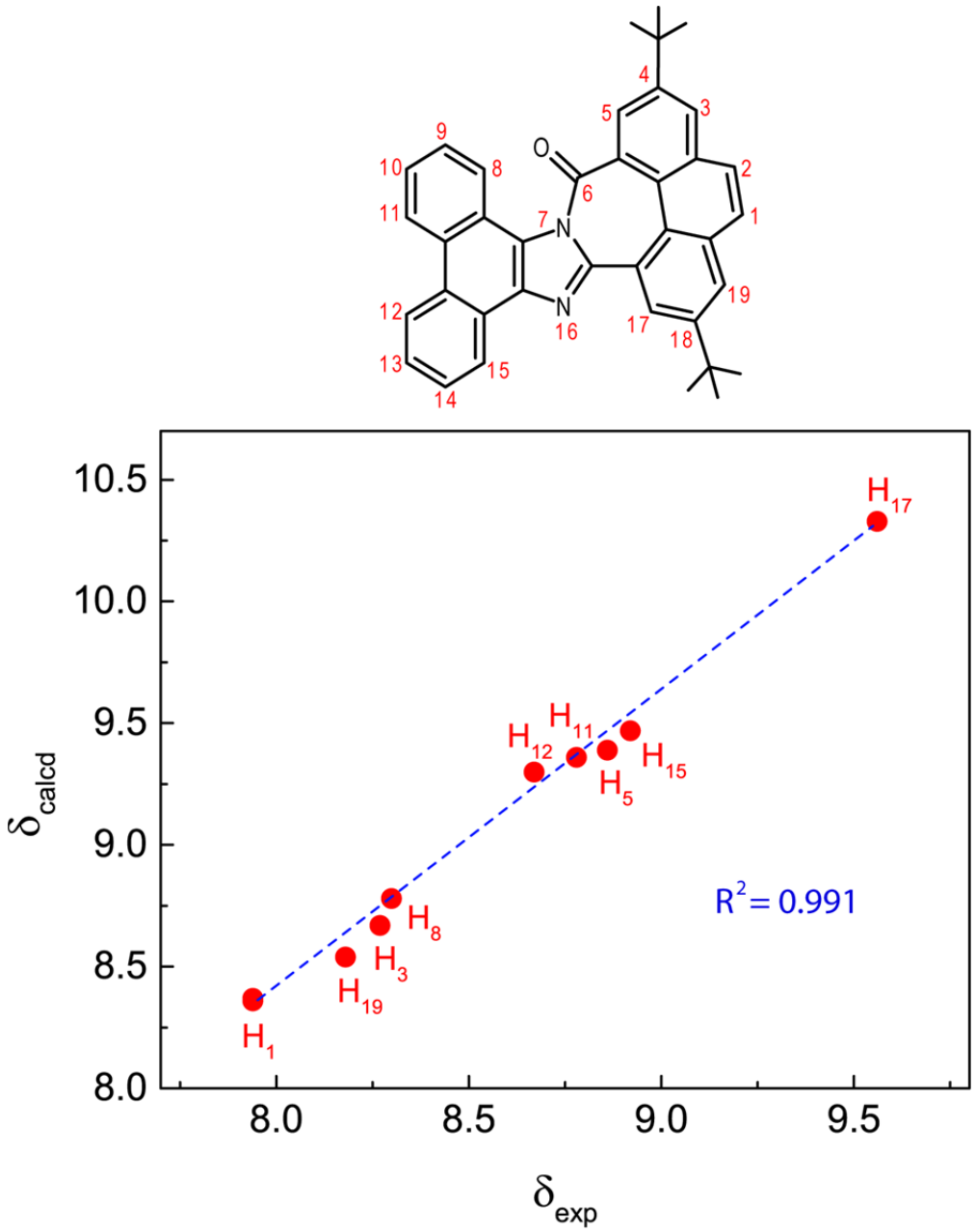

Fig. S-22 Correlation of DFT calculated and experimental observed chemical shifts for the aromatic protons in compound **5**. Signals at positions 2, 14, 9, 13, and 10 are overlapped in the experimental spectrum and they are therefore not shown in this correlation diagram.

Table S-4 Cartesian Coordinates and Energies of Optimized Geometries

2a (E = -1413.315363 Hartree)				Transition state **2a** (E = -1413.307260 Hartree)			
C	2.83194700	-3.50576300	0.09485500	H	-2.81197600	-4.19671300	1.90570300
C	1.78577200	-2.59044800	0.17477700	C	-2.99134700	-3.23927500	1.42695000
C	2.03335300	-1.21532400	0.14765600	C	-3.43490800	-0.73061800	0.25457300
C	3.38042800	-0.75470300	-0.01256800	C	-1.90819100	-2.42916400	1.10313300
C	4.43517600	-1.70554900	-0.07652800	C	-4.28655300	-2.84055800	1.13713000
C	4.14300100	-3.07358200	-0.01388300	C	-4.52746600	-1.58786400	0.56331700
C	1.03434300	-0.17539500	0.22228000	C	-2.09602700	-1.19171600	0.47773400
C	3.69796400	0.64248800	-0.14186300	H	-5.12929800	-3.48525000	1.37156300
C	2.67713100	1.62824200	-0.13940900	C	-3.71596200	0.59174000	-0.23376600
C	1.33049800	1.15939000	0.03808500	C	-4.25781200	3.20671400	-1.11838200
C	2.98895500	2.97701100	-0.29422800	C	-2.66755500	1.51937200	-0.45921400
H	2.18199200	3.70249100	-0.29225400	C	-5.05558400	1.01118600	-0.45461300
C	4.31637600	3.37088800	-0.44349600	C	-5.30120900	2.31535500	-0.90372800
C	5.33206100	2.42457500	-0.44554500	C	-2.94122900	2.81582100	-0.89137100
C	5.04655300	1.05993100	-0.30186300	H	-6.32878000	2.62527400	-1.07434300
C	6.08715100	0.06743500	-0.32441000	H	-2.11385200	3.49926800	-1.05206200
C	5.79306000	-1.24855200	-0.22113200	H	-4.47009300	4.21411700	-1.46245100
H	6.58022100	-1.99714000	-0.25116100	C	-5.87270800	-1.14403800	0.30218800
H	7.11513300	0.40103200	-0.43774100	H	-6.68481000	-1.83179000	0.52252500
H	0.77455700	-2.96101900	0.26474100	C	-6.12745400	0.08914800	-0.19053200
H	4.95816700	-3.79018500	-0.06448700	H	-7.14692100	0.41523200	-0.37791800
H	6.36725600	2.73297100	-0.56517000	C	-1.05254400	-0.25594700	0.11935300
N	0.19993900	1.93110200	0.04553500	C	-1.33255800	1.04371800	-0.23229000
C	-0.80092100	1.10274000	0.21566500	N	0.36284000	-0.31624800	0.15767600
N	-0.35858800	-0.20955000	0.32283700	N	-0.19004400	1.80065700	-0.32516100
C	-1.12575800	-1.26688000	0.87191000	C	0.80363100	0.99813900	-0.06643000
C	-2.44704000	-1.55450300	0.24281100	C	1.04923800	-1.47946800	-0.24828000
C	-3.44754700	-0.61710800	-0.14287400	C	2.52899800	-1.50419700	-0.53332900
C	-2.18873200	1.57795000	0.33118600	C	5.18893900	-2.27344800	-0.95280200
C	-3.37178900	0.83160200	0.04264300	C	2.86603400	-2.72141500	-1.12672500
O	-0.63989500	-1.98406900	1.71067400	C	3.55676300	-0.56319200	-0.20391100
C	-3.79940600	-3.43542600	-0.49744900	C	4.90054100	-1.02603000	-0.37146400
C	-4.79934400	-2.56043500	-0.84820800	C	4.18121200	-3.10600300	-1.36993400
C	-4.66245600	-1.17438400	-0.64089100	H	4.39395200	-4.05925000	-1.84143900
C	-2.64130900	-2.92253100	0.08740800	H	6.23141400	-2.55706900	-1.06842300
H	-5.73444000	-2.92664300	-1.26295900	C	3.37516800	0.81481600	0.25187200
H	-1.86443800	-3.59260600	0.43784400	C	3.23680900	3.55769400	1.04618500
C	-5.78577700	0.96029200	-0.55252100	C	4.53140300	1.55772400	0.64494600
H	-6.66764100	1.58386300	-0.66720300	C	2.13975800	1.52423400	0.25701800
C	-4.58055200	1.57959400	-0.08015500	C	2.09944900	2.86595700	0.63899200
C	-5.81077000	-0.34739600	-0.87470200	C	4.44219300	2.89927400	1.05594000
H	-6.71096400	-0.81600300	-1.26127900	H	1.13850600	3.36304400	0.62334300
C	-2.27431800	2.93809600	0.62355200	H	5.35356700	3.40668400	1.35922000
C	-4.62267000	2.95441300	0.21347400	H	3.16185600	4.59636800	1.35026700
C	-3.48566900	3.62595300	0.59650700	C	5.84277100	0.98461500	0.57853700
H	-1.35285000	3.46338900	0.84129800	H	6.68323900	1.58519600	0.91346300
H	-5.57329100	3.47260800	0.12424200	C	6.02216300	-0.24109500	0.05506900
H	-3.91439800	-4.50455200	-0.63927200	H	7.01433900	-0.66898200	-0.05363000
H	2.61074600	-4.56798100	0.12365300	H	-0.90827600	-2.76864700	1.32936400
H	4.55739400	4.42286400	-0.55989800	H	2.05890000	-3.39764100	-1.37311700
H	-3.51598400	4.68289200	0.83914100	O	0.39661000	-2.48744700	-0.40458300
2b (E = -2042.029809 Hartree)				**2c** (E = -1727.671879 Hartree)			

C	-0.16743400	-4.49711300	0.31219200	C	2.34048500	-4.88665400	0.30505600
C	-0.32210900	-3.10962500	0.30264700	C	1.35983500	-3.89690800	0.30926400
C	0.77063700	-2.24134800	0.24373100	C	1.70757700	-2.54468900	0.26320800
C	2.08514000	-2.77998500	0.12050700	C	3.09125000	-2.18752700	0.16315000
C	2.24697400	-4.19066200	0.13429300	C	4.07701900	-3.21091900	0.17660700
C	1.12423700	-5.01718200	0.24306400	C	3.68318800	-4.55302000	0.25530800
C	0.69807400	-0.80042100	0.25379300	C	0.78651900	-1.43103300	0.26074100
C	3.23849600	-1.94239400	-0.04891200	C	3.51543100	-0.82226100	0.01805700
C	3.11924100	-0.53047800	-0.12112900	C	2.57570200	0.23737900	-0.05746400
C	1.79374400	0.00783000	0.03097100	C	1.18970700	-0.12707300	0.06023500
C	4.24166900	0.26532400	-0.31648300	C	2.99615900	1.55030300	-0.22811000
H	4.09446100	1.34053000	-0.36849800	H	2.23219300	2.32068000	-0.28476000
C	5.52183900	-0.29310300	-0.43788100	C	4.35679000	1.87621300	-0.32059700
C	5.64016100	-1.67907700	-0.36311700	C	5.28175300	0.83881200	-0.24301600
C	4.52772000	-2.51363800	-0.17628600	C	4.89122200	-0.49990000	-0.08147800
C	4.65915900	-3.94606400	-0.12130900	C	5.85937900	-1.56156000	-0.02617100
C	3.57381000	-4.74188700	0.02312600	C	5.46856000	-2.85175600	0.09248200
H	3.68023300	-5.82313200	0.05199500	H	6.20236000	-3.65285300	0.12118700
H	5.65362600	-4.37562000	-0.20943900	H	6.91298200	-1.30366400	-0.09335300
H	-1.31568400	-2.69288200	0.34792200	H	2.04132500	-5.92919200	0.34674600
H	1.28161900	-6.09351500	0.26006200	H	0.32114400	-4.19257200	0.35593400
H	6.61256100	-2.15286900	-0.45479900	H	4.44535400	-5.32742400	0.26394900
N	1.43846600	1.32951900	-0.01770000	H	6.34526900	1.04477100	-0.31289400
C	0.13960100	1.36198800	0.15858100	N	0.12068100	0.72477200	-0.01086100
N	-0.37936300	0.08404800	0.32426500	C	-0.94663900	-0.02310100	0.12692100
C	-1.64445200	-0.20424800	0.89751300	N	-0.60872300	-1.36047300	0.28911400
C	-2.84305900	0.40022000	0.25163600	C	-1.47622100	-2.34562500	0.82447300
C	-2.99914600	1.75066500	-0.17296500	C	-2.78451300	-2.55709600	0.14090300
C	-0.60870400	2.62811900	0.22112700	C	-3.69205400	-1.56161200	-0.32267000
C	-2.00056400	2.80708100	-0.04972500	C	-2.30064500	0.55326000	0.15370100
O	-1.72750900	-1.02516400	1.77748500	C	-3.51621200	-0.11921700	-0.17892700
C	-5.12076400	-0.20263500	-0.43293400	O	-1.08214900	-3.07119900	1.70345800
C	-5.30257100	1.11221000	-0.80371300	C	-4.24172200	-4.35601700	-0.60465300
C	-4.29627600	2.08867700	-0.65018800	C	-5.15411700	-3.42162100	-1.03235900
C	-3.87531600	-0.51877000	0.13519900	C	-4.92121800	-2.04303200	-0.86338500
H	-6.25417100	1.44613900	-1.20588200	C	-3.07567500	-3.91105900	0.01939900
H	-3.69293300	-1.52163900	0.50994500	H	-4.43154300	-5.41786900	-0.71779200
C	-3.76135900	4.44363500	-0.67220900	H	-6.09378100	-3.73129100	-1.48158000
H	-4.03159900	5.48457200	-0.82521900	H	-2.36920100	-4.62473300	0.42799200
C	-2.43033800	4.15278000	-0.22373900	C	-5.87336200	0.17534600	-0.90565800
C	-4.63992600	3.45271600	-0.92624700	H	-6.69643200	0.86016800	-1.08851400
H	-5.63946400	3.66719200	-1.29321100	C	-4.64856700	0.71646100	-0.39056700
C	0.20649100	3.73228400	0.43974200	C	-5.98691100	-1.13869100	-1.18304100
C	-1.56176800	5.24006100	-0.00312000	H	-6.90183300	-1.54983700	-1.59946800
C	-0.24520900	5.05819800	0.36243800	C	-2.30481800	1.92150300	0.39822800
H	1.25147100	3.52984000	0.64434800	C	-4.60015700	2.10254400	-0.14346900
H	-1.97082000	6.23675500	-0.13638900	C	-3.44843300	2.72605600	0.28669200
C	-1.36877800	-5.44153500	0.41539400	H	-1.35190900	2.37172200	0.65103600
C	-2.69883900	-4.67897800	0.45300400	H	-5.51207300	2.66794400	-0.30809400
H	-2.75250300	-4.00272600	1.31414500	C	4.76584800	3.34009100	-0.50209000
H	-2.84246000	-4.09118200	-0.46099200	C	-3.35439100	4.21908200	0.59609000
H	-3.52834500	-5.38979100	0.52769700	C	-4.70199100	4.92479200	0.41906300
C	-1.24888700	-6.26870400	1.70628100	H	-4.59474700	5.98569000	0.66594300
H	-1.23320600	-5.61504100	2.58414200	H	-5.05963900	4.85792100	-0.61398000
H	-2.10057900	-6.95223000	1.79823700	H	-5.46694300	4.50265900	1.07960500
H	-0.33330100	-6.86803800	1.71467800	C	-2.89368500	4.40219800	2.05188400

C	-1.38751300	-6.38566500	-0.79795000
H	-1.46743900	-5.81767500	-1.73053500
H	-0.47888600	-6.99301900	-0.85008100
H	-2.24363200	-7.06671200	-0.73400700
C	0.72708100	6.20395200	0.63787000
C	0.04996200	7.57139200	0.50771300
H	0.77485700	8.36132400	0.72808500
H	-0.32761000	7.73948800	-0.50655400
H	-0.78366900	7.67585300	1.21043700
C	1.27660700	6.06432500	2.06742100
H	0.46615600	6.11169300	2.80197000
H	1.80393900	5.11569900	2.20556300
H	1.98150200	6.87585200	2.27920700
C	1.89003700	6.13615800	-0.36661700
H	2.43548500	5.19071500	-0.29131600
H	1.52202500	6.23296800	-1.39313600
H	2.59756200	6.95063700	-0.17564500
C	-6.18718900	-1.28619400	-0.58223000
C	-7.49121100	-0.72607700	-1.15785500
H	-7.34038300	-0.29672100	-2.15403100
H	-8.22585300	-1.53204100	-1.25011400
H	-7.91985700	0.04460000	-0.50832800
C	-5.66094600	-2.37640700	-1.53051800
H	-4.74673500	-2.83599500	-1.14221100
H	-6.41052700	-3.16667200	-1.64840400
H	-5.43931100	-1.96039000	-2.51861500
C	-6.48638000	-1.90767500	0.79242700
H	-5.60009200	-2.37957200	1.22787900
H	-6.84560400	-1.14807100	1.49401500
H	-7.25885200	-2.67799100	0.69272700
C	6.72469200	0.63084300	-0.64608700
C	6.83339800	1.59804300	0.54475700
H	7.68924300	2.26891500	0.40889000
H	5.93484900	2.21387300	0.64636600
H	6.97242700	1.04662400	1.48032100
C	6.52722800	1.43638500	-1.94124300
H	5.62046800	2.04723300	-1.90151300
H	7.37934100	2.10642700	-2.10238700
H	6.44628400	0.76789300	-2.80450900
C	8.04038800	-0.14566700	-0.75742000
H	8.24727200	-0.72055800	0.15146600
H	8.03091400	-0.83461400	-1.60867000
H	8.86767700	0.55606400	-0.90472500

2d (E = -1727.673628 Hartree)

C	2.46692000	2.80975100	-0.04701500
C	1.64802300	1.67614000	-0.12205400
C	2.16597700	0.38469800	-0.12454500
C	3.57354800	0.19427400	0.02675500
C	4.40703200	1.33859400	0.08967200
C	3.84134200	2.62248500	0.03773600
C	1.39094600	-0.82630200	-0.21323700
C	4.15364000	-1.11397800	0.15536800
C	3.34145100	-2.28004700	0.16212600
C	1.92783400	-2.08003100	-0.01855300
C	3.91332900	-3.53906000	0.32277400
H	3.26601000	-4.41012500	0.32780600
H	-3.60712200	3.94631400	2.74601200
H	-1.91420900	3.94646400	2.22502900
H	-2.81579400	5.46891600	2.28910700
C	-2.33222700	4.87097000	-0.35061100
H	-1.33763800	4.42890900	-0.23918900
H	-2.63962800	4.75230400	-1.39461700
H	-2.25203500	5.94202700	-0.13435500
C	4.24981800	4.16225100	0.69082900
H	4.53248300	5.21458500	0.57396700
H	3.15991300	4.11285300	0.77248100
H	4.67587700	3.79296600	1.62931500
C	6.28581300	3.51147700	-0.58396900
H	6.78023300	3.16384500	0.32929800
H	6.70739400	2.96669400	-1.43533300
H	6.52783600	4.57137400	-0.71243700
C	4.14682500	3.88209400	-1.80149400
H	4.49932700	3.31053400	-2.66618600
H	3.05442000	3.82510600	-1.78206900
H	4.42796900	4.93170800	-1.94375400

2e (E = -1727.671958 Hartree)

C	0.49053800	-4.41355700	0.23722100
C	0.08370500	-3.08315900	0.31293700
C	1.01971700	-2.04648300	0.29128600
C	2.40730500	-2.36751800	0.13923900
C	2.80361000	-3.73079200	0.08015100
C	1.83259900	-4.73898500	0.13846200
C	0.72282900	-0.63442300	0.36234200
C	3.41309400	-1.34912300	0.01246700
C	3.07185200	0.02770900	0.00670200
C	1.67888300	0.34251500	0.17699400
C	4.04994600	1.00209500	-0.14661800
H	3.73063100	2.04048700	-0.14821900

C	5.29408400	-3.66344100	0.46773300	C	5.40329900	0.66377900	-0.28937200
C	6.10570000	-2.53762700	0.46028500	C	5.74164300	-0.68649400	-0.28071400
C	5.55763100	-1.25535300	0.31136800	C	4.77783100	-1.69734400	-0.13872100
C	6.37816500	-0.07383800	0.32648400	C	5.14231500	-3.08822300	-0.15523800
C	5.82918500	1.15968700	0.22535900	C	4.19984200	-4.05432100	-0.05535300
H	6.45492200	2.04789000	0.25236600	H	4.47769900	-5.10463700	-0.08143500
H	7.45269600	-0.19543600	0.43457300	H	6.19287500	-3.34537200	-0.26156000
H	0.57624800	1.81405500	-0.17711200	H	-0.25808100	-5.19913800	0.26170100
H	4.51369200	3.47360700	0.08412800	H	-0.97189000	-2.86426400	0.39435300
H	7.18154700	-2.63770800	0.57727100	H	2.14680700	-5.77810300	0.09164200
N	0.95432900	-3.04466900	-0.02667100	H	6.77679300	-0.99410700	-0.39150200
C	-0.17926200	-2.41259700	-0.21406000	N	1.12491300	1.59418700	0.17819500
N	0.01931700	-1.04241200	-0.33350300	C	-0.16299100	1.41916900	0.34691300
C	-0.88512100	-0.15226400	-0.96760300	N	-0.47888700	0.07098900	0.45928200
C	-2.26026300	-0.06457200	-0.40445000	C	-1.68223200	-0.42501600	1.02115700
C	-3.08489300	-1.14080800	0.03330300	C	-2.96281500	0.02033200	0.40095700
C	-1.46560700	-3.11994600	-0.30070100	C	-3.31806600	1.34103800	0.00242700
C	-2.75962900	-2.56357800	-0.05563700	C	-1.09319000	2.55462500	0.44870800
O	-0.48030400	0.59899600	-1.82029800	C	-2.49327300	2.53533900	0.16614800
C	-3.94525400	1.62409600	0.17118800	O	-1.63468600	-1.28605900	1.86422800
C	-4.76450200	0.59277100	0.57653400	C	-5.12313200	-0.90083600	-0.31192600
C	-4.38326500	-0.76197900	0.47623000	C	-5.49382900	0.37729600	-0.66907800
C	-2.69915100	1.25033800	-0.35648700	C	-4.64706900	1.48987900	-0.48329600
H	-5.75932600	0.79605500	0.96107200	C	-3.85057900	-1.03670300	0.26650900
H	-2.03100600	2.00935600	-0.75132500	H	-6.47901600	0.57203200	-1.08171200
C	-5.12451200	-3.05821900	0.54379600	H	-3.52691200	-2.00505300	0.63419900
H	-5.88945200	-3.81304600	0.70176900	C	-4.48558800	3.89855600	-0.43662300
C	-3.82672100	-3.49560100	0.11691900	H	-4.91208900	4.88929100	-0.56463400
C	-5.37736100	-1.75361100	0.76725200	C	-3.13127900	3.80402700	0.02674000
H	-6.35095400	-1.41991300	1.11410400	C	-5.19476000	2.79150000	-0.73303100
C	-1.32069900	-4.49033000	-0.50823100	H	-6.21083800	2.85795600	-1.11084900
C	-3.63512800	-4.87423200	-0.08745300	C	-0.45172600	3.76186400	0.71947000
C	-2.39961600	-5.36877800	-0.43250000	C	-2.44436500	5.00124200	0.29775100
H	-0.32225100	-4.86570100	-0.69533700	C	-1.12241400	4.98259200	0.67522300
H	-4.48626400	-5.53760400	0.03806200	H	0.60922400	3.72893700	0.93358400
H	-2.25082400	-6.42906600	-0.60734000	H	-2.98246900	5.93959700	0.19650800
C	-4.33700000	3.09958800	0.22278800	C	6.44077900	1.77806500	-0.44800100
C	-5.69440600	3.30334900	0.90206400	C	6.39624800	2.69163300	0.78843800
H	-5.69125700	2.92138400	1.92864600	H	7.13172000	3.49781500	0.68803200
H	-5.92711100	4.37198600	0.94165600	H	5.41044200	3.14849200	0.91640000
H	-6.50048400	2.80895700	0.34977400	H	6.62683100	2.12572600	1.69685800
C	-4.41639800	3.64638000	-1.21290900	C	7.86380800	1.22944900	-0.59084500
H	-3.45734100	3.55456200	-1.73244500	H	8.16321500	0.65176400	0.29006500
H	-5.16957900	3.10489800	-1.79414200	H	7.96249400	0.59034100	-1.47468500
H	-4.69037200	4.70700900	-1.19561800	H	8.56703100	2.06135700	-0.69987600
C	-3.27346700	3.88645200	1.00721700	C	6.11126000	2.60244500	-1.70385300
H	-3.16758700	3.49710300	2.02502000	H	6.13651600	1.97210200	-2.59867200
H	-2.29408200	3.83935300	0.52055700	H	5.11800500	3.05645800	-1.63899000
H	-3.56091300	4.94160400	1.07017100	H	6.84357300	3.40811500	-1.82855400
H	5.73657200	-4.64730200	0.58840900	H	-0.59276800	5.90211000	0.90083100
C	1.80404600	4.18953800	-0.05623400	C	-6.01722500	-2.12801600	-0.47842800
C	0.90138000	4.31936300	1.18264000	C	-7.35499400	-1.77333900	-1.13398200
H	0.13224500	3.54031600	1.20379500	H	-7.21255800	-1.33720900	-2.12851500
H	1.48942700	4.23350200	2.10220700	H	-7.95728000	-2.67985900	-1.24913600
H	0.39710700	5.29268900	1.18426500	H	-7.92871200	-1.06778600	-0.52371600
C	0.95130200	4.33942200	-1.32819600	C	-6.29609400	-2.74396600	0.90304500

H	0.18147500	3.56356700	-1.39882000	H	-5.37364900	-3.05441000	1.40303500
H	0.45354700	5.31588500	-1.33423700	H	-6.80726200	-2.02614800	1.55243700
H	1.57588400	4.26490500	-2.22412100	H	-6.93419300	-3.62803800	0.79657900
C	2.83202200	5.32441100	-0.02740900	C	-5.29730300	-3.15942800	-1.36368800
H	3.44342700	5.29104200	0.88050300	H	-5.08722800	-2.74364400	-2.35437500
H	3.49830800	5.28376500	-0.89557200	H	-4.34810700	-3.47842800	-0.92211800
H	2.31479400	6.28913400	-0.04639200	H	-5.92458100	-4.04867900	-1.48896000
2f (*E* = -1727.673076 Hartree)				**5** (*E* = -1651.463680 Hartree)			
C	4.43180300	1.20421100	-0.16608900	C	-2.05071700	-4.82832300	-0.20530000
C	3.04385200	1.01370000	-0.16843200	C	-1.51995100	-3.55670300	-0.24045200
C	2.46492200	-0.24975000	-0.08890100	C	-2.35056000	-2.42050200	-0.15946200
C	3.30830000	-1.39455800	0.06519800	C	-3.75591300	-2.58968600	0.00830600
C	4.71291100	-1.20561900	0.06372400	C	-4.25986100	-3.90565100	0.02695900
C	5.24831400	0.08541600	-0.06326700	C	-3.43446600	-5.00507100	-0.08477000
C	1.04928700	-0.53025200	-0.10588600	C	-1.87325800	-1.06163600	-0.17019200
C	2.77533900	-2.71560900	0.25290800	C	-4.64446500	-1.43641000	0.20505900
C	1.37420800	-2.93805900	0.31309300	C	-4.10364600	-0.13329100	0.29545100
C	0.53190800	-1.78574200	0.13405300	C	-2.68841500	0.01275300	0.10793200
C	0.86835000	-4.21776500	0.52498800	C	-4.92583100	0.98084700	0.53524400
H	-0.20744000	-4.35322700	0.57038300	H	-4.45885300	1.95831100	0.60134300
C	1.73997500	-5.29553600	0.67019600	C	-6.28776300	0.81921300	0.67243900
C	3.11285000	-5.10106100	0.61118100	C	-6.84620200	-0.46408100	0.56832200
C	3.65145300	-3.82215000	0.40874900	C	-6.04277100	-1.56396400	0.34159700
C	5.07115000	-3.59678800	0.36609700	H	-0.44854100	-3.43530600	-0.32448800
C	5.57438800	-2.35042900	0.20556300	H	-3.85855000	-6.00387000	-0.06229100
H	6.64839800	-2.18527800	0.18594800	H	-7.91910500	-0.59708200	0.66669100
H	5.73190200	-4.45243400	0.47696300	N	-1.97591900	1.18145800	0.16693800
H	2.40549100	1.88289700	-0.24393100	C	-0.72747300	0.85462900	-0.06045200
H	6.32917100	0.18643500	-0.06653800	N	-0.59197700	-0.51329800	-0.26940500
H	3.79052900	-5.94264400	0.72780300	C	0.50371000	-1.11509100	-0.94049700
N	-0.83692500	-1.76359300	0.17521200	C	1.86313200	-0.89085700	-0.37226500
C	-1.18390800	-0.51483800	-0.02089500	C	2.40469200	0.33280100	0.11730200
N	-0.07076800	0.29778000	-0.19390600	C	0.34403300	1.86236700	-0.11177400
C	-0.10086100	1.58568700	-0.78590600	C	1.73760300	1.63005800	0.10272700
C	-0.98188100	2.60864000	-0.15540000	O	0.29423200	-1.89390000	-1.83734800
C	-2.32482200	2.43740600	0.28727500	C	3.91977300	-2.13481400	0.12492200
C	-2.59338200	-0.09786500	-0.09279000	C	4.46743700	-0.95280100	0.57317800
C	-3.10642300	1.20871100	0.17460400	C	3.76260500	0.26883700	0.53775500
O	0.67873800	1.85695000	-1.66567100	C	2.61325000	-2.05703900	-0.38545500
C	-0.96684200	4.94742000	0.50975100	H	5.48735700	-0.92174300	0.94423200
C	-2.27556900	4.82659800	0.91158400	H	2.14968900	-2.93858100	-0.81645600
C	-2.97434800	3.61190200	0.77064800	C	2.53226100	2.79032300	0.32240400
C	-0.34142300	3.83916300	-0.06284800	C	-0.13403000	3.16032500	-0.24570100
H	-2.81005200	5.68076800	1.31824900	C	1.99750100	4.08742600	0.19261400
H	0.66741000	3.92255500	-0.45271200	C	0.67383000	4.30117300	-0.12685700
C	-5.12411100	2.51371700	0.80545500	H	-1.19933700	3.26962500	-0.41284600
H	-6.19873600	2.51858500	0.96363000	H	2.67334200	4.92107200	0.35615900
C	-4.51581400	1.29596200	0.35195200	H	-5.32326900	-4.07133700	0.15091500
C	-4.37888800	3.60788800	1.05850300	H	-6.51380800	-2.53675200	0.26401600
H	-4.82974700	4.52333700	1.43024500	H	-6.92617100	1.67796200	0.85468400
C	-3.46464500	-1.15860200	-0.31045800	H	-1.39253700	-5.68906100	-0.26801400
C	-5.35807000	0.18835500	0.13164700	C	4.48059200	1.46285500	0.87447200
C	-4.86066000	-1.04390400	-0.23510600	C	3.90466000	2.67244500	0.72135700
H	-3.01311300	-2.12315300	-0.51184500	H	5.51237900	1.36806300	1.20026800
H	-6.42433500	0.34148600	0.26592600	H	4.45908200	3.58579600	0.91726400
H	1.34211900	-6.29257100	0.83152500	C	4.65548200	-3.47343500	0.12788100

C	4.97380500	2.63007900	-0.29299800	C	6.05814400	-3.35120000	0.73024000
C	4.46236900	3.47775600	0.88417600	H	6.02165100	-2.99821000	1.76641600
H	3.36903600	3.53028300	0.90090300	H	6.54403800	-4.33188000	0.72748600
H	4.79385800	3.05727100	1.83912900	H	6.68701400	-2.66629000	0.15158700
H	4.84631300	4.50110300	0.80577000	C	3.85285300	-4.48776800	0.96014300
C	4.47879700	3.24011800	-1.61609200	H	2.85023900	-4.64358400	0.54986800
H	3.38551100	3.25228200	-1.67452100	H	4.36588700	-5.45562800	0.96861200
H	4.83887400	4.27059300	-1.71428500	H	3.74607100	-4.14530100	1.99445800
H	4.84941800	2.66276700	-2.46920000	C	4.78530500	-3.98464300	-1.31694500
C	6.50489800	2.66822100	-0.28417100	H	3.80740100	-4.12851300	-1.78628700
H	6.91250500	2.26705100	0.64989000	H	5.35337000	-3.27725100	-1.92946800
H	6.92549600	2.09799900	-1.11907900	H	5.30788800	-4.94741300	-1.32778300
H	6.84649000	3.70377900	-0.38127900	C	0.05550300	5.68629700	-0.30864900
H	-0.43637000	5.88887500	0.60266200	C	1.09313600	6.80071100	-0.14512800
C	-5.73471100	-2.26580100	-0.51187900	H	0.61396900	7.77258500	-0.29965600
C	-7.22615800	-1.94079700	-0.38810900	H	1.52984500	6.80077400	0.85930100
H	-7.81542800	-2.83568100	-0.61146000	H	1.90326700	6.70639100	-0.87621600
H	-7.48561400	-1.61605500	0.62519900	C	-0.55008900	5.78471100	-1.71885700
H	-7.52678900	-1.15720200	-1.09188100	H	0.22060100	5.64431000	-2.48370900
C	-5.45997400	-2.76691900	-1.93964000	H	-1.32631900	5.03015000	-1.87750800
H	-5.70013900	-1.99353600	-2.67642100	H	-1.00413500	6.77112200	-1.86415400
H	-4.41119200	-3.04833500	-2.07327200	C	-1.05153400	5.89050000	0.73955800
H	-6.07505500	-3.64820100	-2.15228700	H	-1.84236200	5.14044600	0.64462500
C	-5.38979800	-3.37548300	0.49592800	H	-0.64307600	5.82421900	1.75312700
H	-4.33988700	-3.67488000	0.42506100	H	-1.50695200	6.87922400	0.61524200
H	-5.57712400	-3.04026400	1.52113100				
H	-6.00710100	-4.26007400	0.30410400				
4 (*E* = -1337.315930 Hartree)				**IM-5** (*E* = -1489.713333 Hartree)			
H	-1.90574600	4.52250400	-1.40978200	H	2.51499200	4.19908700	-2.23841200
C	-2.30935700	3.56282500	-1.10350400	C	2.74672200	3.24209800	-1.78121400
C	-3.38555200	1.06904000	-0.31157000	C	3.35232900	0.76390600	-0.60018100
C	-1.47576000	2.47429200	-0.95867200	C	1.72924200	2.31439600	-1.56735300
C	-3.68321200	3.42266900	-0.85526800	C	4.05408900	2.94993500	-1.41677900
C	-4.20658300	2.20432600	-0.46940200	C	4.37767100	1.72003700	-0.82685300
C	-2.00070500	1.23192900	-0.56503500	C	2.01857000	1.08249400	-0.98339200
H	-0.40892400	2.55104800	-1.14865800	H	0.70347300	2.52738800	-1.85199500
H	-4.34328500	4.27680000	-0.96863200	H	4.84539300	3.67517200	-1.58641900
H	-5.27319400	2.13542700	-0.28928300	C	3.67527400	-0.49869800	0.00946500
C	-3.92066600	-0.23914800	0.09505100	C	4.34141100	-2.95715000	1.20518800
C	-4.92458500	-2.77387600	0.86889000	C	2.67439600	-1.48442600	0.25739300
C	-3.06324600	-1.36398300	0.23549800	C	5.01756300	-0.77955200	0.37755700
C	-5.28976200	-0.44128400	0.36000200	C	5.32849200	-2.01054200	0.97216500
C	-5.78433500	-1.67444800	0.73777500	C	3.01976100	-2.69857100	0.85026300
C	-3.57805800	-2.61515400	0.61914900	H	6.35882600	-2.21480800	1.25007300
H	-5.98431700	0.38546800	0.26851200	H	2.25497400	-3.44753100	1.03631100
H	-6.84546900	-1.79031300	0.93319000	H	4.59785100	-3.90523600	1.66701700
H	-2.90593100	-3.46397000	0.71784200	C	1.01479700	0.08357700	-0.72505700
H	-5.31502300	-3.74223900	1.16448200	C	1.34482600	-1.12558600	-0.13933900
C	-1.15805000	0.08091300	-0.40500300	N	-0.33640500	0.16376800	-0.96101700
C	-1.67510200	-1.14224800	-0.03285800	N	0.15768100	-1.80798900	-0.04594200
N	0.19971700	-0.01020000	-0.58232800	H	-0.02963600	-2.62477000	0.52039200
N	-0.59186500	-1.99379400	0.00520100	C	-0.82312300	-0.98206100	-0.53425900
H	-0.58212000	-2.95928800	0.30029200	C	-2.22185300	-1.43395300	-0.66724800
C	0.51371600	-1.26215500	-0.32385500	C	-4.75329600	-2.25803500	-1.51272800
C	1.87047600	-1.81206200	-0.44019500	C	-3.34118800	-0.60273600	-0.37135700
C	4.45474900	-2.75580900	-0.87958200	C	-2.41096300	-2.67121000	-1.26184600

C	2.96542800	-1.07883600	0.04916800
C	2.07668300	-3.01726800	-1.11696400
C	3.36453500	-3.49488500	-1.32920300
C	4.25248000	-1.56123100	-0.19369500
H	1.22216700	-3.55790200	-1.51568200
H	3.51573800	-4.42703800	-1.86367200
H	5.10007400	-0.99362200	0.17874700
H	5.46483600	-3.11098600	-1.05677100
C	2.80634700	0.12296600	0.92952700
C	2.74197300	2.26911300	2.73453300
C	2.99785700	1.43540400	0.47779000
C	2.56761700	-0.09253300	2.28940900
C	2.51957100	0.97092600	3.18518300
C	2.99188100	2.49417200	1.38600800
H	2.43476600	-1.11110000	2.64384800
H	2.32531900	0.78215800	4.23644500
H	3.17989100	3.49575000	1.01188000
H	2.72369300	3.10154200	3.43065500
C	3.21306300	1.78323500	-0.97394700
O	4.11044600	2.50625700	-1.32815600
O	2.32657800	1.28039200	-1.83242200
H	1.55796200	0.85917300	-1.36427800

C	-3.68591800	-3.11293100	-1.64344900
C	-4.59396200	-0.99049400	-0.91239800
H	-1.54110200	-3.27735900	-1.49777500
H	-3.80835900	-4.08849500	-2.10210500
H	-5.73541600	-2.53544700	-1.88556800
C	-3.28638200	0.63228400	0.40484500
C	-3.20987600	3.16695700	1.68358100
C	-2.26815600	0.95461700	1.34547000
C	-4.34778300	1.56112300	0.26629500
C	-4.27419300	2.82968700	0.88461300
C	-2.22504300	2.20100600	1.94466400
H	-5.09308600	3.52723200	0.73075000
H	-1.45229300	2.41005100	2.67924900
H	-3.15728900	4.14062000	2.15899800
C	-1.35491700	-0.08304900	1.93532500
O	-1.72351200	-1.16918300	2.29964400
O	-0.07913100	0.30683800	2.13621000
H	0.11487500	1.08254500	1.58345300
C	5.72745000	1.40048600	-0.44158000
H	6.50110400	2.14198500	-0.62256100
C	6.03183200	0.21228600	0.13056000
H	7.05401900	-0.01903700	0.41782500
C	-5.54507400	1.18684300	-0.43302800
H	-6.34974600	1.91349700	-0.50052700
C	-5.69288900	-0.06533200	-0.91901400
H	-6.62521800	-0.38102700	-1.37869500

7. X-ray Structure of [2b·(TFA)$_2$]

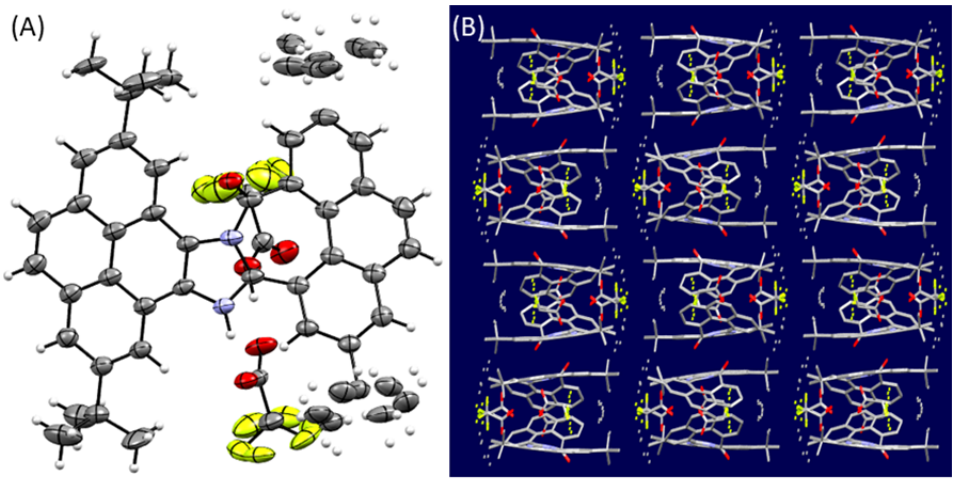

Fig. S-23. (A) ORTEP drawing (50% probability), and (B) crystal packing diagrams of the complex of [**2b**·(TFA)$_2$]. Hydrogen atoms are not shown for clarity.

Appendix V

Supporting Information for Chapter 7

Future Work

Table of Content

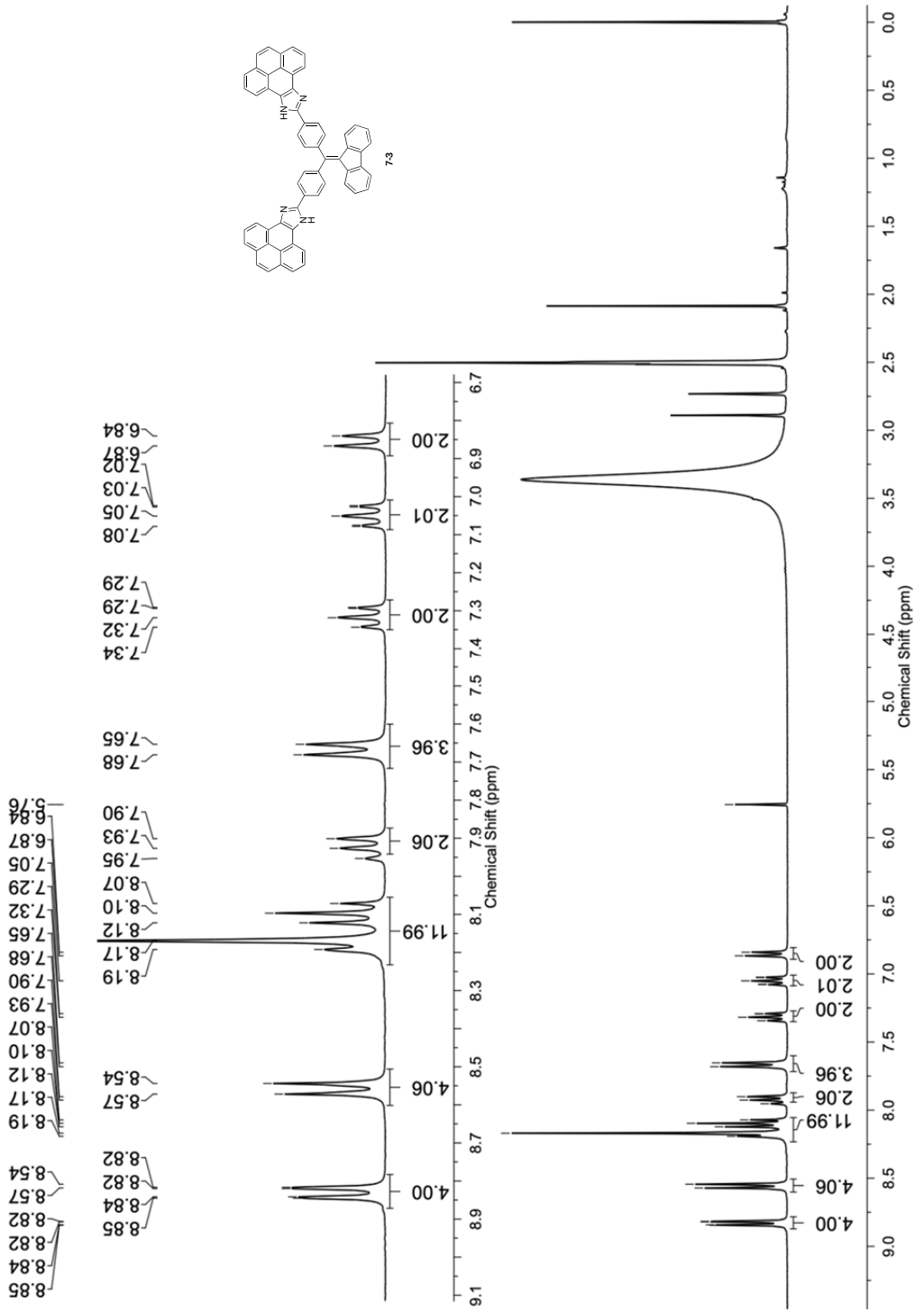

Figure 6.1: ^{1}H NMR (300 MHz CD_2Cl_2) of compound **7-3**

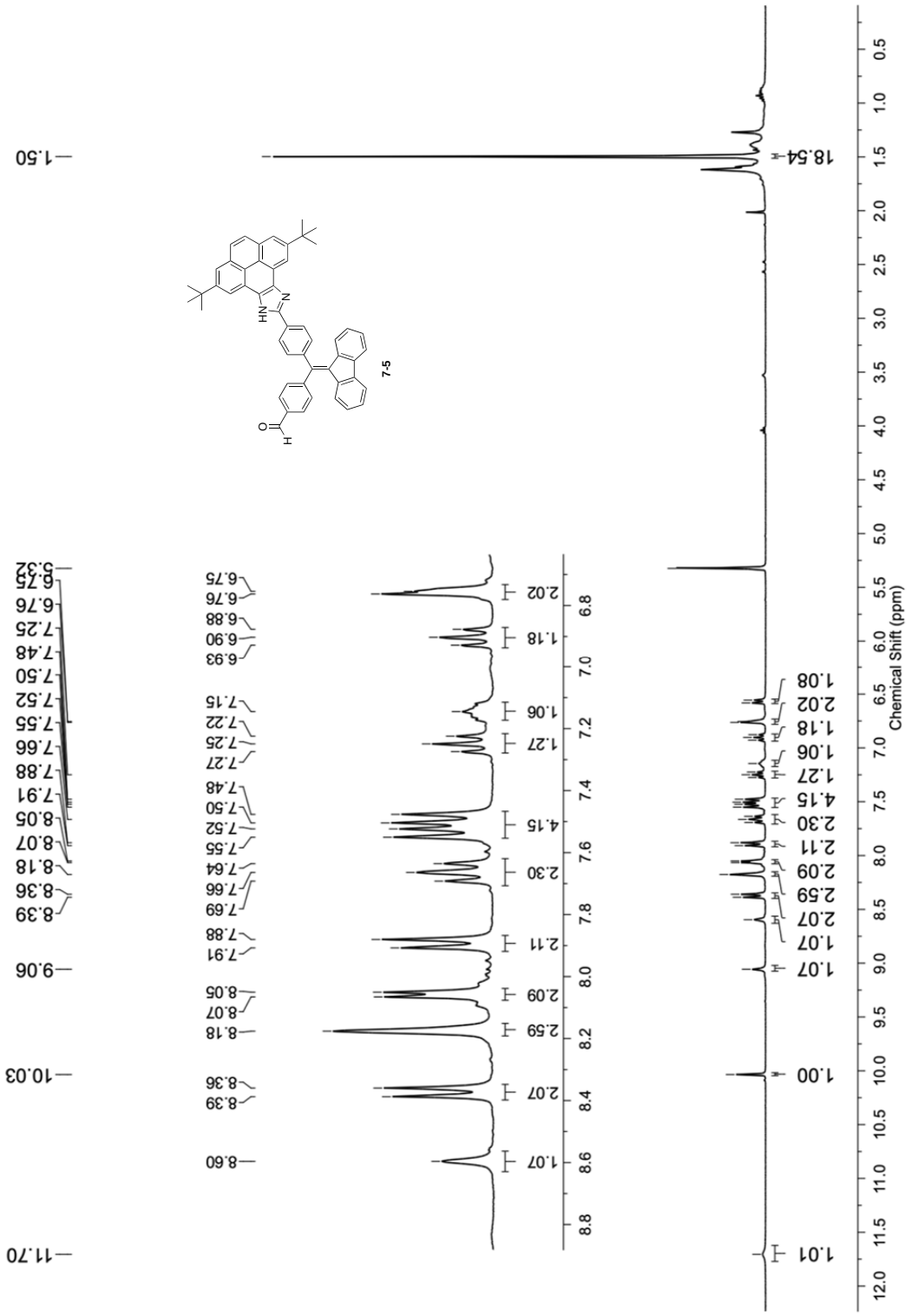

Figure 6.2: ^{1}H NMR (300 MHz DMSO-*d*) of compound **7-5**.

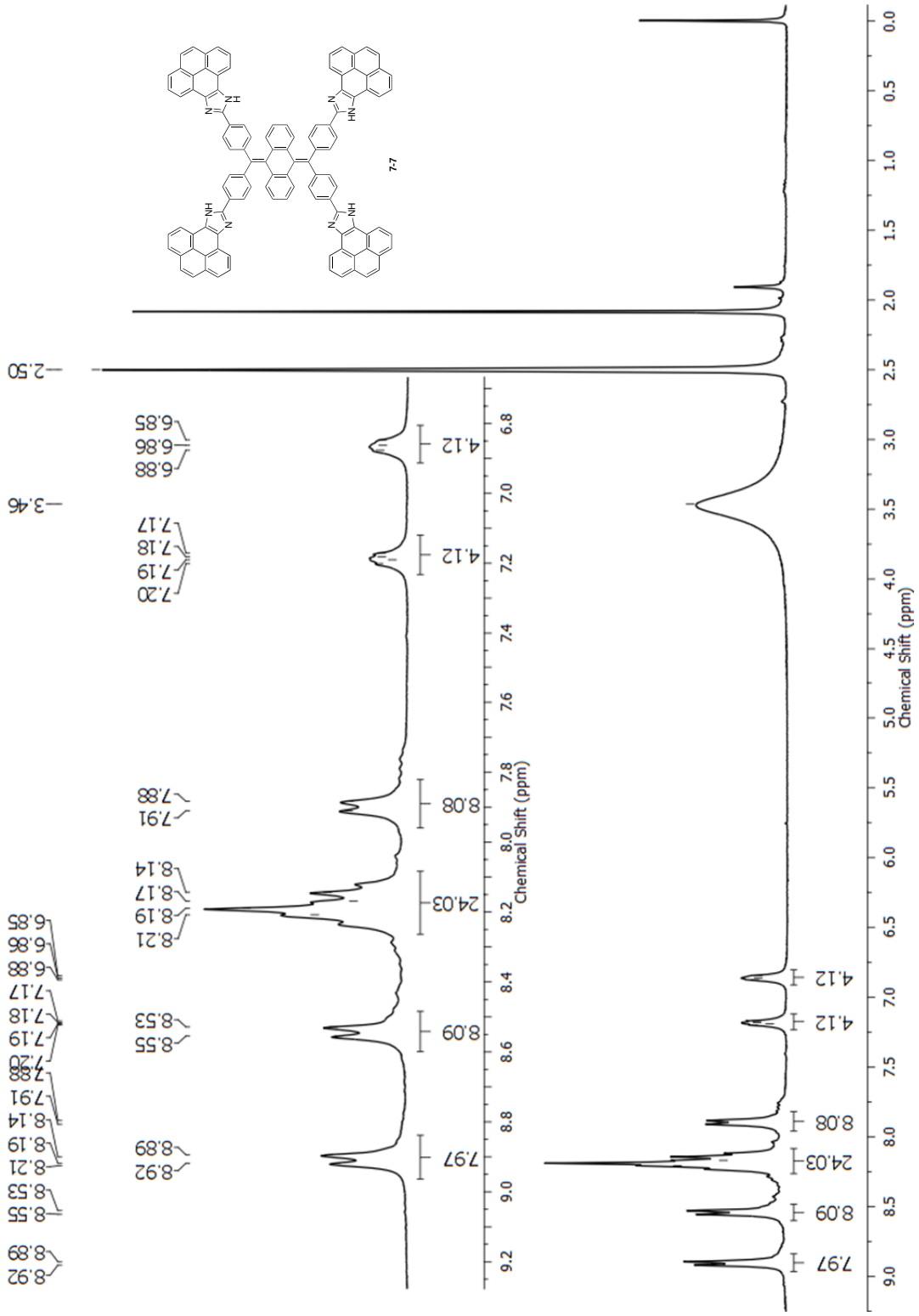

Figure 6.3: ^{1}H NMR (300 MHz DMSO-*d*) of compound **7-7**.

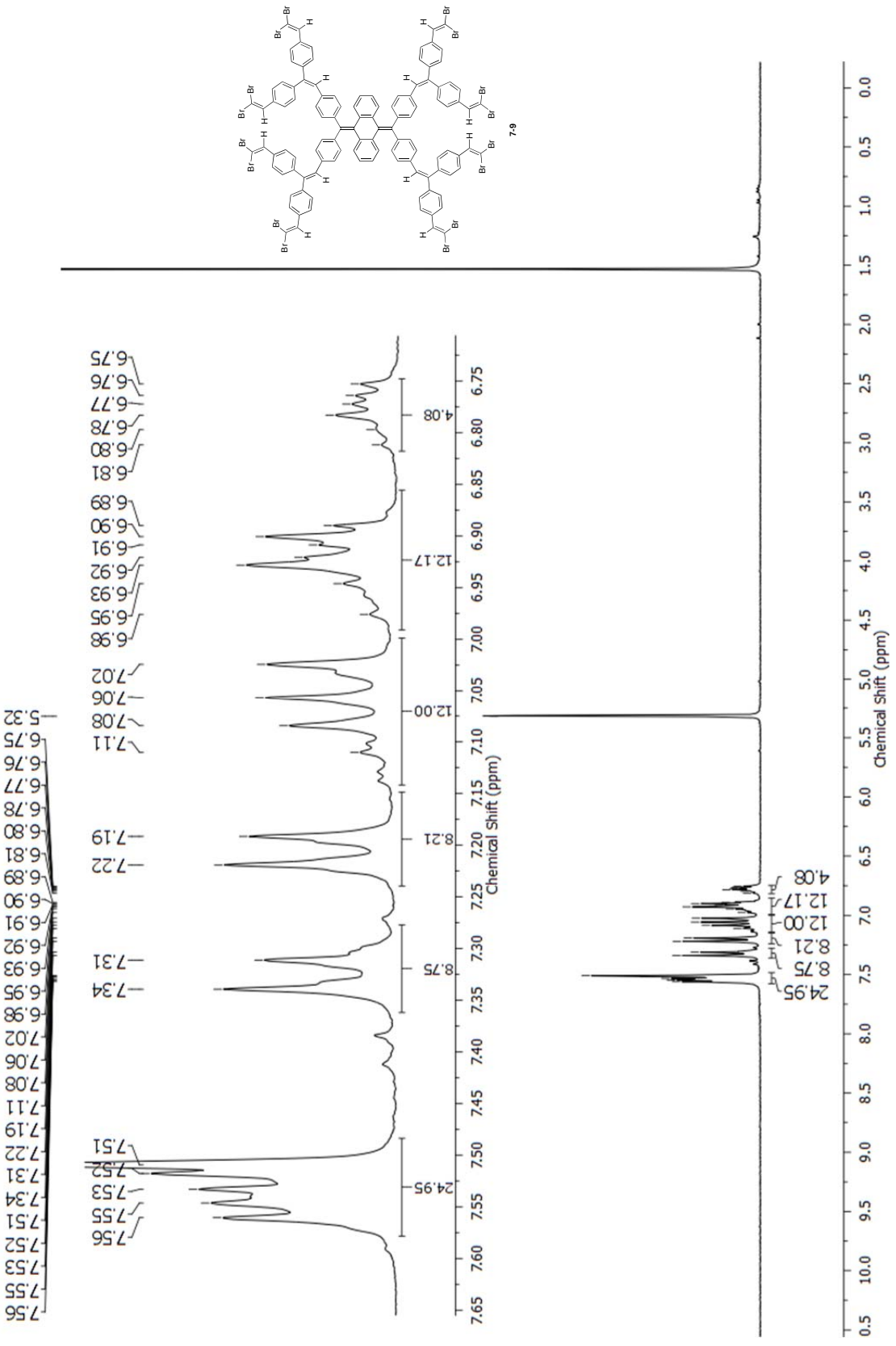

Figure 6.4: ^{1}H NMR (300 MHz CD_2Cl_2) of compound **7-9**.

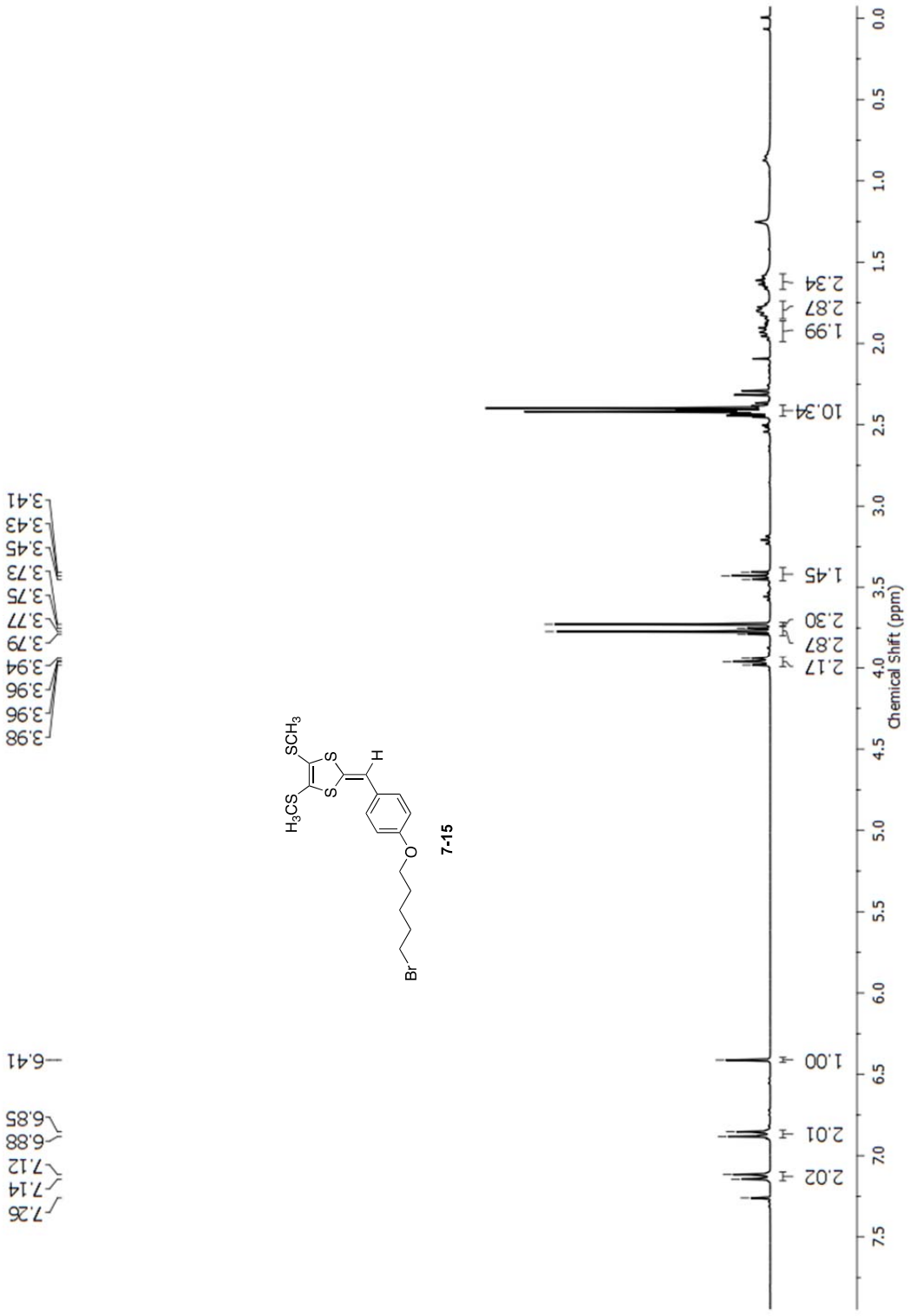

Figure 6.5: ^{1}H NMR (300 MHz CD_2Cl_2) of compound **7-15**.

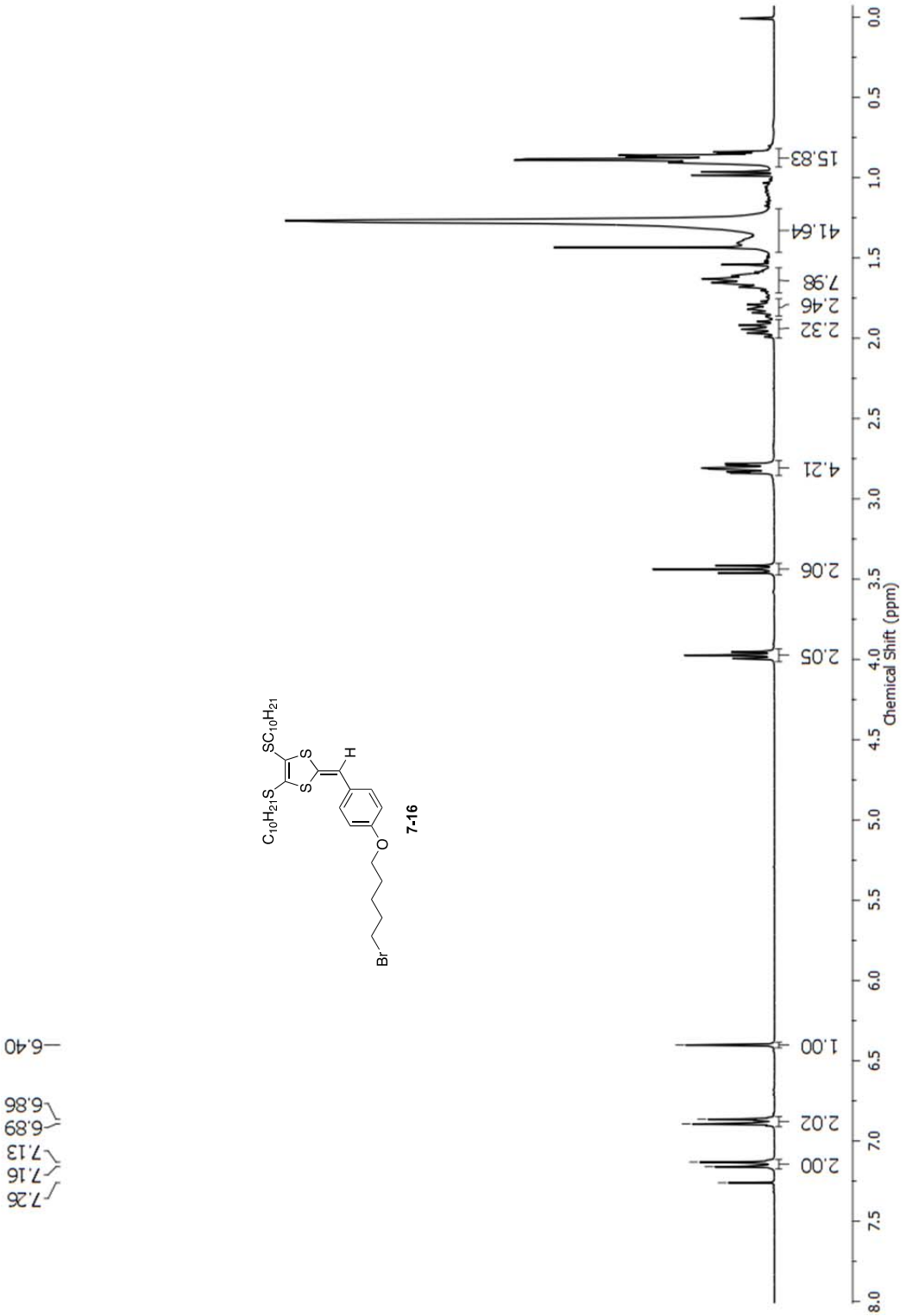

Figure 6.6: ^{1}H NMR (300 MHz CD_2Cl_2) of compound **7-16**.